# Hydrothermal fluid flow through gabbros at IODP site 1309, Atlantis Massif, Mid-Atlantic Ridge

Teddy Castelain

Submitted in accordance with the
requirements for the degree of
Doctor of Philosophy

The University of Leeds
School of Earth and Environment

April 2011

The candidate confirms that the work
submitted is his own and that appropriate credit
has been given where references
have been made to the work of others.



April 2011

The University of Leeds

Teddy Castelain

# Acknowledgements

This work would not have been possible without the support and the valuable help in the writing up of this thesis of Dr. Andrew McCaig, and Dr. Bob Cliff. I wish then to express my gratitude to both them.

I would like also to thank Dr. Eric Condliffe, Christine Rogers, and Linda Forbes for their assistance, guidance and advice during laboratory work. Working with you has been enriching and a real pleasure.

Thanks go to Dr. Anthony Fallick of the University of Glasgow (SUERC) for providing oxygen isotope analyses.

Dr. Adélie Delacour and Dr. Gretchen Früh-Green are thanked for kindly sharing strontium isotope data.

Anja Schmidt and Kay Barbara are thanked for their support and enriching discussions that helped me to go forward.

Thanks go also to Bruce Yardley and Damon Teagle for their valuable critics on my thesis ans advice on the corrections needed to make this thesis better.

Je souhaite ensuite remercier du plus profond de mon cœur ma famille : mon père Rudy, ma mère Martine, mes trois frères David, Sébastien et Frédéric et ma petite sœur Heïdi pour leur soutien moral pendant ces quatre années durant lesquelles j'ai travaillé sur ce projet.

Je voudrais finalement remercier ma fiancée Karlyne Gomez envers qui je suis très reconnaissant pour m'avoir soutenue et donné la force nécessaire pour surmonter tous les moments difficiles. Elle a été extrêmement patiente et compréhensive. Je voudrais aussi remercier mon nouveau-né qui m'apporte beaucoup de joie et de fierté.

# Abstract

Alteration of the oceanic crust by hydrothermal circulation is one of the most important processes in the Earth System, responsible for cooling of ocean lithosphere affecting the heat budget of ocean crust and making a significant contribution to the chemistry and the isotopic composition of oceans. Oceanic crust has been proven to be structurally heterogeneous depending on the rate of spreading. Fast spreading crust is characterised by a layer cake model with pillow lavas underlain by sheeted dykes and plutonics, whereas ultra-slow/slow spreading oceanic crust is more complex with gabbro bodies intruded into peridotites brought to the surface via low angle detachment faults, forming oceanic core complexes (OCCs). Large hydrothermal systems such as TAG (Trans-Atlantic Geotraverse) are associated with detachment faults and may involve much deeper fluid circulation than typical systems at fast spreading ridges. The Atlantis Massif, 30°N is an OCC located at the inside corner high between the Mid-Atlantic Ridge and the Atlantis Transform Fault that has been drilled during IODP legs 304 and 305. IODP Hole U1309B and D are dominated by gabbro with minor interlayered ultramafic rocks and diabases intruded at the top.

The aims of this project are to characterise the fluids that circulated in the section sampled by IODP Holes U1309B and D and to assess what processes control the fluid chemistry, to assess fluid fluxes related to various stages of alteration, and to better constrain how fluids circulate in OCCs by placing the results in the context of models for hydrothermal circulation at TAG. Fluid inclusion analyses – microthermometry and LAICPMS – and isotopic analyses of strontium and oxygen were undertaken in an attempt to answer these questions.

Fluid inclusion microthermometry underlines the occurrence of four types of fluid in the Atlantis Massif. Fluid type 1a is a seawater-like salinity fluid that is observed in late quartz vein precipitating at low pressure low temperature. Fluid type 1b is depleted with respect to seawater salinity and is

observed in plagioclase of gabbros and is the result of mixing with recharge seawater and supercritically phase-separated seawater-derived fluid. High salinity fluid (Type 3a) and halite-saturated fluid (type 3b) are observed in quartz grains of a trondjhemite intrusion. These fluids are interpreted to be generated by condensation of a magmatic fluid. Fluid chemistry is controlled by phase separation processes and mainly by fluid-rock interactions.

Isotopic analyses show that fluids circulated mainly close to the detachment fault and that limited amounts of fluid escaped into the footwall. Whole rock isotopic analyses show that gabbros are relatively little altered while serpentinites show elevated strontium isotope ratios. Small sample analyses show that gabbros are heterogeneous, with amphibole vugs and prehnite showing elevated seawater-like values, amphiboles replacing pyroxene intermediate values, and plagioclase commonly retaining igneous values. Serpentinites might be contaminated by late carbonate precipitation. However, the elevated strontium isotope ratio of prehnite replacing plagioclase during formation of micro-rodingite argues for the serpentinising fluid being seawater like. Oxygen isotope analyses support the conclusions of metamorphic petrology, that the majority of alteration took place at temperatures > 300 °C. The patterns of hydrothermal alteration can be understood in terms of kinetically limited exchange of isotopes between fluid and rock. High flux pathways such as the amphibole vugs were formed at low effective Damköhler numbers ($N_D$), such that the amphibole reflects the fluid composition while the altered plagioclase in the vug walls have rock-dominated isotopic ratios. Tremolite-talc veins also appear to have formed under high flux, low $N_D$ conditions, while tremolite-chlorite coronas and micro-rodingite veins are also quite high flux features. Reaction permeability may have played a role in generating all of these fluid pathways. Although nominal fluid fluxes can be calculated on the basis of the downhole isotopic profile, it is likely that the main direction of fluid flow was parallel to the fault and hence perpendicular to the Hole. The evolution of fluid flow and alteration in the Atlantis OCC can be interpreted in terms of the TAG model in which fluid discharge at black smoker temperatures occurs up the fault zone.

# Table of content

# Table of figures

# Chapter 1. Introduction

## 1.1 Introduction to the scientific problem

Alteration of the oceanic crust by hydrothermal circulation is one of the most important processes in the Earth System, responsible for cooling of ocean lithosphere affecting the heat budget of ocean crust (Stein & Stein, 1994) and making a significant contribution to the chemistry and the isotopic composition of oceans (Edmond, *et al.*, 1979; Palmer & Edmond, 1989). The ocean crust is one of the last frontiers for geological studies but the problem is that key samples are hard to collect and most of the crust is inaccessible. The composition of hydrothermal vent fluids and the composition of seawater are well known, but because of the sampling difficulties, the state of knowledge regarding fluid flow mechanisms is still quite ill-defined.

In addition, heterogeneities of the oceanic lithosphere make the challenge even more difficult. Variations in crust structure are indeed observed between ultraslow/slow spreading crust and fast spreading crust. Fast spreading crust is characterised by a significant magma supply and "cake model" crust with pillow lavas underlain by diabase sheeted dikes and gabbros. Slow spreading ridges crust is structurally more complex and is mainly characterised by a low magma supply and low angle detachment faults responsible for the exhumation of lower crustal and upper mantle rocks on the seafloor forming corrugated massifs. These massifs are known as oceanic core complexes (OCCs) (Blackman, *et al.*, 2002; Cann, *et al.*, 1997; Dick, *et al.*, 1991; Dick, *et al.*, 2000; Karson, 1990; Tucholke & Lin, 1994; Tucholke, *et al.*, 1998). Approximately half of the global mid-ocean ridges spreads at slow rates (Carbotte & Scheirer, 2004) and OCCs have been estimated to cover approximately 30% of the Atlantic Ocean floor (Smith, *et al.*, 2008) so hydrothermal alteration of such crust is important for the evolution of the lithosphere and the geochemical budget of oceans. Large hydrothermal systems such as TAG (Trans-Atlantic Geotraverse) are associated with detachment faults and may involve much deeper fluid circulation than typical systems at fast spreading ridges

Nonetheless, even if an important number of OCCs have been identified along the Mid-Atlantic Ridge, only two have been extensively studied: the 15°45'N Massif and the Atlantis Massif (Blackman, *et al.*, 1998; Blackman, *et al.*, 2006b; Blackman, *et al.*, 2002; Boschi, *et al.*, 2006; Cann, *et al.*, 1997; Delacour, *et al.*, 2008a; Delacour, *et al.*, 2008b; Delacour, *et al.*, 2008c; Escartín, *et al.*, 2003; McCaig, *et al.*, 2010; McCaig, *et al.*, 2007; Nozaka & Fryer, 2011).

The Atlantis Massif (AM) is an Oceanic Core Complex (OCC), which formed in the past 1.08 ± 0.07 My to 1.28 ± 0.05 My (Grimes, *et al.*, 2008), located at the inside corner of the Mid-Atlantic Ridge (MAR) and the Atlantis Transform Fault (ATF) (30°N) (*Figure 2-1*). The AM is composed of three different parts: The central dome dominated by gabbroic rocks, the southern wall dominated by serpentinites, being the host of the Lost City hydrothermal field, and the eastern block, interpreted as a fault-bounded block of basaltic material structurally lying above the central dome. The central dome has been the subject of two consecutive IODP expeditions 304 and 305 in order to investigate processes controlling the formation of OCCs and the exposure of ultramafic rocks in a young oceanic lithosphere. Overall, two deep holes (U1309B and U1309D), and five shallow-penetration holes recovering upper sediment cover and fragments of detachment faults (U1309A and U1309E-H) have been drilled (*Figure 2-1*). More details are provided in chapter 2.

## 1.2 Main goals and objectives of the thesis

The aims of this project are (1) to test and refine models for permeability generation and hydrothermal alteration in oceanic gabbros, (2) to characterise the fluids that circulate in IODP hole U1309D, (3) to assess fluid fluxes related to various stages of alteration, (4) to assess what processes control the fluid chemistry, (5), to better constrain how fluids circulate in OCCs.

To answer these questions, fluid inclusion studies such as microthermometry (Chapter 3), and Laser Ablation Inductively Coupled Plasma Mass Spectrometry (Chapter 4), and geochemical studies of strontium and oxygen isotopes (Chapter 5) were undertaken. These studies were carried out with the support of transmitted microscope and Scanning Electron Microscope (SEM) + Electron Microprobe Microanalyser (EPMA) observations and analyses of alteration fronts and phases.

Fluid inclusion work was conducted on quartz veins and plagioclases in gabbros as well as quartz grains of a trondjemitic intrusion. Strontium and oxygen measurements were carried out on powders and/or mineral extracts of lithologies representative of the diversity of both IODP Hole U1309B and D.

## 1.3 Thesis outline

The following chapters present petrological, chemical, and geochemical studies on samples from IODP Hole U1309B and D located at the central dome of the Atlantis Massif. Throughout the thesis the inferred geology beneath the TAG hydrothermal field is used as a framework within which to interpret the data obtained from the Atlantis massif, an analogy first proposed by McCaig *et al.*, (2010).

This chapter presents the overview of the thesis with scientific background to the research.

Chapter 2 describes the geology of the Atlantis Massif and contains petrographic descriptions of rocks recovered at the central dome of the Atlantis Massif during the 304 and 305 expeditions. Descriptions of all the rock types defined by Blackman *et al.* (Blackman, *et al.*, 2006a; Blackman, *et al.*, 2002) are given. Alteration history and common metamorphic reactions observed in the cores are also reviewed.

In chapter 3, fluid inclusions observed in quartz veins and in plagioclase of gabbros are described petrographically. Results from microthermometry are presented and compared to previous studies in oceanic sections (Kelley & Delaney, 1987; Kelley & Früh-Green, 2001; Kelley & Malpas, 1996; Kelley, *et al.*, 1993; Saccocia & Gillis, 1995; Tivey, *et al.*, 1998; Vanko, 1992) and in ophiolites (Cowan & Cann, 1988; Hopkinson & Roberts, 1996; Kelley & Robinson, 1990; Kelley, *et al.*, 1992; Morgan, 2008; Nehlig, 1991). This chapter also provides a discussion on processes generating salinity variations observed in the fluid inclusions. Results are finally replaced in the context of the TAG model interpreted from seismicity (deMartin, *et al.*, 2007) in order to better constrain the location of trapping of fluid inclusions during the exhumation history of the Atlantis Massif.

Chapter 4 summarises the fluid chemistry of fluid inclusions obtained by Laser Ablation Inductively Coupled Plasma Mass Spectrometry (LAICPMS). The results are compared to data from Troodos and from IODP Hole U1256D (Morgan, 2008) that is to date the only study of fluid inclusion

chemistry in oceanic sections. In the past, Results are compared to TAG vent fluids as a means of constraining the nature of fluid trapped in fluid inclusions in the hydrothermal system. Finally, a discussion on the processes influencing the chemistry of hydrothermal fluids is undertaken in which metamorphic reactions observed in the core are reviewed.

Chapter 5 gives the results from isotopic analyses on samples from IODP Holes U1309B and D. Strontium and oxygen isotopes were combined in order to better constrain the intensity and temperature of seawater/rock interaction at the Atlantis Massif. Previously reported small sample results are also presented. Extracts from individual minerals have been analysed both for strontium and oxygen, in addition to the bulk rock from which they belong. Results are compared to various oceanic sections such as the 15°45'N Massif (McCaig, *et al.*, 2007), IODP Hole 504B (Alt, *et al.*, 1996) and 735B (Hart, *et al.*, 1999). Results are also used to quantify fluid fluxes at the Atlantis Massif and replaced in the context of the TAG model.

Chapter 6 summarises the main results and conclusions of this work, in addition to views on potential and needed future work.

Appendices are presented at the end of the thesis. It comprises all the micro probe analyses (appendix 1), all the microthermometry measurements (appendix 2), LAICPMS data (appendix 3), details on analytical procedures used for strontium analyses (bulk rock and small samples) (appendix 4).

## 1.4 References

Alt, J. C., Teagle, D. A. H., Bach, W., Halliday, A. N. & Erzinger, J., 1996. Stable and Strontium Isotopic Profiles Through Hydrothermally Altered Upper Oceanic Crust, Hole 504B. In: *Proceedings of the Ocean Drilling Program, Scientific Results, Vol.148*, JC Alt, H Kinoshita, L B Stokking, and P J Michael.

Blackman, D. K., Cann, J. R., Janssen, B. & Smith, D. K., 1998. Origin of extensional core complexes: Evidence from the Mid-Atlantic Ridge at Atlantis Fracture Zone. *Journal of Geophysical Research*, **103**, 21.

Blackman, D. K., Ildefonse, B., John, B. E., Ohara, Y., Miller, D. J., McLeod, C. J. & Scientists, E., 2006a. Expedition 304/305 summary. *Proceedings of the Integrated Ocean Drilling Program*, **304/305**, 1-60.

Blackman, D. K., Ildefonse, B., John, B. E., Ohara, Y., Miller, D. J., McLeod, C. J. & Scientists, E., 2006b. Oceanic core complex formation. *Atlantis Massif*, **304/305**, Integrated Ocean Drilling Program Management International, Inc., College Station TX.

Blackman, D. K., Karson, J. A., Smith, D. K., Cann, J. R., Früh-Green, G. L., Gee, J. S., Hurst, S. D., John, B. E., Morgan, J., Nooner, S. L., Ross, D. K., Schroeder, T. J. & Williams, E. A., 2002. Geology of the Atlantis Massif (Mid-Atlantic Ridge, 30°N): Implications for the evolution of an ultramafic oceanic core complex. *Marine Geophysical Researches*, **23**, 443-469.

Boschi, C., Fruh-Green, G. L., Delacour, A., Karson, J. A. & Kelley, D. S., 2006. Mass transfer and fluid flow during detachment faulting and development of an oceanic core complex, Atlantis Massif (MAR 30°N). *Geochemistry Geophysics Geosystems*, **7**(1), 1-39.

Cann, J. R., Blackman, D. K., Smith, D. K., McAllister, E., Janssen, B., Mello, S., Avgerinos, E., Pascoe, A. R. & Escartin, J., 1997. Corrugated slip surfaces formed at ridge-transform intersections on the Mid-Atlantic Ridge. *Letters To Nature*, **385**, 329-332.

Carbotte, S. & Scheirer, D. S., 2004. Variability of ocean crustal structure created along the global mid-ocean ridges. In: *Hydrogeology of the Oceanic Lithosphere*, pp. 59-107, E. E. Davis and H. Elderfield, Cambridge University Press, Cambridge, U.K.

Cowan, J. & Cann, J. R., 1988. Supercritical two-phase separation of hydrothermal fluids in the Troodos ophiolite. *Nature*, **333**, 259-261.

Delacour, A., Früh-Green, G. L., Bernasconi, S. M. & Kelley, D. S., 2008a. Sulfur in peridotites and gabbros at Lost City (30°N, MAR): Implications for hydrothermal alteration and microbial activity during serpentinization. *Geochimica et Cosmochimica Acta*, **72**(20), 5090-5110.

Delacour, A., Früh-Green, G. L., Bernasconi, S. M., Schaeffer, P. & Kelley, D. S., 2008b. Carbon geochemistry of serpentinites in the Lost City Hydrothermal System (30°N, MAR). *Geochimica et Cosmochimica Acta*, **72**(15), 3681-3702.

Delacour, A., Früh-Green, G. L., Frank, M., Gutjahr, M. & Kelley, D. S., 2008c. Sr- and Nd-isotope geochemistry of the Atlantis Massif (30°N, MAR): Implications for fluid fluxes and lithospheric heterogeneity. *Chemical Geology*, **254**(1-2), 19-35.

deMartin, B. J., Sohn, R. A., Canales, J. P. & Humphris, S. E., 2007. Kinematics and geometry of active detachment faulting beneath the TAG hydrothermal field on the Mid-Atlantic Ridge. *Geology*, 711-741.

Dick, H. J. B., Meyer, P., Bloomer, S., Kirby, S., Stakes, D. & Mawer, C., 1991. Lithostratigraphic evolution of an *in situ* section of oceanic layer 3. *Proc. Ocean Drilling Program, Sci. Res.*, **118**, 439-538.

Dick, H. J. B., Natland, J. H., Alt, J. C., Bach, W., Bideau, D., Gee, J. S., Haggas, S., Hertogen, J. G. H., Hirth, G., Holm, P. M., Ildefonse, B., Iturrino, G. J., John, B. E., Kelley, D. S., Kikawa, E., Kingdon, A., LeRoux, P. J., Maeda, J., Meyer, P. S., Miller, D. J., Naslund, H. R., Niu, Y.-L., Robinson, P. T., Snow, J., Stephen, R. A., Trimby, P. W., Worm, H.-U. & Yoshinobu, A., 2000. A long in situ section of the lower ocean crust: results of ODP Leg 176 drilling at the Southwest Indian Ridge. *Earth and Planetary Science Letters*, **179**, 31-51.

Edmond, J. M., Measures, C., Mangum, B., Grant, B., Sclater, F. R., Collier, R., Hudson, A., Gordon, L. I. & Corliss, J. B., 1979. On the formation of metal-rich deposits at ridge crests. *Earth and Planetary Science Letters*, **46**(1), 19-30.

Escartín, J., Mével, C., MacLeod, C. J. & McCaig, A. M., 2003. Constraints on deformation conditions and the origin of oceanic detachments: The Mid-Atlantic Ridge core complex at 15°45'N. *Geochemistry Geophysics Geosystems*, **4**(8).

Grimes, C. G., John, B. E., Cheadle, M. J. & Wooden, J. L., 2008. Protracted construction of gabbroic crust at a slow spreading ridge: Constraints from $^{206}Pb/^{238}U$ zircon ages from Atlantis Massif and IODP Hole U1309D (30°N, MAR). *Geochemistry Geophysics Geosystems*, **9**(8), 1-24.

Hart, S. R., Blusztajn, J., Dick, H. J. B., Meyer, P. S. & Muehlenbachs, K., 1999. The fingerprint of seawater circulation in a 500-meter section of ocean crust gabbros. *Geochimica et Cosmochimica Acta*, **63**(23/24), 4059-4080.

Hopkinson, L. & Roberts, S., 1996. Fluid evolution during tectonic exhumation of oceanic crust at a slow-spreading paleoridge axis:

evidence from the Lizard ophiolite U.K. *Earth and Planetary Science Letters*, **141**, 125-136.

Karson, J. A., 1990. Seafloor spreading onn the Mid-Atlantic Ridge: Implications for the structure of ophioilites and oceanic lithosphere produced in slow-spreading environments. In: *Proceedings of the Symposium "Troodos 1987"*, pp. 125-130, J Malpas, E M Moores, A Panayiotou, C Xenophontos, Nicosia.

Kelley, D. S. & Delaney, J. R., 1987. Two-phase separation and fracturing in mid-ocean ridge gabbros at temperatures greater than 700C. *Earth and Planetary Science Letters*, **83**, 53-66.

Kelley, D. S. & Früh-Green, G. L., 2001. Volatile lines of descent in submarine plutonic environments: Insights from stable isotope and fluid inclusion analyses. *Geochimica et Cosmochimica Acta*, **65**(19), 3325-3346.

Kelley, D. S., Gillis, K. M. & Thompson, G., 1993. Fluid evolution in submarine magma-hydrothermal systems at the Mid-Atlantic Ridge. *Journal of Geophysical Research*, **98**(B11), 19579-19596.

Kelley, D. S. & Malpas, J., 1996. Melt-fluid evolution in gabbroic rocks from Hess Deep. In: *Proceedings of the Integrated Ocean Drilling Program, Scientific Results*, pp. 213-226, C Mével, K M Gillis, JF Allan, P S Meyer.

Kelley, D. S. & Robinson, P. T., 1990. Development of brine-dominated hydrothermal system at temperature of 400-500°C in the upper level plutonic sequence, Troodos ophiolite, Cyprus. *Geochimica et Cosmochimica Acta*, **54**, 653-661.

Kelley, D. S., Robinson, P. T. & Malpas, J. G., 1992. Processes of brine generation and circulation in the oceanic crust: Fluid inclusion evidence fron the Troodos ophiolite, Cyprus. *Journal of Geophysical Research*, **97**(B6), 9307-9322.

McCaig, A., Delacour, A., Fallick, A. E., Castelain, T. & Früh-Green, G. L., 2010. Detachment Fault Control on Hydrothermal Circulation Systems: Interpreting the Subsurface Beneath the TAG Hydrothermal Field Using the Isotopic and Geological Evolution of Oceanic Core Complexes in the Atlantic, *In* Rona, P. A., Devey, C. W., Dyment, J., Murton, B. J. (ed) Diversity of Hydrothermal Systems on, Slow Spreading Ridges, *AGU Geophysical Monograph*, **108**, AGU, pp; 207-240.

McCaig, A. M., Cliff, R. A., Escartin, J., Fallick, A. E. & MacLeod, C. J., 2007. Oceanic detachment faults focus very large volumes of black smoker fluids. *Geology*, **35**(10), 935-938.

Morgan, S. J., 2008. *High temperature fluid-rock interaction in oceanic crust: A study of fluid inclusions from the Troodos ophiolite and ODP/IODP Hole 1256D*, University of Leeds, Leeds.

Nehlig, P., 1991. Salinity of oceanic hydrothermal fluids: a fluid inclusion study. *Earth and Planetary Science Letters*, **102**(310-325).

Nozaka, T. & Fryer, P., 2011. Alteration of the Oceanic Lower Crust at a Slow-spreading Axis: Insight from Vein-related Zoned Halos in Olivine Gabbro from Atlantis Massif, Mid-Atlantic Ridge. *Journal of Petrology*, **52** (4), 643-664.

Palmer, M. R. & Edmond, J. M., 1989. The strontium isotope budget of the modern ocean. *Earth and Planetary Science Letters*, **92**(1), 11-26.

Saccocia, P. J. & Gillis, K. M., 1995. Hydrothermal upflow zones in the oceanic crust. *Earth and Planetary Science Letters*, **136**, 1-16.

Smith, D. K., Escartin, J., Schouten, H. & Cann, J. R., 2008. Fault rotation and core complex formation: Significant processes in seafloor formation at slow spreading mid-ocean ridges (Mid-Atlantic Ridge 13°-15°N. *Geochemistry Geophysics Geosystems*, **9**.

Stein, C. A. & Stein, S., 1994. Constraints on Hydrothermal Heat-Flux Through the Oceanic Lithosphere from Global Heat-Flow. *Journal of Geophysical Research-Solid Earth*, **99**(B2), 3081-3095.

Tivey, M. K., Mills, R. A. & Teagle, D. A. H., 1998. Temperature and salinity of fluid inclusions in anhydrite as indicators of seawater entrainmnent and heating in the TAG active mound. *Proceedings of the Integrated Ocean Drilling Program, Scientific Results*, **158**, 179-190.

Tucholke, B. E. & Lin, J., 1994. A geological model for the structure of ridge segments in low spreading ocean crust. *Journal of Geophysical Research*, **99**(B6), 11937-11958.

Tucholke, B. E., Lin, J. & Kleinrock, M. C., 1998. Megamullions and mullions structure defining oceanic metamorphic core complexes on the Mid-Atlantic Ridge. *Journal of Geophysical Research*, **103**(B5), 9857-9866.

Vanko, D. A., Griffith, J. D. & Erikson, C. L., 1992. Calcium-rich brines and other hydrothermal fluids in fluid inclusions from plutonic rocks, Oceanographer Transform, Mid-Atlantic Ridge. *Geochimica et Cosmochimica Acta*, **56**, 35-47.

# Chapter 2. The Atlantis Massif, IODP Site Hole U1309 B and D, 30°N Mid-Atlantic Ridge: Petrology and Metamorphism

## 2.1 Introduction

This chapter has the aim to set the geological context of this study. A summary of the principal features of the Atlantis Massif (AM) as well as the mechanism of formation of the massif are presented. Following this, the different types of rock recovered at IODP Hole U1309B and D are described with their primary and secondary mineral assemblage. Geochemistry of the principal secondary minerals encountered in all rocks (plagioclase and amphibole) analysed with electron micro probe is also presented in this chapter. The whole collection of analyses is tabulated in *Appendix 1*. The alteration history and metamorphic facies with their main consequences for rocks occurring in the AM are described. Finally, a description of the TAG hydrothermal system model that is going to be used in the following chapters is presented.

## 2.2 The Atlantis Massif

The Atlantis Massif (AM) is an Oceanic Core Complex (OCC), which formed between 1.08 ± 0.07 My and 1.28 ± 0.05 My (Grimes, *et al.*, 2008). It is located at the inside corner of the Mid-Atlantic Ridge (MAR) and the Atlantis Transform Fault (ATF) (30°N) (*Figure 2-1*). The OCC is a dome-like exposure of variably deformed and metamorphosed lower crustal and upper mantle rocks that has been unroofed by movement on a major detachment fault (*Figure 2-2*) (Blackman, *et al.*, 2002; Blackman, *et al.*, 2011; Cann, *et al.*, 1997; Dick, *et al.*, 1991; Dick, *et al.*, 2000; Karson, 1990; Tucholke & Lin, 1994; Tucholke, *et al.*, 1998).

The AM is composed of three different parts: The central dome, the southern wall, being the host of the Lost City hydrothermal field, and the eastern block, interpreted as a fault-bounded block of basaltic material lying structurally above the central dome. The central dome is characterised by a corrugated surface believed to be an exposure of a major detachment fault responsible for the uplift of the massif. The corrugations are parallel to the spreading directions and have a wavelength of approximately 1000 m, amplitude of tens of meters, and length of several kilometres (Cann, *et al.*, 1997).

The central dome has been the subject of two consecutive IODP expeditions 304 and 305 in order to investigate processes controlling the formation of OCCs and the exposure of ultramafic rocks in young oceanic lithosphere. Overall, two deep holes (U1309B and U1309D), and five shallow-penetration holes recovering upper sediment cover and fragments of detachment faults (U1309A and U1309E-H) have been drilled (*Figure 2-1*). Hole U1309B initiated at the same location as Hole U1309A (30°10.11'N, 42°07.11'W; 1642 mbsl) is 20 m away from Hole U1309D and was drilled up to 101.8 mbsf with an average recovery of 46% for the upper 25 m and 52% for the rest of the core. Site U1309 Hole D, located at 30°10.12'N, 40°07.11'W, 1645 mbsl, penetrated 1415.5 mbsf, with a recovery of 75% comprising intrusive basalt (3%), gabbroic (91%) and olivine-rich rock (5%) consisting of dunites, wehrlites, troctolites, as well as a few mantle

peridotites (harzburgite) in the upper 200 m (*Figure 2-3*). The core presents strong evidence of penetration of altering fluids. Alteration occurred over a range of temperatures ranging from granulite facies to zeolite facies. For more details, see paragraph *2.5*.

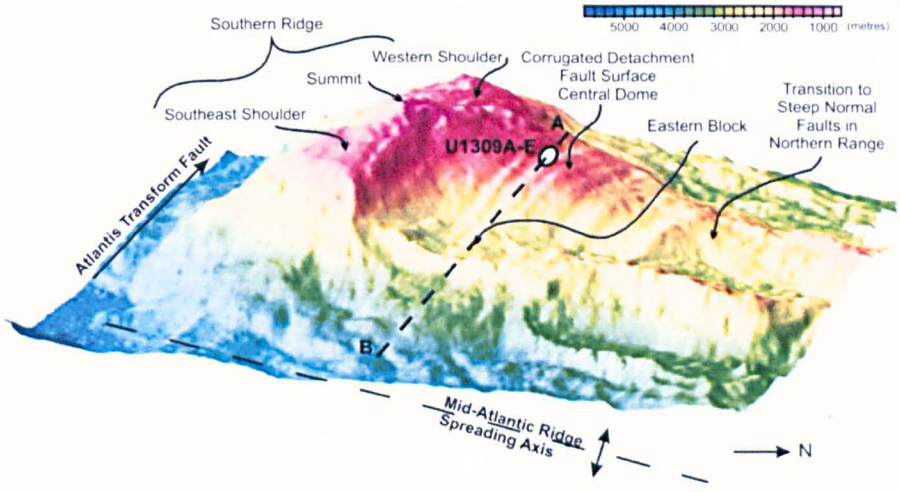


**Figure 2-1: 3D view of the Atlantis Massif from a WSW perspective, showing morphotectonic features (different parts of the massif), and the location of IODP holes U1309A-E. Illumination comes from SE. Vertical exaggeration is about 1.8. A colour scale is shown to indicate the bathymetry.(Blackman, *et al.*, 2006).**

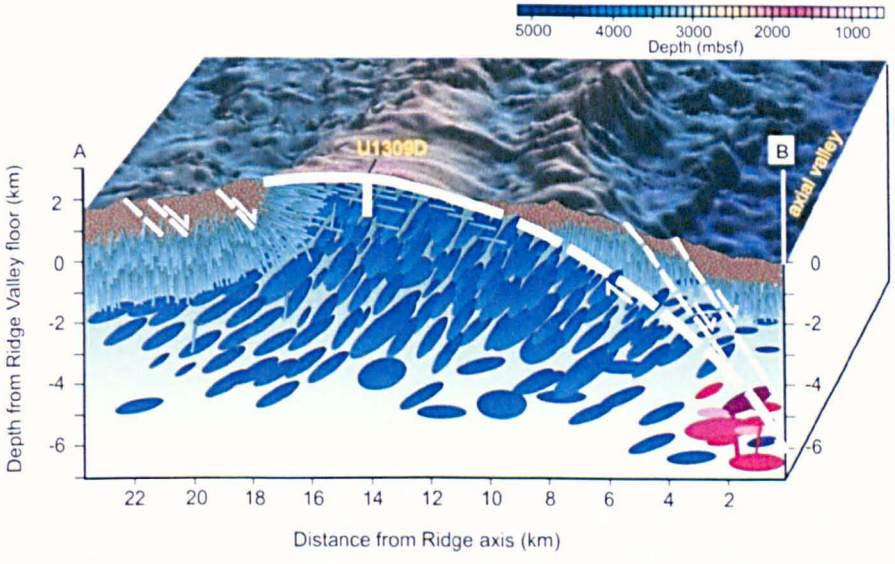


**Figure 2-2: Schematic 3D cross section of the Atlantis Massif. Detachment fault is shown as a curved white line which steepens at depth. Location of U1309D is also shown in white. Red bodies represent active zones of intrusions. Blue sills are gabbro bodies intruding each other and forming the plutonic sequence of the lithospheric crust. Dykes also intrude one another and are shown in blue green. Pillow lavas lie on top of the dykes (from Grimes *et al.*, 2008).**

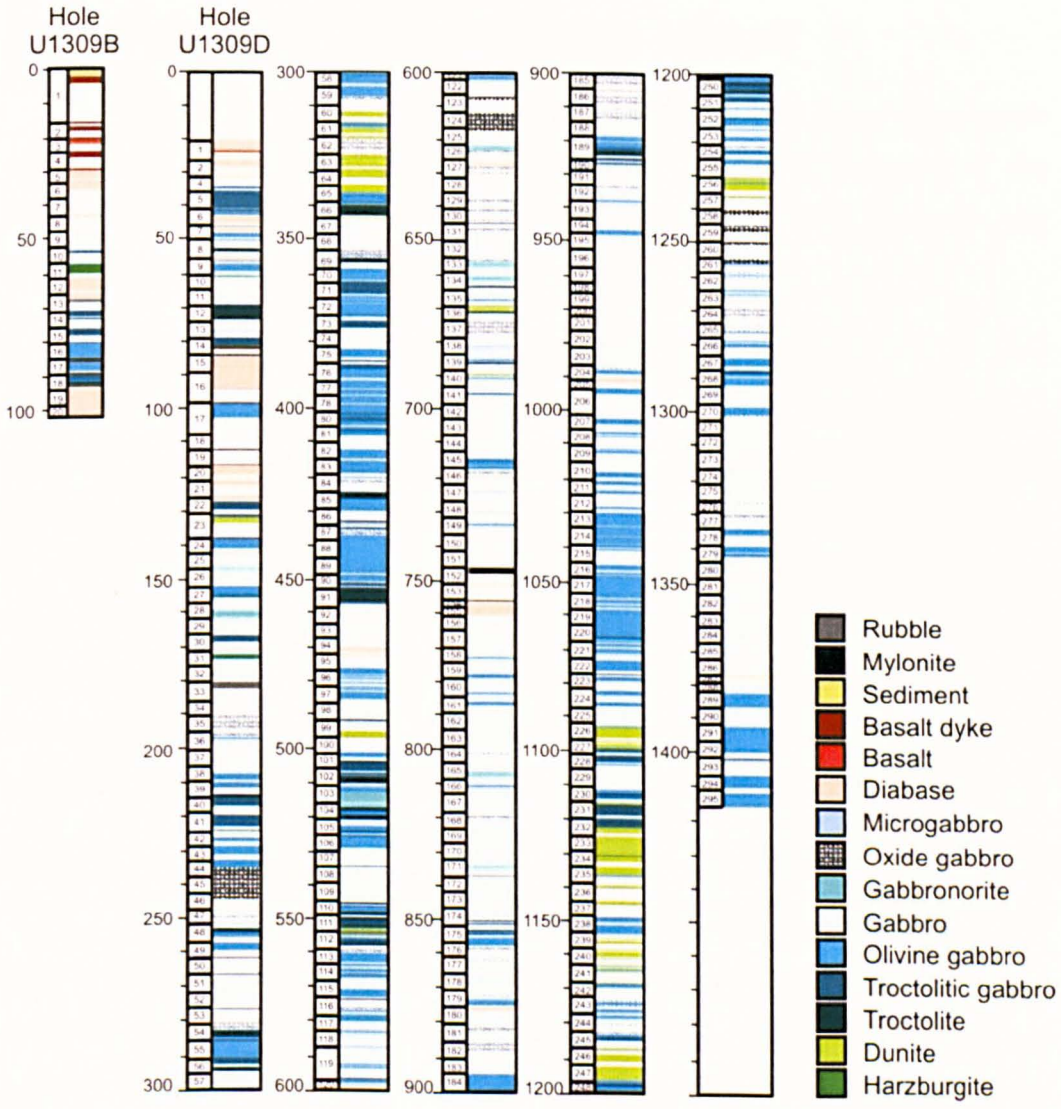


**Figure 2-3: Lilthostratigraphy of holes U1309B and U1309D (Blackman, *et al.*, 2006).**

# 2.3 Petrology of the Atlantis Massif

This section describes the igneous petrology and the metamorphic petrology of lithologies recovered at the two main core sections of the Atlantis Massif during campaign 304 and 305, IODP Hole U1309B and U13409D.

## 2.3.1 Igneous and metamorphic petrology

Samples recovered at IODP Hole U1309B and U1309D are mainly from the gabbro group with a few intercalated serpentinised peridotites and olivine-rich troctolites. Basalts and diabases are recovered in the upper part of the cores and locally as intrusions into other lithologies deeper in the holes. These lithologies represent approximately 3% of the overall coverage. The gabbroic rocks are variable in composition and comprise medium to coarse-grained gabbro and gabbronorites (55.7%), olivine gabbros and troctolitic gabbros (25.5%), troctolites (2.7%), and oxide gabbros (7%).

### 2.3.1.1 Diabase

Diabases are recovered mainly from the upper 150 mbsf of the IODP Hole U1309D but also occur as intrusions into gabbro at several depths (the deepest was recovered at 1377.6 mbsf). In Hole U1309B, diabases are present throughout the entire depth (*Figure 2-3*). Basalt represents the fine-grained margins of diabase intrusions, and the apparently higher proportion of basalt relative to diabase in Hole 1309B is not significant.

Diabases are characterised by a fine to medium-grained ophitic to subophitic texture with laths of plagioclase surrounded by clinopyroxene (*Figure 2-4A*). Clinopyroxene is partially altered to amphibole, and plagioclase is relatively unaltered; non-uniform alteration to albite occurs in the rim or in the core of laths.

### 2.3.1.2 Gabbro and gabbronorite

Gabbros and gabbronorites are the most common lithologies in both IODP Hole U1309B and D (*Figure 2-3*). They are found at all levels in both cores. Primary mineral assemblage for gabbros consists of anhedral

plagioclase of intermediate composition (labradorite/bytownite; see paragraph *2.4.1*) and anhedral clinopyroxene, Fe oxides, and/or orthopyroxene, with a low percentage of olivine rarely exceeding a few percent. Plagioclase is usually anhedral and sometimes deformed (undulose extinction and deformed twins - *Figure 2-4B* and *C*). It shows interlocking textures with clinopyroxene and sometimes high temperature equigranular recrystallisation textures (*Figure 2-4C*), especially at contacts. Grain size varies through depth from microgabbros (grain size <1mm) to seriate medium-grained gabbros to pegmatitic gabbros (grain size >10cm generally above 650 mbsf) (*Figure 2-5A*, *B* and *C*). The mineral assemblage of gabbronorites consists of anhedral plagioclase, clinopyroxene and orthopyroxene >5% (low Ca-pyroxene) occurring as large subhedral grains in coarse gabbros and more commonly anhedral in microgabbros.

Plagioclase is rarely altered to albite and when it is fractured, the fractures are filled in with chlorite. Clinopyroxene is commonly altered to amphibole: hornblende under amphibolite facies, and actinolite and/or tremolite under greenschist facies (*Figure 2-4C*).

#### 2.3.1.3 Olivine gabbro and troctolitic gabbro

Olivine gabbros and troctolitic gabbros (*Figure 2-5D* and *E*) are the second most common lithologies at the Atlantis Massif. They are mostly found in the intervals 400-600 mbsf, 1000-1100 mbsf, 1200-1300 mbsf, and 1380-1415 mbsf in IODP Hole U1309D and between 70 and 90 mbsf in IODP Hole U1309B. Modal composition of olivine gabbros vary greatly with modal olivine raging from 5% to 50%. The primary mineral assemblage consists of interstitial olivine, euhedral to anhedral plagioclases (25% to 80%), anhedral interstitial clinopyroxene (10% to 70%) interlocking with plagioclase and rare orthopyroxene (more common in the upper part of the core).

Olivine is replaced by serpentine and magnetite at depth (*Figure 2-4E*). In the upper part of the core, plagioclase and olivine have reacted together to form a corona texture (*Figure 2-4D* and *Figure 2-5F*) in which chlorite replaces plagioclase and tremolite replaces olivine at the contact

between plagioclase and olivine. Clinopyroxene is partially to completely altered brown amphibole (hornblende, amphibolite facies) and green amphibole (actinolite and/or tremolite, greenschist facies). Alteration occurs particularly along exsolution lamellae. Micro-rodingite (Frost, *et al.*, 2008) occurs as thin seams in which plagioclase is replaced by prehnite +/- hydrogarnet, and olivine by serpentine + magnetite. It occurs below about 350 mbsf where the corona formation had not gone to completion (*Figure 2-4G*; *Figure 2-5G*; see troctolites paragraph for more details *2.3.1.4*).

Plagioclase exhibits high temperature recrystallisation indicating crystal-plastic deformation in rare shear zones at the top of the hole. Secondary minerals indicate static metamorphism under greenschist facies conditions.

#### 2.3.1.4 Troctolite

Troctolites represent only 2.7% of lithologies in IODP Hole U1309D. They are mainly found in the interval 400-600 mbsf. Primary mineral assemblage in modal composition consists of olivine from 30 to 70%, subhedral to anhedral plagioclase form 30 to 50%, and clinopyroxene (≤ 5%). The relative proportion of plagioclase and olivine is significantly variable, and spatial gradation into troctolitic gabbros or olivine gabbros is commonly observed.

Olivine-rich troctolites are rocks with relatively low modal plagioclase and clinopyroxene, comprising dunite and wehrlite, in addition to troctolite. They represent 5.4% of the total recovery of IODP Hole 1309D and are concentrated in the interval between 1092 and 1236 mbsf although they are found throughout the entire core. Olivine-rich troctolite has a high modal olivine percentage (70 to 90%) showing subhedral to rounded grain shape, interstitial to poikilitic plagioclase (5 to 20%) and clinopyroxene (0 to 15%).

Alteration in these particular rocks is significantly variable with the degree of serpentinisation ranging from >90% to nearly unaltered (1%) (*Figure 2-4E* and *F*). The secondary mineral assemblage consists of serpentine ± magnetite after olivine and chlorite + prehnite + hydrogarnet

after the neighbouring plagioclase (*Figure 2-4*G and *Figure 2-5*G). Prior to that reaction, corona forms between olivine and plagioclase as described in *2.3.1.3* but do not go to completion, hence the chlorite rim in *Figure 2-4G*.

The sequence of reactions is as follows: coronas followed by serpentine +/- prehnite and hydrogarnet. However, the high proportion of olivine means that plagioclase is often completely consumed in the corona reaction. In this case olivine alters to serpentine/brucite/magnetite assemblages in a sequence described by Beard *et al.* (2009).

### 2.3.1.5 Oxide gabbro

Oxide gabbros (*Figure 2-4H* and *Figure 2-5H*) represent a relatively important percentage of recovery at IODP Hole U1309D with 7% of the overall lithologies. Apart from the Fe-Ti oxide content (<2%), the primary and secondary mineralogy is similar to the coarse-grained gabbros. Accessory minerals such as apatite and less commonly zircon occur in oxide gabbros. Titanite is also present as an accessory phase. It is nonetheless difficult to determine whether titanite is of magmatic or metamorphic origin. However, brown amphiboles that are believed to be magmatic are relatively common in oxide gabbros.

### 2.3.1.6 Leucocratic intrusions

Leucocratic intrusions occur as veins or dikes crosscutting the general fabric of the surrounding rocks (*Figure 2-5I*). They are centimetre-scale anorthosite, quartz diorite, and tonalite / trondjhemite leucocratic melt intrusions (Grimes, *et al.*, 2008), characterised by a light colour from the albite-rich plagioclase ± chlorite. They consist primarily of brown amphibole (hornblende) to green amphibole (actinolite) and plagioclase. These dikes commonly host accessory minerals such as titanite, epidote (important phase in the alteration assemblage between 380 and 950 mbsf but scarce both below and above this interval), apatite, calcite and zircon and are interpreted as igneous in origin derived from evolved silicate melts with solidus temperatures estimated between ~750 and 850°C (Blackman, *et al.*, 2006).

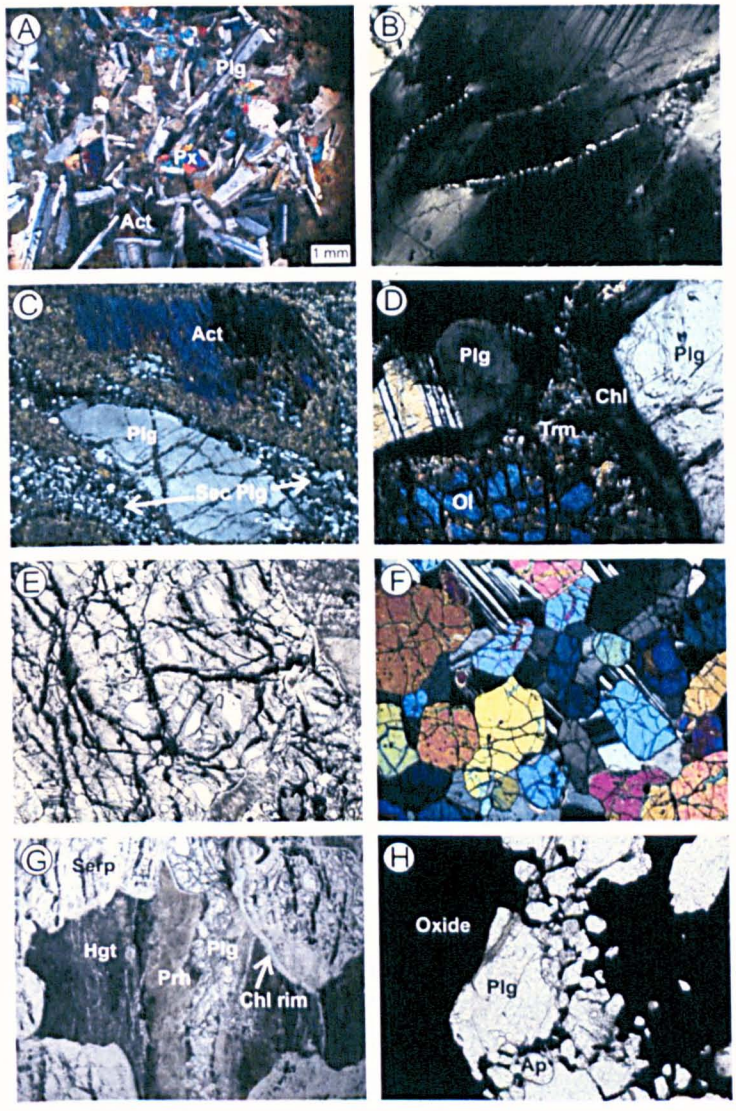


Figure 2-4: Photomicrographs of thin sections from IODP Hole U1309B and D. *A*: Medium-grained diabase (U1309D 16R-2 58-61 cm); subophitic texture with laths of plagioclase in a clinopyroxene matrix often replaced by actinolite (cross polarised light). *B*: Deformed plagioclase showing microfractures and undulose extinction as well as bended twins (U1309B 9R-1 38-41 cm) (cross-polarised light, field of view = 4 mm). *C*: Mylonitic gabbro with high temperature recrystallisation of plagioclase and replacement of clinopyroxene by actinolite and tremolite (U1309D 8R-2 138-141 cm) (cross polarised light). *D*: Corona texture in olivine gabbro consisting of tremolite replacing olivine and chlorite after plagioclase at the original contact between the two initial minerals (U1309D 80R-2 16-19 cm) (cross polarised light, field of view = 1.4 mm). *E*: Troctolite in which olivine is replaced by serpentine + magnetite (U1309D 80R-1 39-41 cm) (plane polarised light, field of view = 5.5 mm). *F*: Fresh olivine and plagioclase in olivine-rich troctolite (U1309D 248R-2 7–9 cm) (cross-polarized light, field of view = 11 mm). *G*: Plagioclase in olivine-rich troctolite that has been partially replaced by prehnite and hydrogrossular during the micro-rodingitisation reaction; chlorite at the contact between serpentine and plagioclase is a relict of the earlier corona forming reaction, although some has also grown during the micro-rodingite development (U1309D 63R-3 54–57 cm) (plane-polarized light, field of view = 10 mm). *H*: Oxide gabbro (U1309D 133R-1 24–26 cm) (plane-polarized light, magnification = 10×). Plg = plagioclase; Px = Clinopyroxene; Act = Actinolite; Chl = Chlorite; Trm = tremolite; Ol = Olivine; Serp = Serpentine; Prh = Prehnite; Hgt = Hydrogarnet; Ap = Apatite.

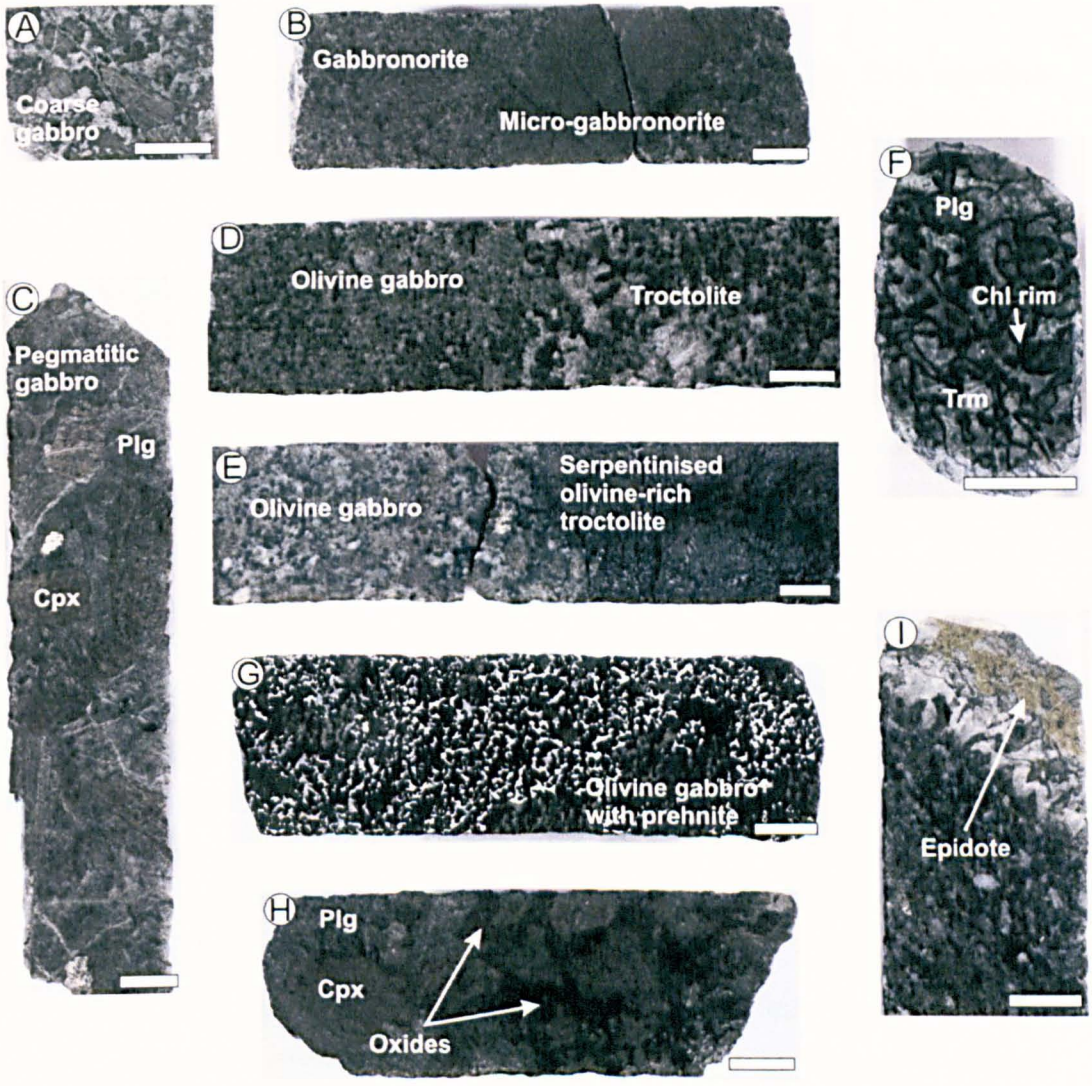


Figure 2-5: Photographs of cored samples of IODP Holes U1309B and D I. *A*: Coarse gabbro (U1309B 9R-1 44-48 cm. *B*: Contact between medium-grained gabbronorite and micro-gabbronorite (U1309D 165R-1 37–57 cm). *C*: Pegmatitic gabbro (U1309D 82R-2 55–67 cm). *D*: Contact and example of spatial gradation from olivine gabbro into troctolite (U1309D 251R-1 44–65 cm). *E*: Contact and example of spatial gradation from olivine gabbro into olivine-rich troctolite; this particular example show a partially serpentinised olivine-rich troctolite (U1309D 227R-2 22–45 cm).*F*: Olivine gabbro showing the corona texture where tremolite and chlorite replace olivine and plagioclase respectively at the contact between those two minerals (U1309B 15R-1 107-113 cm). *G*: Olivine gabbro showing the rodingitisation reaction in which prehnite is replacing plagioclase (U1309D 60R-3 48-68 cm). *H*: Oxide gabbro (U1309D 87R-2 59–76 cm). *I*: Leucocratic dike containing epidote and bladed pyroxene growing inward from margin + secondary plagioclase, titanite and actinolite (U1309D 75R-2 74–82 cm). Plg = plagioclase; Cpx = clinopyroxene; Chl rim = chlorite rim; Trm = tremolite. White boxes represent 2 cm.

#### 2.3.1.7 Amphibole vugs

*Figure 2-6* shows examples of amphibole + clay vugs. One example is observed in Hole U1309B (*Figure 2-6A*) and several in Hole U1309D, one at ~50 mbsf (U1309D 8R-2 55-60 (*Figure 2-6B*)), and below 140 mbsf. They are rare below 1000 mbsf. They occur as dark green patches as long as 8 cm and are filled almost entirely with fine-grained actinolite and have "bleached" milky wallrocks as wide as 2 cm, in which turbid secondary plagioclase and actinolite needles are developed. XRD analyses (*Figure 2-7*) show that those amphibole vugs consist of actinolite + clay, possibly saponite (Blackman, *et al.*, 2006).

#### 2.3.1.8 Serpentinised peridotite

Peridotites represent less than 1% of the total recovery of Hole U1309B and D (*Figure 2-3*). Different peridotites recovered consist of harzburgite (*Figure 2-8A*, *B* and *D*), wehrlite and dunite (*Figure 2-8C*). Primary mineralogy consists of olivine, orthopyroxene and/or clinopyroxene, and chromium spinel. Plagioclase is also present but is the result of melt impregnation (*Figure 2-8B*) (Drouin, *et al.*, 2009). Texturally, serpentine occurs via the development of kernel texture in which olivine grains are penetrated and surrounded by serpentine veinlets, leaving isolated relic olivine. Serpentine forms mesh texture when olivine is completely altered. Pyroxenes are replaced by serpentine as well (bastite pseudomorph). In harzburgite, orthopyroxene and olivine are usually completely replaced by serpentine, and in wehrlite relics of olivine and diopside can be observed. Carbonate such as magnesite appears to replace relict olivine in mesh texture, and calcite veins are also present at contacts with gabbros (Blackman, *et al.*, 2006).

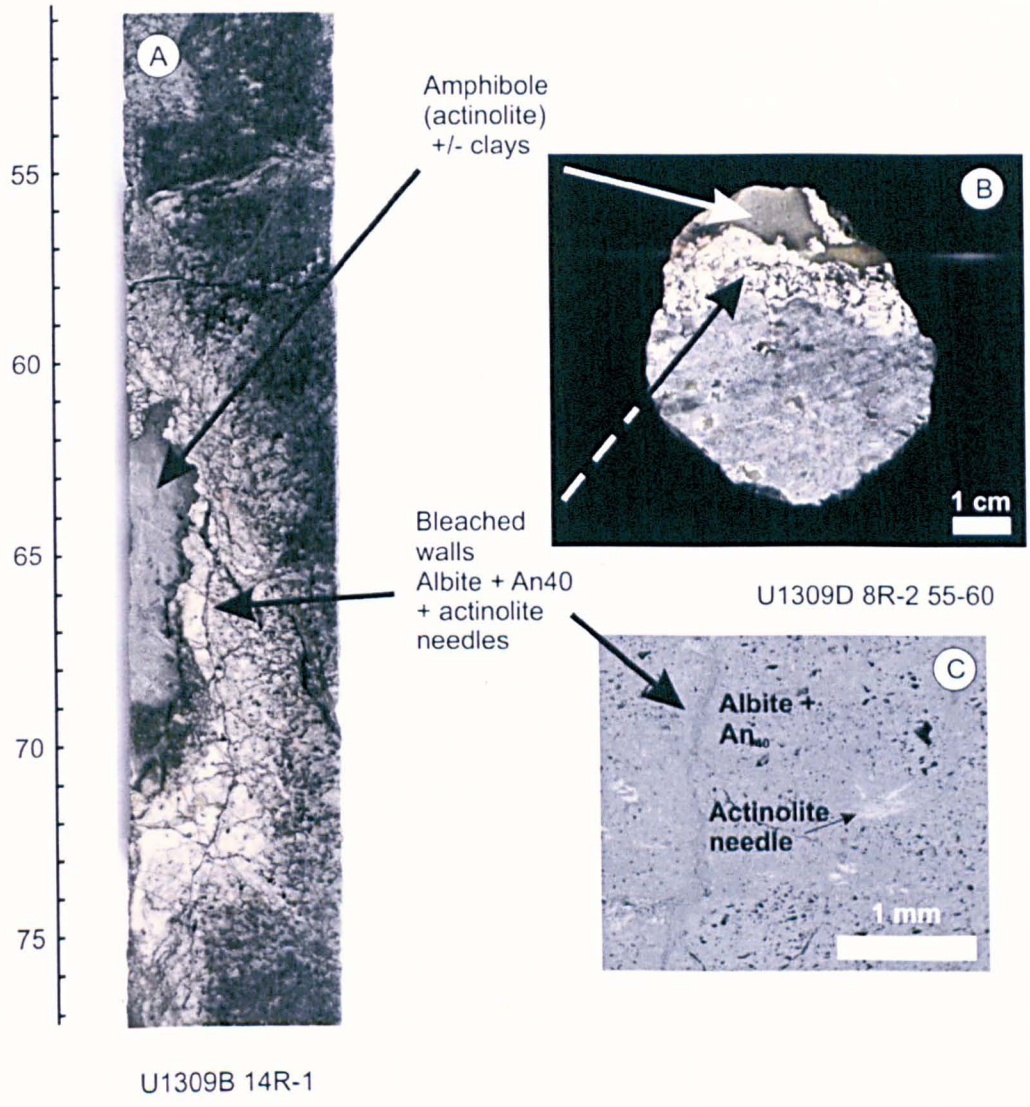


**Figure 2-6: Photographs of cored samples II. Late magmatic intrusion hydrothermally altered. Vugs are filled with fine-grained actinolite + clay and walls contain turbid secondary plagioclase and actinolite needles. A = U1309B 14R-1; B = U1309D 8R-2 55-60 cm. C = Back-scattered electron microphotograph of bleached walls of U1309D 8R-2 55-60 cm**

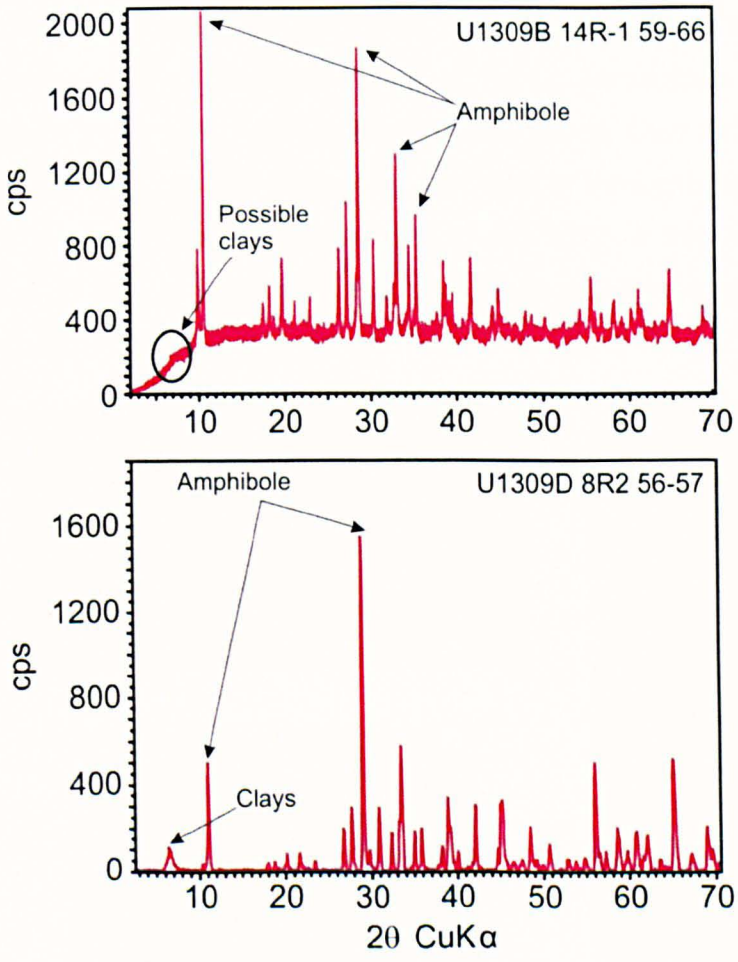


**Figure 2-7: XRD spectra of samples showing green fine-grained amphibole filled vugs. The spectra show that these vugs can contain a certain amount of clays – possibly saponite (Blackman, *et al.*, 2006). U1309B 14R-1 59-66 cm analysed at School of Earth and Environment – Leeds; U1309D 8R-2 56-57 cm analysed on ship board during IODP campaign 304.**

### 2.3.1.9 Talc tremolite schist

Talc tremolite schists and talc tremolite veins are a minor but important component of the rocks recovered in Hole U1309D. Talc tremolite assemblages are commonly found at contacts between ultramafic and mafic rocks and talc tremolite veins cut peridotites (Sample U1309B 11R-2 35-51 cm - *Figure 2-8D*). This sample shows a zone of green tremolite and pale talc replacing serpentinised harzburgite. This zone has undergone reverse shear (in the present core orientation) along talc-rich horizons, but the margin of talc alteration against serpentinite is unsheared, overprinting the preexisting serpentinite foliation defined by magnetite seams and serpentine

ribbons. The zone tapers upward in the present orientation and has an outer talc-rich zone with an isotropic fabric replacing serpentinite and an inner tremolite-rich zone with highly schistose talc bands. Dark grains within the talc alteration are bastites containing serpentine + magnetite assemblages (Blackman, *et al.*, 2006).The metasomatic alteration is due to circulation of fluid rich in Si and Ca from mafic to ultramafic rocks. (Blackman, *et al.*, 2006; Boschi, *et al.*, 2006).

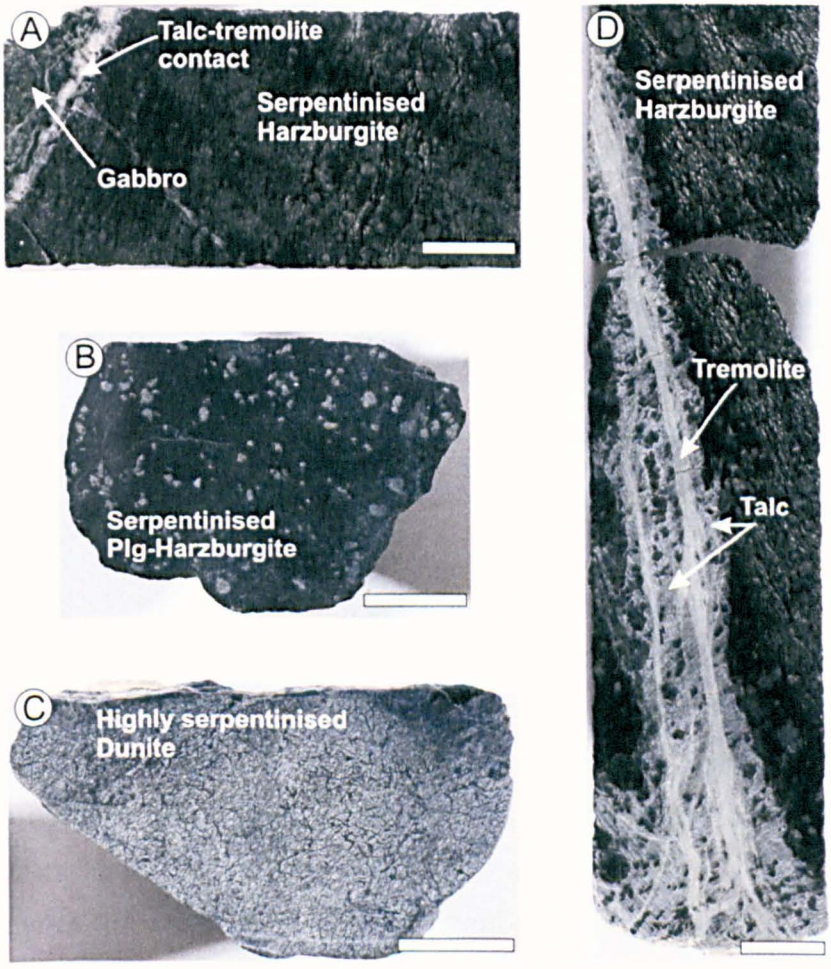


Figure 2-8: Photograph of cored samples from IODP Hole U1309B and D. *A*: Serpentinised harzburgite in contact with a coarse gabbro; the contact is marked by a talc-tremolite alteration (U1309B 11R-1 86–99 cm). *B*: Serpentinised plagioclase-bearing harzburgite (U1309D 27R-3 0–8 cm). *C*: Dunite almost totally serpentinised (U1309D 31R-1 24–33 cm). *D*: Zone of green tremolite and pale talc replacing serpentinised harzburgite (U1309B 11R-2 25–50 cm). This zone has undergone reverse shear along talc-rich horizons, but the margin of talc alteration against serpentinite is unsheared, overprinting the preexisting serpentinite foliation defined by magnetite seams and serpentine ribbons. The zone tapers upward and has an outer talc-rich zone with an isotropic fabric replacing serpentinite and an inner tremolite-rich zone with highly schistose talc bands. Dark grains within the talc alteration are bastites containing serpentine + magnetite assemblages. White boxes represent 2 cm.

# 2.4 Mineral chemistry of gabbroic rocks at Hole U1309B and D

## 2.4.1 Chemistry of plagioclases in IODP Holes U1309B and D

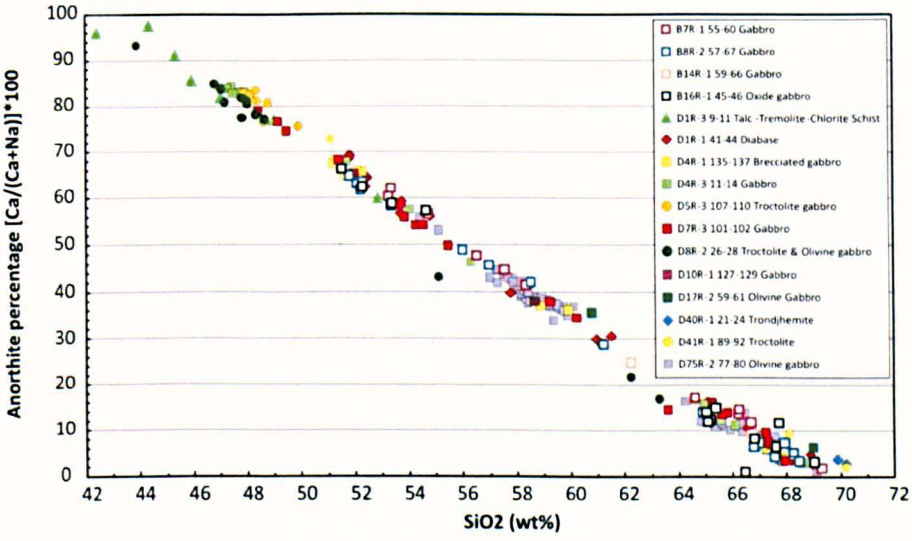


**Figure 2-9: Plagioclase chemistry in IODP Holes U1309B (open symbols) and U1309D (solid symbols). Approximate depth below seafloor can be estimated using the following formulae; For Hole 1309B, depth = (core number)*5 + 5m. For Hole D, depth = (core number)*5 + 20m.**

*Figure 2-9* shows a summary of electron micro probe data for plagioclase of IODP Hole U1309B and Hole U1309D. The whole collection of analyses made in this study is presented in appendix 1, and mainly come from the upper 100m of the two Holes with the exception of two samples coming from about 200 mbsf and one from about 375 mbsf. Open symbols are analyses of Hole B, and solid symbols are analyses of Hole D. Plagioclase chemistry is significantly variable and covers the full range from bytownite to albite with only a few example of anorthite.

In gabbro and diabase, primary igneous plagioclase is generally in the range $An_{40}$ to $An_{65}$, with more An-rich compositions occurring in olivine-rich lithologies such as troctolite. Plagioclases with An contents < 40% are mainly secondary with the exception of late leucocratic veins (trondjemite). Igneous plagioclase commonly shows zoning while secondary plagioclase is present as bleached margins of veins (*Figure 2-6*), thin albitic veinlets and

irregular patches replacing primary plagioclase. An-rich secondary plagioclase, as observed in diabase in ODP Hole 504B (Vanko & Laverne, 1998) has not been observed.

### 2.4.2 Chemistry of amphiboles in IODP Holes U1309B and D

*Figure 2-10* shows the range in amphibole chemistry recovered in both IODP Holes U1309B and D according to the amphibole classification described by Leake *et al.* (1997). The whole collection of amphibole analyses is available in appendix 1. Amphiboles of high temperature (amphibolite facies) and of low temperature (greenschist facies) are recovered. Magnesiohornblende and actinolite are the two main amphiboles found in both cores. Tremolite is usually found in olivine-rich rocks such as troctolite. An unusual enrichment in Fe is observed in olivine gabbro sample (U1309D 144R-1 105-116 cm) in which ferroactinolite is found. Greenschist amphiboles seem to be the most abundant in both cores. Amphiboles from corona formation are systematically tremolite, although hornblende has been identified as a secondary phase (Nozaka & Fryer, 2011). Greenschist facies amphiboles commonly replace clinopyroxene (see paragraph 2.5).

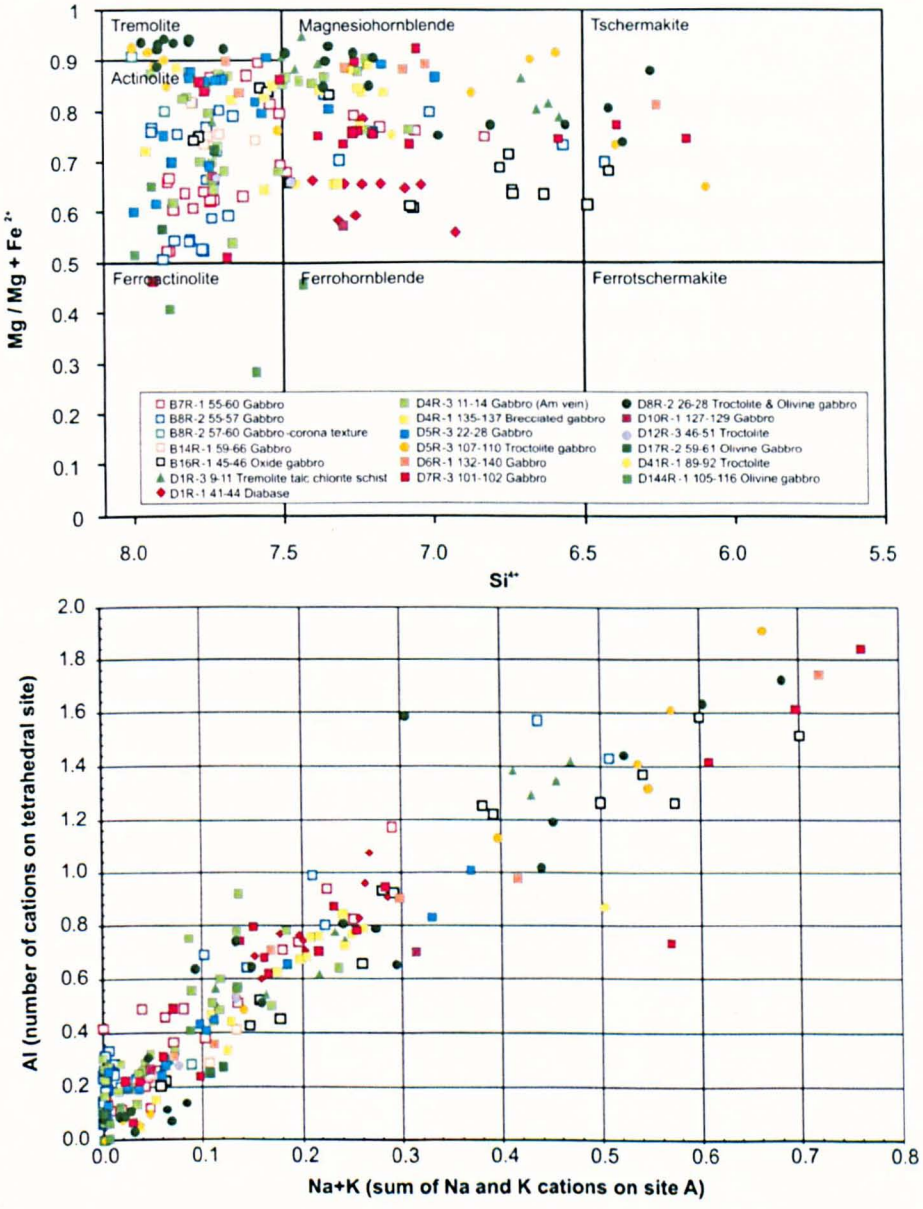


**Figure 2-10: Amphibole chemistry in IODP Holes U1309B and D. Amphiboles from Hole U1309B are plotted with open symbols, and amphiboles from Hole U1309D are plotted with solid symbols. The top panel is a plot of silicon in the tetrahedral site against the Mg number, allowing us to name the amphibole recovered in both IODP Holes U1309B and D. The bottom panel is a plot of the sum of cations K and Na in the site A against the number of Al in the tetrahedral site, allowing us to determine the temperature and the facies of amphiboles present in the cores. The lower the two numbers are, the lower the temperature is.**

## 2.5 Alteration history

IODP Holes U1309B and D record the cooling history of plutonic rocks from magmatic conditions (>1000°C) to zeolite facies conditions (<200°C) during the unroofing and uplift of the AM. Samples from both cores present evidence of penetration of altering fluid. Nonetheless, even if one sample can show a range in metamorphic conditions, no sample contains the entire cooling history. The whole history is therefore inferred from observations on several samples (Blackman, *et al.*, 2006; Backman, *et al.*, 2011). Overall, the intensity of alteration is moderate, decreases downhole, and is related to the intensity of veining below 1000 mbsf (*Figure 2-11*). Exceptions to the downhole decreasing pattern of the alteration are observed in parts of the core where alteration is correlated to the abundance of olivine (interval 1100-1250 mbsf for instance). At great depths alteration is controlled by lithologies rich in olivine, lithological contacts, faults, and veins. The metamorphic chronology at site U1309 can be subdivided as follows and is summarised in *Table 2-1*:

- Granulite facies metamorphism
- Amphibolite facies metamorphism
- Static upper greenschist facies to lower amphibolite facies metamorphism
- Static lower greenschist facies to subgreenschist facies metamorphism
- Zeolite facies and clay grade metamorphism

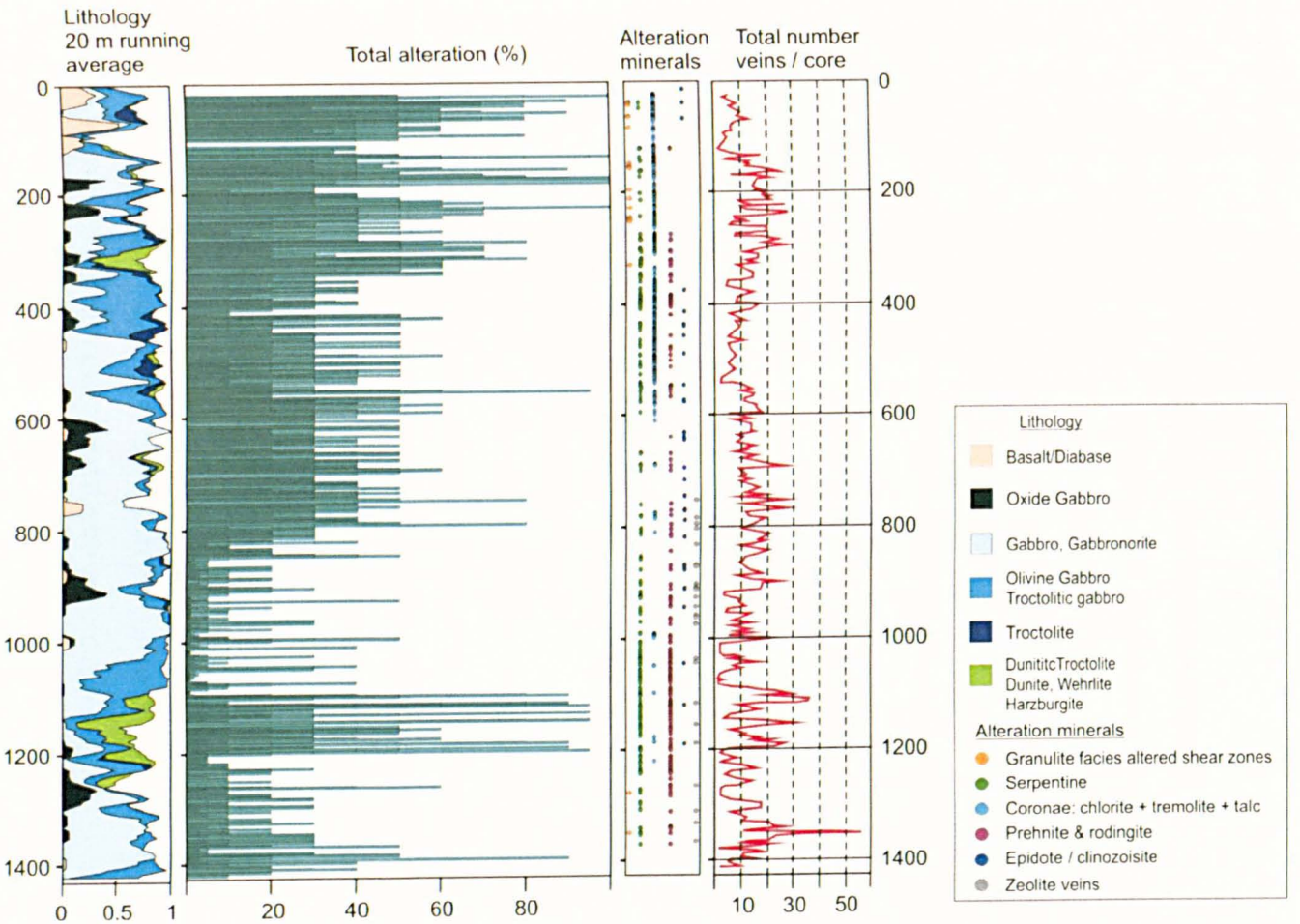


**Figure 2-11: Downhole igneous lithologies with alteration profile (total and mineral associated) and vein intensity of IODP Hole U1309D. Lithology, total alteration and total number of vein are from Blackman *et al.* (2006). Alteration minerals is from Blackman *et al.* (2011)**

### 2.5.1 Granulite facies metamorphism

In more detail, the granulite facies alteration is characterised by mylonitic deformation, dynamic recrystallisation of plagioclase and pyroxene, and the presence of brown amphibole in a few thin shear zones, mainly in the upper part of the section.

### 2.5.2 Amphibolite facies metamorphism

Amphibolite facies alteration is manifested mainly by static replacement of pyroxene by green to brown hornblende in diabases, gabbros and especially in oxide gabbros, and in mylonitic zones. It is nonetheless difficult to estimate the extent of this metamorphic event due to the overprinting by greenschist amphibole alteration (Blackman, *et al.*, 2006).

### 2.5.3 Greenschist facies metamorphism

The main alteration occurs in the greenschist facies. Distinctions between upper greenschist facies alteration and lower greenschist facies alteration are observed.

#### 2.5.3.1 Upper greenschist facies to lower amphibolite facies metamorphism

Upper greenschist facies assemblages have textures indicative of growth under static conditions, without deformation. It is mainly characterised by the formation of secondary plagioclase, and secondary amphibole, with crystallisation of epidote related to late magmatic leucocratic intrusions below 400 mbsf (*Figure 2-5I*).

The major effect of the greenschist alteration in most gabbros and diabases is the replacement of pyroxene by actinolitic amphibole. All samples are affected by this alteration in the upper 300 m of Hole U1309D; deeper, alteration is more associated with amphibole veins.

In rocks containing both plagioclase and olivine, formation of tremolite-chlorite ± talc corona textures occurs. Tremolite replaces olivine and chlorite replaces plagioclase. This reaction is accompanying by a volume expansion which is compensated by radial fractures around the olivine that propagates in plagioclase. Those fractures are filled in with

chlorite. Corona textures are usually observed in the upper 300 m of Hole U1309D (*Figure 2-11 alteration mineral section*) where the reaction goes to completion by removing completely either olivine or plagioclase. At greater depths, this reaction becomes localised by amphibole veins and rims of gabbro dikelets (Blackman, *et al.*, 2006). In the absence of olivine, plagioclase seems to be unaltered, except in the vicinity of veins and late magmatic/leucocratic intrusions, where albitisation occurs.

#### 2.5.3.2 Lower greenschist facies to subgreenschist facies metamorphism

Serpentinisation of olivine occurs above 300 mbsf when olivine is in excess over plagioclase and has survived the corona formation. Below 300 mbsf, rodingitisation takes over from simple serpentinisation and is characterised by the replacement of neighbouring plagioclase by prehnite ± hydrogrossular (Frost, *et al.*, 2008) (*Figure 2-11 alteration mineral section*). The fluid influx that produced the serpentine-prehnite alteration was localised and clearly fracture related and serpentine-prehnite ladder veins commonly appear to follow stress trajectories, so a tectonic control appears probable (Blackman, *et al.*, 2006).

Serpentinisation is overprinted by metasomatic talc-tremolite vein alteration that is the result of fluid rich in Si and Ca circulating form mafic to ultramafic rocks (Blackman, *et al.*, 2006). Talc-tremolite-chlorite schist formation after ultramafic rocks occur in the upper 30 m of both Holes U1309B and D. They are inferred to reflect the deformation on the detachment fault (Boschi, *et al.*, 2006)

### 2.5.4 Zeolite facies and clay grade metamorphism

Zeolites occur in late fractures and veins, and replacing plagioclase, but are only common below 700 mbsf. It is likely that much of the zeolite observed in fractures formed under ambient conditions because temperatures at the bottom of the hole were at least 120°C (Blackman, *et al.*, 2006). The lack of zeolite above 700 mbsf suggests rapid cooling during unroofing from >300°C to <80°C in the upper part of the Hole (Blackman, *et*

*al.*, 2006; McCaig, *et al.*, 2010). Clay minerals forms also in veins and as replacement of serpentine (Nozaka and Fryer, 2011; Nozaka, *et al.*, 2008)

### 2.5.5 Summary paragenetic sequence

The paragenetic sequence in IODP Holes B and D can be summarised as follows: 1) granulite shear zones; 2) corona textures probably formed in amphibolite and upper greenschist facies; 3) microrodingites and serpentinisation at <360°C; 4) talc-tremolite rocks locally overprinting serpentine; 5) zeolites and clays. In parallel with this is the general replacement of pyroxene by amphibole with a wide range of composition, accompanied by partial replacement of igneous plagioclase by more albitic plagioclase. *Table 2-1* gives more details on mineral involved and temperatures of metamorphism.

**Table 2-1: Summary paragenetic sequence in IODP Hole U1309D. Plg = plagioclase; Px = pyroxene; Ilary = secondary; Hb = hornblende; T = temperature; Act = actinolite; Trem = tremolite; Ol = olivine; Serp = serpentine; Preh = prehnite; Hgt = hydrogarnet.**

| | Description | Primary minerals | Secondary minerals | Metamorphic facies | Temperature estimates(°C) |
|---|---|---|---|---|---|
| Time ↓ | Recrystallisation | Plg + Px | $II^{ary}$ Plg + $II^{ary}$ Px+ brown Hb | Granulite facies | High T (800) |
| | Replacement | Px | Brown + green Hb | Amphibolite facies | 600-700 |
| | Replacement | Px | Act and/or Trem | Amphibolite and Greenschist facies | 400-500 |
| | Corona formation | Plg + Ol | Chl + Trem ± Talc | | 450 |
| | Serpentinisation | Ol | Serp ± brucite | Greenschist facies | 300 |
| | Rodingitisation | Plg | Preh + Hgt | | <360 |
| | Steatisation | Serp | Talc | | 400 |
| | Vein filling | | Zeolite + clay | Zeolite facies | <300 |

## 2.6 The TAG Hydrothermal Model

The TAG hydrothermal mound is located at 26°08'N in the middle of a 40 km long segment on the MAR. It is underlain by an arcuate zone of seismicity which steepens downwards beneath the Neo-Volcanic Zone to root at a depth of 7 km below seafloor (deMartin, *et al.*, 2007) where gabbro bodies are emplaced. This arcuate zone of seismicity is inferred to be an active detachment that picks up the intrusive bodies and exhumed them to the seafloor (McCaig, *et al.*, 2010). In this model, the detachment fault feeds the TAG hydrothermal field with hydrothermal fluid that discharges along the fault. However, it is important to remind that the maximum depth at which fluid can circulate and the localisation of any magma chamber is still ill defined.

The evolution of the AM is used as an analogue for processes in the current TAG footwall. *Figure 2-12* shows the position of IODP Hole U1309D in the model before it was exhumed.

In the TAG model, fluid flow occurs along the major detachment fault with potential circulation at various fluid fluxes in the footwall (*Chapter 5*). The model suggests that the gabbroic sequence was altered by fluid flowing mainly upwards and parallel to the detachment fault, more or less perpendicular to the orientation of the hole at the time. Temperatures in the fault zone are buffered to ~400 °C by upward flowing black smoker fluid, and temperatures in the footwall can only fall below this value in the later stages of exhumation.

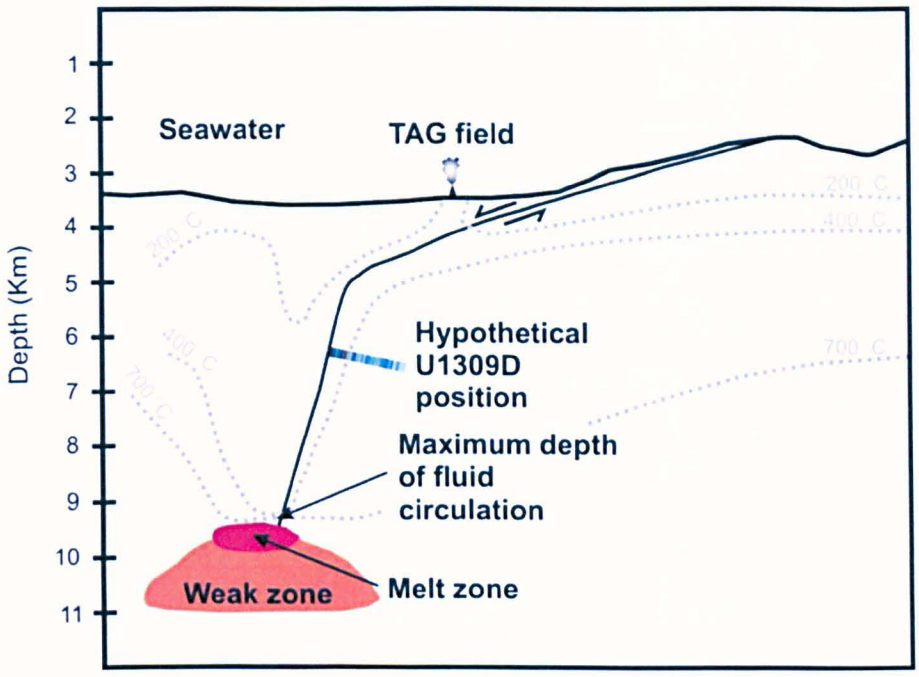


**Figure 2-12: Interpreted cross section through TAG (deMartin, *et al.*, 2007). Maximum depth of circulation of fluid is shown (~9 km), as well as the hypothetical position of IODP Hole U1309D at a time T. Isotherms are from McCaig *et al.* (2010).**

## 2.7 References

Beard, J. S., Frost, B. R., Fryer, P., McCaig, A., Searle, R., Ildefonse, B., Zinin, P. & Sharma, S. K. (2009). Onset and progression of serpentinization and magnetite formation in olivine-rich troctolite from IODP Hole U1309D. *Journal of Petrology* **50**, 387-403.

Blackman, D. K., Ildefonse, B., John, B. E., Ohara, Y., Miller, D. J., McLeod, C. J. & Scientists, E., 2006. Expedition 304/305 summary. *Proceedings of the Integrated Ocean Drilling Program*, **304/305**, 1-60.

Blackman, D. K., Karson, J. A., Smith, D. K., Cann, J. R., Früh-Green, G. L., Gee, J. S., Hurst, S. D., John, B. E., Morgan, J., Nooner, S. L., Ross, D. K., Schroeder, T. J. & Williams, E. A., 2002. Geology of the Atlantis Massif (Mid-Atlantic Ridge, 30°N): Implications for the evolution of an ultramafic oceanic core complex. *Marine Geophysical Researches*, **23**, 443-469.

Blackman, D. K., B. Ildefonse, B. E. John, Y. Ohara, D. J. Miller and Exp. 304/305 Science Party, 2011: Drilling Constraints on Lithospheric Accretion and Evolution at Atlantis Massif, Mid-Atlantic Ridge 30°N, *Journal of. Geophysical Research*, **116**, 1-25.

Boschi, C., Fruh-Green, G. L. & Escartin, J., 2006. Occurrence and significance of serpentinite-hosted talc-and amphibole-rich rocks in modern oceanic settingd and ophiolite complexes: an overview. *Ofioliti*, **31**, 129-140.

Cann, J. R., Blackman, D. K., Smith, D. K., McAllister, E., Janssen, B., Mello, S., Avgerinos, E., Pascoe, A. R. & Escartin, J., 1997. Corrugated slip surfaces formed at ridge-transform intersections on the Mid-Atlantic Ridge. *Letters To Nature*, **385**, 329-332.

deMartin, B. J., Sohn, R. A., Canales, J. P. & Humphris, S. E., 2007. Kinematics and geometry of active detachment faulting beneath the TAG hydrothermal field on the Mid-Atlantic Ridge. *Geology*, 711-741.

Dick, H. J. B., Meyer, P., Bloomer, S., Kirby, S., Stakes, D. & Mawer, C., 1991. Lithostratigraphic evolution of an *in situ* section of oceanic layer 3. *Proc. Ocean Drilling Program, Sci. Res.*, **118**, 439-538.

Dick, H. J. B., Natland, J. H., Alt, J. C., Bach, W., Bideau, D., Gee, J. S., Haggas, S., Hertogen, J. G. H., Hirth, G., Holm, P. M., Ildefonse, B., Iturrino, G. J., John, B. E., Kelley, D. S., Kikawa, E., Kingdon, A., LeRoux, P. J., Maeda, J., Meyer, P. S., Miller, D. J., Naslund, H. R., Niu, Y.-L., Robinson, P. T., Snow, J., Stephen, R. A., Trimby, P. W., Worm, H.-U. & Yoshinobu, A., 2000. A long in situ section of the lower ocean crust: results of ODP Leg 176 drilling at the Southwest Indian Ridge. *Earth and Planetary Science Letters*, **179**, 31-51.

Drouin, M., Godard, M., Ildefonse, B., Bruguier, O. & Garrido, C. J., 2009. Geochemical and petrographic evidence for magmatic impregnation in the oceanic lithosphere at Atlantis Massif, Mid-Atlantic Ridge (IODP Hole U1309D, 30°N). *Chemical Geology*, **264**(1-4), 71-88.

Frost, B. R., Beard, J. S., McCaig, A. & Condliffe, E., 2008. The formation of micro-rodingite from IODP Hole U1309D: Key to understanding the process of serpentinization. *Journal of Petrology*, **49**(9), 1579-1588.

Grimes, C. G., John, B. E., Cheadle, M. J. & Wooden, J. L., 2008. Protracted construction of gabbroic crust at a slow spreading ridge: Constraints from $^{206}Pb/^{238}U$ zircon ages from Atlantis Massif and IODP Hole U1309D (30°N, MAR). *Geochemistry Geophysics Geosystems*, **9**(8), 1-24.

Karson, J. A., 1990. Seafloor spreading onn the Mid-Atlantic Ridge: Implications for the structure of ophioilites and oceanic lithosphere produced in slow-spreading environments. In: *Proceedings of the Symposium "Troodos 1987"*, pp. 125-130, J Malpas, E M Moores, A Panayiotou, C Xenophontos, Nicosia.

Leake, B. E., Woolley, A. R., Arps, C. E. S., Birch, W. D., Gilbert, M. C., Grice, J. D., Hawthorne, F. C., Kato, A., Kisch, H. J., Krivovichev, V. G., Linthout, K., Laird, J., Mandarino, J., Maresch, W. V., Nickel, E. H., Rock, N. M. S., Schumacher, J. C., Smith, D. C., Stephenson, N. C. N., Ungaretti, L., Whittaker, E. J. W.,and Youzhi, G., 1997. Nomenclature of Amphiboles: Report of the Subcommittee on Amphiboles of the International Mineralogical Association (CNMMN). *Mineralogical Magazine*. **61**. pp 295–321.

McCaig, A., Delacour, A., Fallick, A. E., Castelain, T. & Früh-Green, G. L., 2010. Detachment Fault Control on Hydrothermal Circulation Systems: Interpreting the Subsurface Beneath the TAG Hydrothermal Field Using the Isotopic and Geological Evolution of Oceanic Core Complexes in the Atlantic, *In* Rona, P. A., Devey, C. W., Dyment, J., Murton, B. J. (ed) Diversity of Hydrothermal Systems on, Slow Spreading Ridges, *AGU Geophysical Monograph*, **108**, AGU, pp; 207-240.

Nozaka, T. & Fryer, P., 2011. Alteration of the Oceanic Lower Crust at a Slow-spreading Axis: Insight from Vein-related Zoned Halos in Olivine Gabbro from Atlantis Massif, Mid-Atlantic Ridge. *Journal of Petrology*, **52** (4), 643-664.

Nozaka, T., Fryer, P. and Andreani, M., 2008. Formation of clay minerals and exhumation of lower-crustal rocks at Atlantis Massif, Mid-Atlantic Ridge. *Geochemistry Geophysics Geosystems*, **9**, Q11005, doi:10.1029/2008GC002207

Tucholke, B. E. & Lin, J., 1994. A geological model for the structure of ridge segments in low spreading ocean crust. *Journal of Geophysical Research*, **99**(B6), 11937-11958.

Tucholke, B. E., Lin, J. & Kleinrock, M. C., 1998. Megamullions and mullions structure defining oceanic metamorphic core complexes on the Mid-Atlantic Ridge. *Journal of Geophysical Research*, **103**(B5), 9857-9866.

Vanko, D. A. & Laverne, C., 1998. Hydrothermal anorthitization of plagioclase within the magmatic/hydrothermal transition at mid-ocean ridges: examples from deep sheeted dikes (Hole 504B, Costa Rica Rift) and a sheeted dike root zone (Oman ophiolite). *Earth and Planetary Science Letters*, **162**(1-4), 27-43.

# Chapter 3. Fluid evolution in the oceanic crust: a fluid inclusion study from IODP Hole U1309 D - Atlantis Massif, 30 °N. Microthermometry

## 3.1 Introduction

This chapter presents the microthermometric properties of fluid inclusions observed in 6 samples of IODP Hole U1309D. Samples and fluid inclusions are described petrographically. A reminder of what microthermometry is and what it is used for is also given in the methodology section.

Results are compared with various studies of fluid inclusions in oceanic settings along the Mid-Atlantic Ridge such as the MARK area (Kelley & Delaney, 1987; Kelley, *et al.*, 1993) and the Oceanographer Transform (Vanko, *et al.*, 1992), as well as the South West Indian Ridge (Kelley & Früh-Green, 2001) and in ophiolites from Oman (Nehlig, 1991) and Troodos (Cowan & Cann, 1988; Kelley, *et al.*, 1992). There follows a discussion on the processes that generate salinity variation as it is observed in the core. These processes are: subcritical phase separation (boiling) or supercritical phase separation (condensation) of a seawater-like fluid or magmatic fluid; magmatic fluids exsolving from melts; hydration/dehydration reactions; and variable mixing of hydrothermal fluid with a phase-separated brine or vapour. In the discussion, the evolution of fluids in the Atlantic Massif is discussed in the context of the TAG hydrothermal system. Hypotheses on processes and on conditions of trapping of fluids are therefore dependent on the TAG model (McCaig, *et al.*, 2010) that is an interpreted cross section (*Chapter 2*) based on observations of deMartin *et al.* (2007).

## 3.2 Microthermometry methodology

The fluid inclusion study has been undertaken using two methods; is microthermometry (this chapter) which is a non-destructive method, and laser ablation inductively coupled Mass Spectrometry(LAICPMS), which is a destructive method (*Chapter 4*).

Microthermometry is a technique allowing us to witness phase changes in fluid inclusions during cooling and heating. As fluid inclusions (primary inclusions) may either contain the fluid from which the mineral host grew, or fluids that were incorporated after growth of the mineral (secondary fluid inclusions), they are witnesses of fluid circulation. Assuming that the chemical composition of the fluid and the volume of the cavity remain unchanged, it is possible via the results obtained by microthermometry to estimate the salinity and the density (hence the temperature and the pressure) of the fluid circulating at time of trapping.

Nonetheless, processes such as diffusion, precipitation/dissolution and interaction with fluids having circulated previously in the rock can affect the composition of the fluid. Processes such as necking down, stretching, and decrepitation can change the volume of the cavity (Roedder, 1984). Special care must then be taken in order to not use such inclusions in interpretation.

**Figure 3-1: Photograph of the Linkam THMSG 600 (Source: www.linkam.co.uk).**

### 3.2.1 Instrumentation

Microthermometry measurements were carried out on an Olympus BX-50 transmitted light microscope mounted Linkam THMSG 600 heating-freezing stage (*Figure 3-1*) covering a range in temperature from -196°C to +600°C from 300 µm thick double-polished wafers. The stage is controlled by a Linkam TMS 93 programmer via the LinkSys software version 2.15. Observation of fluid inclusions can be made by looking directly down the microscope or on the computer screen via a JVC TK-C1380 colour video camera.

### 3.2.2 Analytical routine and data processing

Repeated homogenisation and freezing measurements were undertaken on individual inclusions in order to observe phase changes (such as ice melting point, halite dissolution temperature, liquid-vapour homogenisation temperature) and to obtain homogenisation temperatures and fluid salinities (in Wt% NaCl equivalent). Salinities were calculated using the temperature of melting of ice (θ) for low salinity fluids from the following equation (Bodnar, 1993):

$$Salinity = 0.00 + 1.78\theta - 0.00442\theta^2 + 0.000557\theta^3 \qquad \textbf{Equation 3-1}$$

Salinities for high salinity fluids were calculated using the temperature of dissolution of solid halite (Sterner, *et al.*, 1988):

$$Salinity = 26.242 + 0.4928\psi + 1.429\psi^2 - 0.223\psi^3 + 4.129 \times 10^{-2}\psi^4 + 6.295 \times 10^{-3}\psi^5 - 1.9675 \times 10^{-3}\psi^6 + 1.112 \times 10^{-4}\psi^7 \qquad \textbf{Equation 3-2}$$

Where $\psi$ is T (°C) $_{\text{dissolution of halite}}$/100.

Ice melting temperatures were reproducible to ± 0.1°C, giving an error of ± 0.17 Wt% NaCl equivalent for unsaturated inclusions. Halite dissolution temperatures were reproducible to ± 0.5°C giving an error of ± 0.03 Wt% NaCl equivalent. Homogenisation temperatures were reproducible to ± 1°C.

### 3.2.3 Calibration

Synthetic fluid inclusions of $CO_2$ (*Figure 3-2A*) and of pure $H_2O$ (*Figure 3-2B*) in quartz have been used to calibrate the microthermometric stage at temperature of -56.6°C (triple point temperature of $CO_2$), 0.0°C (triple point of $H_2O$ pure) and +374.1°C (critical point of $H_2O$ pure). Calibration was always checked previously to a set of measurement. If variations in any of the three temperatures of calibration used were observed, the necessary changes were conducted to the machine.

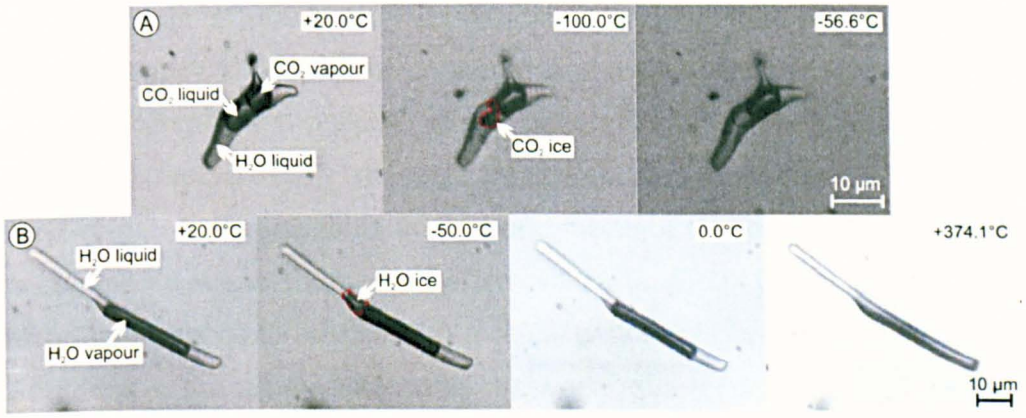


**Figure 3-2: Photomicrographs of synthetic fluid inclusions used for calibration: A = Triple phased $CO_2$ fluid inclusion, containing a $H_2O$ liquid phase and two $CO_2$ phase, liquid and vapour. B = $H_2O$ pure fluid inclusions containing a liquid and a vapour phase.**

## 3.3 Petrography

This section describes the samples that were studied for microthermometry. Petrography of the rock including chemistry of mineral hosts along with petrography of the fluid inclusion populations are described.

### 3.3.1 Diabase

Diabases occur as intrusions mainly in the upper part of the cores, but also rarely deeper down in core U1309D (*Figure 2-3*)

#### 3.3.1.1 Sample U1309D 1R-1 41-44

Sample U1309D 1R-1 41-44 cm is a subophitic medium grained diabase composed of laths of unaltered and fractured plagioclase of 0.1 to 2.5 mm in length, with poikilitic augite generally partially replaced by green hornblende (*Figure 3-3A).* Ilmenite partially replaces magnetite. A 3 mm-wide quartz-chlorite vein crosscuts the general fabric of the matrix. Quartz grains are commonly equant in size and of irregular shape. They exhibit a texture in which the grains go to extinction in a radial pattern (*Figure 3-3B*). It is difficult to determine the time relationship between quartz and the fine grained chlorite. In hand specimen, the chlorite was only on one side of the vein and most of the chlorite was lost during sample preparation. The chemistry of several laths of plagioclase is presented in *Chapter 2* and in *Appendix 1.* Close to the quartz-chlorite vein, laths of plagioclase tend to have an albitic core and intermediqte edges (labradorite), whereas away from the vein (laths 3, 4 and 5), the opposite is observed. Chemistry of amphibole in this sample (see also *Figure 2-10*) is also presented in *Appendix 1.* No particular pattern away from the vein is observed. All amphiboles in this sample are green magnesiohornblende.

#### 3.3.1.2 Fluid inclusions

Fluid inclusions occur as irregular shaped primary (?) inclusions clustering in the centre and clear part of the quartz grains of the vein (*Figure 3-4A*). They are 2 phase liquid-dominated inclusions ranging in size from 5 to 10 μm.

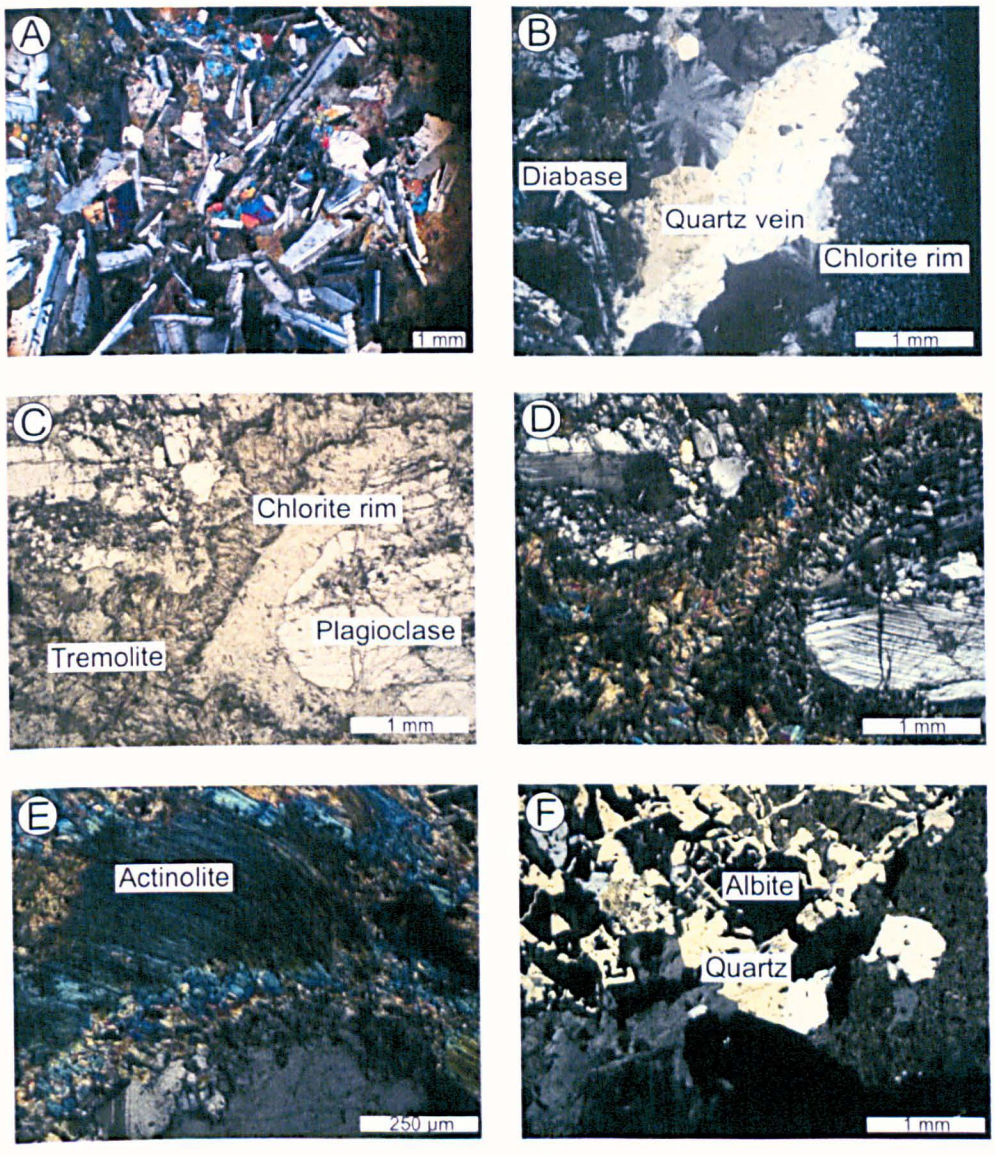


Figure 3-3: Photomicrographs; A = ophitic texture of diabase with laths of plagioclase, green hornblende and clinopyroxene relics as bright colours (sample U1309D 16R-2 58-61 cm piece 4, cross-polarised light). This sample is similar to the sample in which microthermometry was performed except that the grain size is coarser in that one. B = Quartz-chlorite vein in diabase (sample U1309D 1R-1 41-44 cm piece 1, cross-polarised light). C and D= Troctolitic gabbro showing corona texture – tremolite replaces olivine and chlorite replaces plagioclase (sample, plane-polarised light [C] and [D])). E = Actinolite replacing clinopyroxene in troctolitic gabbro (sample U1309D 5R-3 107-110 cm, piece 12, cross-polarised light). F = Graphic texture of trondjhemite (sample U1309D 40R-1 21-24 cm, piece 5, cross-polarised light).

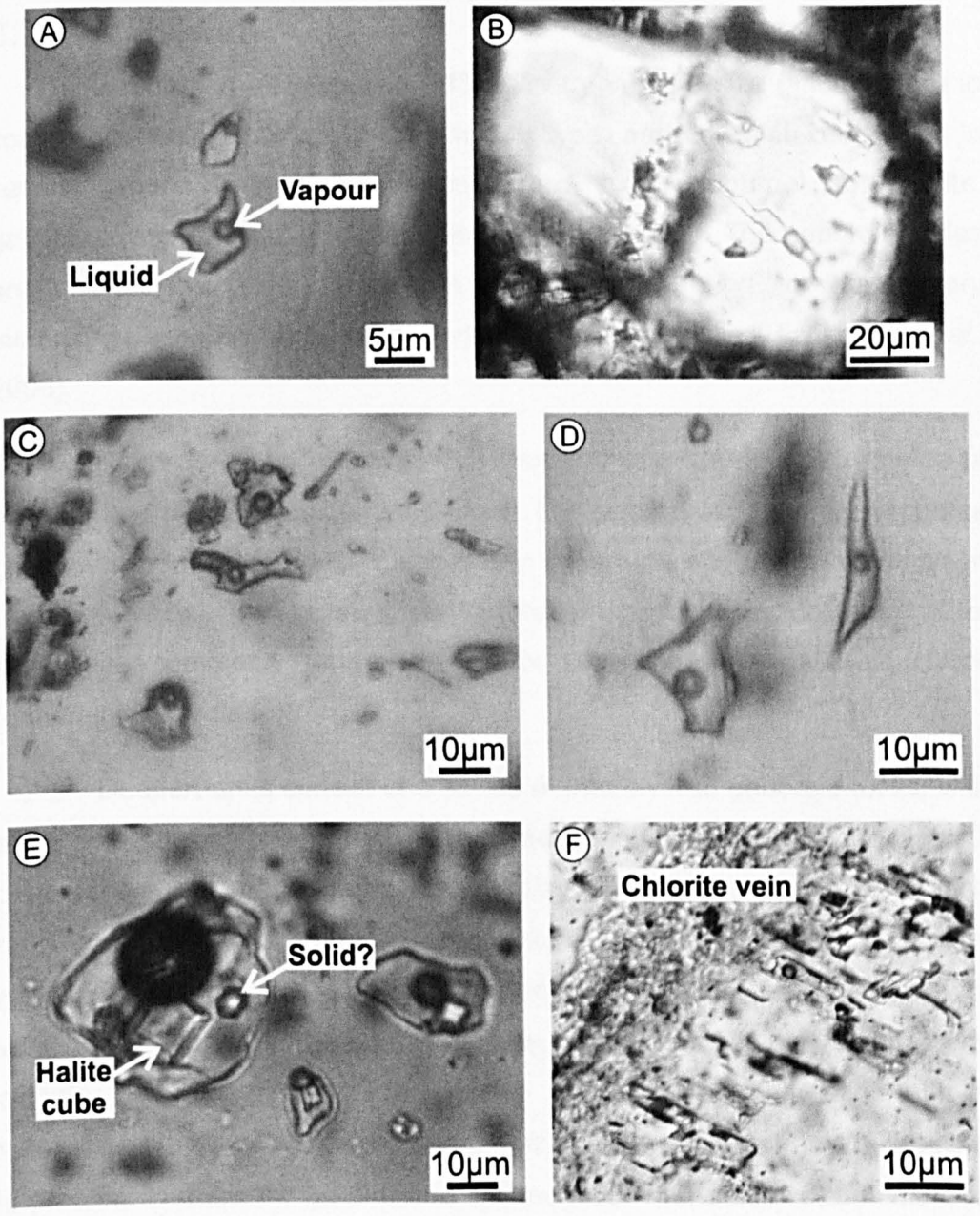


**Figure 3-4: Photomicrographs of fluid inclusions. A: Irregular shape primary (?) fluid inclusions of type 1a (see *3.4.1*) in the quartz chlorite vein of sample U1309D 1R-1 41-44 cm. B: Irregular shape secondary fluid inclusions of type 1b (see *3.4.1*) in plagioclase of sample U1309D 10R-1 127-129 cm. C: Irregular shape primary fluid inclusions of type 1a in quartz vein of sample U1309D 40R-1 17-19 cm. D: Irregular shape primary inclusions of type 1a in quartz vein of sample U1309D 40R-1 21-24 cm. E: Halite bearing fluid inclusions of type 3b (see *3.4.1*) in a quartz grain of a trondjhemite (U1309D 40R-1 21-24 cm). Note that inclusions of fluid type 3a are similar in shape with inclusions of type 2b but do not host a halite cube. F: Secondary fluid inclusions in plagioclase related to chlorite vein.**

### 3.3.2 Gabbro

Gabbros in U1309B and U1309D vary in grain size (microgabbro to coarse grained gabbro), and deformation type, and can also be divided in several groups (*Figure 2-3*): microgabbro, oxide gabbro, gabbronorite, gabbro, olivine gabbro, troctolitic gabbro, and troctolite. The gabbroic series are divided into units throughout the core according to the primary mineralogy, igneous contacts, and variations in grain size (Blackman, *et al.*, 2006).

Gabbros of the upper part of the core are intruded by a series of basaltic and diabasic dikes. Gabbros in this section are commonly coarse grained, extremely brecciated, cataclastic in texture, and show yellow-green alteration veins. The yellow-green alteration, possibly actinolite/tremolite, also quite commonly forms the matrix supporting the gabbroic clasts (generally plagioclase).

Deeper, units consist of a series of interlayered gabbroic rocks, with a general downhole coarsening from medium to coarse-grained. Overall, gabbros are equigranular, but can exhibit different types of deformation ranging from (rare) mylonitic to absolutely undeformed. Plagioclase is generally unaltered, but can show evidence of albitisation in the vicinity of veins and magmatic/leucocratic intrusions. Plagioclase can also be altered to chlorite along fractures. Clinopyroxene rarely survives alteration and is replaced by amphiboles (hornblende, actinolite, and tremolite). When olivine is present, in troctolitic gabbro and olivine gabbro for instance, it is more or less replaced by amphibole and chlorite to form corona texture along with plagioclase. Dynamic recrystallisation of plagioclase and amphibole is a particular feature of a few samples.

#### 3.3.2.1 Sample U1309D 5R-3 107-110

Sample U1309D 5R-3 107-110 is a medium grained troctolitic gabbro exhibiting deformed plagioclase grains partially replaced by chlorite. Olivine is replaced by tremolite (*Figure 2-10*; *Appendix 1*). Amphiboles replacing clinopyroxene are actinolitic in composition (Figure 3-3*E*). Tremolite replaces olivine to form the corona texture with the chlorite around

the plagioclase (*Figure 3-3C and D*). Plagioclase is slightly deformed and exhibits subgrain boundaries and deformation twins. It is also commonly cut by chlorite veins.

#### 3.3.2.2 Sample U1309D 10R-1 127-129

Sample U1309D 10R-1 127-129 cm is a mylonitised coarse gabbro composed of roughly 60% deformed plagioclase, recrystallised in part, 40% clinopyroxene replaced by green-brown hornblende and actinolite. Granoblastic recrystallisation also affects the boundaries of amphibole grains suggesting that the shear zone was active at amphibolite facies conditions.

#### 3.3.2.3 Fluid inclusions

In those two samples, fluid inclusions occur as both regular and irregular shape secondary inclusions in plagioclase (*Figure 3-4B*). They are 2 phase and liquid-dominated, ranging in size from 10 to 20 µm. They occur in trails decorating fractures or perpendicular to chlorite veins.

### 3.3.3 Trondjhemite

#### 3.3.3.1 Sample U1309D 40R-1 21-24

Sample U1309D 40R-1 21-24 cm is a fine to medium grained trondjhemite composed of plagioclase of albitic composition (*Figure 2-9*; *Appendix 1*) and quartz. Plagioclase and quartz are usually anhedral and form also graphic intergrowths (*Figure 3-3F*). Alteration minerals are not common. This sample is a late leucocratic magmatic intrusion crosscut by a late quartz vein of 4 to 5 mm in width. Quartz grains are elongated and show radial extinction as the quartz from the quartz-chlorite vein of sample U1309D 1R-1 41-44 cm.

#### 3.3.3.2 Fluid inclusions

Fluid inclusions in the vein are generally distributed as clusters in the centre and clear part of the grains, and are interpreted as being primary in origin. They are of irregular shape (*Figure 3-4D*) ranging in size from 10 to 20 µm, with some reaching several 10's of µm

A 5 mm quartz grain of the host rock contains a large number of fluid inclusions, making the interpretation of their origin difficult, but nonetheless assumed to be primary. Two populations are observed; one with irregular shaped liquid-dominated inclusions and the other one with a halite daughter crystal. Halite bearing inclusions (*Figure 3-4E)* are generally bigger than the ones without and are irregular in shape (20 to 50 μm).

# 3.4 Results

## 3.4.1 Fluid inclusion petrography and results

Three types of fluid inclusions have been identified in the samples studied (*Figure 3-4*). *Table 3-1* summarises the results obtained for homogenisation temperature and salinity for each type of inclusion and material. Types of fluid inclusions presented in this chapter are classified with the numbering used in Kelley *et al.*, (1992):

- Type 1 inclusions are liquid-dominated low salinity
- Type 2 inclusions are vapour-dominated low salinity
- Type 3 inclusions are high salinity inclusions

**Table 3-1: Fluid inclusion microthermetric analyses. Tdjh = Trondjhemite**

| Sample (U1309D) | Rock | Depth (mbsf) | Mineral host | Inclusion type | N | Th range (°C) | Th mode (°C) | Salinity range (wt% NaCl) | Salinity mode (wt% NaCl) |
|---|---|---|---|---|---|---|---|---|---|
| 1R-1 41-44 | Diabase | 21.93 | Qtz-Chl vein | 1a | 67 | 147.7-285.0 | 161.7 | 3.1-5.1 | 3.7 |
| 5R-3 107-110 | Troctolitic gabbro | 39.96 | Plg | 1b | 96 | 123.2-349.0 | 277.0 | 0.2-1.1 | 0.5 |
| 10R-1 127-129 | Gabbro | 61.48 | Plg | 1a/b | 82 | 220.0-376.5 | 267.3 | 0.7-4.3 | 1.4 |
| 40R-1 6-12 | Troctolite | 214.89 | Qtz vein | 1a | 5 | 167.0-238.8 | - | 3.4-3.9 | 3.7 |
| 40R-1 17-19 | Troctolite | 214.98 | Qtz vein | 1a | 83 | 135.0-289.5 | 210.0 | 2.4-3.7 | 3.4 |
| 40R-1 21-24 | Tdjh | 215.02 | Qtz vein | 1a | 58 | 124.5-204.9 | 166.0 | 2.9-4.0 | 3.4 |
| 40R-1 21-24 | Tdjh | 215.02 | Qtz | 3a | 12 | 314.5->400 | - | 9.5-20.7 | 17.4 |
| 40R-1 21-24 | Tdjh | 215.02 | Qtz | 3b | 7 | 336.4->400 | - | 31.1-37.7 | - |

The origin of fluid inclusions was not always really clear; nonetheless, fluid inclusions in quartz veins were usually concentrated in clusters in the centre of the quartz grains and therefore interpreted as primary inclusions. In plagioclase and in quartz grains of the trondjhemite, fluid inclusions are secondary in origin as they are commonly decorating sealed fractures. Nonetheless, the network of fluid inclusions in the trondjhemite is so complex that it is difficult to have a definite idea on their origin.

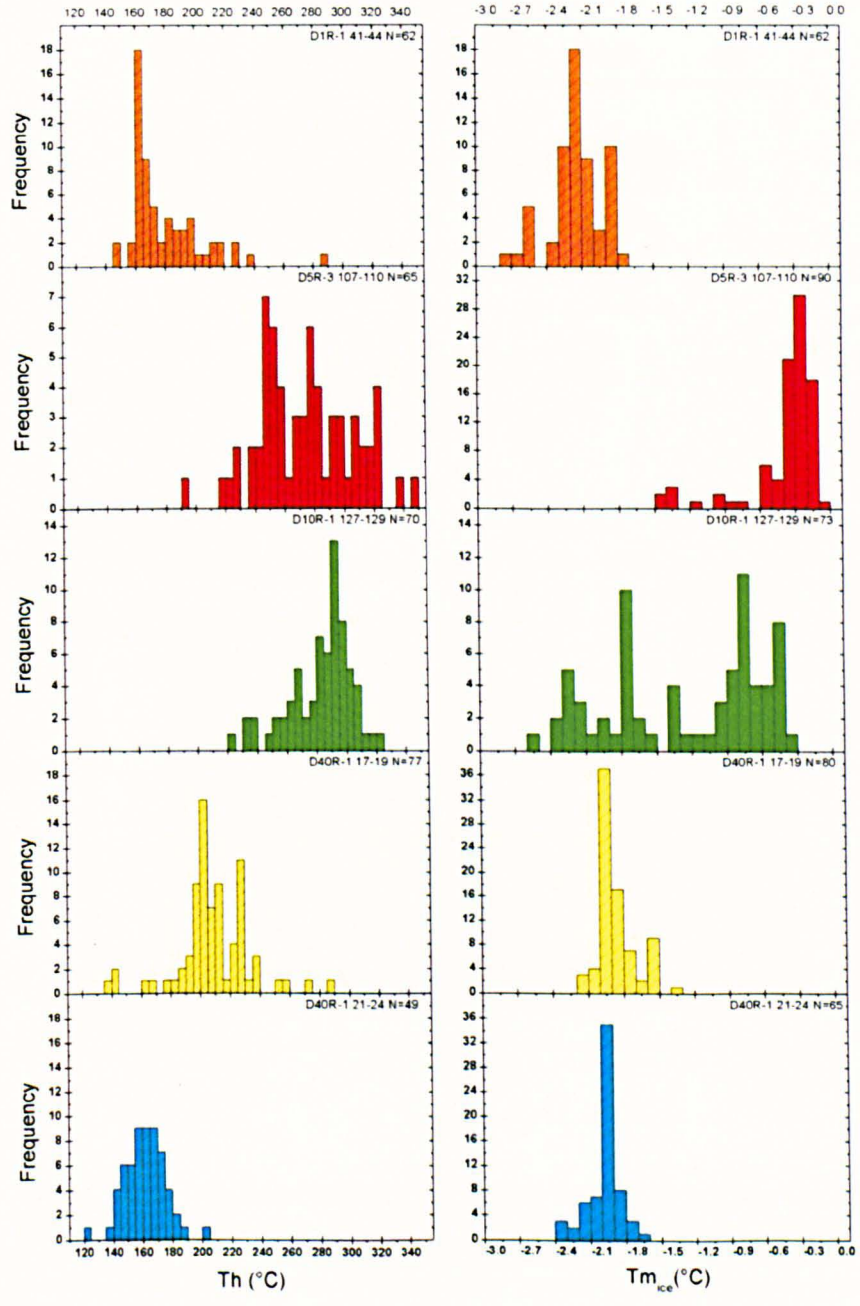


**Figure 3-5: Histograms of homogenisation temperature on left and of temperature of melting of ice on right for type 1 inclusions. Colour scheme is related to samples and is the same in the following figures. Patterns are related to the fluid type. Lines dipping towards the left are for fluid type 1a and lines dipping towards right are for fluid type 1b. Sample D40R-1 6-12 is not represented as the number of measurements was insufficient for generating meaningful statistics (N=5).**

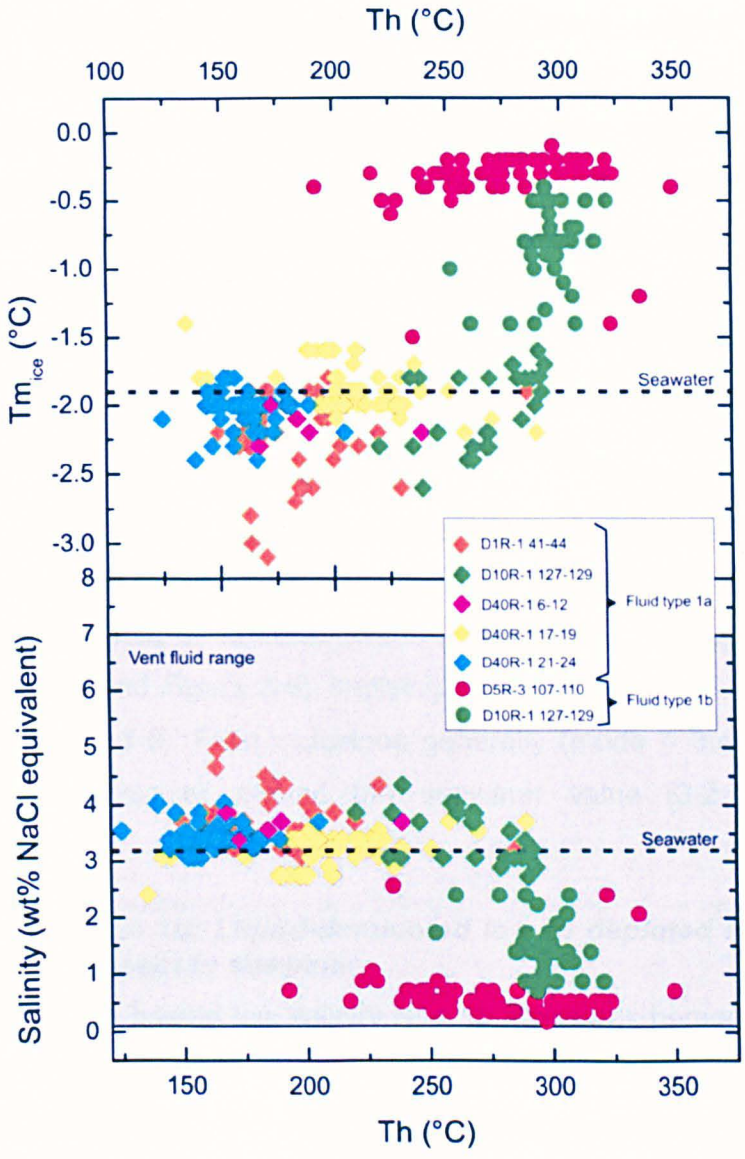


**Figure 3-6: A: Homogenisation temperature against temperature of melting of ice for low salinity inclusions. B: Homogenisation temperature against salinity. Seawater salinity and temperature of ice melting for seawater is shown (dashed line). Range in salinity for fluids exiting submarine hydrothermal vents is also shown (shaded grey area).**

### 3.4.1.1 Type1: Liquid-dominated low salinity inclusions

Liquid-dominated, low salinity inclusions have been found in all the samples in both quartz and plagioclase, and generally occur as irregular inclusions ranging in size from 5 to 30 µm with the exception of sample U1309D 40R-1 17-19 cm, where inclusions up to 100 µm in size have been found. Rare regular shaped inclusions are found in plagioclase grains. Irregular shaped inclusions might be the result of necking-down, stretching and/or leaking. Therefore, particular care has been taken to verify the

similarity in behaviour of irregular shaped inclusions relative to regular shaped ones. Where fluid inclusions exhibited salinities and/or homogenisation temperatures significantly different from the other inclusions inside the same population, those were not included in the statistics.

Type 1 inclusions can be subdivided into two types. Type 1a inclusions are liquid-dominated with seawater-like salinity (*Figure 3-4A, C, and D*) and are generally found in quartz. Type 1b inclusions are liquid-dominated (*Figure 3-4B*) to vapour rich and depleted in terms of salinity compared to seawater (0.1 to 2 Wt% NaCl equivalent).

#### *3.4.1.1.1 Type 1a: Liquid-dominated seawater-like salinity*

Quartz vein-hosted type 1a inclusions homogenise in the liquid phase at temperatures of 124.5 to 349°C and show ice melting at -1.4 to -3.1°C (*Figure 3-5* and *Figure 3-6*), implying salinities of 2.4 to 5.1 Wt% NaCl equivalent (*Figure 3-6*). Fluid inclusions generally (mode = 3.4 ± 1.2 Wt% NaCl equivalent) cluster around the seawater value (3.2 Wt% NaCl equivalent).

#### *3.4.1.1.2 Type 1b: Liquid-dominated low to depleted salinity with respect to seawater*

Plagioclase-hosted low salinity type 1b inclusions homogenise in the liquid phase at temperatures of 192 to 320.3°C and exhibit melting of ice at -0.1 to -1.0°C (*Figure 3-5* and *Figure 3-6*), indicating salinities of 0.2 to 1.7 Wt% NaCl (*Figure 3-6*). Average salinity is 1.4 Wt% NaCl equivalent, depleted relative to the seawater value. In sample U1309D 10R-1 127-129 cm, type 1a inclusions are also present and homogenise in the range of temperatures at equivalent salinities of 2.0 to 4.3 Wt% NaCl.

### 3.4.1.2 Type 2: Vapour-dominated low salinity

Type 2 vapour-dominated low salinity inclusions (Kelley & Delaney, 1987; Kelley & Robinson, 1990; Kelley, *et al.*, 1992) have not been observed in the samples.

### 3.4.1.3 Type 3a: Liquid-dominated high salinity

Liquid-dominated high salinity inclusions lacking daughter minerals are found in quartz grains of the trondjhemite sample (U1309D 40R-1 21-24

cm), and are associated with type 3b inclusions. Their primary or secondary origin is not really clear. They are irregular in shape with a range in size of 5 to 20μm. Homogenisation occurred in the liquid phase at temperatures of 314.5 to >400°C. Melting of ice occurred at -6.2 to -17.6°C (*Figure 3-5* and *Figure 3-6*), indicating salinities of 9.5 to 20.7 Wt% NaCl (*Figure 3-6*).

#### 3.4.1.4 Type 3b: Daughter mineral bearing inclusions

Halite-bearing fluid inclusions have been found in quartz grains of the trondjhemite and are associated with type 3a, although their temporal relationship is not clear. They are irregular in shape with variable size of 10 to 50 μm, liquid-dominated, and rarely contain other daughter mineral than halite. Dissolution of the halite cube (184 to 294°C) always occurred at lower temperatures than the homogenisation temperature, marked by the disappearance of the vapour bubble (336.4 to >400°C). Some inclusions remain unhomogenised at a temperature of 400°C (the limit of the stage used). Halite dissolution has already been observed, and the behaviour of the vapour bubble suggests that the homogenisation is going to occur in the next 20 to 30°C. Those inclusions are indicated by an arrow on *Figure 3-7*. Halite dissolution temperatures indicate equivalent fluid salinities of 31.1 to 37.7 Wt% equivalent.

Cooling experiments have been undertaken in order to test for the presence of additional gas species in the vapour phase, but no clear phase changes have been observed.

#### 3.4.1.5 Liquid-dominated related to chlorite veins

Elongated cigar shape inclusions have been observed in plagioclase, and occur adjacent and perpendicular to chlorite filled veins (*Figure 3-4F*). Attempts at microthermometric analyses have not been successful. The thickness of the wafer made the observation of a single inclusion impossible and therefore, no results will be presented.

### 3.4.2 Summary

- Table 3-2 summarises the characteristics of the different fluid types
- Type 1a fluid has a seawater salinity signature.
- Type 1b fluid is depleted in salinity with respect to the seawater value.
- Type 1b fluid seems to homogenise at temperature greater than type 1a fluid.
- Type 3 fluid shows the highest homogenisation temperatures.
- In the trondjhemite sample (U1309D 40R-1 21-24), type 1a fluid is observed only in the late crosscutting quartz vein. Fluids present in the rock are all high salinity with respect to seawater.
- All inclusions homogenise in the liquid phase. None of the hypersaline inclusions exhibit homogenisation by halite dissolution.
- Some hypersaline inclusions remain unhomogenised at temperature greater than 400°C. The vapour bubble behaviour suggests homogenisation would have occurred in the next 20-30°C.
- No additional gas species have been detected.

**Table 3-2: Summary of microthermometry results**

| Fluid type | Description | Salinity (wt% NaCl) | Homogenisation temperature (°C) | Paragenese |
|---|---|---|---|---|
| 1a | L+V(L) seawater like salinity | 2.4-5.1 | 120-300 | Quartz vein in diabase, troctolite and trondjhemite |
| 1b | L+V(L) low salinity with respect to seawater | 0.7-2.2 | 220-380 | Plagioclase in gabbros |
| 2 | L+V(V) | - | - | Not found |
| 3a | L+V(L) high salinity with respect to seawater | 9.5-20.7 | 315->400 | Quartz grain of trondjhemite |
| 3b | L+V+H(L) High salinity with halite daughter crystal | 31.1-37.7 | 340->400 | Quartz grain of trondjhemite |

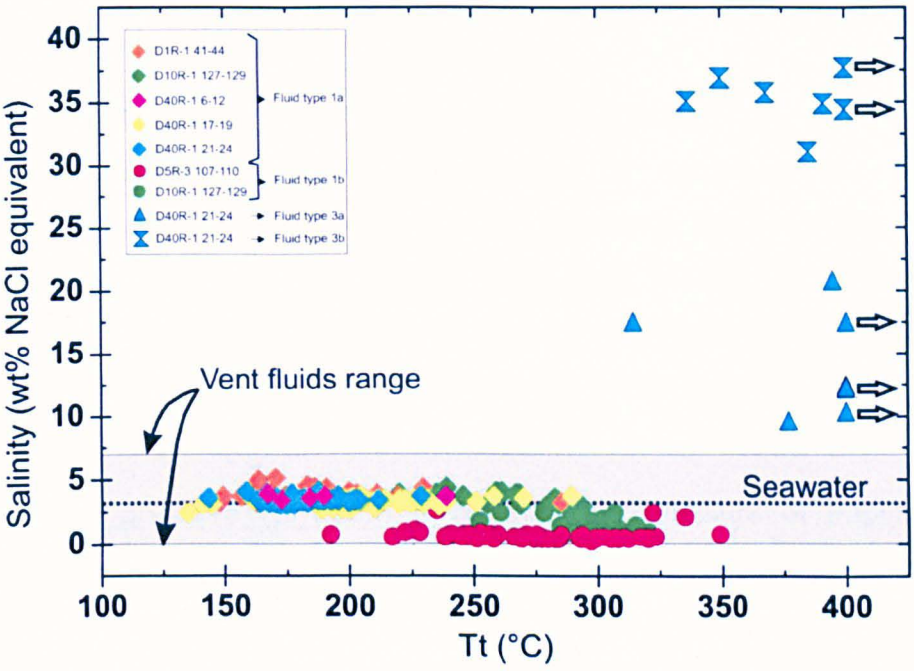


**Figure 3-7 Temperature of homogenisation against salinity for all samples.**

# 3.5 Discussion

## 3.5.1 Temperatures of fluid entrapment

A pressure correction is necessary to determine the actual temperature of entrapment of aqueous inclusions and can be made accurately for inclusions that contain pure NaCl solution, for which the salinity of the fluid has been correctly determined, and for which homogenisation occurs in the liquid phase, and when pressure of formation can be estimated (Roedder, 1984).

Why pressure correction is needed: the pressure of trapping is actually higher than the vapour pressure. To calculate it, pressure of trapping is estimated from the recorded depth of the sample in the hole in addition to the water column. Pressure of trapping is then estimated to be at a minimum of 400 bars, assuming a water column of 2000m, with samples subject to hydrostatic pressure only, and at a maximum of 2800 bars, assuming a water column of 3500 m as suggested by the TAG model, and with a lithostatic pressure.

Temperatures of trapping were calculated from the software Loner38© from http://fluids.unileoben.ac.at, that computes the following equation (Zhang & Frantz, 1987).

$$P = A_1 + A_2 T \qquad \textbf{Equation 3-3}$$

Where P is the pressure, T the corrected temperature, and A1 and A2 constant calculated from the following:

$$A_1 = 6.100 \cdot 10^{-3} + (2.385 \cdot 10^{-1} - a_1)T_h - (2.855 \cdot 10^{-3} + a_2)T_h^2 - (a_3 T_h + a_4 T_h^2)m$$

$$A_2 = a_1 + a_2 T_h + 9.888 \cdot 10^{-6} T_h^2 + (a_3 + a_4 T_h)m$$

Where m is the molality, $T_h$ the homogenisation temperature and $a_1$, $a_2$, $a_3$, and $a_4$ are parameters specific to the studied system, which is $H_2O$-NaCl in the study's case. This is justified by results to be presented in *Chapter 4*. Their values are shown in *Table 3-3*.

**Table 3-3: Parameters for the system $H_2O$-NaCl (Zhang & Frantz, 1987).**

| a1 | a2 | a3 | a4 |
|---|---|---|---|
| $2.873 \cdot 10^{1}$ | $-6.477 \cdot 10^{-2}$ | $-2.009 \cdot 10^{-1}$ | $3.186 \cdot 10^{-3}$ |

The temperature of trapping is generally 20 to 30°C higher than the temperature of homogenisation for the minimum pressure correction (*Figure 3-9A*) and ~150°C (for quartz vein samples) to ~240°C (for plagioclase samples) higher than the temperature of homogenisation for the maximum pressure correction (*Figure 3-9B*). The correction is not constant because it depends on the composition of the fluid and the temperature of homogenisation as isochores calculated show a higher angle from vertical at higher temperature.

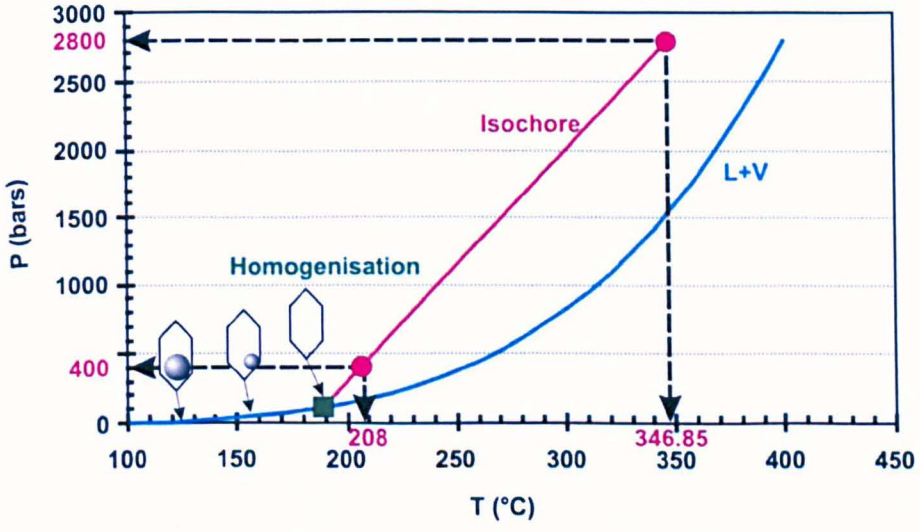


**Figure 3-8: Temperature-pressure projection of the $H_2O$-NaCl system showing the path followed by a fluid inclusion of 3.5 Wt.% NaCl. At room temperature, the inclusion contains a vapour bubble and liquid. With heating, the inclusion follows the liquid-vapour curve (Khaibullin and Borisov, 1966) and the vapour bubble decreases before disappearing at homogenisation temperature. At this temperature, the inclusion follows the isochore (dependent on the salinity and the homogenisation temperature of the inclusion). The isochore is calculated with the software Loner38© from http://fluids.unileoben.ac.at. The pressure of trapping is estimated and the temperature of trapping can be read on the x axis.**

*Figure 3-8* shows an example of the P-T path followed by a fluid inclusion with heating. The average salinity of fluid type 1a (3.5 Wt.% NaCl) and the average temperature of homogenisation (185.5°C) is used in this diagram. The L+V curve is from Khaibullin and Borisov (1966) that present

temperature-pressure-composition-density data for the $H_2O$-NaCl liquid-vapour surface. At homogenisation, the fluid inclusion follows the isochore, and at selected or estimated pressure of trapping (400 and 2800 bars), the temperature of trapping is read on the x axis (208 and 346.85°C respectively), that is 22.5°C higher than the temperature of homogenisation for the minimum pressure correction and 161.35°C higher than the temperature of homogenisation for the maximum pressure correction.

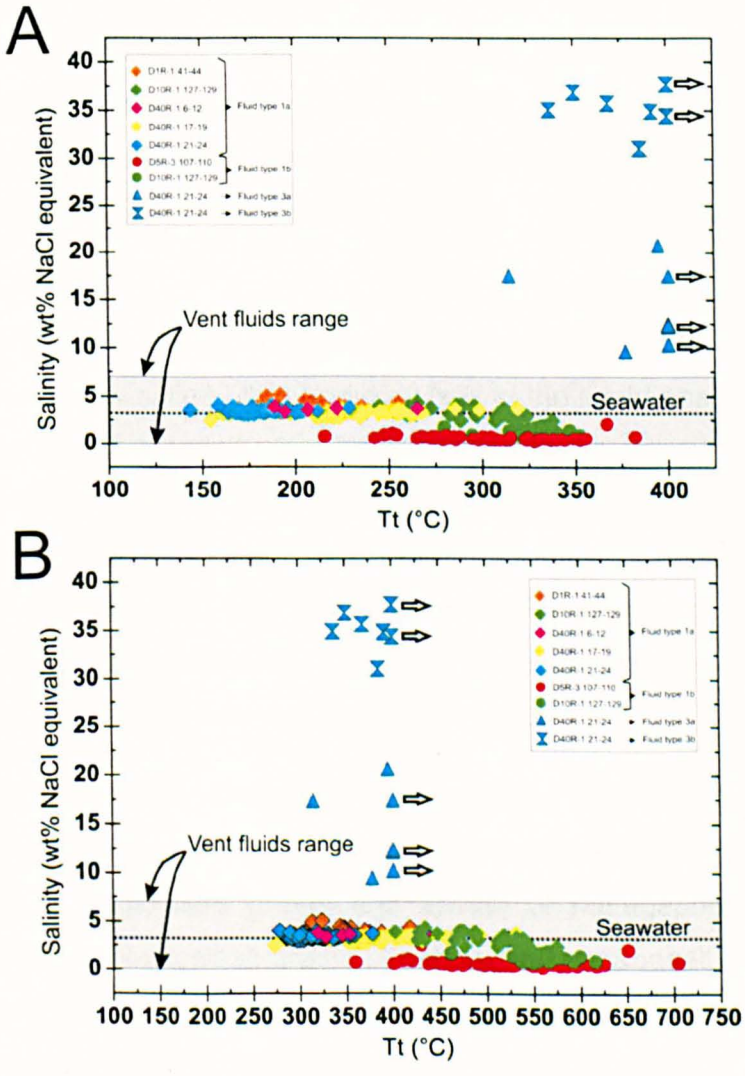


**Figure 3-9: Salinity against temperature of trapping for a minimum pressure of 400 bars (A) and a maximum pressure of 2800 bars (B). Pressure correction applied on low salinity inclusions only.**

## 3.5.2 Previous work on fluid inclusions in oceanic settings

### 3.5.2.1 Fluids in the oceanic crust

Fluids in the oceanic crust have been studied in the past in order to better understand the seawater circulation in the crust at various places including the Mid-Atlantic Ridge - Kane Fracture Zone (MAR-KFZ) which is very similar to the Atlantis Massif in terms of geological, geophysical and tectonic setting (Kelley & Delaney, 1987; Kelley, *et al.*, 1993), the MAR Oceanographer Transform (Vanko, *et al.*, 1992), Hole 894G at Hess Deep (Kelley & Malpas, 1996; Saccocia & Gillis, 1995), Hole 504B near the Costa Rica Rift (Kelley, *et al.*, 1995), the Hole 735B at the Southwest Indian Ridge (SWIR) (Kelley & Früh-Green, 2001), and the TAG hydrothermal mound (Tivey, *et al.*, 1998).

Overall, fluid inclusions in the oceanic crust occur in three types: A liquid-dominated low salinity that homogenises in the liquid phase (type 1), a vapour-dominated low salinity that homogenises in the vapour phase (type 2), and a daughter mineral-bearing (generally halite) inclusion of high salinity that homogenises either in the liquid phase, or the vapour phase or even by halite dissolution (type 3). This general observation may vary according to the behaviour at homogenisation, the presence of various gas phase and/or other daughter crystals inside one single inclusion.

Fluid type 1a (liquid-dominated low salinity) are common in oceanic crust samples and in ophiolite samples. This type of fluid is found in the MARK area in plagioclase grains and apatite of metagabbros (Kelley & Delaney, 1987), in plagioclase grains of gabbro and metabasalt and in quartz grains of quartz breccias and metabasalts (Kelley, *et al.*, 1993). It is also present at Hess Deep in plagioclase and apatite of gabbros and quartz grains of quartz breccias (Kelley & Malpas, 1996; Saccocia & Gillis, 1995), in the Southwest Indian Ridge hole 735B in plagioclase, apatite and quartz of gabbros (Kelley & Früh-Green, 2001), in quartz and plagioclase of plagiogranite and epidosite from the Oceanographer Transform (Vanko, *et al.*, 1992), in plagioclase and quartz of diabase from the Costa Rica Rift hole

504B (Kelley, *et al.*, 1995), and in anhydrite of breccias from TAG (Tivey, *et al.*, 1998).

Fluids of salinity depleted with respect to seawater salinity (3.2 Wt% NaCl equivalent) are less common in oceanic crust. They are found in plagioclase of metagabbros and gabbros from the MARK area (Kelley & Delaney, 1987; Kelley, *et al.*, 1993), in plagioclase and apatite of gabbros and quartz of breccias and gabbros from Hess Deep and SWIR (Kelley & Früh-Green, 2001; Kelley & Malpas, 1996; Saccocia & Gillis, 1995), in plagioclase and quartz of diabase from the Costa Rica Rift hole 504B (Kelley, *et al.*, 1995), and in anhydrite of breccias from TAG (Tivey, *et al.*, 1998).

Type 3a fluid is a fluid of moderate to high salinity without halite daughter crystals at room temperature. This type of fluid is less common in oceanic sections but quite often present in ophiolites. It is found in apatite and plagioclase from Hess Deep (Kelley & Malpas, 1996), in quartz of gabbros from SWIR (Kelley & Früh-Green, 2001), in plagioclase of diabase from hole 504B of the Costa Rica Rift (Kelley, *et al.*, 1995).

Fluid type 3b is a saturated fluid in NaCl. They contain a halite daughter crystal at room temperature. This type of fluid is found in apatite and quartz of metagabbros from the MARK area (Kelley & Delaney, 1987; Kelley, *et al.*, 1993), in apatite and plagioclase of gabbros from Hess Deep (Kelley & Malpas, 1996), in quartz of gabbros from the SWIR (Kelley & Früh-Green, 2001), in quartz and plagioclase of plagiogranite and epidosite from the Oceanographer Transform (Vanko, *et al.*, 1992).

*Table 3-4* gives a detailed summary of studies carried out in those areas.

### 3.5.2.2 Fluid inclusions in Ophiolites

Fluid inclusions studies have also been carried out in samples from ophiolite complexes such as the Troodos ophiolite (Cowan & Cann, 1988; Kelley & Robinson, 1990; Kelley, *et al.*, 1992; Morgan, 2008; Spooner &

Bray, 1977; Vibetti, 1993), the Oman ophiolite (Nehlig, 1991), and the Lizard ophiolite (Hopkinson & Roberts, 1996).

As for fluid inclusions studied in samples from sections of oceanic crust, three types of fluids are found in ophiolites.

- A liquid-dominated fluid with low salinity (type 1)
- A vapour-dominated low salinity fluid (type 2)
- A high salinity halite bearing fluid (type 3)

Fluid type 1a is quite commonly found in ophiolites. It is found in quartz and epidote of plagiogranite, gabbros, sheeted dykes, and stockwork from the Troodos ophiolite (Cowan & Cann, 1988; Kelley & Robinson, 1990; Kelley, *et al.*, 1992; Morgan, 2008; Spooner & Bray, 1977; Vibetti, 1993), in quartz of sheeted dykes, plagiogranite and gabbros from the Oman ophiolite (Nehlig, 1991), and in quartz of gabbros from the Lizard ophiolite (Hopkinson & Roberts, 1996).

Fluid type 1b is also found commonly in ophiolite samples. It is found in quartz and epidote of plagiogranite, gabbros, sheeted dykes, and stockwork from the Troodos Ophiolite (Cowan & Cann, 1988; Kelley & Robinson, 1990; Kelley, *et al.*, 1992; Morgan, 2008; Spooner & Bray, 1977; Vibetti, 1993), in quartz of sheeted dykes, plagiogranite and gabbros from the Oman ophiolite (Nehlig, 1991), and in quartz of gabbros from the Lizard ophiolite (Hopkinson & Roberts, 1996).

Fluid type 3a is quite commonly present in ophiolites. Examples include inclusions in quartz of stockworks, sheeted dyke, gabbros and plagiogranite from the Troodos, Oman and Lizard ophiolites (Hopkinson & Roberts, 1996; Morgan, 2008; Nehlig, 1991).

Fluid type 3b is found in quartz of plagiogranite and gabbros from the Troodos and Oman ophiolites (Cowan & Cann, 1988; Kelley & Robinson, 1990; Kelley, *et al.*, 1992; Morgan, 2008; Nehlig, 1991; Vibetti, 1993).

Data collected in ophiolites are shown in *Table 3-5*.

**Table 3-4: Review of oceanic crust fluid inclusions data available in the literature. $3b_L$ = type 3 inclusions with halite cube and homogenisation occurring in the liquid phase. $3b_H$ = type 3 inclusions with homogenisation occurring by halite dissolution.**

| Site | Rock | Mineral host | Type | Homogenisation | Th (°C) | Salinity wt% NaCl) | Reference |
|---|---|---|---|---|---|---|---|
| MARK | metagabbros | Plg | 1 | liquid | 270-300 | 1-7 | (Kelley & Delaney,1987) |
| | metagabbros | Ap | 1 | liquid | 260-300 | 4-5 | |
| | metagabbros | Ap | 2 | vapour | 370-400 | 1-2 | |
| | metagabbros | augite | 2 | vapour | 380-440 | 3.5-6.5 | |
| | metagabbros | epidote | 2 | vapour/liquid/pseudocritic | 370-440 | 4-6 | |
| | metagabbros | Ap | $3b_L$ | liquid | >700 | 38-48 | |
| | gabbros | Plg | 1 | liquid | 240-326 | 0.4-7.6 | (Kelley *et al.*, 1993) |
| | Qtz bcc | Qtz | 1 | liquid | 187-343 | 3.5-6.5 | |
| | metabasalt | Qtz | 1 | liquid | 266-303 | 3.8-4.8 | |
| | metabasalt | Plg | 1 | liquid | 193-313 | 3.8-6.9 | |
| | gabbros | Ap | 2 | vapour | 364-416 | 1-2 | |
| | gabbros | augite | 2 | vapour | 387-433 | 3.5-6.5 | |
| | gabbros | epidote | 2 | vapour | 397-435 | 4.4-5.9 | |
| | gabbros | Plg | $3b_L$ | liquid | 330-349 | 0.4-0.9 | |
| | gabbros | Plg | $3b_L$ | liquid | 257-311 | 0.4-7 | |
| | gabbros | FAp | $3b_L$ | liquid | >700 | 41-47 | |
| | gabbros | Qtz | $3b_H$ | halite diss | 312-338 | 39-41 | |
| Hess Deep 894G | gabbros | Plg | 1 | liquid | 207-323 | 0.1-13.4 | (Kelley & Malpas, 1995) |
| | gabbros | Ap | 1 | liquid | 216-372 | 0.9-19.3 | |
| | gabbros | Ap | $3b_L$ | liquid | 193-346 | 29-32 | |
| | gabbros | Plg | $3b_H$ | halite diss | 191-305 | 31-39 | |
| | Qtz bcc | Qtz | 1 | liquid | 160-370 | 0.1-4.8 | (Saccocia & Gillis, 1995) |
| SWIR 735b | gabbros | Plg | 1 | liquid | 190-292 | 2.3-6.7 | (Kelley & Früh-Green, 2001) |
| | gabbros | Ap | 1 | liquid | 339-395 | 1.4-4.5 | |
| | gabbros | Qtz | 1 | liquid | 333-465 | 3.3-18 | |
| | gabbros | Ap | 2 | vapour | 369-401 | 1.4-4.5 | |
| | gabbros | Qtz | $3b_L$ | liquid | 333-418 | 32-51 | |
| | gabbros | Qtz | $3b_H$ | halite diss | 255-418 | 32-47 | |
| Oceanographer | metag, plggranite, epidosite | Qtz / Plg | 1 | liquid | 150-400 | 3-8 | (Vanko *et al.*, 1992) |
| | plgg /epi | Qtz / Plg | 2 | vapour | 370->500 | 3.2-8 | |
| | plgg /epi | Qtz / Plg | 2 | liquid | 125-395 | 3.5-8 | |
| | plgg /epi | Qtz / Plg | $3b_L$ | liquid | 247-362 | 14.8-27.7 | |
| | plgg /epi | Qtz / Plg | $3b_H$ | halite diss | 293->500 | 37.6-59.8 | |
| Costa Rica Rift 504b | diabase | Plg | 1 | liquid | 124-202 | 0.0-11.7 | (Kelley, *et al.*, 1995) |
| | diabase | Qtz | 1 | liquid | 140-146 | 2.9-4 | |
| TAG | anhydrite bcc | anhydrite | 1 | liquid | 168-361 | 1.2-5.1 | (Tivey, *et al.*, 1998) |

**Table 3-5: Review of ophiolite fluid inclusions studies. *= Calculation made on melting of ice instead of halite dissolution.**

| Site | Rock | Mineral host | Type | Homogenisation | Th (°C) | Salinity (wt% NaCl) | Reference |
|---|---|---|---|---|---|---|---|
| Troodos | plggranite (dykes) | Qtz / epidote | 1 | liquid | 330-410 | 0-2 | (Cowan & Cann, 1988) |
| | plggranite (dykes) | | $3b_L$ | liquid | 330-430 | 37-48 | |
| | plggranite (dykes) | Qtz | 1 | | 200-400 | 2-7 | (Kelley & Robinson, 1990) |
| | plggranite (dykes) | Qtz / epidote | 2 | vapour | 360-420 | 1-5 | |
| | plggranite (dykes) | Qtz | $3b_H$ | halite diss | 400-500 | 46-56 | |
| | plggranite / gabbros | Qtz / epidote | 1 | Liquid | 182-437 | 2-7 | (Kelley *et al.*, 1992) |
| | plggranite / gabbros | Qtz / epidote | 2 | Vapour | 378-413 | 1-5 | |
| | plggranite / gabbros | Qtz | $3b_L$ | Liquid | 375-400 | 36-45 | |
| | plggranite / gabbros | | $3b_H$ | Halite diss | 302-537 | 38-61 | |
| | stockwork | Qtz | 1 | liquid | 319-422 | 3.3-10.9 | (Morgan, 2008) |
| | sheeted dyke | Qtz | 1 | liquid | 280-418 | 0.17-8.2 | |
| | plutonic sequence sheeted dyke transition | Qtz | 1 | liquid | 314-477 | 1.8-19 | |
| | plutonic sequence sheeted dyke transition | Qtz | $3b_L$ | liquid | 272-377 | 31-44 | |
| | plutonic sequence | Qtz | 1 | liquid | 298-433 | 1.8-22.7 | |
| | plutonic sequence | Qtz | $3b_L$ | liquid | 259-345 | 34.9-37.1 | |
| | sulphide deposit | | 1 | liquid | 300-350 | 2.7-4 | (Spooner & Bray, 1977) |
| | sheeted dykes | Qtz | 1 | liquid | 140-354 | 0.2-7.8 | (Vibetti, 1993) |
| | gabbros | Qtz | 3b | ? | 130-300 | 22-35* | |
| Oman | extrusive | Qtz | 1 | ? | 130-400 | 1.4-10 | (Nehlig, 1991) |
| | sheeted dyke | Qtz | 1 | ? | 150-400 | 1.1-13 | |
| | plggranite | Qtz | 1 | liquid | 213-429 | 1.9-8.9 | |
| | plggranite | Qtz | 2 | vapour | 390-452 | 3.7-4.3 | |
| | plggranite | Qtz | $3b_H$ | halite diss | 333-456 | 40-52 | |
| | gabbros | Qtz / Am | 1 | ? | 106-390 | 1.4-6 | |
| Lizard | plutonic sequence | Qtz | 1 | liquid | 190-410 | 2.1-8 | (Hopkinson & Roberts, 1996) |
| | plutonic sequence | Qtz | 2 | vapour | 268-408 | 0.0-6.1 | |
| | plutonic sequence | Qtz | 1 | liquid | 240-310 | 1.2-2.2 | |
| | plutonic sequence | Qtz | 2 | vapour | 320-370 | 0.3-1.6 | |

## 3.5.3 Comparison with literature data set

In this section, the new data are compared with literature data and results compiled in *Figure 3-10* for sections of oceanic crust and in *Figure 3-11* for ophiolites.

### 3.5.3.1 Type 1a

Samples from the Atlantic oceanic crust (MARK, Oceanographer and TAG) exhibit roughly the same range in salinity as the samples of fluid type 1a (*Figure 3-10*). Samples from the Pacific, Indian oceanic crust (Hess Deep and SWIR 735B), Troodos, Oman and Lizard ophiolite cover the range in salinity of the type 1a samples but reach much higher values (up to ~22Wt% NaCl equivalent). These salinities are comparable to fluid type 3a (see *3.5.3.3 au-dessous*). Temperatures of homogenisation are roughly similar, although almost all oceanic sections reported show higher maximum temperatures. Higher temperatures are common for ophiolite samples where the temperature of homogenisation can reach 475°C (Morgan, 2008) (*Figure 3-10*, and *Figure 3-11*).

### 3.5.3.2 Type 1b

In this study, this type of fluid was only found in plagioclase in secondary fluid inclusions. *Figure 3-11* shows that these type 1b samples give comparable ranges of salinity to samples from the Troodos ophiolite (Cowan & Cann, 1988), with the difference that homogenisation occurs at higher temperature in the ophiolite. In oceanic crust sections, homogenisation temperatures are similar (*Figure 3-10*).

### 3.5.3.3 Type 3a

*Figure 3-10* shows that only fluids from SWIR hole 753B match the existing data. Samples from Hess Deep exhibit high salinity but homogenise at lower temperature than fluids from the Atlantis Massif. Troodos and Oman ophiolite samples (Morgan, 2008; Nehlig, 1991) also show moderately high salinity at homogenisation temperatures in the same range as those of fluid from U1309D (*Figure 3-11*).

#### 3.5.3.4 Type 3b

Fluid inclusions of type 3b always homogenise in the liquid phase with halite dissolution occurring before the disappearance of the vapour phase. This is illustrated in *Figure 3-10* and *Figure 3-11* where fluid inclusions cluster beneath the equilibrium curve of halite + liquid + vapour. The same observations are made in samples from the MARK area, Hess Deep and hole 735B (Kelley & Delaney, 1987; Kelley & Früh-Green, 2001; Kelley & Malpas, 1996) (*Figure 3-10*), and samples from Troodos (Kelley & Robinson, 1990; Kelley, *et al.*, 1992) (*Figure 3-11*).

Several studies show that homogenisation can also occur by halite dissolution. This is the case in quartz of gabbros from the MARK area, in plagioclase of Hess Deep, in hole 735B of the SWIR and in quartz of plagiogranite from the Oceanographer (Kelley & Früh-Green, 2001; Kelley, *et al.*, 1993; Kelley & Malpas, 1996; Vanko, *et al.*, 1992) (*Figure 3-10*), as well as in quartz of plagiogranite and gabbros from the Troodos and Oman ophiolite (Cowan & Cann, 1988; Kelley & Robinson, 1990; Kelley, *et al.*, 1992; Morgan, 2008; Nehlig, 1991) (*Figure 3-11*). This type of homogenisation indicates that the fluid has been trapped in the presence of halite. In that case, fluid inclusions lie on the H + L + V curve or above.

Fluid type 3b is best compared to fluid in quartz from hole 735B where both salinity and homogenisation temperature match the Atlantis Massif data. The same range in homogenisation temperature is also observed in samples from Troodos but with higher salinities (Kelley & Robinson, 1990; Kelley, *et al.*, 1992).

#### 3.5.3.5 Other types of fluid

Unlike samples of the Atlantis Massif, oceanic crust sections and ophiolite samples may contain vapour-rich, low salinity fluid inclusion populations (*Table 3-4* and

Table 3-5). As for fluid type 1, these vapour rich fluids can be divided in two different populations in which one is less saline than seawater, and the other is equivalent and/or enriched. In general terms, these fluids had been

trapped at higher temperature than fluids of IODP Hole U1309D (270°C - >500°C).

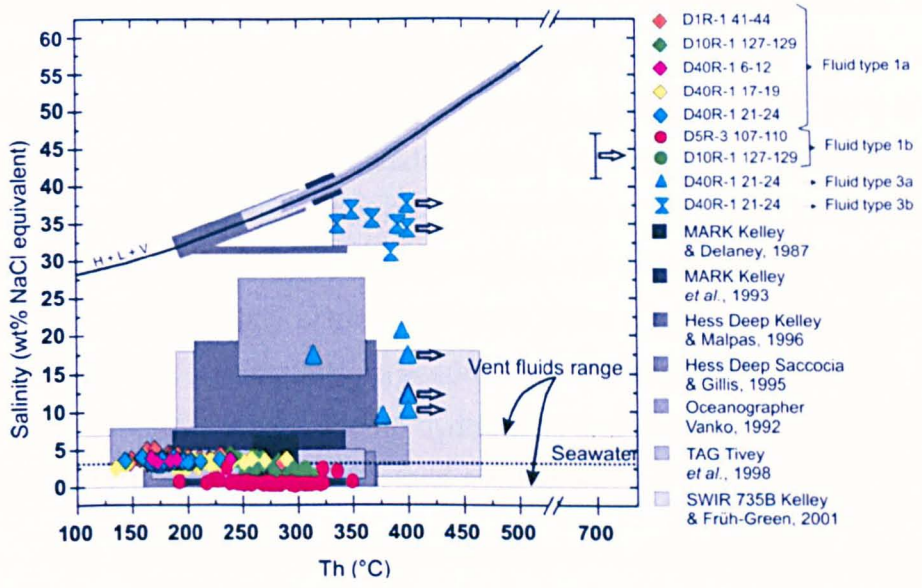


**Figure 3-10: Microthermometric data compared to available data in literature for various oceanic samples. Seawater salinity (3.2Wt% NaCl equivalent) is shown as well as the range of salinities for fluids exiting hydrothermal vents. Inclusions which homogenise by halite dissolution lie on the Halite + Liquid + Vapour curve (H + L + V). Arrows mean that inclusions remain unhomogenised at temperature of 400°C. The behaviour of the vapour bubble suggests that homogenisation is close to being reached (in the next 20-30°C).**

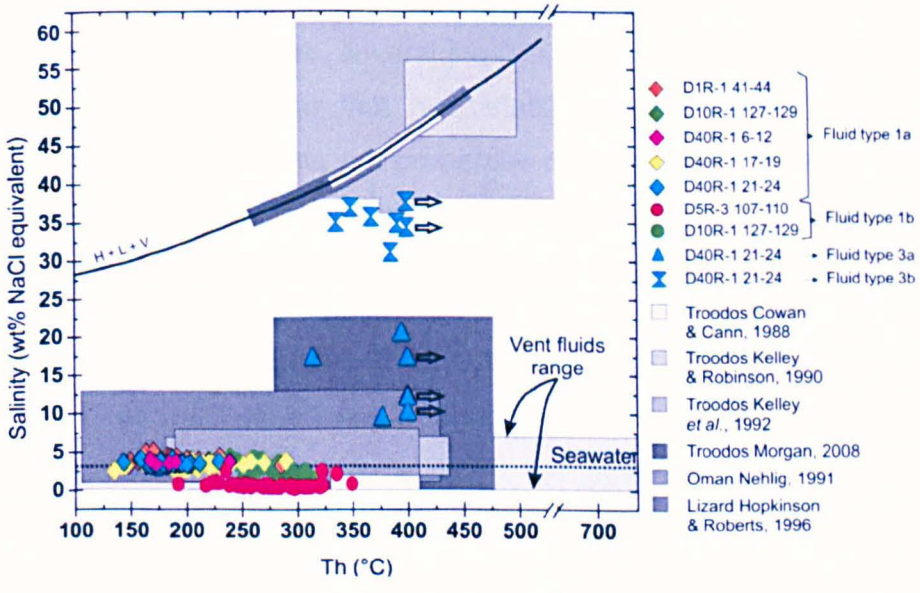


**Figure 3-11: Microthermometric data compared to ophiolite fluid inclusions studies.**

### 3.5.4 Hydrostatic versus lithostatic pressure

Interpretations of the temperature and pressure conditions of the two-phase curve are strongly dependent on the type of fluid pressure which occurs in the crust. Hydrostatic pressure applies to fluids in cracks under brittle conditions. Lithostatic pressure applies to fluids exsolving from a melt under ductile conditions and to fluids isolated from the convective circulation. The change between those conditions is relative to the depth interval of the brittle-ductile transition. Calculations estimate this transition at temperature of 700-800°C in moderately shallow gabbroic rocks (Hirth, *et al.*, 1998). For a seawater model, hydrostatic pressure will be favoured, whereas in a magmatic fluid source model, both hydrostatic and lithostatic pressure will be discussed depending on depth of fluid circulation.

The hydrostatic pressure can show a wide range of gradient whether circulation of cold water or hot water is considered. A cold hydrostatic pressure gradient is ~10000 Pa/m or 100 bars/km, whereas a hot hydrostatic pressure gradient is ~3000 Pa/m or 30 bars/km (Coumou, *et al.*, 2009) (see discussion *3.5.5.2* and *Figure 3-12*). The vertical pressure gradient must be small enough for cold water to flow down in the recharge zone, and large enough for hot water to flow up in the discharge zone, making therefore the pressure gradient lying between cold and hot hydrostatic pressure (Jupp & Schultz, 2000). Nonetheless, several studies (Jupp & Schultz, 2004; Wilcock & McNabb, 1996) assume that hydrostatic pressure very close to cold hydrostatic pressure defines the properties of the circulating fluids such as viscosity and flow resistance. Conditions will be closer to cold hydrostatic in recharge zones, and closer to hot hydrostatic in discharge zones.

### 3.5.5 Processes modifying the salinity

Several processes have been suggested to explain the variations in salinity observed in fluids circulating in the oceanic crust. They include subcritical phase separation (boiling) or supercritical phase separation (condensation) of a seawater-like fluid (Kelley, *et al.*, 1993; Kelley & Malpas, 1996) or magmatic fluid (Kelley & Früh-Green, 2001), magmatic fluids exsolving from melts (Kelley, *et al.*, 1993; Kelley & Malpas, 1996; Kelley, *et*

*al.*, 1992), hydration/dehydration reactions with precipitation/dissolution of associated chloride-bearing minerals (Kelley & Robinson, 1990; Kelley, *et al.*, 1992), and variable mixing of hydrothermal fluid with a phase-separated brine or vapour (Kelley & Robinson, 1990). The commonest explanation for the generation of low salinity fluids is phase separation of seawater-like fluids, and the most approved explanation for generation of high fluid salinities is phase separation of magmatic or seawater-like fluids, without neglecting the possible role of hydration reactions in certain cases. Variable mixing of hydrothermal seawater with phase-separated brines and vapour can change the salinity and temperature of fluids as a late process.

#### 3.5.5.1 Hydration/Dehydration

Under rock dominated condition, hydration reactions or retrograde dissolution of chloride bearing mineral phases have the potential to modify the ionic strength of hydrothermal fluids by consuming or liberating chloride ions (Kelley & Robinson, 1990; Kelley, *et al.*, 1992). Formation of secondary amphibole containing up to 4 Wt% chlorine (Vanko, 1986) can then result in the decrease of fluid salinities, and dissolution of such phases might increase fluid salinities by opposition (Seyfried, *et al.*, 1986).

These processes could then account for slight changes in fluid salinities (low temperature, low salinity fluid generation) at relatively low water-rock ratio conditions, preferentially in a near axis environment recharge zone (Kelley, *et al.*, 1995), in opposition to an outflow zone where fluids rapidly pass through the oceanic crust (Delaney, *et al.*, 1987).

Nonetheless, electron microprobe data of amphiboles in U1309B and U1309D indicate a Cl content of 0.00 to 0.32 Wt% with a mean at 0.05 Wt% (*appendix 1*). Those data are comparable with concentrations of chlorine observed in amphiboles of gabbros of the MARK area (0.3 Wt% on average - (Delaney, *et al.*, 1987; Kelley, *et al.*, 1993)) By considering the highest concentration, and admitting perfect partitioning between chlorine and hydrous mineral phases, at least 50% of gabbros would have to be altered to decrease the fluid salinity by half, or double it if 50% of the initial seawater is consumed (Cathles, 1983; Delaney, *et al.*, 1987; Kelley, *et al.*, 1993). These

processes are therefore unlikely to have a significant impact on through going fluids, although it may have play an important role in the vicinity of veins.

### 3.5.5.2 Phase separation

#### *3.5.5.2.1 Generation of brines*

Fluid sources and pressure conditions for brine-bearing inclusions are difficult to determine. Brine inclusions homogenise by disappearance of the vapour bubble at temperature >400°C. Two models for the generation of brine are as follow: (1) brine and vapour are generated during supercritical phase separation or condensation of either magmatic or seawater-derived fluids with segregation of the phases driven by density differences and entrapment of the brine at depth; (2) direct exsolution of magmatic brine from late stage melts with significant cooling during the migration of the brines along the microfractures (*Figure 3-12*). The system $H_2O$-NaCl will be used in the discussion below as an analogue for fluid circulating in the oceanic crust.

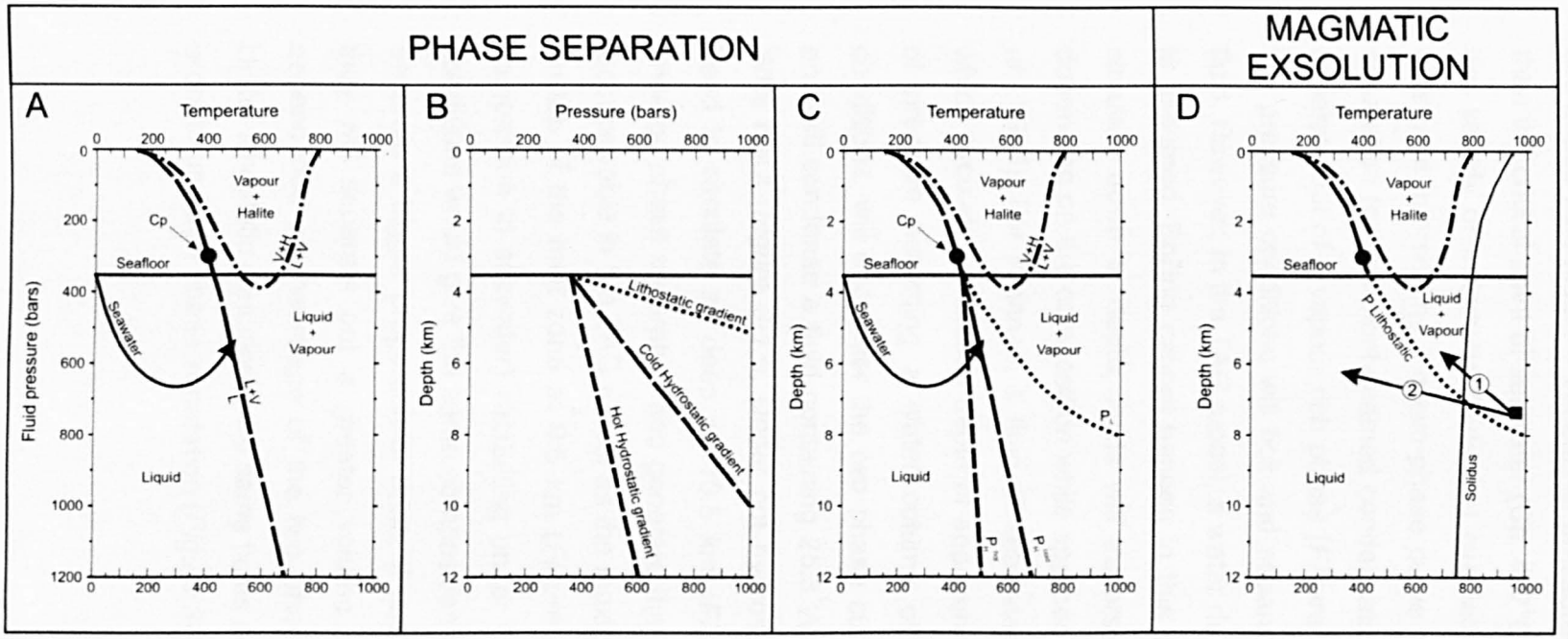


**Figure 3-12: Temperature/Fluid pressure and Pressure/Depth diagram in the system $H_2O$-NaCl for a fluid of seawater composition (3.2Wt% NaCl equivalent). The figure is separated according to two processes: phase separation and magmatic exsolution. Section A: Seafloor is at an approximate depth of 3500 mbsf as constrained by the TAG model. The two phase curve is shown for hydrostatic conditions and separates the one field liquid from the two phase vapour + liquid field (Sourirajan & Kennedy, 1962). The Cp of seawater is also shown (407°C, 298 bars) as well as the three phase curve that separates the stability field of liquid and vapour from that of vapour and halite. Section B: Relationship between pressure and depth for hydrostatic pressure under cold (100 bars/km) and hot (30 bars/km) gradient (Coumou, *et al.*, 2009) and lithostatic pressure gradient. Section C: The two phase curve is shown here in a temperature against depth diagram for cold and hot hydrostatic conditions using both diagram of section A and B, and for lithostatic conditions. In that case, at a given depth, phase separation will occur at higher temperature under lithostatic conditions than under cold hydrostatic conditions, and in turn at higher temperature under cold hydrostatic conditions than under hot hydrostatic conditions. Section D: The solidus of a water-saturated tonalite (Wyllie, 1977) whose intersection with the two phase curve under lithostatic pressure separates the crystal + melt + liquid + vapour field from the crystal + melt + liquid field, is plotted. At depth < 8 km and temperature > to that of the solidus, an exsolved fluid following path 1 will consists of supercritical droplets of brines in a vapour phase; whereas a fluid exsolving along a path similar to 2 will exsolve as a single phase.**

The two-phase curve separates the one phase field (liquid) from the two-phase field (liquid + vapour) at pressure-temperature conditions greater than the critical point of seawater (Cp: 407°C; 298 bars). Fluids of seawater-like salinity or magmatic fluids that circulate at deep levels of the oceanic crust and intersecting the two-phase curve will undergo supercritical phase separation (or commonly named condensation) where droplets of brines will separate out of a vapour rich phase (*Figure 3-12A*). Fluids circulating under low pressure conditions will boil and separate a vapour from a low salinity fluid. However, in the TAG model, a water depth of approximately 3500 mbsf is assumed. Boiling cannot happen in this system. As seawater-like fluids circulate down to depth, fluids will traverse several condensation curves depending on the composition while approaching the heat source (Kelley, *et al.*, 1993). For instance, a fluid of seawater composition (3.2 Wt% NaCl), which circulates at crustal depth of approximately 2 km and under 550 bars of pressure assuming a water column of 3.5 km and cold hydrostatic conditions, will encounter the two phase curve at a temperature of 500°C, and will condense a fluid containing 25.3 Wt% NaCl and a vapour with 2.2 Wt% NaCl (*Figure 3-13*). Under hot hydrostatic conditions, the fluid would need to circulate as deep as 10.5 km (*Figure 3-12B and C*) in order to undergo phase separation and generate the same result, which is obviously inconceivable in the TAG model as the maximum depth of circulation is right on top of the melt zone at 9.5 km (*Figure 2-12*). Higher salinity fluids (in comparison to seawater) circulating under the same pressure temperature conditions would give the same composition for brine and vapour, but would separate a bigger proportion of brine. If fluids circulate at shallower levels, they will separate out a greater volume of vapour given the pressure dependence on the shape of the two phase curve (Kelley, *et al.*, 1993). Under lithostatic conditions, the same fluids must be at higher temperature in order to undergo phase separation (*Figure 3-12C*).

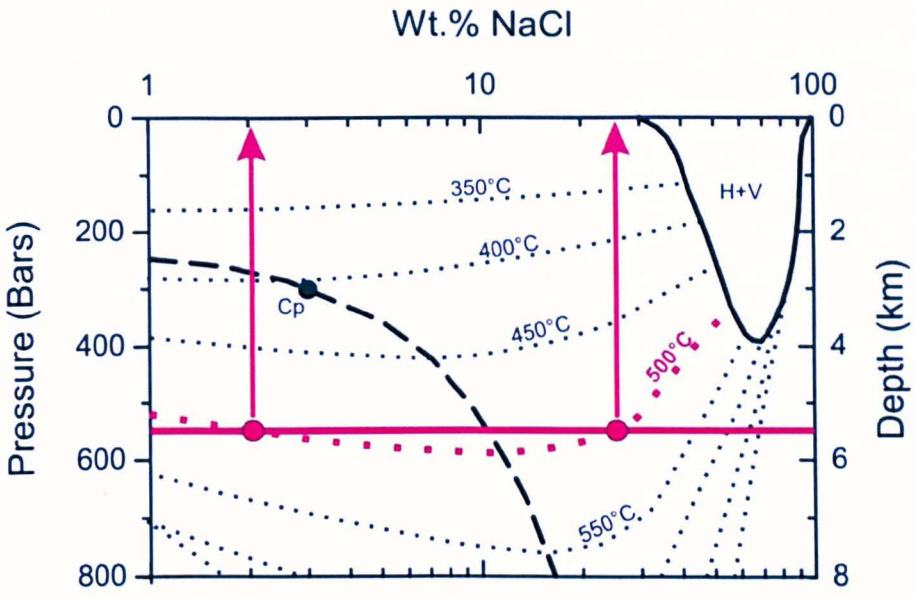


**Figure 3-13: P-X projection of the system $H_2O$-NaCl contoured for T under hydrostatic conditions I. The critical curve (dashed line), the isotherms (dotted lines) and the three phases curve (plain line) are from Sourirajan & Kennedy (1962). A seawater-like fluid which intersects the two phase curve, at temperature of 500°C at pressure of ~550 bars will undergo supercritical phase separation and separate droplets of brines with salinities of ~25.3 Wt% NaCl equivalent from a vapour of salinity close to 2.2 Wt% NaCl equivalent.**

Generation of hypersaline magmatic brines can be explained by two different processes. Vapour and brine can be formed by (1) exsolution of magmatic fluids under supercritical conditions and condensation of droplets of brines in a vapour phase (*Figure 3-12 path D1*) (Kelley & Delaney, 1987; Kelley & Früh-Green, 2001), or (2) by direct exsolution of brines in the absence of a vapour phase (*Figure 3-12 path D2*). *Figure 3-12D* shows the two phase curve for a fluid of seawater salinity (3.2 Wt% NaCl equivalent) for lithostatic conditions. Fluids in the melt are under lithostatic pressure, and at depth < 8 km and at temperature > to the solidus, crystal, melt, liquid and vapour coexist. A fluid exsolving under conditions of the two phase field will undergo exsolution under supercritical conditions and condensation of immiscible droplets of brine in a vapour phase (*Figure 3-12D1*). At pressure-temperature conditions greater than that, the solidus separates a field where crystal, melt and liquid coexist from a single phase liquid field, such that any fluid under those conditions would be exsolved as one single phase. A similar result can be obtained from a fluid originally in the field where crystal,

melt, liquid and vapour coexist, if it encounters the two phase field curve during the cooling history. Such fluid would then be exsolved as a single phase (*Figure 3-12 path D2*).

A minimum and a maximum temperature and pressure for the generation of brine from a seawater-derived parent fluid can be estimated for sample U1309D 40R-1 21-24 cm. Fluid inclusion microthermometry shows that this sample contains brines of ~35Wt% NaCl equivalent. In order to produce such a brine and assuming TAG model conditions, the initial seawater derived fluid must lie between 500°C at 450 bars (*Figure 3-14 dark blue*) and 625°C at 900 bars (*Figure 3-14 sky blue*). These various conditions would generate vapour of extremely different salinity (0.3 Wt% NaCl for the minimum and ~5 Wt% NaCl for the maximum).

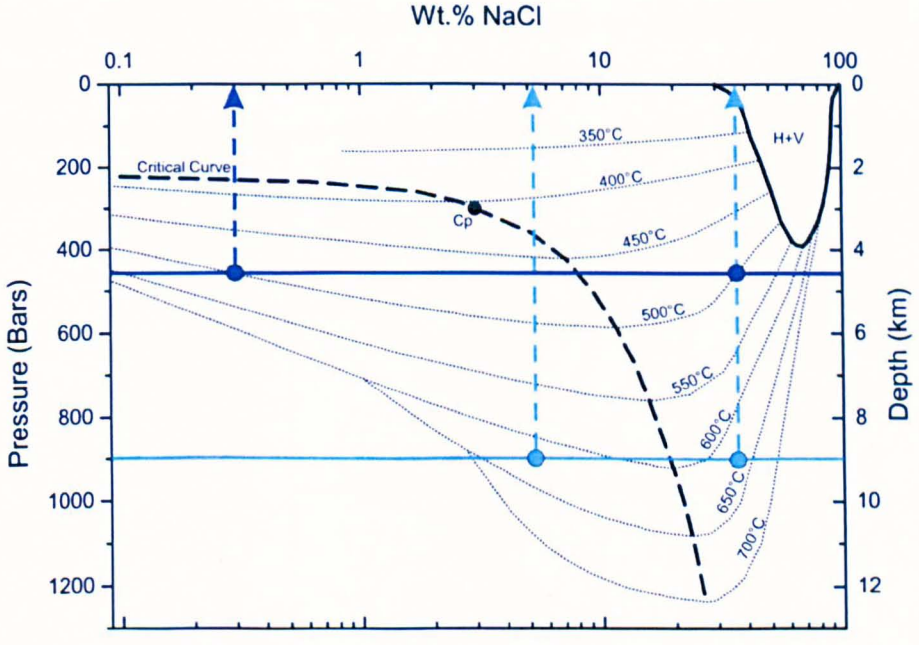


**Figure 3-14: P-X projection of the system $H_2O$-NaCl contoured for T under hydrostatic conditions II. The critical curve (dashed line), the isotherms (dotted lines) and the three phases curve (plain line) are from Sourirajan & Kennedy (1962). A seawater-like fluid which intersects the two phase curve, at temperature of 500°C and at pressure of ~475 bars will undergo supercritical phase separation and separate droplets of brines with salinities of ~12.5 Wt% NaCl equivalent from a vapour of salinity close to 0.3 Wt% NaCl equivalent (dark blue). At a temperature of 625°C and a pressure of 900 bars, a seawater-like fluid that intersect the two phase boundary, will undergo phase separation for which the brine would have a salinity of ~12.5 Wt% NaCl equivalent and the vapour a salinity of ~5 Wt% NaCl equivalent.**

However, as halite-bearing inclusions have been found only in trondjhemite, a magmatic fluid source for generation of hypersaline inclusions seems to be the most probable. The condensation model is preferably applicable for brines and associated low salinity vapour rich inclusions, whereas the direct exsolution of brines model is more applicable to inclusions that homogenise by halite dissolution (Kelley & Früh-Green, 2001). From these statements, it is suggested that brines have been formed by condensation of a magmatic fluid at maximum conditions of 770°C and ~7 km depth (which is equivalent to ~1690 bars according to the lithostatic gradient of *Figure 3-12B*) and at minimum conditions of 790°C and ~4 km depth (which is equivalent to ~540 bars according to *Figure 3-12B*) (*Figure 3-15*). Note that as it concerns a magmatic intrusion (trondjhemite), the maximum conditions seem to be the most probable. Condensation of the magmatic fluid is located in the TAG model in *Figure 3-17 location A*. Homogenisation temperature of those inclusions is ~400°C. Trapping must therefore be preceded by an event of significant cooling during the ascent of the fluid towards shallower depth.

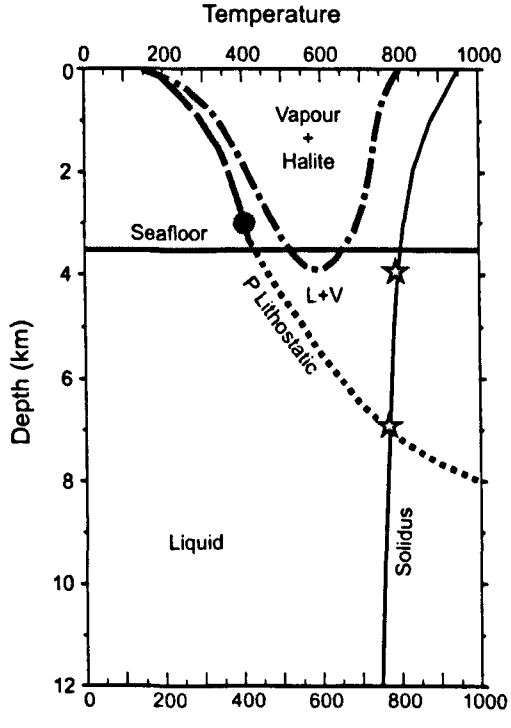


**Figure 3-15: Temperature-depth diagram under hydrostatic conditions above seafloor (dashed line) (Sourirajan and Kennedy, 1962) and lithostatic conditions under seafloor (dotted line), showing maximum and minimum conditions for brine generation by exsolution under supercritical conditions and condensation.**

#### *3.5.5.2.2 Generation of low salinity fluid*

Low salinity fluid in plagioclase

Fluid of low salinity relative to seawater can be generated by phase separation as described above. Trapping of a low salinity vapour fluid has not been observed. What is observed are liquid-dominated low salinity fluids in plagioclase at lower temperature than the brine inclusions and higher in the stratigraphy. As brine and vapour are segregated after separation by density effects, it is suggested that a late mixing of seawater-like fluid occurs with the initial vapour fluid-like to reach the salinity and temperatures of homogenisation observed. Note that the phase separation event does not have to be the same event described in the previous paragraph for generation of brine observed in trondjhemite.

In the model of *Figure 3-16* it is assumed than the vapour fluid generated by phase separation has a salinity of ~0.2 Wt% NaCl. That salinity can be obtained at various conditions that will generate different brine salinities. The minimum temperature, at which supercritical phase separation generates a vapour phase of 0.2 Wt% NaCl under hydrostatic conditions, is 450°C at a pressure of 340 bars (*Figure 3-16 dark green*). The maximum temperature is ~600°C at 550 bars (*Figure 3-16 light green*). In both case, significant cooling must occur in order to reach the trapping temperature of such inclusions that does not go beyond 350°C under the minimum conditions of pressure corrections. Cooling is however not needed if inclusions are subject to the maximum pressure corrections assumed in *3.5.1. Figure 3-17* (location B) shows the hypothetic position of the core when these fluids were trapped.

Seawater like salinity fluid in quartz vein

Quartz being a mineral that precipitates when pressure drops, it is easy to assume that fluids of seawater-like salinity have been trapped in quartz veins at relatively low pressure. It is suggested therefore that seawater-like salinity fluid have been trapped after an event of recharged seawater at shallow depth in the system. Those fluids have therefore been trapped when the core was close to the surface (*Figure 3-17 location C*).

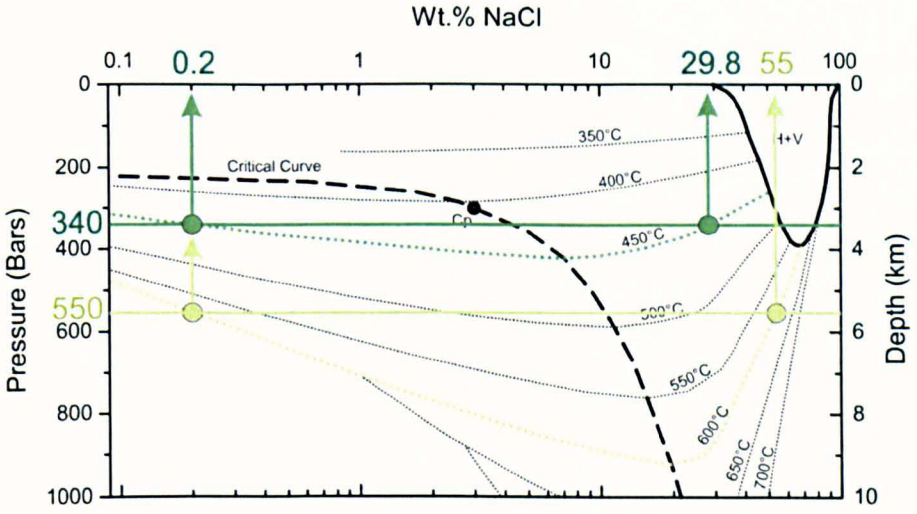


**Figure 3-16: P-X projection of the system $H_2O$-NaCl contoured for T under hydrostatic conditions III. The critical curve (dashed line), the isotherms (dotted lines) and the three phases curve (plain line) are from Sourirajan & Kennedy (1962). In this model, it is assumed than the vapour fluid generated by phase separation has a salinity of ~0.2 Wt% NaCl. That salinity can be obtained at various conditions that will generate different brine salinities. The minimum temperature, at which supercritical phase separation generates a vapour phase of 0.2 Wt% NaCl under hydrostatic conditions, is 450°C at a pressure of 340 bars (*dark green*) and the maximum temperature is ~600°C at 550 bars (*light green*).**

## 3.6 Conclusions

- Fluid inclusion microthermometry demonstrates the occurrence of four different types of fluids in IODP Hole U1309D:
    - Type 1a fluid - liquid-dominated seawater-like salinity (L-V).
    - Type 1b fluid - liquid-dominated low salinity (L-V).
    - Type 3a fluid – liquid domimnated high salinity (L-V)
    - Type 3b fluid - high salinity with halite daughter crystal (L-V-H).
- L-V homogenisation temperatures vary between different fluid type. The lowest homogenisation temperature is exhibited by fluid type 1a, and the highest by fluid type 3. Homogenisation of high salinity fluids occur in the liquid phase. Halite crystal always dissolves before the disappearance of the vapour bubble.
- Type 3 fluid is only found in evolved trondjhemite intrusion and is therefore assumed to have been generated by condensation of a magmatic fluid at maximum temperature of 770°C at depth of 7 km (*Figure 3-17 location A*). Significant cooling occurs during the segregation of brine and vapour before trapping. The associated low salinity vapour fluid has not been identified.
- Low salinity fluid (Type 1b) are believed to have been generated by mixing with seawater derived fluid after supercritical phase separation of a seawater-like fluid at temperatures of 450 to 600°C and pressures of 340 to 550 bars and assumed to have been trapped at depth of ~5 km (*Figure 3-17 location B*).
- Late stage fracturing event has provoked precipitation of quartz veins at low pressure low temperature that have trapped seawater-like salinity fluid (*Figure 3-17 location C*).

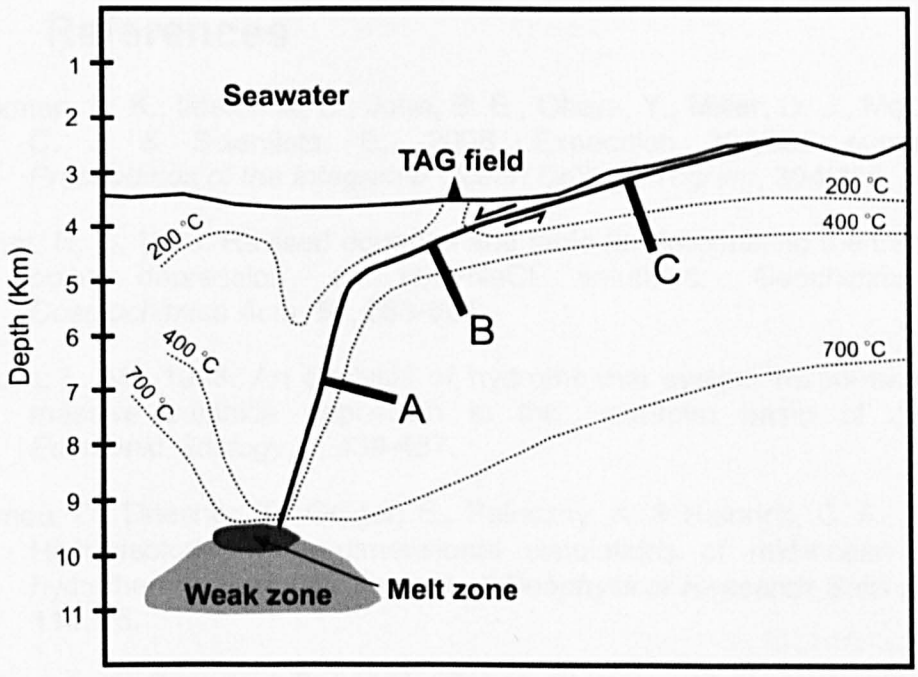


**Figure 3-17: Interpreted cross section of TAG (deMartin, *et al.*, 2007) showing the position of IODP Hole U1309D at different times of the fluid history.Isotherms are from McCaig *et al.* (2010). A: Condensation of exsolved magmatic fluid generating hypersaline brine observed in trondjhemite. B: Trapping of low salinity fluid in plagioclase. The vapour fluid phase of a phase-separated, seawater-derived fluid is mixed with recharged seawater. C: Late stage quartz precipitation and trapping of seawater like salinity fluid.**

# 3.7 References

Blackman, D. K., Ildefonse, B., John, B. E., Ohara, Y., Miller, D. J., McLeod, C. J. & Scientists, E., 2006. Expedition 304/305 summary. *Proceedings of the Integrated Ocean Drilling Program*, **304/305**, 1-60.

Bodnar, R. J., 1993. Revised equation and table for determining the freezing point depression of $H_2O$-NaCl solutions. *Geochimica et Cosmochimica Acta*, **57**, 683-684.

Cathles, L. M., 1983. An analysis of hydrothermal system responsible for massive sulphide deposition in the Hokuroku basin of Japan. *Economic Geology*, **5**, 439-487.

Coumou, D., Driesner, T., Geiger, S., Paluszny, A. & Heinrich, C. A., 2009. High-resolution three-dimensional simulations of mid-ocean ridge hydrothermal systems. *Journal of Geophysical Research-Solid Earth*, **114**, 15.

Cowan, J. & Cann, J. R., 1988. Supercritical two-phase separation of hydrothermal fluids in the Troodos ophiolite. *Nature*, **333**, 259-261.

Delaney, J. R., Mogk, D. W. & Mottl, M. J., 1987. Quartz-cemented breccias from the Mid-Atlantic Ridge: Samples of a high-salinity hydrothermal upflow zone. *Journal of Geophysical Research*, **92**(B9), 9175-9192.

deMartin, B. J., Sohn, R. A., Canales, J. P. & Humphris, S. E., 2007. Kinematics and geometry of active detachment faulting beneath the TAG hydrothermal field on the Mid-Atlantic Ridge. *Geology*, 711-741.

Hirth, G., Escartin, J. & Lin, J., 1998. The rheology of the lower oceanic crust: Implications for lithospheric deformation at mid-ocean ridges. In: *Faulting and Magmatism at Mid-Ocean Ridges*, pp. 291-303, W R Buck, P T Delaney, J A Karson, Y Lagabrielle, American Geophysical Union, Washington D.C.

Hopkinson, L. & Roberts, S., 1996. Fluid evolution during tectonic exhumation of oceanic crust at a slow-spreading paleoridge axis: evidence from the Lizard ophiolite U.K. *Earth and Planetary Science Letters*, **141**, 125-136.

Jupp, T. & Schultz, A., 2000. A thermodynamic explantion for black-smoker temperatures. *Nature*, **403**(6772), 880-883.

Jupp, T. E. & Schultz, A., 2004. Physical balances in subseafloor hydrothermal convection cells. *J. Geophys. Res.*, **109**(B5), B05101.

Khaibullin, I. Kh. and Borisov, N. M., 1966. Experimental investigation of the thermal properties of aqueous and vapor solutions of sodium and potassium chlorides at phase equilibrium. *High Temperature*, **4**: 489-496.

Kelley, D. S. & Delaney, J. R., 1987. Two-phase separation and fracturing in mid-ocean ridge gabbros at temperatures greater than 700C. *Earth and Planetary Science Letters*, **83**, 53-66.

Kelley, D. S. & Früh-Green, G. L., 2001. Volatile lines of descent in submarine plutonic environments: Insights from stable isotope and fluid inclusion analyses. *Geochimica et Cosmochimica Acta*, **65**(19), 3325-3346.

Kelley, D. S., Gillis, K. M. & Thompson, G., 1993. Fluid evolution in submarine magma-hydrothermal systems at the Mid-Atlantic Ridge. *Journal of Geophysical Research*, **98**(B11), 19579-19596.

Kelley, D. S. & Malpas, J., 1996. Melt-fluid evolution in gabbroic rocks from Hess Deep. In: *Proceedings of the Integrated Ocean Drilling Program, Scientific Results*, pp. 213-226, C Mével, K M Gillis, JF Allan, P S Meyer.

Kelley, D. S. & Robinson, P. T., 1990. Development of brine-dominated hydrothermal system at temperature of 400-500°C in the upper level plutonic sequence, Troodos ophiolite, Cyprus. *Geochimica et Cosmochimica Acta*, **54**, 653-661.

Kelley, D. S., Robinson, P. T. & Malpas, J. G., 1992. Processes of brine generation and circulation in the oceanic crust: Fluid inclusion evidence fron the Troodos ophiolite, Cyprus. *Journal of Geophysical Research*, **97**(B6), 9307-9322.

Kelley, D. S., Vanko, D. A. & Gu, C., 1995. Fluid evolution in oceanic crustal layer 2: Fluid inclusion evidence from the sheeteed dike complex, Hole 504B, Costa Rica Rift. In: *Proceedings of the OceanDrilling Program, Scientific Results*, **137/140**, pp. 191-198, J Erzinger, K Becker, H J B Dick, L B Stokking.

McCaig, A., Delacour, A., Fallick, A. E., Castelain, T. & Früh-Green, G. L., 2010. Detachment Fault Control on Hydrothermal Circulation Systems: Interpreting the Subsurface Beneath the TAG Hydrothermal Field Using the Isotopic and Geological Evolution of Oceanic Core Complexes in the Atlantic, *In* Rona, P. A., Devey, C. W., Dyment, J., Murton, B. J. (ed) Diversity of Hydrothermal Systems on, Slow Spreading Ridges, *AGU Geophysical Monograph*, **108**, AGU, pp; 207-240.

Morgan, S. J., 2008. *High temperature fluid-rock interaction in oceanic crust: A study of fluid inclusions from the Troodos ophiolite and ODP/IODP Hole 1256D*, University of Leeds, Leeds.

Nehlig, P., 1991. Salinity of oceanic hydrothermal fluids: a fluid inclusion study. *Earth and Planetary Science Letters*, **102**(310-325).

Roedder, E., 1984. Fluid inclusions. *Mineralogy*, **12**.

Saccocia, P. J. & Gillis, K. M., 1995. Hydrothermal upflow zones in the oceanic crust. *Earth and Planetary Science Letters*, **136**, 1-16.

Seyfried, W. E., Berndt, M. E. & Janecky, D. R., 1986. Chloride depletions and enrichments in seafloor hydrothermal fluids: Constraints from experimental basalt alteration studies. *Geochimica et Cosmochimica Acta*, **50**, 459-475.

Sourirajan, S. & Kennedy, G. C., 1962. The system $H_2O$-NaCl at elevated temperatures and pressures. *American Journal of Science*, **260**(2), 115-141.

Spooner, E. T. C. & Bray, C. J., 1977. Hydrothermal fluids of seawater salinity in ophiolitic sulphide ore deposits in Cyprus. *Nature*, **266**, 808-812.

Sterner, S. M., Hall, D. L. & Bodnar, R. J., 1988. Synthetic fluid inclusions. V. Solubility relations in the system NaCl-KCl-$H_2O$ under vapor-saturated conditions. *Geochimica et Cosmochimica Acta*, **52**, 989-1005.

Tivey, M. K., Mills, R. A. & Teagle, D. A. H., 1998. Temperature and salinity of fluid inclusions in anhydrite as indicators of seawater entrainmnent and heating in the TAG active mound. *Proceedings of the Integrated Ocean Drilling Program, Scientific Results*, **158**, 179-190.

Vanko, D. A., 1986. High chlorine amphiboles from oceanic rocks: product of highly-saline hydrothermal fluids. *American Mineralogist*, **71**, 51-59.

Vanko, D. A., Griffith, J. D. & Erikson, C. L., 1992. Calcium-rich brines and other hydrothermal fluids in fluid inclusions from plutonic rocks, Oceanographer Transform, Mid-Atlantic Ridge. *Geochimica et Cosmochimica Acta*, **56**, 35-47.

Vibetti, N. J., 1993. Chemical alteration trends, fluid inclusion patterns and stable isotope compositions in the plutonic sequence of the Troodos ophiolite, Cyprus. *Journal of African Earth Sciences*, **17**(2), 193-202.

vanko, W. S. D. & McNabb, A., 1996. Estimates of crustal permeability on the endeavour segment of the Juan de Fuca mid-ocean ridge. *Earth and Planetary Science Letters*, **138**(1-4), 83-91.

Wyllie, P. J., 1977. Crustal Anatexis - Experimental Review. *Tectonophysics*, **43**(1-2), 41-71.

Zhang, Y.-G. & Frantz, J. D., 1987. Determination of the homogenisation temperature and densities of supercritical fluids in the system NaCl-KCl-$CaCl_2$-$H_2O$ using synthetic fluid inclusions. *Chemical Geology*, **64**, 335-350.

# Chapter 4. Fluid evolution in the oceanic crust: a fluid inclusion study from IODP Hole U1309D - Atlantis Massif, 30 °N. Fluid chemistry

## 4.1 Introduction

This chapter presents the chemistry of hydrothermal fluids that circulated in the Atlantis Massif. These fluids have been characterised in chapter 3 in terms of temperature and salinity by microthermometry. Here results obtained by Laser ablation ICPMS are presented. Instrumentation and methodology of LAICPMS is described.

The results include data from three samples:

- U1309D 1R-1 41-44: A quartz-chlorite vein in diabase
- U1309D 40R-1 17-19: A quartz vein in troctolite
- U1309 40R-1 21-24: A quartz vein in trondjhemite and quartz grains of the host rock.

Sample names in the text will be as in *Table 4-1*. IODP identification numbers of the samples will nonetheless be repeated in the legends of figures. Other samples analysed for microthermometry did not produce LAICPMS data. Reasons are given in the chapter.

**Table 4-1: Nomenclature for samples in that chapter**

| IODP identification number | Fluid inclusion host | Fluid type | Name used in this chapter |
|---|---|---|---|
| U1309D 1R-1 41-44 | Quartz-chlorite vein | 1a | Sample 1 |
| U1309D 40R-1 17-19 | Quartz vein | 1a | Sample 2 |
| U1309D 40R-1 21-24 | Quartz vein | 1a | Sample 3 |
| U1309D 40R-1 21-24 | Quartz from matrix | 3b | Sample 4 |

The chapter also presents a discussion where Atlantis Massif data are compared with data collected by Morgan (2008) on Troodos ophiolite samples and on ODP Hole 1256D, as well as a comparison to the TAG vent fluids, leading to a discussion of the processes that control the fluid chemistry. TAG vent fluids are also used as a subject of comparison to test the possibility of fluid mixing between seawater and fluid inclusions to achieve vent fluid compositions.

## 4.2 Methodology

### 4.2.1 LAICPMS

Laser ablation inductively coupled plasma mass spectrometry (LAICPMS) is a destructive technique. Therefore, microthermometry (*Chapter 3*) was undertaken prior to ablation.

LAICPMS combines the high spatial resolution of laser probes with the high sensitivity, low detection limits, and multi-element capabilities of ICP-MS analysis (Allan, *et al.*, 2005 and references therein). Because of these reasons, this technique is best suited to the *in situ* analysis of geological materials. The LAICPMS has been used for mineral, melt inclusion analysis, but has become more and more popular for individual fluid inclusion analysis, especially in ore deposit (Audétat, *et al.*, 1998 and 2000; Müller, *et al.*, 2001; Rusk, *et al.*, 2004; Ulrich, *et al.*, 2002) with the first study on natural fluid inclusions reporting analytical precision (Ghazi, *et al.*, 1996). Allan *et al.* (2005) have addressed the remaining uncertainties in the analytical procedure and the data quality.

The procedures used in this study have been described by Allan *et al.* (2005).

#### 4.2.1.1 Instrumentation

LAICPMS is an *in situ* technique permitting the acquisition of quantitative multi-element microanalyses for major, minor and trace elements. This method has been used in this study in order to analyse concentrations of a list of elements in fluid inclusions.

The system used in this study couples a 193 nm ArF Geolas Q Plus exciplex laser (ArF, 193 nm, Microlas, Göttingen, Germany) ablation unit to an Agilent 7500c quadrupole ICP-MS equipped with an octopole reaction cell, and consists of the following parts:

- A laser source: 193 nm ArF excimer, allowing the ablation of material from a selected area of the order of 5 µm in diameter or larger

- An ablation cell containing the sample
- Flexible tubing
- A gas mixing device
- An ICP
- A mass spectrometer

An optical system (described in detail in Günther *et al.* (1997)) is set up in order to observe in real time the ablation process via a LED (Light Emitting Diode) source and a CCD camera (Charge Coupled Device).

Once the inclusion is targetted by the laser, the ablated material is transported in 0.68 L.min$^{-1}$ He from a cylindrical chamber via a Teflon® tube to a cyclone gas mixer where the analyte is combined with 0.94-0.98 L.min$^{-1}$ Ar before introduction into the plasma. The analyte is then analysed with an Agilent 7500c quadrupole ICPMS (Allan, *et al.*, 2005).

#### 4.2.1.2 Isotope list and dwell times

The isotope list and dwell times selected were dependent on the salinity, the size and the number of inclusions of a definite population. A short list of isotopes is preferable for low salinity inclusions and a longer list can be used for brine inclusions. The number of elements analysed does indeed (amongst with other parameters such as the dwell times, the volume of the inclusion, the concentration...) influence the signal intensities of the analytes which governs the precision of the analysis. Dwell times of 10 ms for Na and 5 ms for other elements have been used throughout.

Two different methods have been used to maximise the quality of data of elements analysed:

- Major and minor elements analysed without a reaction gas. The list of isotopes is the full list of all isotopes used in the whole study but have not been analysed all the time altogether: $^{7}$Li, $^{23}$Na, $^{24}$Mg, $^{27}$Al, $^{29}$Si, $^{35}$Cl, $^{39}$K, $^{44}$Ca, $^{55}$Mn, $^{58}$Ni, $^{59}$Co, $^{63}$Cu, $^{66}$Zn, $^{75}$As, $^{85}$Rb, $^{88}$Sr, $^{107}$Ag, $^{121}$Sb, $^{133}$Cs, $^{208}$Pb.

- Major and minor elements analysed with $H_2$ (2.5mL.min$^{-1}$) as a reaction cell gas: $^{23}$Na, $^{39}$K, $^{44}$Ca, $^{55}$Mn, $^{57}$Fe, $^{88}$Sr.

Note that the element list varied between samples such that not all the samples have been analysed for all the elements described in the lists above. Note that one individual inclusion can only be analysed by one method or the other.

#### 4.2.1.3 Calibration

Calibration has been performed at the beginning of a session and at the end of the session of analyses of fluid inclusions using NIST SRM 610 and 612 (where SRM stands for Standard Reference Material). Composition of the two standards is shown in Table 4-2 only for the elements relevant to this study (Pearce, *et al.*, 1996; Allan, *et al.*, 2005 and references therein).

The standards were ablated twice each for 200 pulses using a repetition rate of 5Hz and laser fluence of 10 J.cm$^{-2}$ over a spot of 50 µm.

**Table 4-2: Chemical composition of NIST SRM 610 and NIST SRM 612.**

| | NIST SRM 610 (ppmw) | NIST SRM 612 (ppmw) |
|---|---|---|
| $^{7}$Li | 484.6 | 41.5 |
| $^{23}$Na | 99052.0 | 103704.0 |
| $^{24}$Mg | 465.3 | 77.4 |
| $^{27}$Al | 10791.1 | 11166.9 |
| $^{29}$Si | 327115.5 | 336114.4 |
| $^{35}$Cl | 470.0 | - |
| $^{39}$K | 486.0 | 66.3 |
| $^{44}$Ca | 81833.3 | 85263.8 |
| $^{55}$Mn | 433.3 | 38.4 |
| $^{57}$Fe | 457.1 | 56.3 |
| $^{58}$Ni | 443.9 | 38.4 |
| $^{59}$Co | 405.0 | 35.3 |
| $^{63}$Cu | 430.3 | 36.7 |
| $^{66}$Zn | 456.3 | 37.9 |
| $^{75}$As | 317.4 | 37.3 |
| $^{85}$Rb | 431.1 | 31.6 |
| $^{88}$Sr | 497.4 | 76.2 |
| $^{107}$Ag | 239.4 | 21.9 |
| $^{121}$Sb | 368.5 | 38.4 |
| $^{133}$Cs | 360.9 | 41.6 |
| $^{208}$Pb | 413.3 | 39.0 |

#### 4.2.1.4 Ablation of fluid inclusions in quartz and plagioclase

Small chips of microthermometry wafers (approximately 300 µm in thickness) were stuck to a slide with a sugary solution and placed in the ablation chamber. Individual fluid inclusions were relocated after having been observed, photographed and sketched under transmitted light microscope in order to be sure that only inclusions that have been analysed previously by microthermometry are ablated.

Ablation was started after recording a minimum of 20 seconds of gas blank. The laser was fired for 200 pulses at a repetition rate of 5Hz and at a laser fluence of 10 $J.cm^{-2}$ and with a laser aperture of similar size to the fluid inclusions.

Si was included in the isotope list in order to observe the beginning of ablation of quartz and to better identify the fluid signal. Frequently however, the quartz matrix undergoes fracturing shortly after the start of ablation so that only a small amount of material is ablated and the Si signal is not significant, leaving only the fluid signal. Measurement of Si was abandoned after a few analyses, in order to maximise the dwell time spent on the masses of interest.

Ablation of plagioclase has been proved to be rather difficult as signal from the mineral host was overprinting the fluid signal. An attempt was made to subtract the signal of an inclusion-free area in plagioclase from an area with inclusions in order to counter that overprinting effect. Results have not been conclusive. Data will not be presented.

#### 4.2.1.5 Data processing

The output files from the ICPMS are spreadsheet tables and spectra for individual inclusions. Those files are imported into software called SILLS© (Signal Integration for the Leeds Laser System) (Guillong, *et al.*, 2008) where the individual fluid inclusion signal is shown graphically. The signal selected has to be the smoothest possible avoiding any background noise and is generally determine by the peak of Na. The absolute concentration of other elements is calculated by multiplying the concentration ratios to Na by the Na

concentration (in Wt% NaCl equivalent) determined by microthermometry. Absolute concentrations are then output in an Excel® spreadsheet alongside with the composition of standards and limits of detection for every single inclusion.

#### 4.2.1.6 Data reduction

Absolute concentrations from LAICPMS analysis were calculated on the basis of a known Na concentration. However, establishing an internal standard concentration can be challenging. Na is commonly chosen as the internal standard for natural inclusions, and its concentration is estimated from microthermometric data (chapter 3) using the temperature of melting of ice for fluid type 1a (Bodnar, 1993) or the halite dissolution temperature (Sterner *et al.*, 1988) for fluid type 3b.

In this study, thermodynamic equivalency to a pure NaCl-$H_2O$ solution is assumed. There are different approaches to quantify complex chloride fluids from LAICPMS and microthermometric data: the mass-balance approach (Heinrich, *et al.*, 1992) and the charge balance approach (Allan, *et al.*, 2005). In this study, the charge balance method was used with the assumption that chloride is the dominant anion species. The approach is based on the following equation:

$$mCl = mNa + \sum_i n_i \cdot mX_i$$

Where $m$ is molality (mol.kg$^{-1}$) and $n_i$ is the charge on each secondary cation $X_i$. The internal standard concentration (Na) is calculated from the molar ratios $mX_i/m$Na obtained by LAICPMS analyses using the following equation:

$$mNa = \frac{mCl}{\left(1 + \sum_i \frac{n_i \cdot mX_i}{mNa}\right)}$$

#### 4.2.1.7 Quality of the data set

The analyses were selected according to a set of criteria. Likely effects of solid impurities were carefully "scanned" for Al data. Most of the Al signals were indeed not interpreted as being the fluid signal as peaks of Na and peaks of Al in the output charts were not coming out at the same time. Al data were therefore excluded from the data reduction calculation. Limits of detection (LOD) were calculated as the concentration equivalent of three times the standard deviation in the gas blank, over a time interval approximately equal to the signal duration (Allan, *et al.*, 2005). Signals of fluid inclusions below this limit were rejected especially when the average of signals above the LOD is significantly different. However, in the case of elements consistently near the LOD, the signals below the LOD were preferred to the only few fluid inclusion signals showing suspiciously high level (see below).

# 4.3 Fluid chemistry results

## 4.3.1 Variations in fluid chemistry

This section reports laser ablation results for all four samples (*Table 4-1*). When possible, data for individual fluid inclusion are plotted and, when needed, median concentrations are used for a population of fluid inclusions (for comparison for instance). Fluid types 1a (liquid dominated seawater salinity) and 3b (liquid dominated with halite daughter crystal) are presented. Measurements on fluid type 1b were attempted but since plagioclase is the mineral host, the fluid signal for Na was hidden by the mineral signal. Fluid type 3a inclusions did not give quality data with more than 95% of concentrations under the detection limit.

Errors in concentrations are expected to mainly arise from the spiky nature of the signal derived from a fluid inclusion, and at a smaller extent, the result of analytical uncertainties (salinity and data reduction calculation).

### 4.3.1.1 Type 1a fluids

Type 1a fluids have been found in samples 1, 2 and 3 (*Table 4-1*). The results are shown in *Figure 4-1* and presented in *Table 4-3*. Median concentration is preferred over mean concentration in order to avoid distortion by outliers. Generally, elements for which the concentration is below the limit of detection (LOD) are elements for which no signals were observed during ablation. Such elements were not included in the statistics (*e.g.* Ca). Numbers can nonetheless be found in the appropriate appendix. However in some circumstances, values below the LOD were calculated for elements that showed a distinct signal corresponding to the Na signal (sample 1, Li signal for fluid inclusions 2 9 and 10 of zone 1; K signal for fluid inclusion 2 zone 1 (see *Appendix 3*)). Concentrations of these signals were included in the statistics. As and Cs were consistently below the LOD but yielded consistent calculated concentrations. They are shown in *Figure 4-1* for information.

Na is the major cation species in the fluid with median concentration of ~6830 ppm (N=66). Median concentration varies between samples from

~6270 for sample 3 (N=20) to 9870 ppm for sample 1 (N=15) and 6380 ppm for sample 2 (N=31). K and Ca represent the other major cation species with Ca being the most concentrated. Sample 1 is distinguished by a lower concentration in K relative to the two other samples; K being 4 to 8 times more concentrated in other quartz.

Mg contributes to the cation population with moderate concentrations relative to the major cations with median concentration of 180 ppm (N=61). Sample 1, 2 and 3 are depleted relative to seawater. Sample 1 is also depleted relative to the two other samples as per K. Fe also contributes to the major cation species present in this fluid with median concentration of ~500 ppm with a range of concentrations from ~125 ppm (sample 3; N=3; 170 ppm in mean concentration) to ~425 ppm (sample 2; N=17).

Transition metals such as Cu are present in the order of 10's of ppm (Cu=70 ppm; N=39) with a great variation between samples, sample 3 being enriched relative to sample 1 and 2

Li is present in the fluid at a lower concentration than the other alkali-metals (Na and K) (~40 ppm). Ni, Zn and Pb are present in the same sort of range. Mn, Co, Rb, Sr, Ag, and Sb are the metals that are the least concentrated with median concentrations ranging from <1 ppm to 10 ppm. As and Cs were also analysed with As concentrations under ~25 ppm and Cs concentrations under 1.5 ppm (all the measurements wer below the LOD for these two elements).

Seawater is also plotted in *Figure 4-1* for comparison. Samples generally show metal concentrations greater than those of seawater, with the exception of Na, Mg and Sr. Sample 1 is generally depleted in metal concentrations relative to samples 2 and 3 with the exception of Cu which is more concentrated in sample 1 than in sample 2. Sample 1 is also depleted in K relative to seawater.

*Figure 4-2* shows a comparison of the cation to Na ratios for samples of fluid type 1a. Great variation in the ratio to Na is observed between the 3 samples for K, Mg, Cu, Zn, Sr, and Pb (± Rb). Depletion in metal concentration relative to Na is again observed in sample 1 for K, Mg, and Zn. Ratios to Na of sample 1 overlap those of sample 2 for Ca and Cu. Sample 2

is in turn generally depleted in metal concentration relative to Na compare to sample 3 (Ca, Mg, Cu, Pb, and Sr). The opposite relationship is nonetheless observed for K.

Ratios to Na do not vary between samples for other elements (Ca and Fe). Data is insufficient to make good comparison for the rest of the elements Mn, Li, Ni, Sb, Ab, and Co). Note that data that align with median ratio (solid black line in *Figure 4-2*), are data with constant cation to Na ratio. Values of the ratios are given in the figure. All element concentrations correlate positively with Na.

Ca/Sr ratios are shown in *Figure 4-3* for samples 2 and 3. The plot shows a positive correlation between Ca and Sr for samples 2 and 3. Sample 2 has a higher Ca/Sr (1000) than sample 3 (250). All fluid inclusions have a Ca/Sr greater than seawater. Mg/Fe (*Figure 4-4*), Fe/Mn (*Figure 4-5*), show also a positive correlation for sample 2. Measurements in sample 3 are insufficient to discuss trend in this particular case. Mg/Fe is greater in seawater than in all samples. K/Ca (*Figure 4-6*) is characterised by a negative correlation in sample 2 in contrast to Ca/Sr, Mg/Fe, and Fe/Mn. K and Ca of sample 1 and 3 do not correlate.

*Figure 4-7* shows a plot of Ca/Sr against Ca/K. This diagram indicates that those two ratios correlate for both samples 2 and 3. Great variations are again observed between samples of same fluid type with sample 2 having a K/Sr approximately 10 times greater than sample 3.

Relative proportions of Pb, Cu and Zn are shown in *Figure 4-8*. Those three elements all together were measured only for sample 2. Nonetheless, it is observed that there is a trend between the pole Cu and the pole Zn. Seawater and TAG vent fluids are also plotted for comparison. Concentrations in Zn and Cu in Atlantis Massif fluid and in seawater and TAG are in good agreement. It is not the case for Pb which seems to be enriched.

A ternary diagram showing the relative proportion of Na, Ca and K (*Figure 4-9*) underlines a trend for sample 2 between the pole Ca and the pole K. This is not the case for sample 1 and 3 for which the data scatter. *Figure 4-10* shows the relative proportion of Mg, Fe, and Mn. Sample 2 is

characterised by Mn being depleted relative to Mg and Fe, and by the trend from the pole Mg (characteristic of seawater) and the pole Fe (characteristic of TAG vent fluids).

#### 4.3.1.2 Type 1b fluid

Fluid of type 1b was found only in plagioclase grains. Signal depicted by the ICPMS was contaminated by the mineral composition and the fluid signal was therefore not detected. Thus, results are not available.

**Table 4-3: Fluid composition in ppm of sample 1, 2, 3 and 4.**

| | Sample 1 | | Sample 2 | | Sample 3 | | Sample 4 | |
|---|---|---|---|---|---|---|---|---|
| | Mean (ppm) | Median (ppm) | Mean (ppm) | Median (ppm) | Mean (ppm) | Median (ppm) | Mean (ppm) | Median (ppm) |
| Cl | 21385,9 | 21524,3 | 19629,7 | 19571,6 | 20179,5 | 20061,2 | 210596,7 | 212258,9 |
| Li | 51,9 | 47,2 | - | - | - | - | | |
| Na | 10258,6 | 9864,9 | 6435,9 | 6382,4 | 6688,6 | 6265,8 | 89393,5 | 76731,9 |
| Mg | 86,4 | 40,3 | 508,7 | 347,9 | 757,2 | 674,9 | 1448,9 | 1148,6 |
| K | 363,7 | 313,9 | 2068,9 | 2682,7 | 1159,1 | 1356,3 | 29470,9 | 24011,5 |
| Ca | 2648.2 | 2648,2 | 3112,2 | 2944,7 | 3003,2 | 3321,2 | 15265,3 | 10015,9 |
| Mn | - | - | 3,9 | 2,2 | 69,6 | 69,6 | 3520,8 | 1452,6 |
| Fe | - | - | 506,7 | 428,2 | 170,9 | 124,4 | 18424,5 | 18424,5 |
| Ni | - | - | - | - | 74,8 | 74,2 | 845,4 | 622,2 |
| Co | - | - | - | - | 1,8 | 1,8 | 12,2 | 13,2 |
| Cu | 139,4 | 128,2 | 113,7 | 66,4 | 291,4 | 282,3 | 571,4 | 697,6 |
| Zn | 42,4 | 36,9 | 98,8 | 73,2 | - | - | | |
| Rb | 1,6 | 1,6 | - | - | 2,7 | 2,6 | | |
| Sr | - | - | 4,9 | 2,9 | 10,4 | 12,1 | 22,7 | 22,0 |
| Ag | - | - | - | - | 12,3 | 12,3 | 775,7 | 624,8 |
| Sb | 16,6 | 16,6 | - | - | - | - | | |
| Pb | - | - | 13,1 | 7,3 | 273,9 | 257,4 | 126,8 | 124,8 |

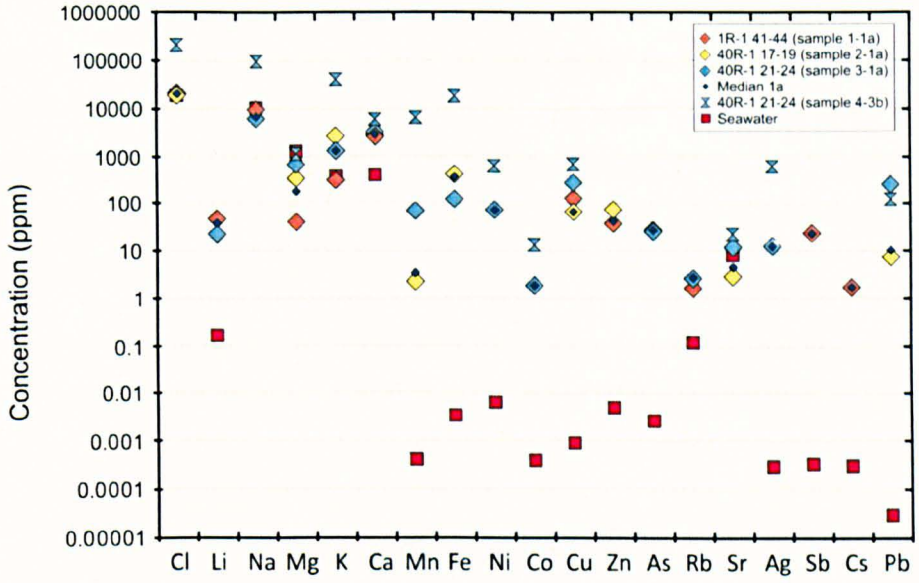


**Figure 4-1: Chemical composition of fluid of type 1a in samples 1, 2 and 3 and of fluid of type 3b in sample 4. Median values are plotted for each sample. Y axis is displayed in logarithmic scale. Seawater concentrations are also plotted for comparison.**

#### 4.3.1.3 Type 3b fluid

Fluid type 3b has only been found in sample 4. The chemical composition of this fluid is shown in *Figure 4-1* and presented in *Table 4-3*. The median calculation includes five measurements made on fluid inclusions with the halite daughter crystal being included in the calculation of the solution's concentration.

Na is again the dominant cation with a median concentration of ~76730 ppm. K, Ca, Fe and Mn are major cations with median concentrations in the order of 10000's ppm. Mg is also highly concentrated in that fluid (1000 ppm).

Transition metals such as Ni, Cu and Ag are present at a median concentration of ~620 ppm, ~700 ppm and ~625 ppm respectively. Pb contributes at a minor scale with a median concentration of ~125 ppm.

Co and Sr contribute to the cation population of type 3b fluid at an even smaller scale with median concentration of ~10 ppm and ~20 ppm respectively.

Ca and Sr (*Figure 4-3*), do not correlate in sample 4. As Ca/Sr of sample 3 and 4 are different, Ca/Sr of fluid type 1a (sample 3) cannot be inherited from fluid type 3b (sample 4). Ca and K (*Figure 4-6*) do not correlate either with the data showing a wide spread. Data are insufficient to interpret Mg/Fe and Mn/Fe for sample 4 (*Figure 4-4* and *Figure 4-5*). *Figure 4-7* shows that sample 4 has a K/Sr of approximately 1000.

*Figure 4-9* shows no correlation between Na, Ca and K for sample 4. The triangular plot between Mg, Fe, and Mn (*Figure 4-10*) for sample 4 shows that Fe proportion is close to TAG vent fluids. This indicates a potential mixing between seawater and fluid from sample 4 to reach TAG vent fluids composition in those three elements.

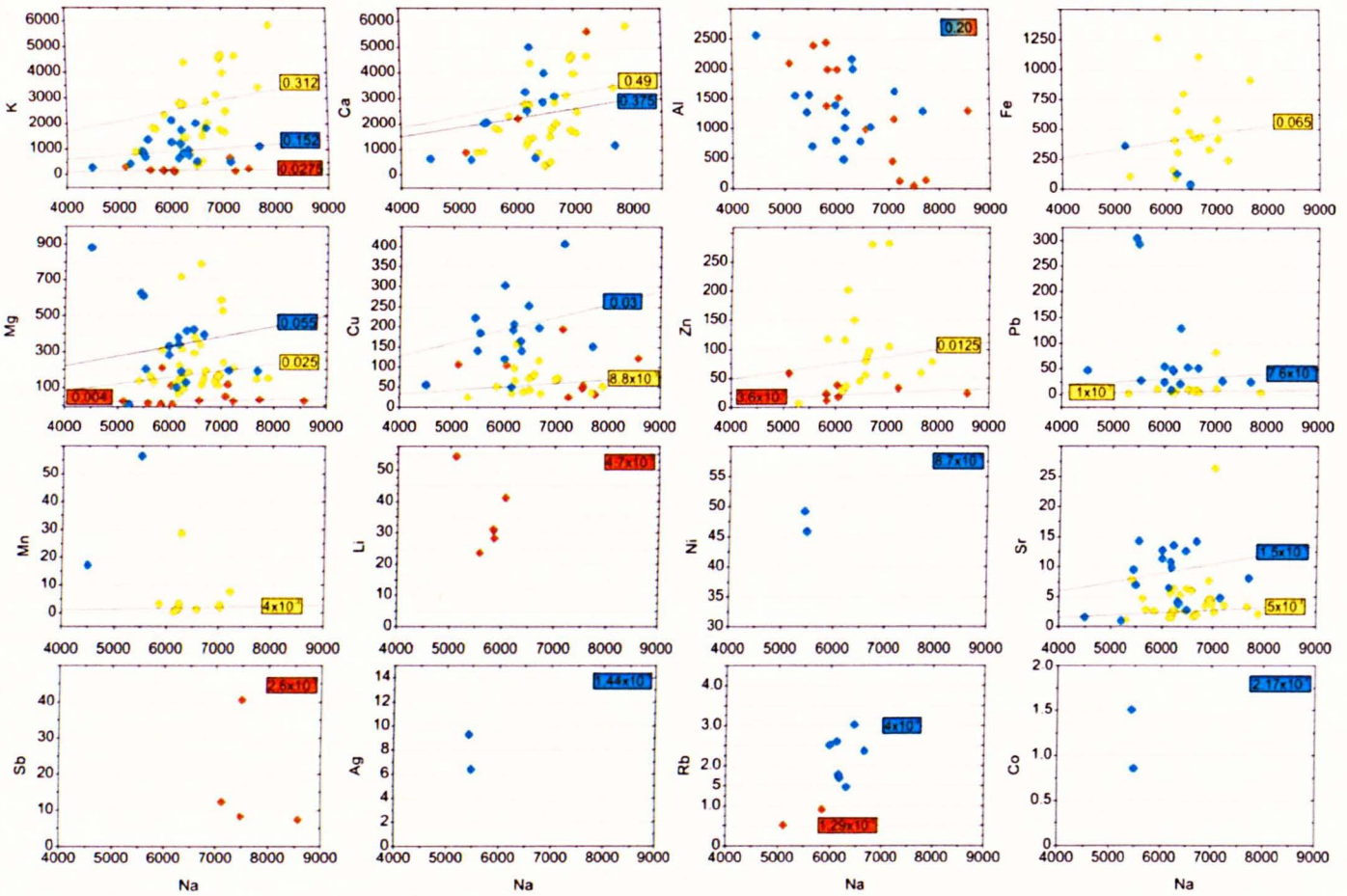


**Figure 4-2: X/Na concentration ratio in ppm for all elements analysed in the three fluid type 1a samples. Legend is the same as in *Figure 4-1*. Every symbol represents a single fluid inclusion. Lines represent the median value of the sample; numbers are given in boxes of the same colour code as the samples. Clouds indicate here a variable X/Na ratio whereas alignment of the data with median value indicates a constant X/Na ratio.**

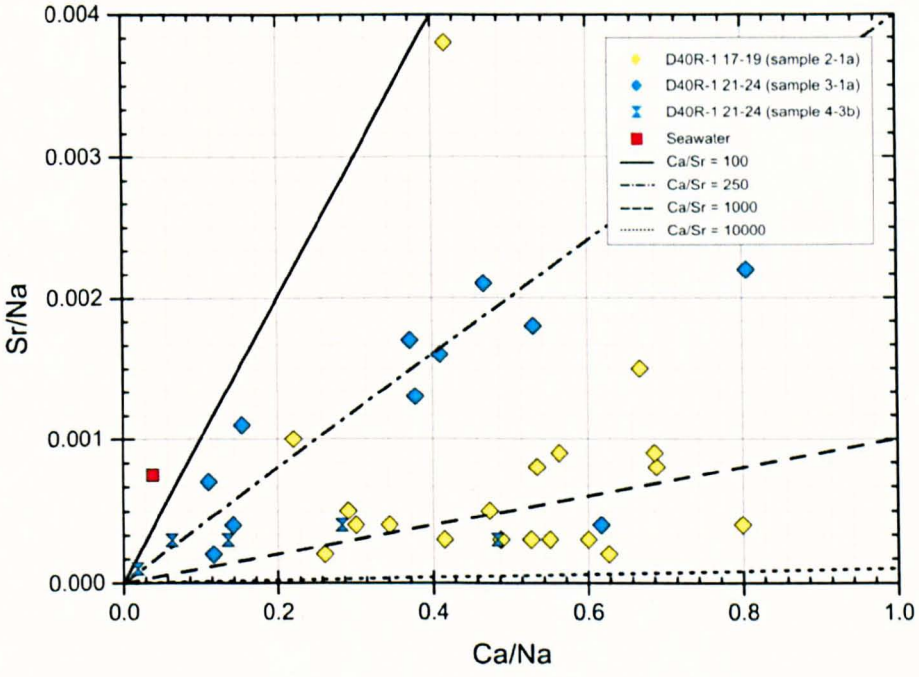


**Figure 4-3: Ca/Na concentration ratio (ppm/ppm) plotted against Sr/Na concentration ratio (ppm/ppm).**

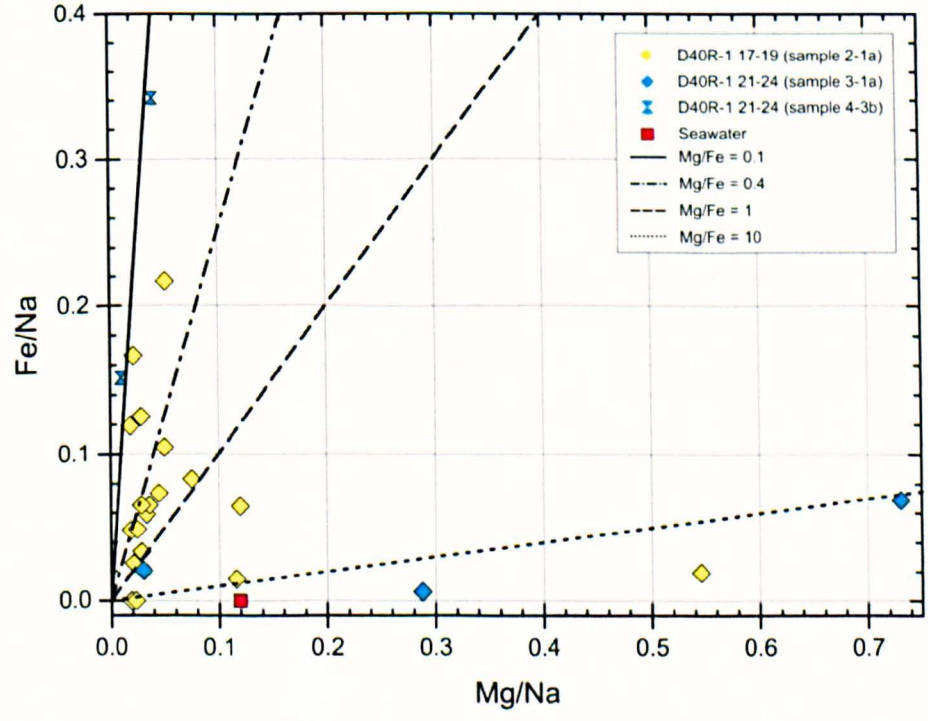


**Figure 4-4: Mg/Na concentration ratio (ppm/ppm) plotted against Fe/Na concentration ratio (ppm/ppm).**

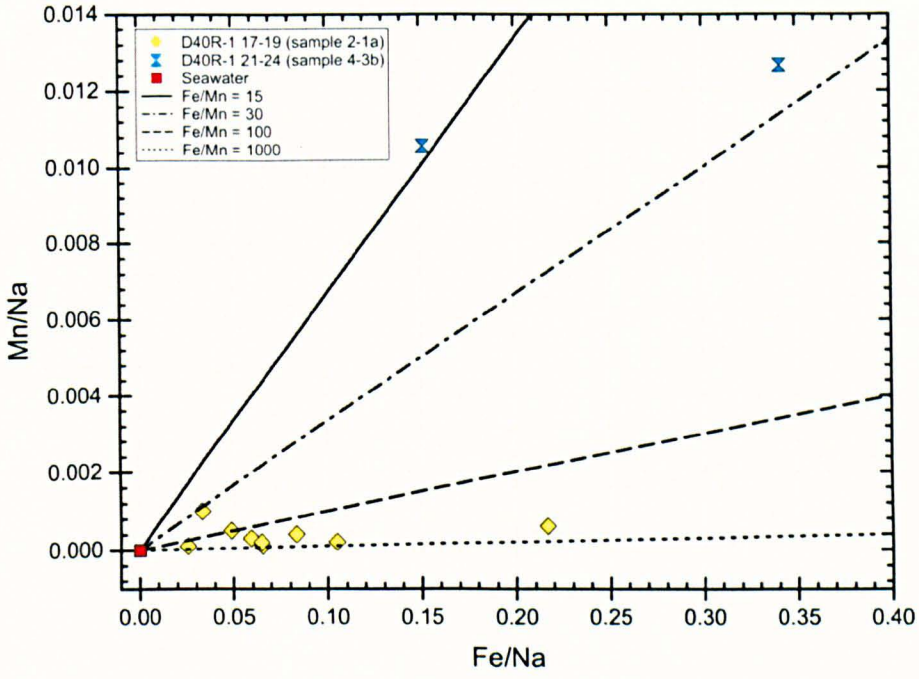


**Figure 4-5: Fe/Na concentration ratio (ppm/ppm) against Mn/Na concentration ratio (ppm/ppm).**

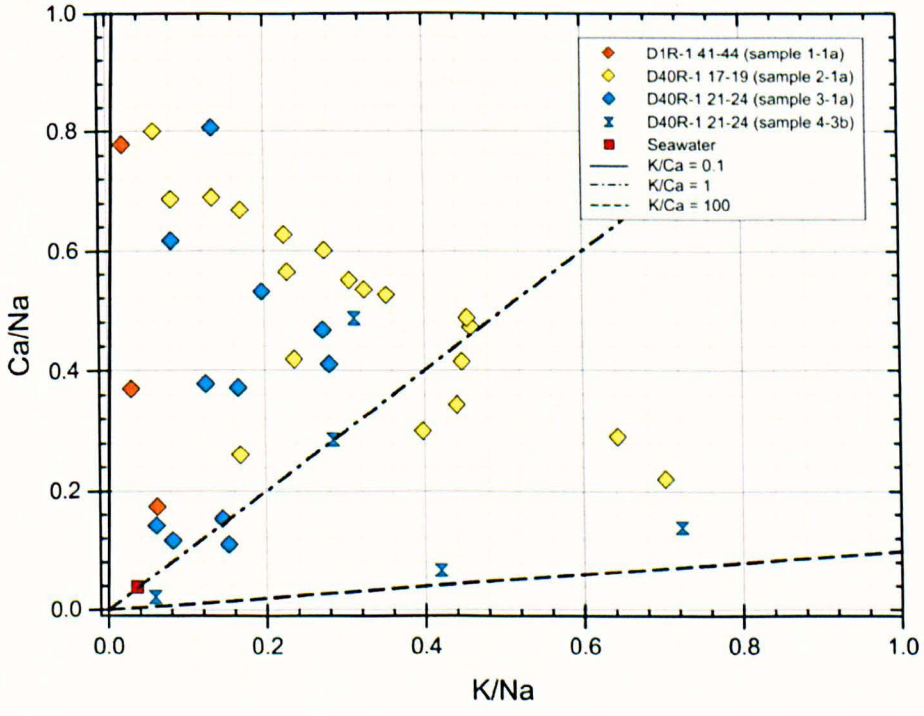


**Figure 4-6: K/Na concentration ratio (ppm/ppm) against Ca/Na concentration ratio (ppm/ppm)**

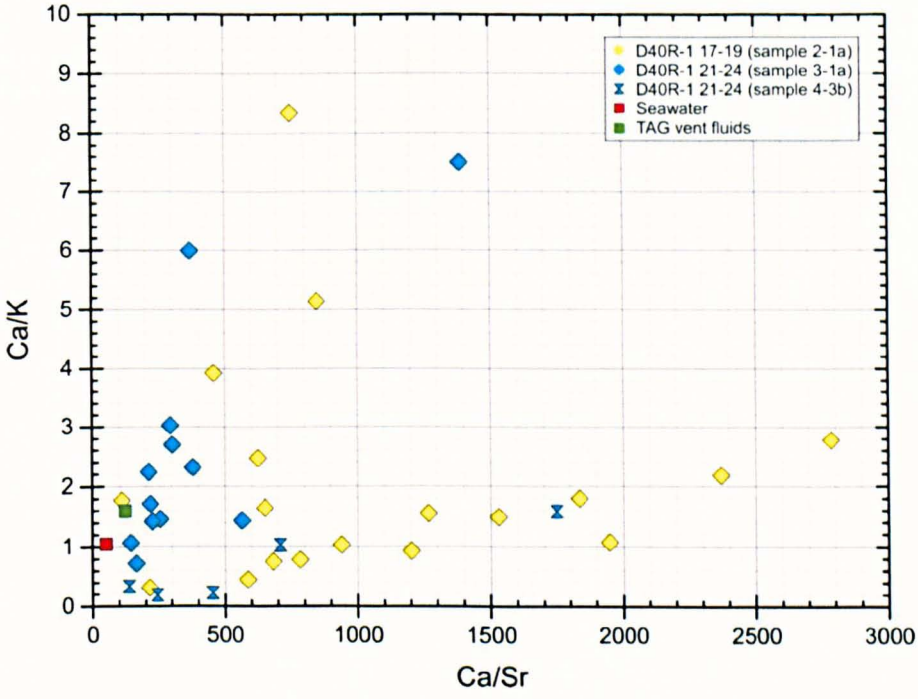


**Figure 4-7: Ca/Sr concentration ratio (ppm/ppm) against K/Ca concentration ratio (ppm/ppm).**

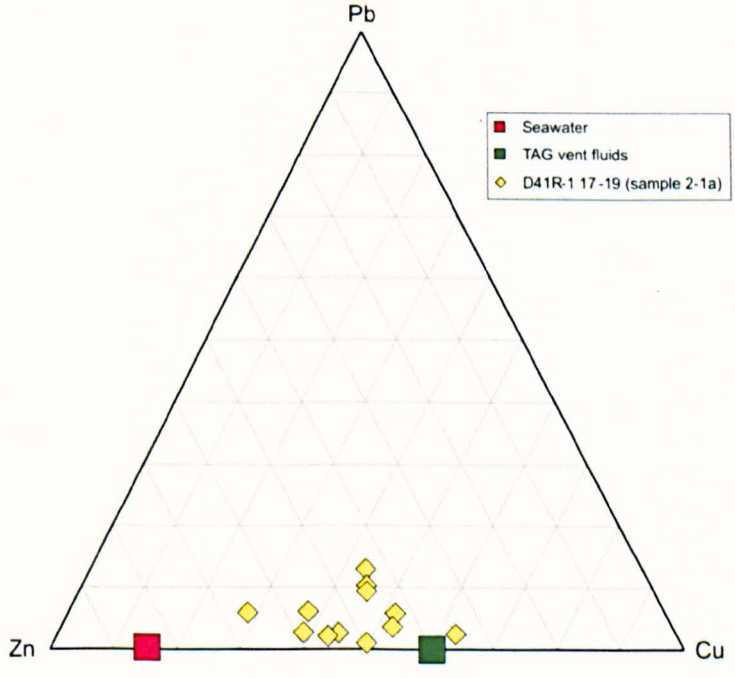


**Figure 4-8: Ternary diagram of Pb-Cu-Zn. Pb, Cu and Zn are relative proportion calculated from the respective concentration in ppm.**

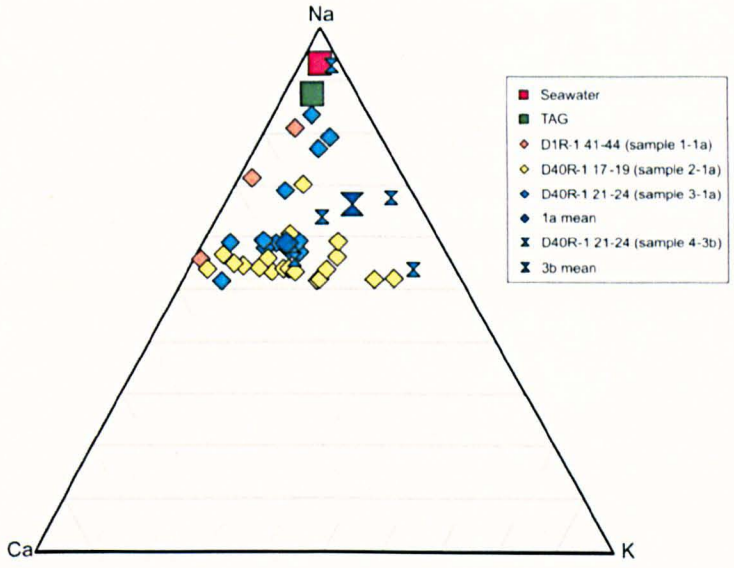


**Figure 4-9: Ternary diagram of Na-Ca-K. Na, Ca and K are relative proportion calculated from the respective concentration in ppm**

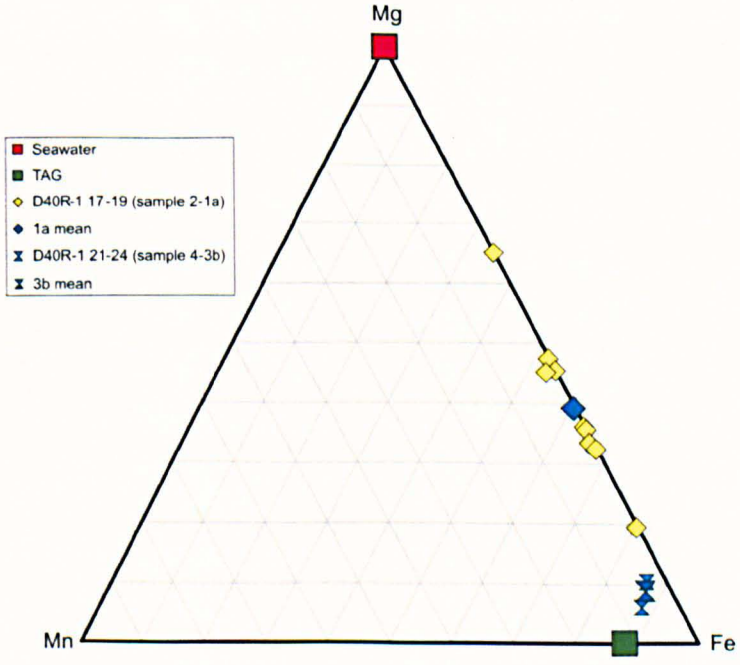


**Figure 4-10: Ternary diagram of Mg-Mn-Fe. Mg, Mn and Fe are relative proportion calculated from the respective concentration in ppm**

#### 4.3.1.4 Fluid type 1a versus fluid type 3b

Results in *Figure 4-1* show that all elements are more concentrated in fluid type 3b than in fluid type 1a, as a consequence of the difference in salinity. Co, Sr and Pb are the cations for which the difference between fluid type 1a and fluid type 3b is the least important while the biggest shift in median concentration between the two types of fluids apart from Na is shown by K.

*Figure 4-11* shows a comparative plot of cations to Na ratio for both fluid types and for seawater. Fluid type 1a has Mg, Ca, Ni, Co, Cu, Sr and Pb to Na ratio greater than fluid type 3b which has in turn Al, K, Mn, Fe and Ag to Na ratio greater than fluid type 1a. Mg/Na is the only ratio for which all fluids have a smaller ratio to that of seawater (0.12). Nonetheless, ratios of Co/Na and Sr/Na are pretty similar in both fluid types since the difference is at the fifth decimal place and the fourth decimal place respectively. The biggest shift in ratios between the two types of fluid is observed by Ca/Na, Fe/Na and K/Na.

Mg/Fe and Fe/Mn of fluid type 3b are lower than that of fluid type 1a (sample 2 and 3), while K/Ca of fluid type 3b is greater than that of fluid type 1a for which sample 1 has the lowest K/Ca and sample 2 and 3 spreading between those two extremes. K/Sr (*Figure 4-7*) seems to be equivalent in sample 2 and sample 4. Sample 3 shows a ratio much smaller. All samples have a greater K/Sr than seawater (50) and TAG vent fluids (75).

Ternary plots (*Figure 4-9* and *Figure 4-10*) show enrichment in K and in Fe in fluid type 3b relative to Na and Ca and relative to Mg and Mn in comparison to fluid type 1a.

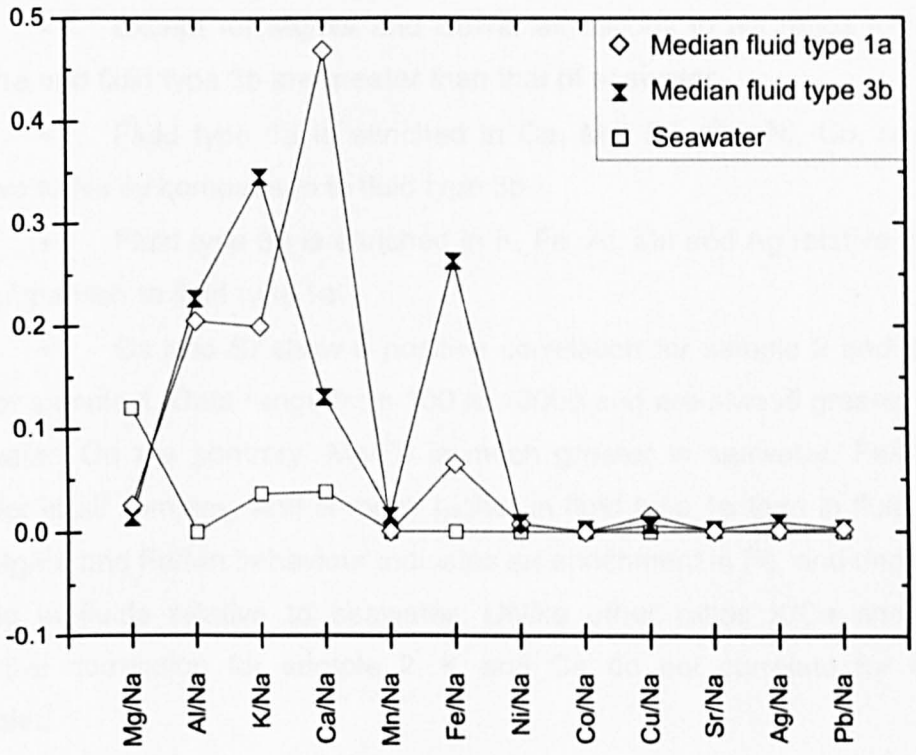


**Figure 4-11: X/Na concentration ratio (ppm/ppm) for both fluid type 1a and 3b. Symbols represent here the median of all inclusions for fluid type 1a and all inclusions for fluid type 3b.**

### 4.3.2 Summary

This paragraph summarises the big trends and patterns observed in the fluid chemistry data set.

- Na is the major cation species in both fluid types 1a and 3b.
- Data set show significant variations in median concentrations between samples 1, 2, and 3, which all contain type 1a fluids of similar salinity. Concentrations are generally lower in sample 1 than in samples 2 and 3.
- The general concentration pattern in fluid type 1a is: Na > Ca > K > Fe > Mg > Cu > Zn > Li -Ni > Pb > Sb > Ag.> Sr > Mn–Rb > Co.
- Type 3b median concentrations are greater than in fluid type 1a, owing to the difference in salinity.
- The general concentration pattern in fluid type 3b is: Na > K > Fe > Ca > Mn > Mg > Ni-Ag > Cu > Pb > Sr > Co.

- Except for Mg/Na and Sr/Na, all cations to Na ratios for fluid type 1a and fluid type 3b are greater than that of seawater.
- Fluid type 1a is enriched in Ca, Mg, Pb, Cu, Ni, Co, and Sr relative to Na by comparison to fluid type 3b.
- Fluid type 3b is enriched in K, Fe, Al, Mn and Ag relative to Na by comparison to fluid type 1a.
- Ca and Sr show a positive correlation for sample 2 and 3 but not for sample 4. Data range from 100 to 10000 and are always greater than seawater. On the contrary, Mg/Fe is much greater in seawater. Fe/Mn is greater in all samples, and is much higher in fluid type 1a than in fluid type 3b. Mg/Fe and Fe/Mn behaviour indicates an enrichment in Fe, and depletion in Mg in fluids relative to seawater. Unlike other ratios K/Ca shows a negative correlation for sample 2. K and Ca do not correlate for other samples.

## 4.4 Discussion

### 4.4.1 Deep fluid chemistry in oceanic settings

The only fluid chemistry analysis of fluid inclusions from oceanic settings has been done by Morgan (2008). Her study consisted of analysing fluid inclusions from diverse "stratigraphic levels" from the Troodos ophiolite, and fluid inclusions from ODP Hole 1256D. Comparing data from Morgan (2008) and data from the Atlantis Massif might be considered controversial due to the different settings in which samples are set. Samples from the Troodos ophiolites are indeed issued from a supra-subduction zone. Alteration observed in Troodos is different from IODP Hole U1309D with abundant epidosites. Samples from Hole 1256D come from a super-fast spreading rate crust compared to slow spreading crust for IODP Hole U1309D and from just above the dyke-gabbro contact. Nonetheless, it is the only comparable LAICPMS study to date.

In Troodos, fluids of low salinity were found, and separated into two sets: those less saline than seawater and those of greater salinity. Fluid type 1a (seawater-like salinity, this study) are compared with Troodos fluids of salinity in the range 5.5-3.5 Wt% NaCl equivalent. For fluids from ODP Hole 1256D, comparison is with fluids with salinity in the range 2.5-5.5 Wt% NaCl equivalent. Comparison of hypersaline fluids with halite daughter crystals is also done in this chapter.

### 4.4.2 Fluid chemistry in ophiolites – example of the Troodos ophiolite

Comparison of data from IODP Hole U1309D and that of Morgan (2008) is shown in *Figure 4-12*. One of the most striking observations is that fluid type 1a samples from this study (*Figure 4-12 top*) are depleted in all elements relative to Troodos. Variation in the magnitude of depletion between the samples is observed. Note that sample 1 is the most depleted. Comparison of hypersaline fluid (*Figure 4-12 bottom*) shows that sample 4 is not depleted in all elements relative to Troodos samples. Na, K, and Pb are enriched in Atlantis Massif fluids, whereas Mg, Ca, Mn, Fe, Cu, and Sr are

depleted relative to Troodos samples. The order of magnitude is also highly variable.

*Figure 4-13* shows a plot of Atlantis data and Troodos data normalised to seawater. The plot shows a consistent pattern of depletion and enrichment relative to seawater which might suggest similar processes of fluid-rock reaction. Fluid type 1a samples and Troodos samples of the same type are generally enriched relative to seawater, and depleted in Mg. Sr concentration is enriched relative to seawater in Troodos samples and depleted in samples 1, 2, 3 and 4. Concentration of Na is roughly similar to seawater and generally greater in Troodos samples. *Figure 4-14* shows a plot of samples 1, 2, 3 and 4 and Troodos ophiolite samples normalised to seawater after being normalised to seawater salinity to remove any effects of dilution and/or passive enrichment. Although this reduces the differences between samples, significant differences are still present, and the large differences between all the fluid inclusions and seawater are not removed.

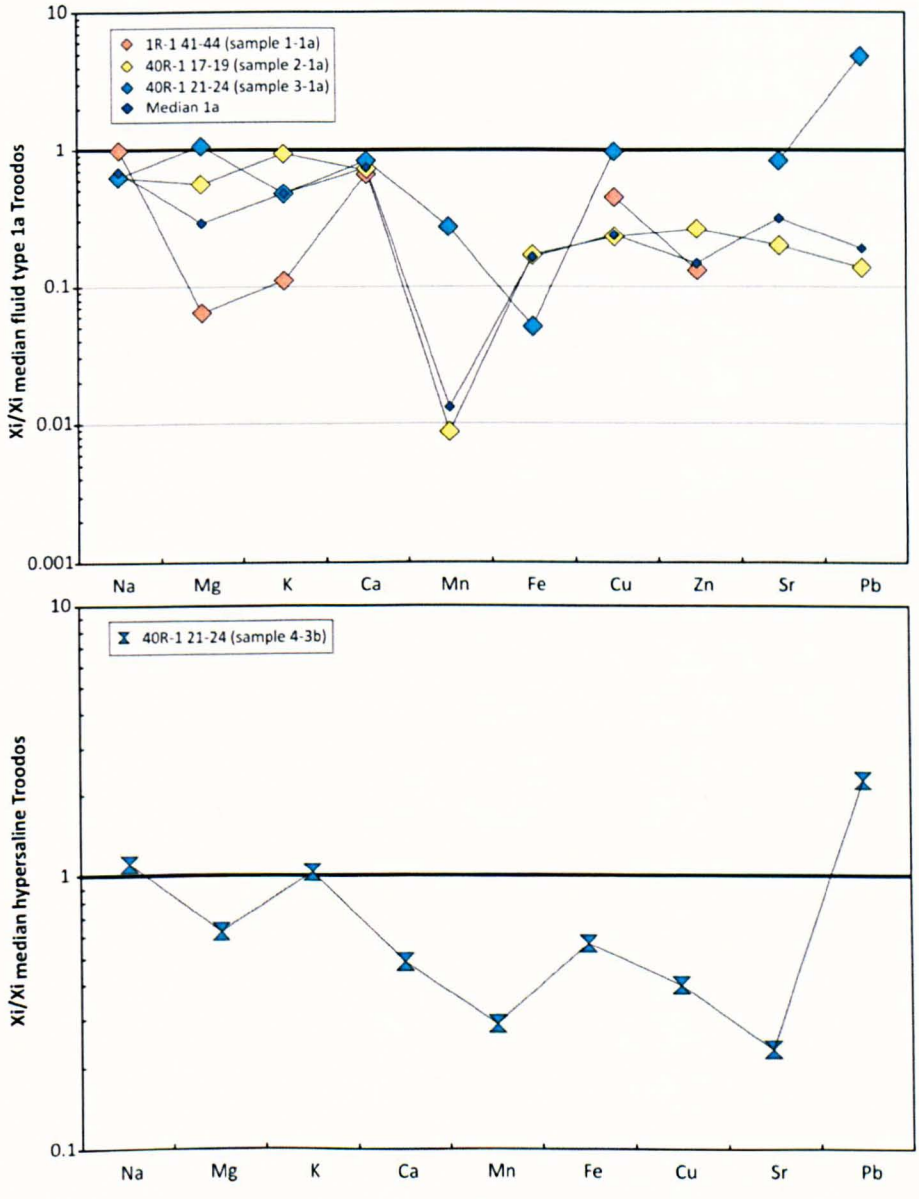


**Figure 4-12: Fluid chemistry of samples of fluid type 1a (top) and of fluid type 3b (bottom) normalised to Troodos ophiolite from (Morgan, 2008).**

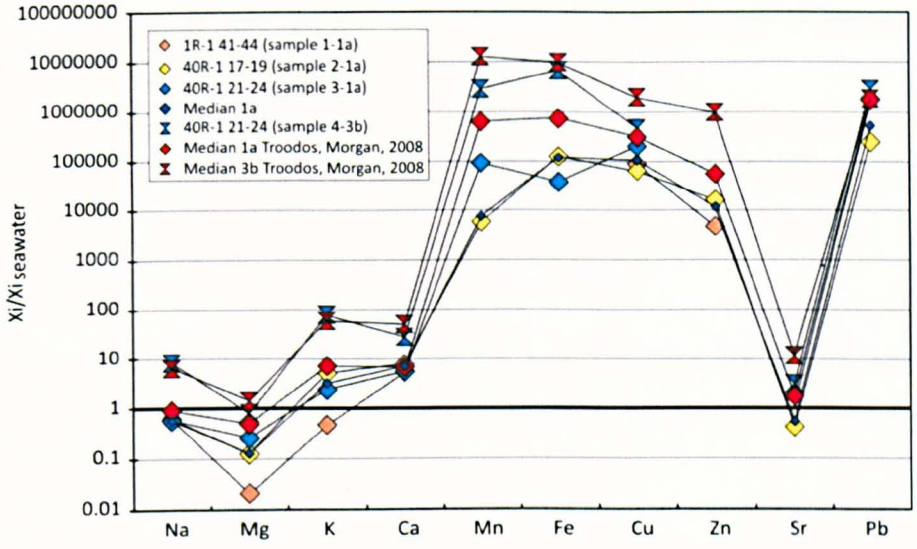


**Figure 4-13: Seawater-normalised fluid chemistry for all fluid types from this study and samples from the Troodos ophiolite (Morgan, 2008).**

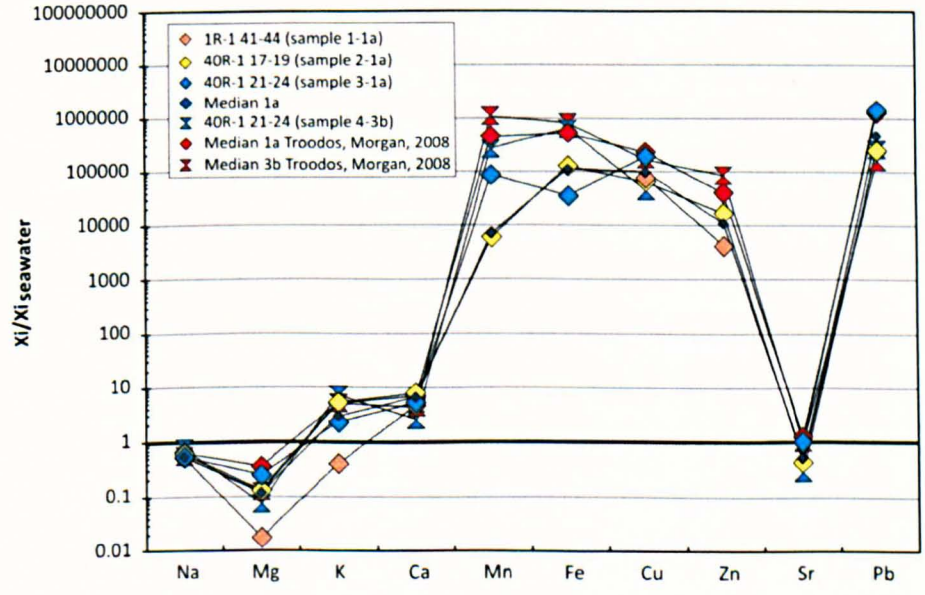


**Figure 4-14: Seawater normalised fluid chemistry for all fluid types of this study and for samples from Troodos ophiolites (Morgan, 2008) after being normalised to seawater salinity in order to remove any dilution or passive enrichment.**

### 4.4.3 Fluid chemistry in oceanic sections – example of ODP Hole 1256 D

Comparison of samples 1, 2, 3 and 4 to samples from ODP Hole 1256D is shown in *Figure 4-15*. Fluid type 1a is normalised to samples from 1256D of type 1 (top), and hypersaline fluid is normalised to Hole 1256D hypersaline fluid (bottom).

In general, fluid type 1a samples are depleted relative to samples from ODP Hole 1256D as for the comparison with Troodos samples. Sample 1 is again the most depleted.

Comparison of hypersaline fluids shows the same pattern with all elemental concentrations depleted in Atlantis Massif fluid relative to ODP Hole 1256D samples (*Figure 4-15* bottom).

*Figure 4-16* shows a plot of samples 1, 2, 3 and 4 and samples from ODP Hole 1256D both normalised to seawater. As in *Figure 4-13*, the consistent pattern of depletion and enrichment is still observed. Mg is still depleted with respect to seawater except for hypersaline fluid from ODP Hole 1256D. Sr is depleted in Atlantis Massif samples and enriched in ODP Hole 1256D relative to seawater. *Figure 4-17* shows a plot of IODP Hole U1309D samples and Troodos ophiolite samples normalised to seawater after being normalised to seawater salinity to remove effect of dilution and/or passive enrichment

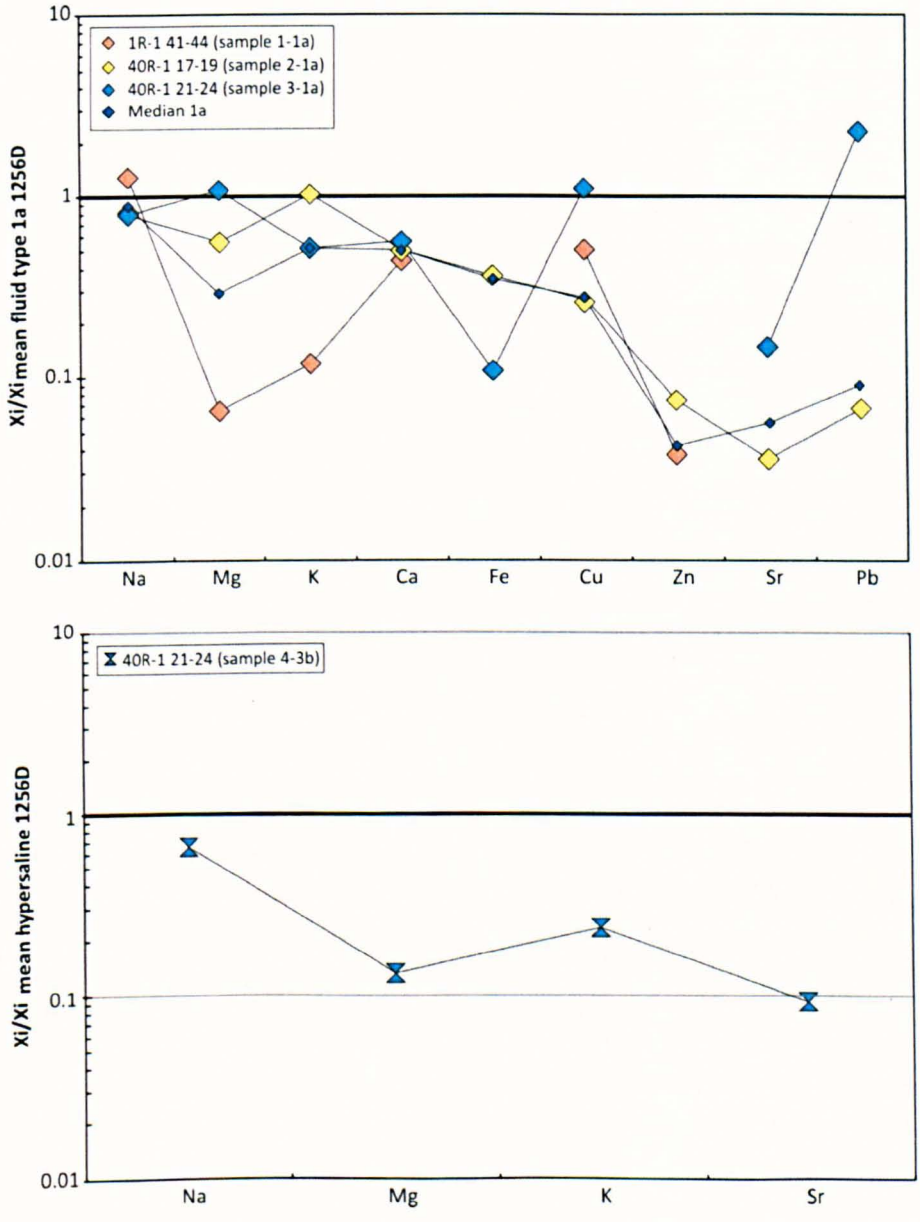


**Figure 4-15: Fluid chemistry for all samples normalised to data from IODP hole U1256D (Morgan, 2008), when data available.**

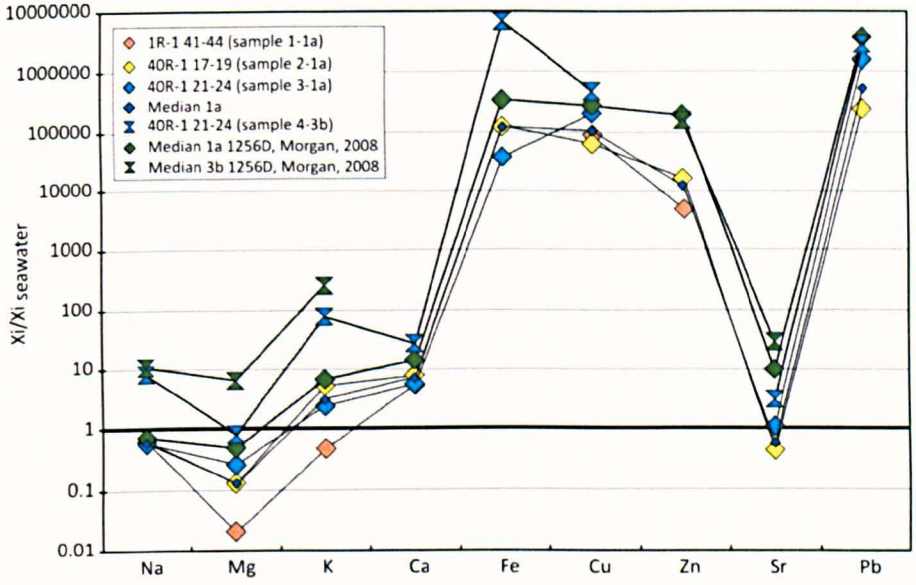


**Figure 4-16: Seawater-normalised fluid chemistry for samples of fluid type 1a and 3b and for sample from ODP Hole 1256D (Morgan, 2008).**

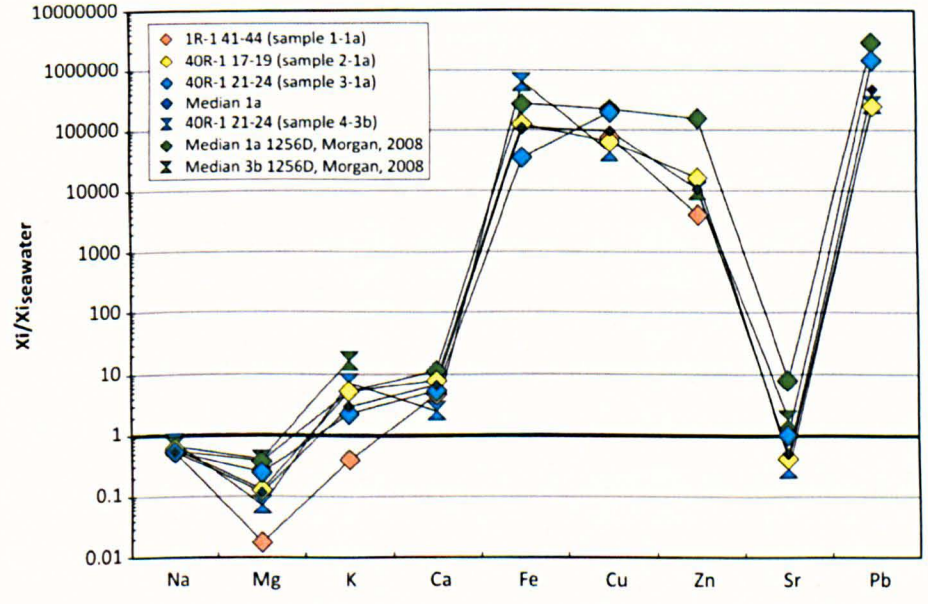


**Figure 4-17: Seawater normalised fluid chemistry for all fluid types of this study and for samples from ODP Hole 1256D (Morgan, 2008) after being normalised to seawater salinity in order to remove any dilution or passive enrichment.**

## 4.4.4 Processes modifying the fluid chemistry

### 4.4.4.1 Are vent fluids a simple mixing between hydrothermal fluids and seawater?

#### *4.4.4.1.1 The concept of backwater*

Hydrothermal systems are systems in which heated cold seawater penetrates oceanic crust to vent as a hydrothermal fluid after having interacted with rocks. Such fluids may have a short residence time with limited fluid-rock reaction, and may never approach equilibrium with any assemblage. In a more complex system, cold seawater penetrates the oceanic crust before being heated at depth, interacts with rocks and some is trapped in inclusions and/or stays longer in the system without being part of the main circulation that vents. These fluids which may have a much longer residence time in the crust represent backwater fluids. They are much more likely to approach equilibrium with particular assemblages. Later, that backwater can be mixed with recharged cold seawater to form the hydrothermal fluid that is going to vent. In this section IODP Hole U1309D fluid inclusions are treated as being inclusions that trapped backwater fluid.

#### *4.4.4.1.2 Comparison with vent fluids – the example of the TAG vent fluid*

The Atlantis Massif can be used as an analogue for the geological setting of the TAG Hydrothermal system (McCaig, *et al.*, 2010). The TAG vent fluid composition (Douville, *et al.*, 2002) is therefore used here for comparison to IODP Hole U1309D fluid inclusion chemistry.

Fluid inclusions and TAG vent fluids are normalised to seawater concentrations *Figure 4-18*. For most elements, TAG vent fluid plots outside the range of the fluid inclusions, and intermediate between seawater and the fluid inclusion concentrations. For some elements (Na, K, Mn, Fe, Rb and Sr), TAG vent fluid has a concentration within the range of the fluid inclusions (*Figure 4-18*).

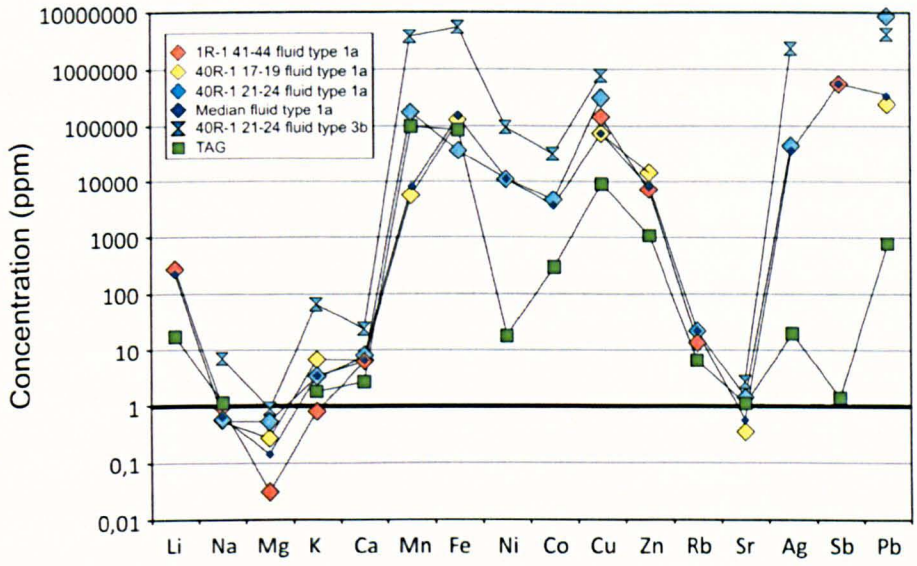


**Figure 4-18: Type 1a, 3b and TAG vent fluids normalised to seawater. TAG vent fluid concentrations are from Douville *et al.* (2002).**

#### *4.4.4.1.3 Fluid mixing calculation*

Observations from *Figure 4-18* lead to the following hypothesis:

Are vent fluids a simple mixing between seawater and deep fluid represented by IODP Hole U1309D inclusion fluids? This hypothesis can be simply tested by a calculation involving the concentration in vent fluids, the concentration in seawater, and the concentration in fluid inclusions, with the following equation where ($\mathcal{X}$) is the proportion of seawater needed to mix with the inclusion fluid in order to reach the vent fluids composition and X the concentration of an element. *Table 4-4* shows the results multiplied by 100. Concentrations used in this calculation are presented in *Table 4-3* and *Table 4-5*.

$$\mathcal{X} = (\mathbf{X}_{\mathbf{Inclusion\ fluid}} - \mathbf{X}_{\mathbf{Vent}})/(\mathbf{X}_{\mathbf{Inclusion\ fluid}} - \mathbf{X}_{\mathbf{Seawater}}) \qquad \textbf{4-1}$$

Results show that a simple mixing between seawater and fluid inclusions cannot result in TAG vent fluids on its own. In order for it to be a true mixing, the proportion of seawater would need to be the same across the elements. Instead, numbers show a certain inconsistency across the elements. Nonetheless, results for type 3b fluid indicate a range in value from 93 to almost 100%. However, this observation is the result of these fluids being much more concentrated than either vent fluid or seawater.

Bigger ranges in values are observed for samples of fluid type 1a. This characteristic might be a result of the difference in salinity. Inconceivable values (greater than 100% or negative) are reported in red in the table. Negative numbers are the results of the fact that concentration in that particular element is greater in the vent fluids than in fluid inclusions, which is in turn greater than in seawater, or that this element is less concentrated in fluid inclusions than in seawater and absent in vent fluids (case of Mg). Values greater than 100% are the result of the element being more concentrated in the vent fluid than in seawater, which is in turn more concentrated than in Atlantis Massif fluids. Values close to 100 % are quite common in all samples. They indicate that only a small amount of fluid needs to be added to seawater to generate vent fluids. The calculation show results that are variable, indicating that simple mixing is not the process that leads to the generation of vent fluids. Different processes such as phase separation, exsolution of brines from magmatic fluids, fluid rock interaction, and mineral precipitation must also have a control on fluid chemistry. The results show also that fluids from IODP Hole U1309D can be interpreted as backwater fluids that need to interact more with the surrounding rocks to reach vent composition.

**Table 4-4: Fluid mixing calculations. Numbers are the proportion of seawater needed to be mixed with fluid inclusions to result in TAG vent fluids composition. Report to text for significance of red numbers.**

| | Sample 1 | Sample 2 | Sample 3 | Fluid 1a | Fluid 3b |
|---|---|---|---|---|---|
| Li | 94.02 | - | - | 92.76 | - |
| Na | 297.25 | 141.75 | 140.68 | 146.42 | 97.20 |
| Mg | -3.22 | -36.93 | -109.74 | -16.31 | -812.60 |
| K | 499.24 | 86.39 | 67.67 | 67.82 | 98.68 |
| Ca | 68.21 | 71.93 | 75.56 | 71.93 | 92.60 |
| Mn | - | -1642.63 | 43.95 | -1062.81 | 97.31 |
| Fe | - | 32.57 | -132.01 | 42.40 | 98.43 |
| Ni | - | - | 99.85 | 99.85 | 99.98 |
| Co | - | - | 93.63 | 91.71 | 99.11 |
| Cu | 93.56 | 87.55 | 97.07 | 88.02 | 98.82 |
| Zn | 85.29 | 92.60 | - | 86.87 | - |
| Rb | 54.37 | - | 72.32 | 73.57 | - |
| Sr | - | 117.64 | 76.65 | 125.88 | 93.36 |
| Ag | - | - | 99.93 | 99.95 | 99.99 |
| Sb | 99.99 | - | - | 99.99 | - |
| Pb | - | 99.70 | 99.95 | 99.78 | 99.98 |

**Table 4-5: Fluid composition of fluid type 1a and 3 b (sample 1, 2 and 3 – presented in *Table 4-3*, and of seawater and TAG hydrothermal fluids from Douville, *et al.*, 2002.**

| | Fluid type 1a (ppm) | | Fluid type 3b (sample 4) (ppm) | | Seawater (ppm) | TAG hydrothermal fluids (ppm) |
|---|---|---|---|---|---|---|
| | Mean | Median | Mean | Median | | |
| Cl | 20119,6 | 20550,7 | 210596,7 | 212258,9 | 19400 | 23044,4 |
| Li | 41,9 | 39,0 | | | 0,17 | 2,9 |
| Na | 7558,2 | 6826,4 | 89393,5 | 76731,9 | 10800 | 12644,4 |
| Mg | 423,9 | 180,9 | 1448,9 | 1148,6 | 1290 | |
| K | 1592,9 | 1360,9 | 29470,9 | 24011,5 | 392 | 703,8 |
| Ca | 2896,2 | 2944,7 | 15265,3 | 10015,9 | 411 | 1122,2 |
| Mn | 19,7 | 3,3 | 3520,8 | 1452,6 | 0,0004 | 39,0 |
| Fe | 581,1 | 501,2 | 18424,5 | 18424,5 | 0,0034 | 288,7 |
| Ni | 54,8 | 73,8 | 845,4 | 622,2 | 0,0066 | 0,117 |
| Co | 1,4 | 1,4 | 12,2 | 13,2 | 0,00039 | 0,118 |
| Cu | 140,5 | 68,9 | 571,4 | 697,6 | 0,0009 | 8,261 |
| Zn | 68,3 | 41,3 | | | 0,005 | 5,426 |
| Rb | 2,9 | 2,7 | | | 0,12 | 0,812 |
| Sr | 6,5 | 4,5 | 22,7 | 22,0 | 8,1 | 9,025 |
| Ag | 9,0 | 10,7 | 775,7 | 624,8 | 0,00028 | 0,0055 |
| Sb | 7,7 | 5,5 | | | 0,00033 | 0,00047 |
| Pb | 55,4 | 10,1 | 126,8 | 124,8 | 0,00003 | 0,0228 |

### 4.4.4.2 Phase separation and magmatic exsolution

Phase separation accompanied by seawater mixing has been inferred to be the major process generating the populations of various salinities encountered in IODP Hole U1309D, although magmatic exsolution was described as being the processus generating the brines (*Chapter 3*).

High chloride contents of fluids are likely attributable to phase separation (Butterfield, *et al.*, 1990; Douville, *et al.*, 2002). The consequence of that enrichment in chloride is that $Cl^-$ will be the dominant ligand. Metals that form chloride complexes will then be stabilised in the fluid. Calculations show that Atlantis Massif fluids are enriched in chloride relative to seawater and in the same order of magnitude as Rainbow or TAG fluids (*Table 4-6*). Results show also enrichment in metal concentrations relative to seawater.

The origin of the fluids in sample 1, 2, 3 and 4 was discussed in *Chapter 3*. Type 1 fluids were seawater-derived fluids trapped at at shallow hydrostatic conditions. Type 3b fluids in sample 4 fluids were generated by direct exsolution of brine from melt. Any vapour phase from that exsolved fluid was not found.

The fluid chemistry of sample 4 is inferred to represent brine exsolved from a melt. Metals for which concentrations would be similar in low and/or high chloride fluid (Butterfield, *et al.*, 1990) are metals for which other processes than phase separation (*e.g.* fluid-rock interaction) must have occurred to control their concentration. However, such processes can also occur to a fluid that underwent phase separation.

**Table 4-6: Content in Cl in fluids of this study and fluid from Rainbow and TAG vent from Douville *et al.* (2002).**

| | Sample1 (ppm) | Sample2 (ppm) | Sample3 (ppm) | Sample4 (ppm) | Rainbow (ppm) | TAG (ppm) | Seawater (ppm) |
|---|---|---|---|---|---|---|---|
| Cl content | 21380 | 19630 | 20180 | 210600 | 26590 | 23045 | 19400 |

### 4.4.4.3 Reactions controlling the fluid chemistry

Fluid-rock interactions involving specific reactions are assumed to have a major control on fluid chemistry apart from phase separation. These reactions include albitisation, replacement of clinopyroxene by amphibole, corona texture formation, serpentinisation + rodingitisation, steatization, chloritisation, epidotisation and anhydrite precipitation. Many of these reactions are observed in U1309D core, and will be investigated as potential controls on fluid chemistry through the following paragraphs. Epidotisation is not an important reaction in IODP Hole U1309D but can influence the fluid chemistry of local fluids when occurring. Anhydrite does not occur in Atlantis Massif samples either, owing to its retrograde solubility. Nevertheless, the precipitation of anhydrite may have occurred at the time of hydrothermal circulation and therefore might have influenced fluid chemistry.

#### *4.4.4.3.1 Albitisation of plagioclase*

Albitisation reaction involves consumption of Na and Si from the interactive fluid and release of Ca if Al is immobile. The reaction can involve mobilisation of trace elements as well, leading to formation of ore deposits (Hövelmann, *et al.*, 2010).

As albitisation occurs, Na/Cl would tend to decrease (if chlorinity is constant) and Ca/Na would increase since Ca is released. Those two ratios

can then be plotted together to test the possibility of albitisation occurring in the Atlantis Massif samples as a control on fluid chemistry.

*Figure 4-19* shows a plot of Na/Cl molar ratios against Ca/Na molar ratios. An albitisation vector is also plotted to show the influence of albitisation of seawater. The vector has been calculated on the basis of mass balancing that occurs through the reaction: for every mole of Ca released to the fluid, 2 moles of Na are consumed from the fluid (*Equation 4-2*).

$$Ca\,Al_2Si_2O_8 + 2Na^+ + 4SiO_2 \rightarrow 2NaAlSi_3O_8 + Ca^{2+} \qquad \text{4-2}$$

Only one data point lies on the vector whereas all the other fluid inclusion molar ratios lie to the left. Albitisation seems to have no effect or at least not alone on the fluid chemistry of brines as Na/Cl decreases while Ca/Na decreases. The only sample for which albitisation seems to be likely to control fluid chemistry is sample U1309D 40R-1 17-19. Nonetheless, data points are not lying on the albitisation vector of seawater meaning that other reactions involving Na and Ca exchange must be taken into account. This indicates that fluids form IODP Hole 1309D are influenced by several combined reactions.

K content of plagioclase (even if minor) can also influence the fluid chemistry during albitisation (*Figure 4-6*). Concentration in K in solution increases indeed with albitisation and increased temperature (Berndt & Seyfried, 1993; Seyfried, 1987; Seyfried, *et al.*, 1991).

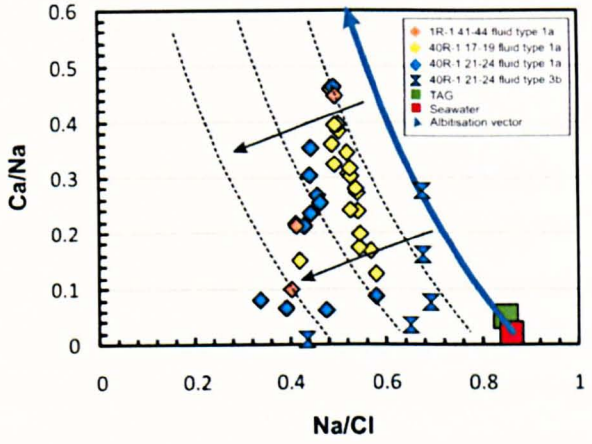


**Figure 4-19: Na/Cl versus Ca/Na. The vector of albitisation is calculated on the basis of mass balancing in which 1 mole of Ca is added to the fluid for every 2 moles of Na removed from it. Dashed lines and black arrows represent reactions that would influence those ratios leading to decreasing Ca/Na Na/Cl.**

#### *4.4.4.3.2 Replacement of clinopyroxene by amphiboles*

The most common reaction observed in IODP Hole U1309D is the replacement of clinopyroxene (diopside-augite) by amphiboles (magnesiohornblende and actinolite). At high temperature, pyroxene is replaced by green-brown hornblende. At lower temperature conditions (greenschist facies), the same reaction can occur with replacement of pyroxene by green and acicular actinolite. Observation of thin sections and electron microprobe analysis show that the most common reaction is the replacement of clinopyroxene by actinolite.

Replacement of clinopyroxene by hornblende

A model for the replacement of pyroxene by hornblende is given by the following reaction (*4-3*) (Blackman, *et al.*, 2006):

$$\text{plagioclase} + \text{augite} + \text{orthopyroxene} + H_2O = \text{hornblende} \qquad \textbf{4-3}$$

Balancing that reaction can be difficult because the composition of hornblende is changing with temperature-pressure conditions. In addition, orthopyroxene does not commonly occur in recovered rocks from IODP hole U1309D, with a few exceptions especially in ultramafic rocks and in the gabbronorite deeper in the hole. The reaction assuming constant volume would imply that 1 hornblende replaces ~4 augites, this being based on the

molar volume of end member minerals in Holland & Powell (1998). Diopside and enstatite are used as a proxy for augite (6.619 and 6.262 $J.bar^{-1}$ respectively), and ferroactinolite and tremolite are used as a proxy for hornblende (28.28 and 27.27 $J.bar^{-1}$ respectively). This reaction must be accompanied by plagioclase as a source of Al (assumed to be immobile). The combined effect of the molar ratio of pyroxene consumed to amphibole of 4:1 and the albitisation of anorthite have for consequence to release Ca and to consume Na. According to mineral compositions (*appendix 1*) and the molar ratio of 4:1, it is likely that Fe will be consumed and Mg will be released. The reaction can be written as follows (*4-4*). Note that the reaction is not balanced in full.

$$4\ \text{augite} + \text{anorthite} + \text{water} + Fe^{2+} + Na^{+} \rightarrow \text{hornblende} + \text{albite} + \text{quartz} \pm H^{+} + Ca^{2+} + Mg^{2+} \qquad \textbf{4-4}$$

Replacement of clinopyroxene by actinolite

In gabbros, clinopyroxene is more commonly replaced by actinolite. At constant volume, 4 clinopyroxenes are needed to form 1 amphibole (Holland and Powell, 1998 – see above). Again, as per the reaction in which clinopyroxene is replaced by hornblende, this reaction implies the involvement of plagioclase, and can be written as follows (*4-5*). Note that the reaction is not balanced as presented.

$$4\ \text{augite} + \text{anorthite} + \text{water} + Na^{+} + Fe^{2+} \rightarrow \text{actinolite} + \text{albite} + \text{quartz} \pm H^{+} + Ca^{2+} + Mg^{2+} \qquad \textbf{4-5}$$

Both reactions imply the release of Ca and Mg and the consumption of Na and Fe. If release of major cations and heavy metal seems reasonable owing to the fluid chemistry recorded in fluid inclusions, Mg should be removed from solution in chlorite as it is assumed to be removed during hydrothermal alteration of basalt (Seyfried, 1987; Seyfried & Mottl, 1982) and of ultramafic substratum at Rainbow and Logatchev site (Douville, *et al.*, 2002). Experimental studies of Seyfried and Mottl (1982) shows that Mg is completely removed from solution at 150°C and at seawater/rock ratio of 50.

Microthermometry (*Chapter 3*) indicates that fluid type 1a has been trapped at temperature of ~ 150-200°C. At such temperature, and assuming a system dominated by fluid (seawater/rock W/R = 50), fluid inclusions should contain 0 Mg. The fact that Mg is still in solution in fluid inclusions indicates that IDOP Hole U1309D fluid is influenced by the amphibole after clinopyroxene reactions but that the results of those reactions must be accompanied by reactions that mobilise Mg in the solid phase in order to allow for Mg concentration (depleted relative to seawater – see *Figure 4-1*).

#### *4.4.4.3.3 Corona texture formation*

In olivine rich rocks, corona formation is a common reaction observed in the core especially above 350 mbsf. Under that depth, the reaction does not go to completion and olivine is replaced by serpentine instead.

The corona texture reaction involves olivine and plagioclase which are being replaced at the contact by tremolite and chlorite respectively. The reaction can be written only if one component is mobile (CaO or $SiO_2$ here) since $Al_2O_3$ has generally a limited mobility. This reaction can then be modelled with 2 different reactions depending on which component is considered as being the most mobile (reaction *4-6* for $SiO_2$ and reaction *4-7* for CaO) (Blackman, *et al.*, 2006).

4 anorthite + 15 olivine + 5 silica + 18 water → 2 tremolite + 4 chlorite

$$4CaAl_2Si_2O_8 + 15Mg_2SiO_4 + 5SiO_2 + 18H_2O \rightarrow 2Ca_2Mg_5Si_8O_{22}(OH)_2 + 4Mg_5Al_2Si_3O_{10}(OH)_8 \quad \text{4-6}$$

11 anorthite + 35 olivine + 47 water → 3 tremolite + 11 chlorite + 5 CaO

$$11CaAl_2Si_2O_8 + 35Mg_2SiO_4 + 47H_2O \rightarrow 3Ca_2Mg_5Si_8O_{22}(OH)_2 + 11Mg_5Al_2Si_3O_{10}(OH)_8 + 5CaO \quad \text{4-7}$$

Those two reactions seem a bit unrealistic as they involve huge amount of olivine for a significantly smaller amount of amphibole. In addition, those two reactions use end member minerals. In IODP Hole U1309B and D, corona texture is composed of intermediate mineral composition of solid solution. Using electron microprobe data on corona texture for tremolite (average of three measurements in U1309D 5R-3 107-110 cm, see *Appendix 1*), assuming a $X_{Mg}$ = 0.6 for chlorite (Nozaka, *et al.*, 2008), and assuming a maximum volume increase of ~20% owing to the replacement of olivine by tremolite (justified by micro cracks observed in surrounding plagioclase - *Figure 4-20*), approximately 4.5 olivine is needed to form 1 tremolite. Note that the percentage in volume increase (10% for instance making the olivine:tremolite ratio equal to 5:1) during the reaction has no influence on the behaviour of the cations. The only thing that changes is the coefficient of water, quartz, $Mg^{2+}$ and $Fe^{2+}$. The corona texture formation reaction (*4-8*) can be balanced as follows:

1.15 bytownite + 4.5 olivine + 6.96 water + 3.92 quartz + 1.56 $Fe^{2+}$ + 1.03 $Ca^{2+}$ → tremolite + chlorite + 3.92 $H^+$ + 0.54 $Mg^{2+}$ + 0.18 $Na^+$

$$1.15\,(Ca_{0.8}Na_{0.2})[Si_{2.2}Al_{1.8}O_8] + 4.5Mg_{1.8}Fe_{0.2}[SiO_4] + 6.96H_2O + 3.92SiO_2 + 1.56Fe^{2+} + 1.03Ca^{2+} \rightarrow (Ca_{1.95}Na_{0.05})(Mg_{4.56}Fe_{0.46}Al_{0.02})[Si_{7.95}Al_{0.05}O_{22}](OH)_2 + (Mg_3Fe_2)Al_2[Si_3O_{10}](OH)_8 + 3.92H^+ + 0.54Mg^{2+} + 0.18Na^+ \quad \text{4-8}$$

LAICPMS data of IODP Hole U1309D fluid inclusions show an enrichment in Ca and Fe with a depletion in Na and Mg relative to seawater. Corona texture formation reaction shows the exact opposite (Fe and Ca are consumed from the fluid, while Mg and Na are released to the fluid), meaning either that fluid from IODP Hole U1309D are not influenced by the corona texture formation, or that other reactions must be taken into account. The resulting Na release and the consumption of Ca can be compensated by albitisation in order to generate a fluid depleted in Na and enriched in Ca relative to seawater. The resulting release of Mg from corona formation must

be compensated by reactions that mobilise it in the solid phases such as the serpentinisation and the steatisation (see *4.4.4.3.4 and 4.4.4.3.6* below).

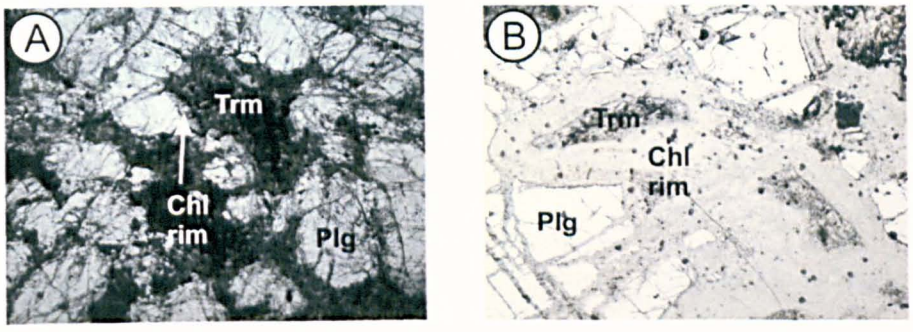


**Figure 4-20: Photomicrograph of thin sections showing cracks in plagioclase generated by formation of corona texture: A:U1309D 12R-1 65-67 cm (plane polarised light) ; B: U1309D 33R-2 41-43 cm (plane polarised light). Trm = tremolite; Chl rim = chlorite rim; Plg = plagioclase.**

#### *4.4.4.3.4 Serpentinisation*

Serpentinisation is another common reaction occurring in olivine-bearing rocks. When plagioclase is present, rodingitisation can be associated with serpentinisation (see below *4.4.4.3.5*).

Serpentine is the product of different reactions. It can be obtained in the presence of pyroxene where olivine + clinopyroxene + fluid = serpentine or olivine + tremolite+ fluid = serpentine + clinopyroxene. It can be formed from hydration of olivine by a silica rich fluid. Finally, it can be the product with brucite from pure hydration of olivine (*4-9*):

2 olivine + 3 water → serpentine + brucite

$$2Mg_2SiO_4 + 3H_2O \rightarrow Mg_3Si_2O_5(OH)_4 + Mg(OH)_2 \qquad \textbf{4-9}$$

Serpentinisation does not release anything to the fluid. However this conclusion is based on the Mg-end member mineral reaction. With real composition measured by electron microprobe, an intermediate olivine of composition $Fo_{80}$ reacts with fluid to form an intermediate composition serpentine ($X_{Mg}$ = 0.83) + brucite and magnetite and produces $H_2$.

4 olivine + 5.6 water → 2 serpentine + 1.4 $Mg(OH)_2$ + 0.2 $Fe_3O_4$ + 0.4 $H_2$

$$4Mg_{1.6}Fe_{0.4}SiO_4 + 5.6H_2O \rightarrow 2Mg_{2.5}Fe_{0.5}Si_2O_5(OH)_4 + 1.4Mg(OH)_2 + 0.2Fe_3O_4 + 0.4H_2 \quad \text{4-10}$$

This reaction shows that serpentinisation does not release anything to the fluid. On the contrary, it immobilises Mg and Fe in the solid phases with formation of serpentine, brucite and magnetite. In fluid inclusions of IODP Hole U1309D, concentration of Fe is greater than in seawater. This indicates that other processes must be taken into account to allow for generation of fluid chemistry such as the ones observed in fluid inclusions.

Note that olivine has a significant Ni content, which is not the case of serpentine. The Ni enrichment observed in fluid inclusion chemistry can therefore be explained by leaching occurring during serpentinisation.

#### *4.4.4.3.5 Rodingitisation*

Rodingites are rocks containing Ca-rich silicates that are associated with serpentinites. They are classically believed to be the result of intense Ca metasomatism (Coleman, 1963; O'Hanley, 1996). Nonetheless, rodingitisation in Atlantis Massif is usually associated with serpentinisation and occurs with no addition of Ca as long as Si and Al are mobile (Frost, *et al.*, 2008). In that case there are a series of reactions that influence one another. Alteration of plagioclase into prehnite in these rocks occurs as a result of the low silica activity that characterises serpentinisation (Frost & Beard, 2007). The replacement of plagioclase by prehnite and prehnite by hydrogrossular provide indeed a source of $SiO_2$ which permits the olivine to alter into serpentine. The alteration of plagioclase produces an excess of $Al_2O_3$ which is in turn used to react with serpentine and form chlorite plus $SiO_2$. *Figure 4-21* shows a diagram which represents what happens during rodingitisation in a sample of IODP Hole U1309D.

The only metal which is therefore released to the fluid during rodingitisation with associated serpentinisation is $Na^+$ (Frost, *et al.*, 2008). This should result in a shift in Na concentration in fluid inclusions relative to seawater. And yet, Na median concentrations in fluid type 1a are lower than that of seawater. As rodingitisation implies release of Na into the reactive

fluid and albitisation implies consumption of Na from the reactive fluid, the median concentrations of fluid from fluid inclusions could be the combine effect of albitisation and rodingitisation. However, as seen in corona formation (*4.4.4.3.3 au-dessus*), corona formation also produces Na. It is unclear whether albitisation overtakes rodingitisation and corona formation, or other processes must be taken into account (*e.g.* phase separation) to allow for the generation of fluid chemistries observed in fluid inclusions.

Note that fluid type 3b has indeed Na concentration greater than seawater but this is a result of the generation of brines by magmatic exsolution and has nothing to do with metamorphic reactions.

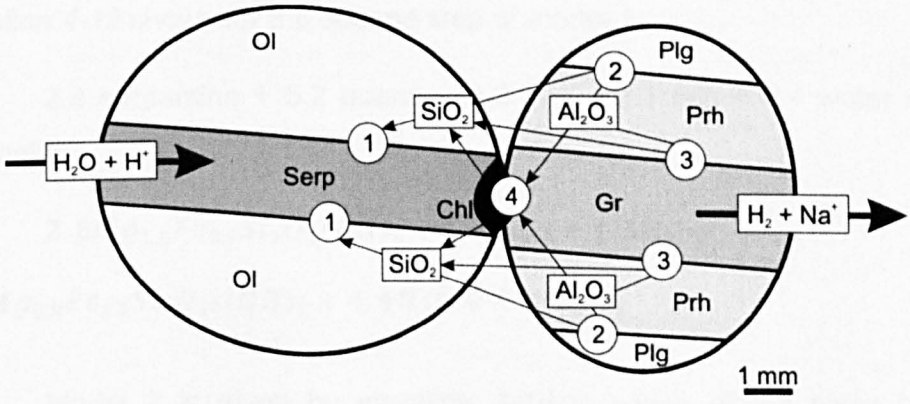


**Figure 4-21: Schematic representation of the processes of rodingitisation (from Frost, *et al.*, 2008). Ol = olivine; Serp = serpentine; Plg = plagioclase; Prh = prehnite; Gr = grossular; Chl = chlorite.**

#### *4.4.4.3.6 Steatization*

Steatization is the processes from which olivine is replaced by serpentine which is in turn replaced by talc (model 1). Sample U1309D 117R-2 24-32 shows an example of steatization where talc replaces serpentine after olivine (*Figure 4-22*). These reactions are observed in olivine rich rocks in the upper part of the core and can be modelled by the reactions (*4-9* – see serpentinisation paragraph) and (*4-11*) below:

serpentine + 2 quartz → talc + water

$$Mg_3Si_2O_5(OH)_4 + 2SiO_2 \rightarrow Mg_3Si_4O_{10}(OH)_2 + H_2O \qquad \textbf{4-11}$$

Steatization can also replace olivine directly by talc (model 2) without the intermediate serpentine (*4-12*).

3 olivine + 5 quartz +2 water → 2 talc

$$3Mg_2SiO_4 + 5SiO_2 + 2H_2O \rightarrow 2Mg_3Si_4O_{10}(OH)_2 \qquad \textbf{4-12}$$

These reactions imply consumption of silica from the fluid and do not imply any metal release to the fluid. Nevertheless, these reactions are written for pure forsterite and pure Mg talc without considering the Fe content of the olivine and talc. Olivine gives serpentine + brucite + magnetite and $H_2$ as equation *4-10* shows for the first step of model 1. Serpentine gives talc as equation *4-13* shows for the second step of model 1:

2.8 serpentine + 5.2 quartz + 1.3 $H_2$ → 2.5 talc + 4.4 water + 0.3 magnetite

$$2.8Mg_{2.5}Fe_{0.5}Si_2O_5(OH)_4 + 5.2SiO_2 + 1.3H_2 \rightarrow$$

$$2.5Mg_{2.8}Fe_{0.2}Si_4O_{10}(OH)_2 + 4.4H_2O + 0.3Fe_3O_4 \qquad \textbf{4-13}$$

Model 2 is given by equation *4-14* in which olivine gives talc + magnetite + $H_2$:

2.8 olivine + 3.6 silica + 10.268 water → 1.6 talc + 0.267 magnetite + 8.668 $H_2$

$$2.8Mg_{1.6}Fe_{0.4}SiO_4 + 3.6SiO_2 + 10.268H_2O \rightarrow$$

$$1.6Mg_{2.8}Fe_{0.2}Si_4O_{10}(OH)_2 + 0.267Fe_3O_4 + 8.668H_2 \qquad \textbf{4-14}$$

Steatisation consumes silica and fixes Mg and Fe in solid phases. IODP Hole U1309D fluids show an enrichment in Fe relative to seawater. This indicates that other reactions or processes must be taken into account to allow for Fe concentrations.

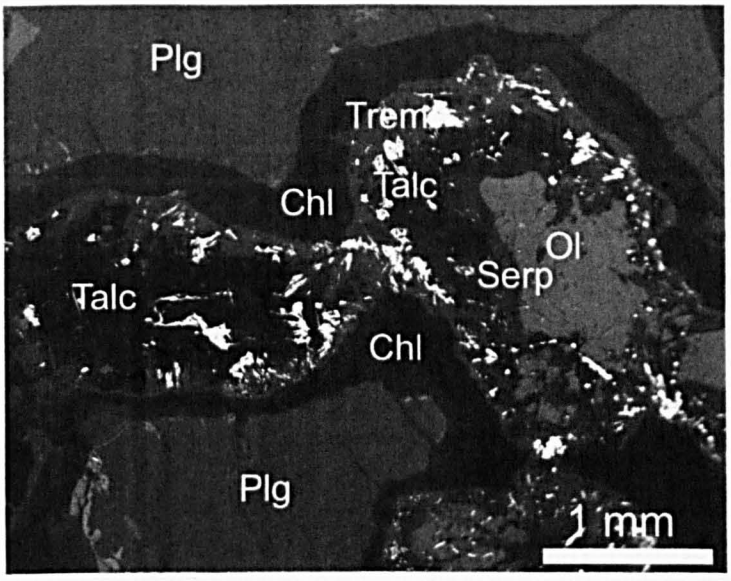


**Figure 4-22: Microphotograph showing the replacement of serpentine after olivine by talc in a corona texture (U1309D 117R-2 24-32 cm)**

#### *4.4.4.3.7 Epidotisation*

Epidotisation is another reaction that involves consumption of Ca from the fluid. It is a hydrothermal process by which feldspars, pyroxenes and amphiboles are altered to epidote. Epidote in the core is not really common but occurs in one or two samples (U1309D 75R-2 77-80 cm for instance) in which it is believed to replace clinopyroxene (Blackman, *et al.*, 2006).

#### *4.4.4.3.8 Anhydrite precipitation*

Anhydrite precipitation also potentially consumes Ca from the fluid. However, anhydrite is not common in the core and occurs in only one sample (U1309D-150R-3, 22–23 cm). This absence can be explained by its retrograde solubility amongst other explanations. However, at time of hydrothermal circulation anhydrite precipitated and could have influenced the fluid chemistry of fluid.

Experimental studies on hydrothermal alteration of basalt have shown that anhydrite precipitation causes the loss of $SO_4$ from seawater at temperature > 150°C (Mottl & Holland, 1978; Seyfried & Bischoff, 1979; Seyfried & Mottl, 1982). As S has not been measured, the loss or enrichment in $SO_4$ in the system cannot be estimated. However, the high Ca requires

that SO4 is low (Yardley B., pers.comm.) indicating that anhydrite has not contributed to Ca concentration of IODP Hole U1309D fluids to increase.

#### *4.4.4.3.9 Considerations on trace elements*

Strontium

In samples 1, 2 and 3, Sr is depleted relative to seawater. Sample 4 shows a greater concentration but this particularity is the result of the greater salinity of that fluid. In experimental studies of alteration of basalt and diabase (Seyfried, *et al.*, 1998; Seyfried & Mottl, 1982) and of peridotite (Seyfried & Dibble, 1980), Sr is taken from the fluid to incorporate into secondary phases. It is even sometimes completely removed from fluid. Nonetheless, Sr is also leached from silicates, and mobilised in the fluid. As shown by Menzies and Seyfried (1979), this Sr was in anhydrite and substituted with Ca. Its presence in the Atlantis Massif fluids might therefore come from the alteration of anhydrite, assuming anhydrite was occurring at time of hydrothermal circulation and to a lesser extent plagioclase.

The transition metals

Experimental studies show that transition metals, namely Fe Mn Zn Cu Pb Ni Co are leached and maintained in fluid reacting with basalt and diabase during hydrothermal alteration at various temperature and water/rock ratios (Menzies & Seyfried, 1979; Mottl & Holland, 1978; Seewald & Seyfried Jr, 1990; Seyfried, 1987; Seyfried & Bischoff, 1977; Seyfried & Bischoff, 1979; Seyfried & Bischoff, 1981; Seyfried & Mottl, 1982). Those studies demonstrate also that the concentrations in fluid of those metals depend on the pH of the solution which is controlled by the loss in Mg and Ca from seawater (Seyfried & Bischoff, 1981; Seyfried & Mottl, 1977), which in turn frees $H^+$ (decreasing the pH). Concentrations of heavy metals are therefore essentially controlled by fluid rock interactions and mineral equilibria. Concentrations of heavy metals in fluid type 1a agree with estimates from these studies.

## 4.5 Conclusions

- Fluid chemistry shows variations throughout IODP Hole U1309D samples resulting from the coactions of several processes.
- All samples show enrichment in major cations and heavy metals, except Mg and Sr with respect to seawater.
- Phase separation clearly influences the salinity variation but can also play a role in concentration of major and trace elements.
- It has been clearly shown that Atlantis Massif fluids are not an intermediate composition fluid between seawater and vent fluid. They are instead back-water fluid that can mix with recharged seawater and interact further with the rock in order to reach vent fluid compositions.
- Fluid rock interactions clearly play a major role in the variation of fluid chemistry. Replacement of clinopyroxene by amphiboles in addition to serpentinisation and steatisation control the concentration in Mg. Ca is mainly controlled by alteration of plagioclase. Na is controlled by albitisation and corona formation. Fe is controlled by steatization and serpentinisation + oxide minerals.

# 4.6 References

Allan, M. M., Yardley, B. W. D., Forbes, L. J., Shmulovich, K. I., Banks, D. A. & Shepherd, T. J., 2005. Validation of LA-ICP-MS fluid inclusions analysis with synthetic fluid inclusions. *American Mineralogist*, **90**, 1767-1775.

Audétat, A., Günther, D. and Heinrich, C. A., 1998. Formation of a Magmatic-Hydrothermal Ore Deposit: Insights with LA-ICP-MS Analysis of Fluid Inclusions, *Science*, **279**, 2091-2094.

Audétat, A., Günther, D. and Heinrich, C. A., 2000. Causes for large-scale metal zonation around mineralized plutons: fluid inclusion LA-ICP-MS evidence from the Mole Granite, Australia. *Economic Geology*, **95**, 1563-1581.

Berndt, M. E. & Seyfried, W. E., 1993. Calcuim and Sodium Exchange During Hydrothermal Alteration of Calcic Plagioclase at 400°C and 400 Bars. *Geochimica et Cosmochimica Acta*, **57**(18), 4445-4451.

Blackman, D. K., Ildefonse, B., John, B. E., Ohara, Y., Miller, D. J., McLeod, C. J. & Scientists, E., 2006. Expedition 304/305 summary. *Proceedings of the Integrated Ocean Drilling Program*, **304/305**, 1-60.

Bodnar, R. J., 1993. Revised equation and table for determining the freezing point depression of $H_2O$-NaCl solutions. *Geochimica et Cosmochimica Acta*, **57**, 683-684.

Butterfield, D. A., Massoth, G. J., McDuff, R. E., Lupton, J. E. & Lilley, M. D., 1990. Geochemistry of Hydorthermal Fluids From Axial Seamount Hydrothermal Emissions Study Vent Field, Juan de Fuca Ridge: Subseafloor Boiling and Subsequent Fluid-Rock Interaction. *Journal of Geophysical Research*, **95**(B8), 12895-12921.

Coleman, R. G., 1963. Serpentinites, Rodingites, and Tectonic Inclusions in Alpine-type Mountain Chains. *Geological Society of America, Special Papers*, **73**.

Douville, E., Charlou, J. L., Oelkers, E. H., Bienvenu, P., Jove Colon, C. F., Donval, J. P., Fouquet, Y., Prieur, D. & Appriou, P., 2002. The rainbow vent fluids (36°14'N, MAR): the influence of ultramafic rocks and phase separation on trace metal content in Mid-Atlantic Ridge hydrothermal fluids. *Chemical Geology*, **184**(1-2), 37-48.

Drouin, M., Godard, M., Ildefonse, B., Bruguier, O. & Garrido, C. J., 2009. Geochemical and petrographic evidence for magmatic impregnation in the oceanic lithosphere at Atlantis Massif, Mid-Atlantic Ridge (IODP Hole U1309D, 30°N). *Chemical Geology*, **264**(1-4), 71-88.

Frost, B. R. & Beard, J. S., 2007. On silica activity and serpentinisation. *Journal of Petrology*, **48**(7), 1351-1368.

Frost, B. R., Beard, J. S., McCaig, A. & Condliffe, E., 2008. The formation of micro-rodingite from IODP Hole U1309D: Key to understanding the process of serpentinization. *Journal of Petrology*, **49**(9), 1579-1588.

Ghazi, A. M., McCandless, T. E., Vanko, D. A., and Ruiz, J., 1996. New quantitative approach in trace elemental analysis of single fluid inclusions: applications of laser ablation inductively coupled plasma mass spectrometry (LA-ICP-MS). *Journal of Analytical Atomic Spectrometry*, **11**, 667–674.

Guillong, M., Meier, D. L., Allan, M. M., Heinrich, C. A., and Yardley, B. W. D., 2008. Appendix A6: SILLS: A matlab-based program for the reduction of laser ablation ICP-MS data of homogeneous materials ans inclusions. *In* Sylvester, P. (ed) Laser Ablation ICP–MS in the Earth Sciences: Current Practices and Outstanding Issues, *Mineralogical Association of Canada, Short Course* Vol. **40**, 328-333.

Günther, D., Frischknecht, R., Heinrich, C. A., and Kahlert, H.-J., 1997. Capabilities of an argon fluoride 193 nm Excimer Laser for laser ablation inductively coupled plasma mass spectrometry microanalysis of geological materials. *Journal of Analytical Atomic Spectrometry*, **12**, 939–944.

Heinrich, C. A., Ryan, C. G., Mernagh, T. P., and Eadington, P. J., 1992. Segregation of ore metals between magmatic brine and vapor: a fl uid inclusion study using PIXE microanalysis. *Economic Geology*, **87**, 1566–1583.

Holland, T. J. B. and Powell, R., 1998. An internally consistent thermodynamic data set for phases of petrological interest. *Journal of Metamorphic Geology*, **16**, 309-343.

Hövelmann, J., Putnis, A., Geisler, T., Schmidt, B. C., and Golla-Schindler, U., 2011. The replacement of plagioclase feldpars by albite: observations from hydrothermal experiments. *Contributions to Mineralogy and Petrology*, **159**, 43-59. DOI: 10.1007/s00410-009-0415-4

McCaig, A., Delacour, A., Fallick, A. E., Castelain, T. & Früh-Green, G. L., 2010. Detachment Fault Control on Hydrothermal Circulation Systems: Interpreting the Subsurface Beneath the TAG Hydrothermal Field Using the Isotopic and Geological Evolution of Oceanic Core Complexes in the Atlantic, *In* Rona, P. A., Devey, C. W., Dyment, J., Murton, B. J. (ed) Diversity of Hydrothermal Systems on, Slow Spreading Ridges, *AGU Geophysical Monograph*, **108**, AGU, pp; 207-240.

Menzies, M. M. & Seyfried, W. E., 1979. Basalt seawater interaction: trace element and strontium isotopic variations in experimentally altered basalt and peridotite. *Earth and Planetary Science Letters*, **44**, 463-472.

Morgan, S. J., 2008. *High temperature fluid-rock interaction in oceanic crust: A study of fluid inclusions from the Troodos ophiolite and ODP/IODP Hole 1256D*, University of Leeds, Leeds.

Mottl, M. J. & Holland, H. D., 1978. Chemical exchange during hydrothermal alteration of basalt by seawater_I. Experimental results for major and minor components of seawater. *Geochimica et Cosmochimica Acta*, **42**(8), 1103-1115.

Müller, B., Frischknecht, R., Seward, T. M., Heinrich, C. A., and Gallegos, W. C., 2001. A fluid inclusion reconnaissance study of the Huanuni tin deposit, Bolivia, using LA-ICP-MS micro-analysis. *Mineralium Deposita*, **36**, 680-688.

Nozaka, T., Fryer, P. and Andreani, M., 2008. Formation of clay minerals and exhumation of lower-crustal rocks at Atlantis massif, Mid-Atlantic Ridge. *Geochemistry Geophysics Geosystems*, **9**, 1-19. doi: 10.1029/2008GC002207

O'Hanley, D. S., 1996. Serpentinites: Records of Tectonic and Petrological History, pp. 277, Oxford.

Pearce, N. J. G., Perkins, W. T., Westgate, J. A., Gorton, M. P., Jackson, S. E., Neal, C. R. & Chenery, S. P., 1996. A compilation of new and published major and trace element data for NIST SRM 610 and NIST SRM 612 glass reference materials. *Geostandards Newsletter*, **21**, 115-144.

Rusk, B. G., Reed, M. H., Dilles, J. H., Klemm, L. M., and Heinrich, C. A., 2004. Compositions of magmatic hydrothermal fluids determined by LA-ICP-MS of fluid inclusions from the porphyry copper-molybdenum deposit at Butte, MT. *Chemical Geology*, *210*, 173–199.

Seewald, J. S. & Seyfried Jr, W. E., 1990. The effect of temperature on metal mobility in subseafloor hydrothermal systems: constraints from basalt alteration experiments. *Earth and Planetary Science Letters*, **101**(2-4), 388-403.

Seyfried, W. E., 1987. Experimental and Theoretical Constraints on Hydrothermal Alteration Processes at Mid-Ocean Ridges. *Annual Review of Earth and Planetary Sciences*, **15**, 317-335.

Seyfried, W. E. & Bischoff, J. L., 1977. Hydrothermal transport of heavy metals by seawater: The role of seawater/basalt ratio. *Earth and Planetary Science Letters*, **34**, 71-77.

Seyfried, W. E. & Bischoff, J. L., 1979. Low temperature basalt alteration by seawater: an experimental study at 70°C and 150°C. *Geochimica et Cosmochimica Acta*, **43**, 1937-1947.

Seyfried, W. E. & Bischoff, J. L., 1981. Experimental seawater-basalt interaction at 300°C, 500 bars, chemical exchange, secondary mineral

formation and implications for the transport of heavy metals. *Geochimica et Cosmochimica Acta*, **45**, 135-147.

Seyfried, W. E., Chen, X. & Chan, L.-H., 1998. Trace element mobility and lithium isotope exchange during hydrothermal alteration of seafloor weathered basalt: An experimental study at 350°C, 500 bars. *Geochimica et Cosmochimica Acta*, **62**(6), 949-960.

Seyfried, W. E. & Dibble, W. E., 1980. Seawater-peridotite interaction at 300° and 500 bars: implications for the origin of oceanic serpentinites. *Geochimica et Cosmochimica Acta*, **44**, 309-321.

Seyfried, W. E., Ding, K. & Berndt, M. E., 1991. Phase-Equilibria Constraints on the Chemistry of Hot-Spring Fluids at Mid-Ocean Ridges. *Geochimica et Cosmochimica Acta*, **55**(12), 3559-3580.

Seyfried, W. E. & Mottl, M. J., 1977. Origin of submarine-metal rich hydrothermal solutions: experimental basalt-seawater interaction in a seawater dominated system at 300°C, 500 bars. In: *Proc. Second Int. Sym. Water-Rock Interaction*, pp. 173-180, I.A.G.C. Strasbourg, France IV.

Seyfried, W. E. & Mottl, M. J., 1982. Hydrothermal alteration of basalt by seawater under seawater-dominated conditions. *Geochimica et Cosmochimica Acta*, **46**, 985-1002.

Sterner, S. M., Hall, D. L. & Bodnar, R. J., 1988. Synthetic fluid inclusions. V. Solubility relations in the system NaCl-KCl-$H_2O$ under vapor-saturated conditions. *Geochimica et Cosmochimica Acta*, **52**, 989-1005.

Ulrich, T., Golding, S. D., Kamber, B. S., Zaw, K., and Taube, A., 2002. Different mineralization styles in a volcanic-hosted ore deposit: the fluid and isotopic signatures of the Mt Morgan Au-Cu deposit, Australia. *Ore Geology Reviews*, **22**, 61–90.

# Chapter 5. Geochemistry of mafic rocks from IODP Holes U1309 B and D of the Atlantis Massif – 30°N: a study of strontium and oxygen isotopes.

## 5.1 Introduction

Hydrothermal circulation at Mid-Ocean Ridges exercises a control on the structure of the oceanic crust and interactions between fluids and rocks induced by this hydrothermal circulation control in part the chemical and isotopic composition of the oceanic crust and the ocean. Past studies have documented variations and changes in chemistry and mineralogy of basalts and sheeted dikes (Alt, *et al.*, 1996; Gillis, *et al.*, 2005; Teagle, *et al.*, 1998a; Teagle, *et al.*, 1998b; Teagle, *et al.*, 2003) and ophiolite complexes (Bickle & Teagle, 1992) during hydrothermal circulation. Studies quantifying the geochemical variations due to hydrothermal circulation in sections of oceanic crust dominated by gabbros and ± interlayered serpentinites are much less common (Delacour, *et al.*, 2008; McCaig, *et al.*, 2007). The Atlantis Massif is a perfect site to monitor fluid circulation into oceanic crust dominated by gabbros.

In this chapter, strontium and oxygen isotope data for gabbros and serpentinites of the Atlantis Massif, IODP Hole U1309B and D are presented. The difference in the Sr ratio between seawater (0.70916, 7.6 ppm (Hodell, *et al.*, 1991; Palmer & Edmond, 1989) and MORB (average = 0.70247 (Hart, *et al.*, 1974), 117 ppm for fresh basalt (Teagle, *et al.*, 1998b)) makes $^{87}Sr/^{86}Sr$ an excellent tracer for seawater alteration of oceanic crust. Interaction between fresh crustal rocks and seawater leads to an increase in the strontium isotope ratio of the rock. Oxygen isotopes exhibit large temperature dependent fractionations between fluids and minerals, such that oceanic crust altered at low temperature (<250°C) is generally enriched in $^{18}O$, while higher alteration temperature leads to depletion in $^{18}O$. Alteration

temperature is estimated using experimental fractionation curves that are calculated for individual minerals and water of $\delta^{18}O$ = 0‰ (seawater composition) (Bottinga & Javoy, 1973; Cole & Ripley, 1998; Saccocia, *et al.*, 1998; Saccocia, *et al.*, 2009; Wenner & Taylor, 1971; Zheng, 1993). The influence of the oxygen composition of the circulating fluid on the resulting $\delta^{18}O$ of the rock is discussed below (see *5.4.1*). Difference in oxygen isotopic compositions is also present between seawater and unaltered oceanic crust ($\delta^{18}O$ ~ 6‰).

Here, analyses of bulk rock isotopic composition and of separated micro samples are presented in order to better constrain the circulation of fluids into the oceanic crust at OCCs. Variations observed in micro-sample analyses show that secondary minerals in oceanic crust samples can be significantly more radiogenic than bulk rock. Data are then compared with published results from oceanic sections such as IODP Hole 735B (Hart, *et al.*, 1999), Hole 504B (Alt, *et al.*, 1996), anhydrite from TAG hydrothermal field 1 and 2 (Teagle, *et al.*, 1998b), and the 15°45'N massif (McCaig, *et al.*, 2010; McCaig, *et al.*, 2007).

Estimation of the amount of fluid that circulated in the Atlantis Massif was conducted using the approach of Bickle (1992) and Bickle and Teagle (1992). All these results and interpretations are compiled in a model for hydrothermal circulation at Atlantis Massif in which fluid flow is concentrated along the detachment fault. Hydrothermal fluids mainly circulate in the hanging wall of the detachment fault with local escape into the footwall. The TAG model suggested by deMartin *et al.* (2007) in which a detachment fault is deduced from the distribution of seismicity is used to better constrain hydrothermal circulation in the Atlantis Massif.

# 5.2 Analytical methodology

## 5.2.1 Analytical procedure for strontium isotopic measurement

Samples representative of different mineral assemblages and extent of alteration were selected for strontium analyses. They were reduced to powders after being rinsed with deionised water (18MΩ) and dried down with acetone. As isotopic analysis by Thermal Ionisation Mass Spectrometry (TIMS) requires the strontium to be analyzed in the form of a pure salt, minerals have to be decomposed and brought to solution in an appropriate acid before chemical separation.

### 5.2.1.1 Whole rock samples preparation procedure

The samples are weighed with an appropriate amount of $^{84}Sr$ spike. Powders were then left to dissolve in a 1:5 concentrated sub-boiling distilled nitric acid and 48% hydrofluoric acid mix. Following decomposition, fluorides were dissolved by treatment with concentrated $HNO_3$, followed by conversion to chloride and dissolution in 2.5M HCl. Strontium separated on cation exchange columns in 2.5M HCl and further purified by a second pass through the same column (details in *Appendix 4*).

### 5.2.1.2 Micro-drilled samples preparation procedure

Micro-samples were extracted from uncovered thin sections approximately 150 µm thick using a microscope-stage-mounted drill (manufactured by Ulrike Medenbach, Witten, Germany) which removes an annulus of material allowing core samples to be extracted. The diameter of samples was decided in advance depending on the mineral density and estimated Sr concentration. Samples were cleaned in dilute HCl and rinsed in water several times before dissolution.

Amounts of Sr were determined by isotope dilution with a $^{84}Sr$ spike. Concentrations are only known to *ca.* 10% due to uncertainties in sample weight which were calculated from optical estimates of sample volume. Samples were dissolved in 1:4 concentrated UpA $HNO_3$ and 48% UpA HF mix. Chemical separation is performed twice in Sr-spec columns as described in appendix 4.

Some of the samples were analysed for strontium isotope ratios at the National Oceanography Centre (NOC) in Southampton, UK. These samples are marked with a star in column 3, in *Table 5-2*.

#### 5.2.1.3 Dentist-drilled samples preparation procedure

Small samples were reduced to powder using a dentist drill. The same chemical treatment as for micro-drilled samples was used on these samples, except for the cleaning in dilute HCl. Composition of the powders is uncertain as more than one type of mineral can be included during drilling generating uncertainties on isotope ratio.

Some of these samples were also analysed for strontium isotope ratios at the National Oceanography Centre (NOC) in Southampton, UK, and are also marked with a star in column 3, in *Table 5-2*.

#### 5.2.1.4 Standards and uncertainties

At Leeds, Sr extract was loaded onto a tungsten filament using a $TaCl_5$ loading solution and analysed for strontium isotope ratio ($^{87}Sr/^{86}Sr$) in the Thermo-Finnigan Triton® TIMS. The mean value for the SRM 987 standard during bulk rock measurements was 0.710279 ± 0.000050 (N=8) and 0.710247 ± 0.000086 (N=20) for micro-sample measurements. Samples analysed at the NOC in Southampton were subject to the same analytical procedures and analysed using a VG/Micromass Sector 54 TIMS. The mean value for SRM 987 in Southampton was 0.710238 ± 0.000091 (N=8).

Sr isotope compositions were adjusted to be consistent with a SRM 987 value of 0.710248. Final data were corrected for $^{87}Rb$ and for blanks. The maximum $^{87}Rb$ correction affects the final $^{87}Sr/^{86}Sr$ composition at the fifth decimal only. Blank correction affects samples for which the Sr content is ≤ 1ng (amphiboles and pyroxenes) at the fourth or fifth decimal, and at the sixth decimal for other samples. Blanks of less than 100 pg Sr were difficult to obtain. The calculated error (presented as 2σ) incorporates errors in blank and spike corrections, the measured value of $^{85}Rb/^{86}Sr$, and the assumed values of $^{87}Rb/^{85}Rb$ (0.386 ± 5%). Sr concentration (in ppm) for micro-samples has to be used with caution as it is dependent on the estimation of

the sample weight that is calculated from the diameter and thickness of the annulus and the density of the mineral.

### 5.2.2 Analytical procedure for oxygen isotopic measurement

Samples that were analysed for strontium isotope ratios were also subject to oxygen isotope composition determination. Sample preparation and isotope composition were executed at the Scottish Universities Environmental Research Centre (SUERC) by Dr. Anthony Fallick. They are presented as $\delta$ values in per mil (‰) relative to Vienna Standard Mean Ocean Water (V-SMOW).

Samples were first reduced to powder (at least 50 mg) using a dentist drill at Leeds University before being chemically prepared at the SUERC. The powders were heated to 200°C overnight under high vacuum in order to remove interlayered and absorbed water. $\delta^{18}O$ values are determined by laser fluorination techniques (Macaulay, *et al.*, 2000). Powders were heated with a $CO_2$ laser in a $ClF_3$ atmosphere in order to extract the oxygen out of the powders. The resultant oxygen was purified and converted to $CO_2$. The yield was measured by a capacitance manometer. Oxygen isotope compositions of the $CO_2$ were measured by a dual-inlet mass spectrometer. Precision of measurements are ± 0.2‰ (1$\sigma$).

# 5.3 Results

## 5.3.1 Bulk rock Strontium and Oxygen variation

### 5.3.1.1 A downhole profile

Variations in strontium and oxygen compositions from whole rock samples are presented in *Table 5-1* and $^{87}Sr/^{86}Sr$ ratios as well as $\delta^{18}O$ are plotted against depth (*Figure 5-1*). Strontium isotope data presented here are a compilation of analyses done at the School of Earth and Environment in Leeds by the author and analyses collected at ETH Zurich by Adélie Delacour (Delacour, 2007; Delacour, *et al.*, 2008). These data have been published in an AGU Monograph (McCaig, *et al.*, 2010). All the Sr data lie between seawater ($^{87}Sr/^{86}Sr$ = 0.70916 (Palmer & Edmond, 1989); $\delta^{18}O$ = 0‰) and oceanic crust MORB ($^{87}Sr/^{86}Sr$ = 0.70247 (average of MORB values (Hart, *et al.*, 1974)); $\delta^{18}O$ = 6 (Gregory & Taylor, 1981)).

The first striking observation is the decreasing in strontium and oxygen isotope ratios with increasing depth indicating a decreasing effect of seawater, with the most intense alteration occurring in the first 400 mbsf. Note that depth here is not the depth of penetration of seawater since the core was ~ perpendicular to the detachment fault orientation at time of hydrothermal circulation; depth is therefore the distance away from the major detachment fault.

The second striking information is that there is a major difference in $^{87}Sr/^{86}Sr$ between mafic rocks and ultramafic rocks. Mafic rocks range from 0.70261 to 0.70429 and average at 0.70319, whereas ultramafic rocks give more radiogenic values in the upper part of the core with a minimum of 0.70687 and a maximum of 0.70904. Serpentinites deeper down in the core (~ 600 mbsf) show intermediate values (0.7052 and 0.7058) before unaltered igneous values at the bottom of the core (0.702964; 0.702909; 0.702745). A serpentinite at ~310 mbsf shows a relatively low strontium isotope ratio (0.703797). Late carbonates such as magnesite, calcite and dolomite have been observed in serpentinite (Blackman, *et al.*, 2006; Klein, 2010). The occurrence of such phase influences the isotopic composition of serpentinite,

and the elevated ratio showed by some ultramafic rocks may be the result of carbonates. A leaching experiment to test this has been undertaken and results are presented below (paragraph *5.3.3*; *Table 5-3*).

No obvious variation between mafic (1.44 to 5.62‰), and ultramafic rocks (1.38 to 4.64‰) is observed for oxygen. As no whole rock samples show $\delta^{18}O$ greater than the unaltered oceanic crust, alteration occurred at temperatures greater than 200-250°C (Shanks, 2003; Alt, *et al.*, 2007) (see discussion *5.4.1* below).

Variations in both $^{87}Sr/^{86}Sr$ and in $\delta^{18}O$ between the different mafic rocks are not obvious. Overlap between rock types is common (*Figure 5-1*). Olivine gabbros show nonetheless the widest range in $^{87}Sr/^{86}Sr$ (0.70262 to 0.70429) and in $\delta^{18}O$ (1.44 to 4.38‰). Diabases of the top 100 mbsf range for strontium from not altered (0.70268) to slightly altered (0.70328) and average 0.70294. They give $\delta^{18}O$ in the same range as troctolites (2.25 to 4.27‰). Talc tremolite schists and vein material (U1309B 11R-2 35-55 cm; *Figure 2-8D*) at the top of the core show elevated strontium isotope ratios (0.70448 to 0.70563) and are among the most altered for oxygen (two measurements: 1.41 and 1.93‰).

#### 5.3.1.2 Correlation between Sr and O isotopes

*Figure 5-2* shows plot of $^{87}Sr/^{86}Sr$ against Sr concentration (A) and against $\delta^{18}O$ (B). The $^{87}Sr/^{86}Sr$ - $\delta^{18}O$ plot show that there is a negative correlation between $^{87}Sr/^{86}Sr$ ratios and $\delta^{18}O$, with the most altered samples in terms of $^{87}Sr/^{86}Sr$ being generally the most altered in $\delta^{18}O$. This trend is obvious for gabbro samples and is not verified for diabase that show $\delta^{18}O$ values lower than some serpentinites with low value of $^{87}Sr/^{86}Sr$. *Figure 5-2A* shows no evident correlation between $^{87}Sr/^{86}Sr$ and the strontium concentration except for the serpentinites and talc-tremolite schists that are the most altered with the lowest strontium content. However the less altered serpentine show strontium content in the same order of magnitudes as the most altered ones. Strontium content of olivine gabbros is relatively constant whichever the strontium isotope ratio. One sample of olivine gabbro (U1309D

75R-2 77-80 cm) is however really high in strontium (334 ppm). This sample contains a leucocratic alteration vein with epidote. Gabbro samples seem to show a positive correlation.

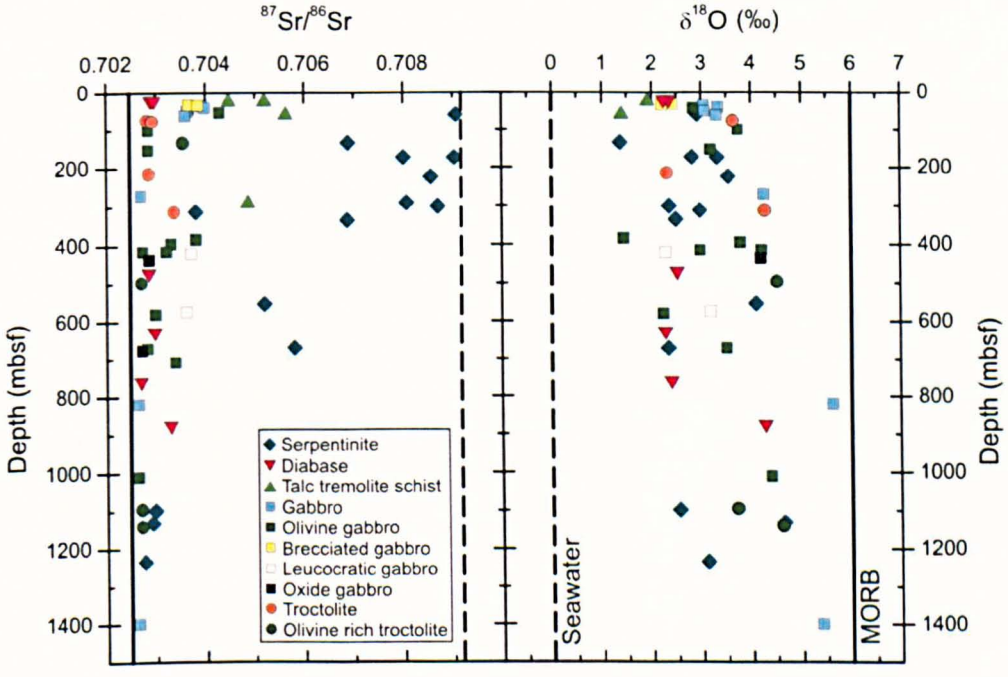


**Figure 5-1: Strontium and oxygen isotope ratio against depth in IODP Hole U1309D.Vertical lines represent seawater and MORB value. Note that two samples are from IODP Hole U1309B: a talc tremolite schist (B11R-2 62-66 cm) and a serpentinite (B11R-2 23-31 cm).**

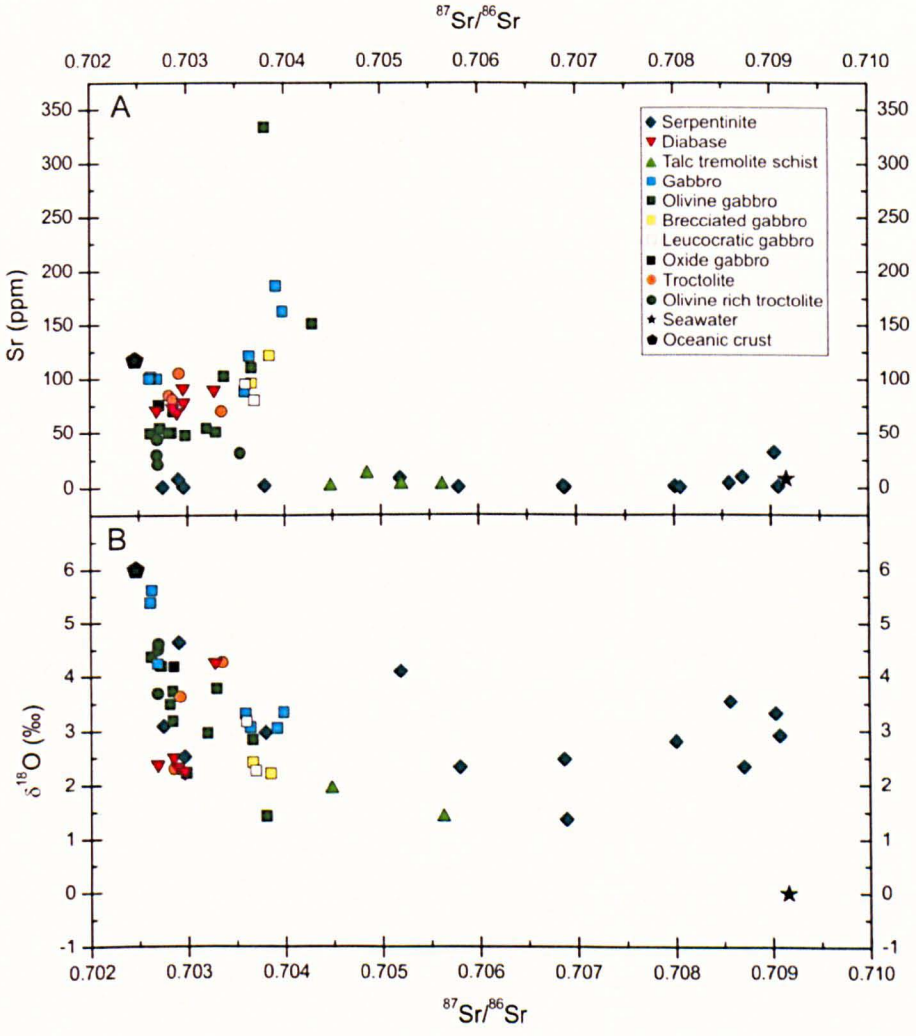


**Figure 5-2: A Sr contents against $^{87}Sr/^{86}Sr$ for bulk rock of IODP Hole U1309B and D all together. B Oxygen isotope compositions against $^{87}Sr/^{86}Sr$ ratios for bulk rock of IODP Hole B and D.**

**Table 5-1: Whole rock geochemical composition in Strontium and oxygen. Error at 2σ is given for $^{87}Sr/^{86}Sr$. * are data from Delacour (2007)**

| Sample number | Rock type | Sr content (ppm) | $^{87}Sr/^{86}Sr$ | Error (2 σ) | $\delta^{18}O$ (‰ V-SMOW) | Depth (mbsf) |
|---|---|---|---|---|---|---|
| B11R-2 23-31 | Serpentinite | 1.0 | 0.708862 | 0.000064 | 2.92 | 58.79 |
| B11R-2 62-66 | Talc schist | 1.8 | 0.705631 | 0.000096 | 1.41 | 59.14 |
| D1R-1 41-44 | Diabase | 69.0 | 0.702897 | 0.000010 | 2.35 | 20.93 |
| D1R-1 72-80* | Diabase | 91.5 | 0.702962 | 0.000011 | 2.25 | 21.26 |
| D1R-3 4-8* | Talc-schist | 2.0 | 0.704477 | 0.000014 | 1.93 | 23.33 |
| D4R-1 80-89 | Brecciated gabbro | 96.3 | 0.703667 | 0.000006 | 2.42 | 32.25 |
| D4R-1 135-137 | Brecciated gabbro | 121.8 | 0.703848 | 0.000010 | 2.22 | 32.76 |
| D4R-3 11-14 | Gabbro | 186.7 | 0.703914 | 0.000010 | 3.05 | 34.53 |
| D5R-3 22-28 | Gabbro | 162.7 | 0.703983 | 0.000110 | 3.34 | 39.57 |
| D6R-1 132-140 | Olivine gabbro | 110.7 | 0.703666 | 0.000010 | 2.84 | 42.16 |
| D7R-3 101-102 | Gabbro | 121.2 | 0.703641 | 0.000010 | 3.07 | 49.05 |
| D8R-2 56-59 | Olivine gabbro | 151.6 | 0.704287 | 0.000001 | - | 52.54 |
| D10R-1 127-129 | Gabbro | 88.2 | 0.703592 | 0.000010 | 3.31 | 61.48 |
| D12R-3 46-51 | Troctolite | 84.5 | 0.702810 | 0.000002 | 2.76 | 73.07 |
| D13R-2 8-22 | Troctolitic gabbro | 105.3 | 0.702915 | 0.000072 | 3.64 | 75.98 |
| D17R-2 9-17* | Olivine gabbro | 50.0 | 0.702841 | 0.000014 | 3.74 | 99.93 |
| D23R-2 29-36 | Olivine rich troctolite | 31.5 | 0.703544 | 0.000002 | - | 132.83 |
| D23R-2 98-101 | Serpentinite | 0.3 | 0.706890 | 0.000110 | | 133.49 |
| D27R-1 36-42.5 | Olivine gabbro | 50.6 | 0.702822 | 0.000028 | 3.19 | 152.69 |
| D31R-1 128-132 | Serpentinite | 1.2 | 0.708012 | 0.000128 | 2.81 | 172.80 |
| D31R-2 19-30* | Serpentinite | 32.0 | 0.709036 | 0.000011 | 3.32 | 173.21 |
| D40R-1 6-12 | Troctolite | 80.8 | 0.702854 | 0.000006 | 2.31 | 214.89 |
| D42R-1 0-8* | Serpentinite | 4.0 | 0.708571 | 0.000015 | 3.54 | 224.34 |
| D51R-4 30-38* | Gabbro | 86.0 | 0.702686 | 0.000011 | 4.25 | 271.02 |
| D56R-1 35-45 | Serpentinite | 0.4 | 0.708071 | 0.000656 | | 291.20 |
| D58R-1 22-25 | Serpentinite | 9.6 | 0.708707 | 0.000026 | 2.35 | 300.60 |
| D60R-3 35-45 | Serpentinite | 1.8 | 0.703797 | 0.000152 | 2.97 | 313.23 |
| D60R-3 35-45* | Troctolite | nd | 0.703354 | 0.000013 | 4.27 | 313.23 |
| D65R-2 22-30* | Serpentinite | nd | 0.706870 | 0.000079 | 2.48 | 335.40 |
| D75R-2 77-80 | Olivine gabbro | 334.1 | 0.703802 | 0.000010 | 1.44 | 383.83 |

**Table 5-1 continued**

| Sample number | Rock type | Sr (ppm) | $^{87}Sr/^{86}Sr$ | Error (2 σ) | $\delta^{18}O$ (‰ V-SMOW) | Depth (mbsf) |
|---|---|---|---|---|---|---|
| D77R-4 0-10 | Olivine gabbro | 50.6 | 0.703296 | 0.000010 | 3.78 | 395.37 |
| D83R-1 16-26* | Olivine gabbro | 54.0 | 0.702721 | 0.000013 | 4.20 | 415.21 |
| D83R-1 53-64* | Olivine gabbro | nd | 0.703202 | 0.000012 | 2.97 | 415.59 |
| D84R-2 8-17* | Oxide gabbro | nd | 0.703698 | 0.000012 | 2.27 | 421.01 |
| D87R2 63-71* | Oxide gabbro | 95.0 | 0.702857 | 0.000013 | 4.19 | 436.33 |
| D94R-3 46-48 | Diabase | 73.0 | 0.702849 | 0.000008 | 2.51 | 471.24 |
| D100R-1 42-46* | Olivine rich troctolite | 44.0 | 0.702688 | 0.000010 | 4.51 | 497.04 |
| D111R-4 25-26 | Serpentinite | 8.6 | 0.705194 | 0.000164 | 4.09 | 553.80 |
| D116R-1 58-68* | Oxide gabbro | nd | 0.703604 | 0.000013 | 3.17 | 574.03 |
| D117R-2 24-32 | Olivine gabbro | 47.8 | 0.702980 | 0.000010 | 2.23 | 579.69 |
| D127R-1 145-148 | Diabase | 78.3 | 0.702969 | 0.000010 | 2.27 | 627.67 |
| D136R-2 21-29 | Serpentinite | 0.2 | 0.705802 | 0.000118 | 2.33 | 671.01 |
| D136R-2 21-29* | Olivine gabbro | 29.0 | 0.702814 | 0.000012 | 3.50 | 671.01 |
| D137R-2 85-91* | Oxide gabbro | nd | 0.702709 | 0.000012 | | 676.48 |
| D144R-1 105-116 | Olivine gabbro | 102.9 | 0.703381 | 0.000001 | | 708.91 |
| D155R-2 68-72 | Diabase | 70.9 | 0.702684 | 0.000012 | 2.39 | 759.64 |
| D169R-1 90-100* | Gabbro | 101.7 | 0.702627 | 0.000012 | 5.62 | 819.00 |
| D180R-1 13-17 | Diabase | 89.6 | 0.703281 | 0.000010 | 4.27 | 875.95 |
| D210R-1 43-46 | Olivine gabbro | 49.7 | 0.702622 | 0.000008 | 4.38 | 1010.85 |
| D227R-3 6-12* | Olivine rich troctolite | 29.8 | 0.702686 | 0.000013 | 3.70 | 1095.02 |
| D228R-2 18-22 | Serpentinite | 0.8 | 0.702973 | 0.000172 | 2.53 | 1098.20 |
| D235R-2 100-114 | Serpentinite | 7.6 | 0.702909 | 0.000342 | 4.64 | 1131.80 |
| D237R-2 6-18* | Olivine rich troctolite | 21.0 | 0.702693 | 0.000010 | 4.61 | 1140.64 |
| D256R-3 88-93 | Serpentinite | 0.6 | 0.702745 | 0.000072 | 3.10 | 1233.76 |
| D292R-2 78-88* | Gabbro | nd | 0.702614 | 0.000012 | 5.39 | 1398.68 |

## 5.3.2 Micro-sample Sr and O isotope variation

Micro-sample data for $^{87}Sr/^{86}Sr$ and $\delta^{18}O$ are summarised in *Table 5-2* and are plotted against depth for both holes U1309B and D in *Figure 5-3*.

Results show that igneous plagioclase and clinopyroxene range from a MORB-like strontium isotope ratio of 0.70260 to slightly altered value of 0.70348 for plagioclase and from 0.70256 to 0.70302 for clinopyroxene. Sr concentration in igneous plagioclase (generally of bytownitic composition - see *Figure 2-9*) is typically ~100 ppm (*Table 5-2*). Some samples (plagioclase 3 [$An_{35}$] and 4 [$An_{80}$] from a troctolite - U1309D 12R-3 46-51 cm) show suspiciously high concentration (*e.g.* 500 ppm). Low Sr concentration (*e.g.* plagioclase $An_{30}$ and $An_{50}$ of sample U1309D 144R-1 105-116 cm) can be explained by loss of material during transfer and/or washing. However, these uncertainties in Sr concentrations do not mean that the strontium isotope ratios cannot be trusted.

Actinolite replacing pyroxene exhibits intermediate ratios ranging from 0.70366 to 0.70410 and is significantly more radiogenic than the whole rock composition (*Figure 5-5*). Even if the Sr fraction analysed is usually small (<1ng; *e.g.* U1309D 117R-2 24-32 cm - *Table 5-2*), the consistency in actinolite strontium isotope ratios makes the values truthful.

Epidote vein shows also intermediate ratio in sample U1309D 75R-2 77-80 cm (0.70389, average of 3 samples). This sample is a coarse-grained gabbro cut by a leucocratic dike with epidote (*Figure 2-5I*). Plagioclase is fairly unaltered except close to the epidote where albite is present. Secondary minerals consist of actinolite after pyroxene and chlorite after plagioclase. Titanite and zircon are accessory minerals associated to the leucocratic dike.

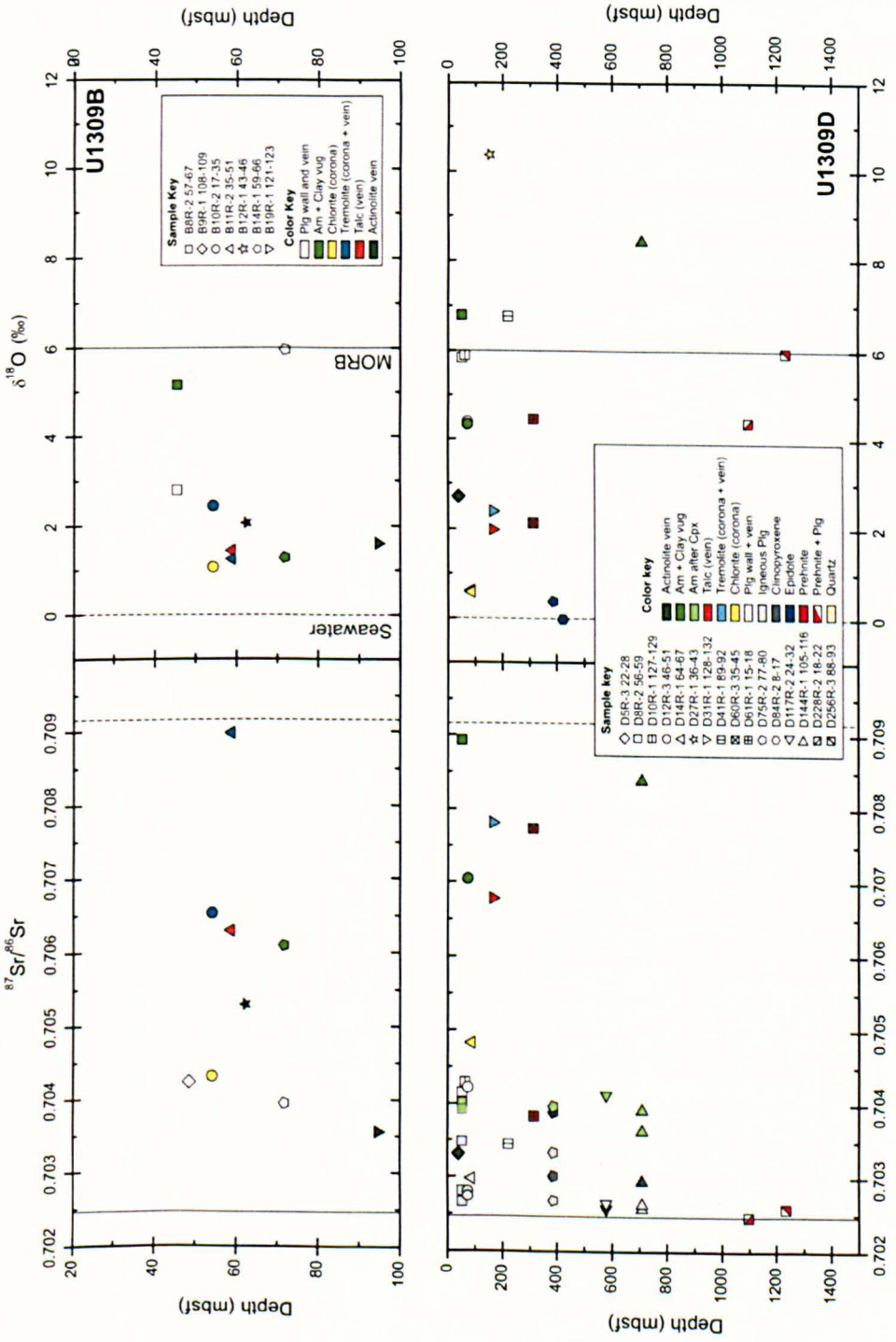


**Figure 5-3: Micro-sample $^{87}Sr/^{86}Sr$ and $\delta^{18}O$ plotted against depth for both Hole U1309B and U1309D.**

Ratios approaching seawater isotopic composition have been found in actinolite ± clay vug veins (*Figure 2-6 and Figure 2-7*) (0.70608 to 0.70893 - Figure 5-3; average of 4 samples = 0.70762) of gabbro samples (U1309B 14R-1 59-66, U1309D 8R-2 56-59, U1309D 12R-3 46-51 and U1309D 144R-1 105-116) with coarse-grained plagioclase of bytownitic composition and clinopyroxene replaced by actinolite. (*Figure 2-9 and 2-10, appendix 1*). White bleached walls related to actinolite vugs are composed of plagioclase (albite + $An_{40}$ in a ~50:50 proportion) + randomly orientated and actinolite needles. Plagioclase of these walls shows elevated $^{87}Sr/^{86}Sr$ ratios compare to igneous plagioclase (0.70414 to 0.70416). Data also suggest that plagioclase is less radiogenic away from the vugs (*Figure 5-4* and *Figure 5-5*).

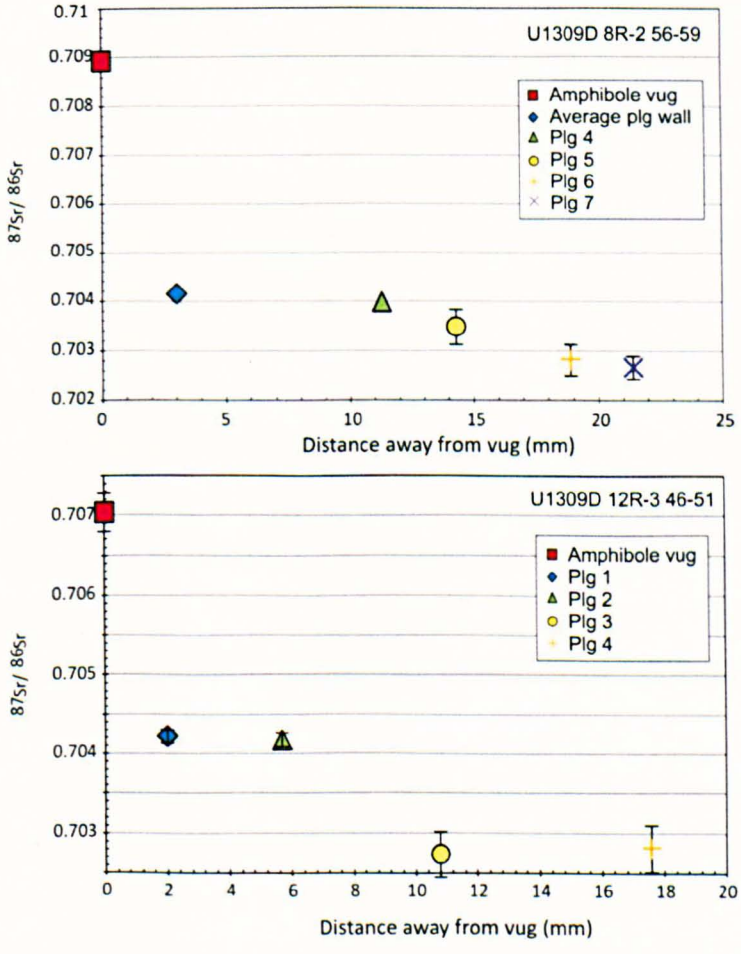


**Figure 5-4: Strontium isotopic composition of minerals away from amphibole + clay vugs in sample U1309D 8R-2 56-59 cm and U1309D 12R-3 46-51 cm. Errors are indicated when possible.**

Sample U1309B 11R-2 35-51 cm is a serpentinite cut by a talc tremolite vein (*Figure 2-8D*). This sample shows a zone of green tremolite and pale talc replacing serpentinised harzburgite. This zone has undergone reverse shear along talc-rich horizons, but the margin of talc alteration against serpentinite is unsheared, overprinting the pre-existing serpentinite foliation defined by magnetite seams and serpentine ribbons. The zone tapers upward in the present orientation and has an outer talc-rich zone with an isotropic fabric replacing serpentinite and an inner tremolite-rich zone with highly schistose talc bands. Dark grains within the talc alteration are bastites containing serpentine + magnetite assemblages (Blackman, *et al.*, 2006).

Elevated $^{87}Sr/^{86}Sr$ ratios are also found in this sample. Serpentine (whole rock - *Table 5-1*) and tremolite give seawater-like values (0.709077 and 0.709018 respectively). Talc that occurs as replacement of serpentine gives intermediate ratio (0.706288) (*Figure 5-3*, *Figure 5-6A* and *Table 5-2*).

Samples U1309B 10R-2 17-35 cm and U1309D 14R-1 64-67 cm are olivine gabbros showing corona texture (*Figure 2-4D* and *Figure 2-5F*). In corona texture, plagioclase is replaced by chlorite and olivine is replaced by tremolite at the contact between plagioclase and olivine (*Figure 5-6B*). The tremolite rim (sample U1309B 10R-2 17-35 cm; *Table 5-2*) around olivine gives an elevated ratio (0.70652) and chlorite replacing plagioclase a much lower but nonetheless intermediate ratio (0.70458 = average of 2 measurements in sample U1309B 10R-2 17-35 cm and U1309D 14R-1 64-67 cm; *Table 5-2*). The relatively high strontium concentration of chlorite in sample U1309B 10R-2 17-35 cm makes this analysis doubtful. Relic plagioclase in sample U1309D 14R-1 64-67 cm still shows an igneous value (0.70297) (*Table 5-2*; *Figure 5-6 B*).

Prehnite from micro-rodingite samples give a range of strontium isotope ratios. Only sample U1309D 60R-3 35-45 cm of the four is certified to be 100% prehnite because it is the only one to have been micro-drilled from a thin section analysed in SEM and the microprobe. Sample U1309D 60R-3 35-45 cm is a troctolite that is altered at ~80% with olivine being replaced by serpentine + magnetite and plagioclase altered to prehnite (see electron microprobe analyses in *Appendix 1*) and is rimmed by chlorite. Micro-

rodingites are described in *Chapter 2 and 4* (refer to *Figure 2-4G* and *Figure 4-21*). Prehnite in sample U1309D 60R-3 35-45 cm shows elevated $^{87}Sr/^{86}Sr$ ratios (0.707736; *Table 5-2* and *Figure 5-6C*). Other samples containing prehnite have been reduced to powder using a dentist drill and mineralogy can therefore not been certified to be 100 % prehnite. Ratios indicate that the powder might be contaminated by "fresh" plagioclase that has not been replaced. This is the case for samples U1309D 228R-2 18-22 cm and U1309D 256R-3 88-93 cm recovered deep down in the core (at depth of 1000 mbsf) that show igneous value. XRD analyses show that the powders contain prehnite (~30%), Ca-plagioclase (~45%), and serpentine. Sample U1309D 61R1 15-18 cm for which the XRD analyses shows only 25% of prehnite, 60% of garnet, and 15% of serpentine has a strontium isotope ratio of 0.703835.

Oxygen data for micro-samples are summarised in *Figure 5-3* in a plot against depth and in *Table 5-2*. All samples except four show oxygen isotope compositions that scatter between modern seawater composition (0‰) and unaltered oceanic crust composition (6‰). Results show that amphibole + clay vugs have high $\delta^{18}O$ values (4.33 to 8.45‰) except for one sample (U1309B 14R01 59-66 cm) which shows a much lower $\delta^{18}O$ (1.29‰). Plagioclases of bleached walls show value of ~5‰ (U1309B 14R-1 59-66 cm; U1309D 8R-2 56-59 cm; U1309D 12R-3 46-51 cm). Plagioclases in vein give similar results (U1309B 9R-1 108-109 cm; U1309D 10R-1 127-129 cm; U1309D 41R-1 89-92 cm). Amphiboles in vein (U1309B 12R-1 43-46 cm; U1309B 19R-1 121-123 cm; U1309D 5R-3 22-28 cm) give lower $\delta^{18}O$ than amphiboles in vugs. One quartz sample (U1309D 27R-1 36-43 cm) shows elevated $\delta^{18}O$ (10.38‰).

**Table 5-2: Micro-samples geochemical composition in Strontium and oxygen. Error at 2σ is given for $^{87}Sr/^{86}Sr$. Samples marked by a star were analysed at NOC in Southampton.**

| Sample number | Rock type | Mineral | XRD | Drill type | Sr analysed (ng) | Sr (ppm) | $^{87}Sr/^{86}Sr$ | Error (2 σ) | $\delta^{18}O$ (‰) | Depth (mbsf) |
|---|---|---|---|---|---|---|---|---|---|---|
| B8R-2 57-67 | Gabbro | Am + Clay? vug | | Micro | - | - | - | - | 5.16 | 45.29 |
| | | Plg wall | | Micro | - | - | - | - | 2.79 | 45.29 |
| B9R-1 108-109 | Gabbro | Plg (VEIN) | | Micro | 82.2 | 20.5 | 0.704240 | 0.000034 | 5.34 | 48.58 |
| B10R-2 17-35 | Gabbro | Tremolite (corona) | | Micro | 10.3 | 2.5 | 0.706521 | 0.000104 | 2.44 | 54.13 |
| | | Chlorite (corona) | | Micro | 84.2 | 12.2 | 0.704322 | 0.000052 | 1.08 | 54.13 |
| B11R-2 35-51 | Serpentinite | Serpentine | | Dentist | 21.1 | 2.9 | 0.709077 | 0.000292 | 1.43 | 58.90 |
| | | Tremolite (VEIN) | | Dentist | 207.9 | 35.0 | 0.708976 | 0.000104 | 1.26 | 58.90 |
| | | Talc (VEIN) | | Dentist | 2.1 | 0.4 | 0.706288 | 0.000166 | 1.45 | 58.90 |
| B12R-1 43-46 | Diabase | Am (VEIN) | | Micro | 25.5 | 2.8 | 0.705287 | 0.000044 | 2.06 | 62.00 |
| B14R-1 59-66 | Gabbro | Am + Clay vug | X | Micro | 52.6 | 4.7 | 0.706082 | 0.000088 | 1.29 | 71.73 |
| | | Plg wall | | Micro | 477.4 | 238.7 | 0.703957 | 0.000018 | 5.95 | 71.73 |
| B16R-1 33-44 | Brcc gabbro | Matrix | | Dentist | 123.0 | 34.2 | 0.704361 | 0.000018 | 5.69 | 80.68 |
| B19R-1 121-123 | Diabase | Am (VEIN) | | Dentist | 39.9 | 12.1 | 0.703560 | 0.000026 | 1.59 | 95.20 |
| D5R-3 22-28 | Gabbro | Am (VEIN) | | Micro | 5.6 | 2.0 | 0.703314 | 0.000110 | 2.71 | 39.57 |
| | | Plg wall | | Micro | 40.3 | 125.0 | 0.703980 | 0.000028 | 4.90 | 39.57 |
| D8R-2 56-59 | Olivine gabbro | Am + Clay vug | X | Micro | 5.6 | 4.1 | 0.708931 | 0.000036 | 6.79 | 52.54 |
| | | Plg wall 1 | | Micro | 89.1 | 115.0 | 0.704161 | 0.000016 | - | 52.54 |
| | | Plg wall 2 | | Micro | 89.4 | 132.7 | 0.704139 | 0.000012 | - | 52.54 |
| | | Plg wall 3 | | Micro | 86.9 | 118.2 | 0.704157 | 0.000012 | - | 52.54 |
| | | Average Plg wall | | Micro | 88.5 | 122.0 | 0.704152 | 0.000013 | 5.84 | 52.54 |
| | | Plg 4 | | Micro | 106.0 | 152.0 | 0.703981 | 0.000016 | - | 52.54 |
| | | Plg 5* | | Micro | 4.5 | 110.4 | 0.703476 | 0.000352 | - | 52.54 |
| | | Plg 6* | | Micro | 3.7 | 108.7 | 0.702814 | 0.000312 | - | 52.54 |
| | | Plg 7* | | Micro | 5.1 | 101.3 | 0.702665 | 0.000232 | - | 52.54 |
| | | Actinolite 1* | | Micro | 2.4 | 4.3 | 0.704015 | 0.000160 | - | 52.54 |
| | | Actinolite 2* | | Micro | 0.9 | 10.9 | 0.703925 | 0.000436 | - | 52.54 |
| D10R-1 127-129 | Gabbro | Plg + Am (VEIN) | X | Dentist | 334.6 | 128.7 | 0.704292 | 0.000026 | 5.89 | 61.50 |
| | | Am | | Dentist | - | - | - | - | 0.39 | 61.50 |
| D12R-3 46-51 | Troctolite | Am vug* | | Micro | 1.5 | 11.7 | 0.707041 | 0.000240 | 4.33 | 73.06 |
| | | Plg wall 1* | | Micro | 16.7 | 558.0 | 0.704220 | 0.000084 | 4.38 | 73.06 |
| | | Plg wall 2* | | Micro | 30.5 | 117.0 | 0.704172 | 0.000086 | - | 73.06 |

**Table 5-2 continued**

| Sample number | Rock type | Mineral | XRD | Drill type | Sr analysed (ng) | Sr (ppm) | $^{87}Sr/^{86}Sr$ | Error (2 σ) | $\delta^{18}O$ (‰) | Depth (mbsf) |
|---|---|---|---|---|---|---|---|---|---|---|
| D12R-3 46-51 | Troctolite | Plg 3* | | Micro | 3.5 | 500.1 | 0.702735 | 0.000282 | - | 73.06 |
| | | Plg 4* | | Micro | 7.5 | 381.3 | 0.702811 | 0.000290 | - | 73.06 |
| D14R-1 64-67 | Olivine gabbro | Tremolite (corona) | | Micro | - | - | - | - | 0.62 | 80.05 |
| D14R-1 64-67 | Olivine gabbro | Chlorite (corona) | | Micro | 1.6 | 1.0 | 0.704830 | 0.000170 | 0.59 | 80.05 |
| | | Plagioclase | | Micro | 23.9 | 75.0 | 0.702975 | 0.000240 | - | 80.05 |
| D27R-1 36-43 | Olivine gabbro | Quartz (VEIN) | | Dentist | - | - | - | - | 10.38 | 153.12 |
| D31R-1 128-132 | Serpentinite | Tremolite (VEIN) | | Dentist | 4.3 | 0.8 | 0.707811 | 0.000140 | 2.39 | 172.80 |
| | | Talc (VEIN) | | Dentist | 2.4 | 0.4 | 0.706779 | 0.000180 | 1.99 | 172.80 |
| D41R-1 89-92 | Troctolite | Plg-Am (VEIN) | | Dentist | 34.8 | 5.3 | 0.703447 | 0.000026 | 6.76 | 220.40 |
| D60R-3 35-45 | Troctolite | Prehnite* | | Micro | 13.5 | 800.0 | 0.707736 | 0.000284 | 2.13 | 313.24 |
| D61R-1 15-18 | Ol-rich troct | Prehnite + Garnet + Serp | X | Dentist | 5.2 | 4.4 | 0.703835 | 0.000078 | 4.45 | 315.00 |
| D75R-2 77-80 | Olivine gabbro | Epidote 1 (VEIN) | | Micro | 44.2 | 289.6 | 0.703900 | 0.000038 | - | 383.83 |
| | | Epidote 2* (VEIN) | | Micro | 148.6 | 1000.0 | 0.703876 | 0.000534 | - | 383.83 |
| | | Epidote 3* (VEIN) | | Micro | 88.8 | 808.0 | 0.703887 | 0.000082 | - | 383.83 |
| | | Average Epidote | | Micro | 93.9 | 699.2 | 0.703888 | 0.000218 | 0.39 | 383.83 |
| | | Plg 1 | | Micro | 34.3 | 126.9 | 0.702685 | 0.000028 | - | 383.83 |
| | | Plg 2 | | Micro | 19.9 | 210.6 | 0.703336 | 0.000028 | - | 383.83 |
| | | Actinolite | | Micro | 0.7 | 3.1 | 0.703966 | 0.000362 | - | 383.83 |
| | | Clinopyroxene | | Micro | 0.5 | 2.6 | 0.703018 | 0.000496 | - | 383.83 |
| | | Calcite* | | Micro | 8.5 | 26.6 | 0.704513 | 0.000280 | - | 383.83 |
| | | Apatite | | Micro | 6.3 | 22.3 | 0.702823 | 0.000056 | - | 383.83 |
| D84R-2 8-17 | Oxide gabbro | Epidote (VEIN) | | Dentist | - | - | - | - | -0.03 | 421.00 |
| D117R-2 24-32 | Olivine gabbro | Plg (corona) | | Micro | 14.9 | 97.0 | 0.702639 | 0.000026 | - | 579.69 |
| | | Actinolite | | Micro | 0.7 | 2.8 | 0.704102 | 0.000288 | - | 579.69 |
| | | Clinopyroxene | | Micro | 2.3 | 3.2 | 0.702556 | 0.000184 | - | 579.69 |
| D140R-2 57-60 | Diabase | Altered diabase | | Dentist | 52.7 | 6.9 | 0.705569 | 0.000014 | 3.08 | 690.10 |
| D144R-1 105-116 | Olivine gabbro | Am + Clay? vug | | Micro | 1.1 | 1.5 | 0.708419 | 0.000386 | 8.45 | 708.91 |
| | | Plg (albite) | | Micro | 4.3 | 29.2 | 0.703072 | 0.000040 | - | 708.91 |
| | | Plg (An30) | | Micro | 8.2 | 76.1 | 0.702658 | 0.000026 | - | 708.91 |
| | | Plg (An50) | | Micro | 18.5 | 82.6 | 0.702601 | 0.000022 | - | 708.91 |

**Table 5-2 continued**

| Sample number | Rock type | Mineral | XRD | Drill type | Sr analysed (ng) | Sr (ppm) | $^{87}Sr/^{86}Sr$ | Error (2 σ) | $\delta^{18}O$ (‰) | Depth (mbsf) |
|---|---|---|---|---|---|---|---|---|---|---|
| | | Actinolite 1 | | Micro | 2.4 | 1.4 | 0.703662 | 0.000264 | 3.52 | 708.91 |
| | | Actinolite 2 | | Micro | 3.6 | 2.3 | 0.703946 | 0.000172 | - | 708.91 |
| | | Clinopyroxene | | Micro | 15.1 | 3.5 | 0.702968 | 0.000050 | - | 708.91 |
| D228R-2 18-22 | Ol-rich troct | Prehnite + Plg + Serp | X | Dentist | 1.3 | 0.2 | 0.702469 | 0.000278 | 4.38 | 1098.20 |
| D256R-3 88-93 | Ol-rich troct | Prehnite + Plg + Serp | X | Dentist | 211.7 | 70.6 | 0.702582 | 0.000024 | 5.96 | 1233.80 |

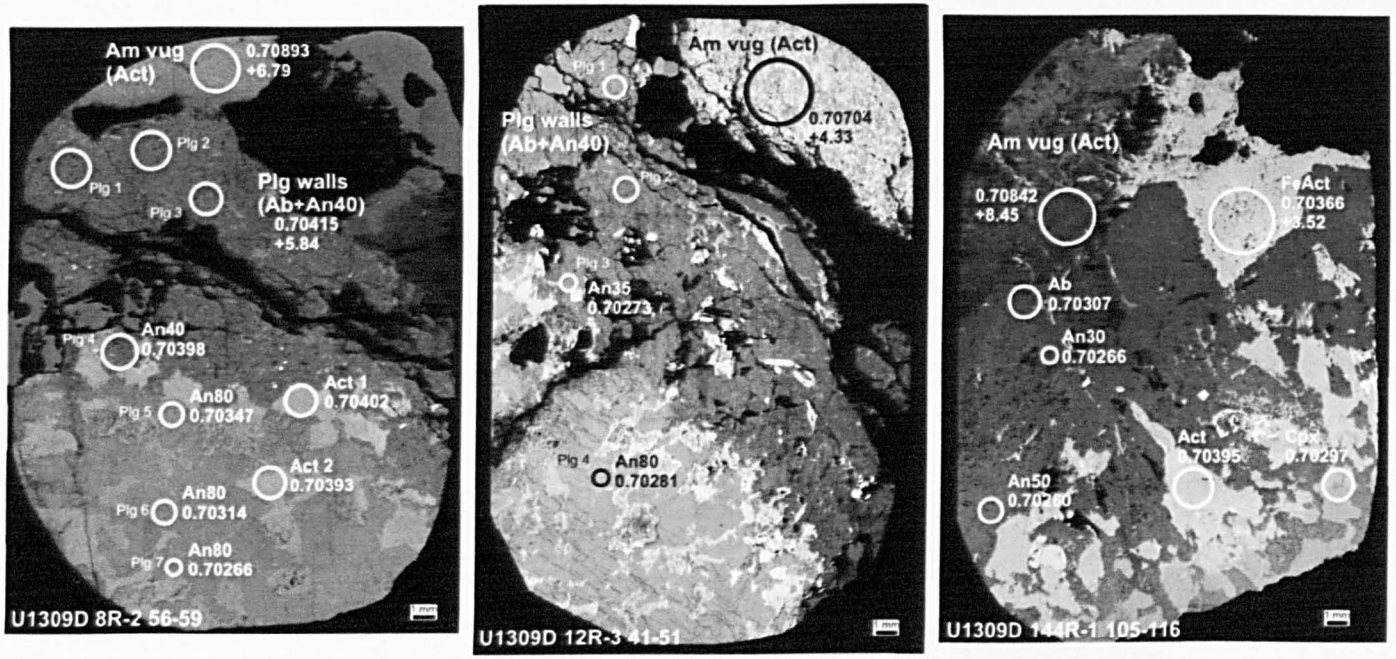


**Figure 5-5: Backscatter electron microphotographs montages. All 3 samples show actinolite vugs with white plagioclase walls, together with host rock. Am = amphibole; Act = actinolite; Plg = plagioclase; Ab = albite; An = anorthite; FeAct = ferroactinolite; Cpx = clinopyroxene.**

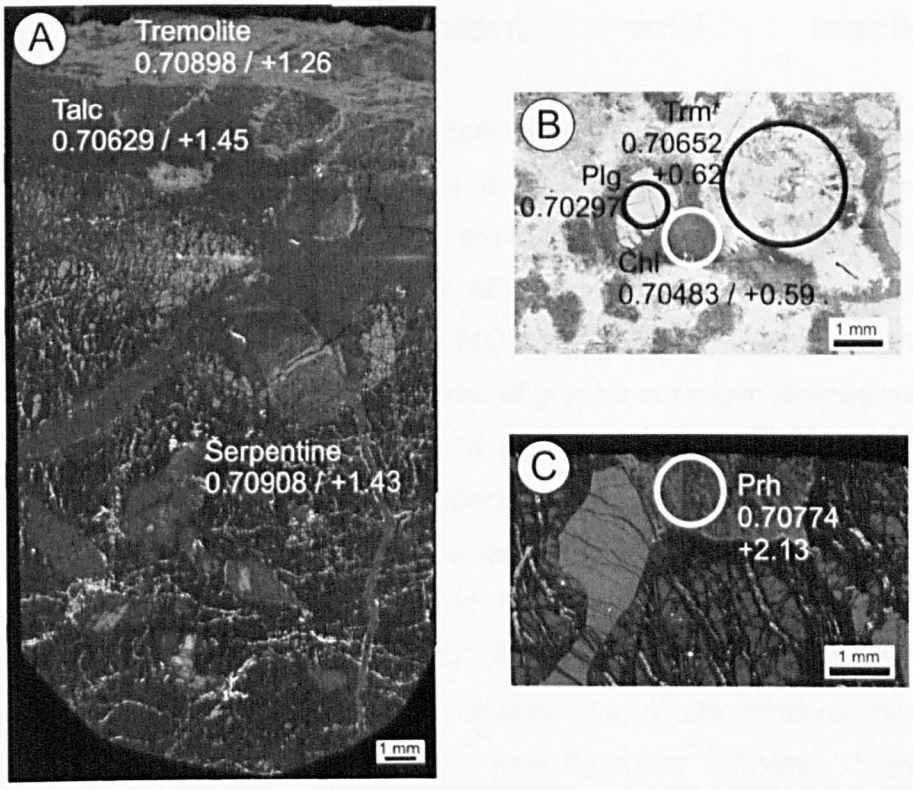


**Figure 5-6: Backscatter electron microphotograph montages. A: Serpentinite with a talc tremolite vein running through it. Samples were reduced to powders using a dentist drill on this sample in order to generate enough powder for strontium and oxygen analyses. Locations of actual sampling are therefore not included in the montage (U1309B 11R-2 35-51 cm). B: Olivine gabbro (U1309D 14R-1 64-67 cm) showing corona texture with chlorite replacing plagioclase and tremolite replacing olivine. $^{87}Sr/^{86}Sr$ of the tremolite (marked with a star *) was analysed from an other sample that shows corona texture (U1309B 10R-2 17-35 cm). C: Micro-rodingite showing alteration of plagioclase into prehnite (U1309D 60R-3 35-45 cm).**

### 5.3.3 Carbonate content and leaching experimentation

In this section, the influence of late carbonate on isotopic compositions of serpentinite samples is assessed. Serpentinites are the result of alteration of an ultramafic protolith with low Sr content and a strontium isotope ratio representative of oceanic crust samples (MORB = 0.70247 average of typical range for MORB (Barrett & Friedrichsen, 1982; Hart, *et al.*, 1974)), modified by seawater of greater strontium isotope ratio of 0.70916 (Hodell, *et al.*, 1991; Palmer & Edmond, 1989). Interaction at any fluid flux between those two end members will lead to serpentinite with a low Sr content and a high strontium isotope ratio. It is true for serpentinites of the upper part of the core (*Figure 5-1* and *Table 5-1*). However, Sr content is sometimes relatively high (Sample U1309D 31R-2 19-30cm, Sr = 32 ppm; *Table 5-1*). This is difficult to explain unless serpentinite contains minerals that are rich in strontium and that can therefore influence both the concentration and the strontium isotope ratio. Magnesite, calcite and dolomite have been found by electron microprobe and described in the literature (Blackman, *et al.*, 2006; Klein, 2010).

A leaching experiment (details in *Appendix 5*) was conducted on one serpentinite sample that showed relatively high strontium content (Sample U1309D 31R-2 19-30cm, Sr = 32 ppm; *Table 5-1*) in order to assess the influence of potential carbonate content. Results are summarised in *Table 5-3*. 95% of the Sr of the initial powder was removed after the leaching step. The leached serpentine shows 0.1 ppm Sr and is comparable to analyses on serpentinite of oceanic crust. The leachate strontium isotope ratio is greater than that of the leached serpentine (0.708208 against 0.707941). Compared to the bulk analysis previously done, greater difference between the strontium isotope ratios was expected. However, both analyses were not conducted on the same powders. There is also a significant difference between the calculated integrated strontium concentration from the leaching experiment and the strontium concentration of the original bulk analysis. This might be the result of a highly heterogeneous distribution of the strontium, which might concentrate in veins.

This experiment shows that Sr isotope analyses of serpentinite samples from the upper part of the core are influenced by the presence of late carbonate veins. Results show also that the leached serpentine still has a relatively elevated strontium isotope ratio with a low strontium content (0.1 ppm). Nonetheless, nothing in this experiment allows to certify that the 0.1 ppm of strontium in the leached serpentine are not even more carbonate that have not been leached during the experimental procedure. However, prehnite (sample U1309D 60R-3 35-45 cm) also has an elevated strontium isotope ratio (0.707736; *Table 5-2*). Prehnite and serpentine are coeval in micro-rodingites (Frost, *et al.*, 2008), and this indicates that the serpentinising fluid was close to seawater strontium isotopic composition.

**Table 5-3: Leaching experiment result of sample U1309D 31R-2 19-30 cm.**

| Nature of sample | Sample weight before analyses (g) | Sr analysed (ng) | Mass balance | Sr content (ppm) | $^{87}Sr/^{86}Sr$ | 2σ error |
|---|---|---|---|---|---|---|
| Serpentinite bulk rock | - | - | - | 32.0 | 0.709036 | 0.000011 |
| Leached serpentine | 0.0095 | 0.95 | 5% | 0.10 | 0.707941 | 0.000298 |
| Leachate | | 19.99 | 95% | | 0.708208 | 0.000028 |
| Leached serpentine + leachate | 0.0128 | 20.94 | - | 1.6 | 0.708196 | 0.000069 |

## 5.3.4 Comparison with literature dataset

*Figure 5-7* shows a comparison of our data with those from the 15°45'N massif which was drilled during cruise JR63, and composed of peridotites intruded by a gabbro body in the footwall of a fault zone of talc schist rocks (MaCaig, *et al.*, 2007), Hole 504B drilled in sheeted dikes of the EPR (East pacific Rise – fast spreading crust) (Alt, *et al.*, 1996), Hole 735B drilled in deformed gabbros of an OCC of the SWIR (Hart, *et al.*, 1999), and with serpentinites of the southern wall of the Atlantis Massif (Boschi, *et al.*, 2008). Anhydrite samples from TAG 1 and 2 (Teagle, *et al.*, 1998b) are also plotted for comparison with the serpentinite high value of strontium isotope ratio (see below).

Samples from 15°45'N show a negative correlation that is more pronounced than Atlantis Massif samples with a trend towards seawater that is remarkable (McCaig, *et al.*, 2007). Talc schists are more altered in both strontium and oxygen than Atlantis Massif ones and show strontium isotope ratios close to seawater composition comparable to IODP Hole U1309D serpentinites. Diabases are slightly more altered in strontium and show lower $\delta^{18}O$. Our gabbros show a wider range both in oxygen and in strontium. Sheeted diabases of Hole 504B show the same degree of alteration in terms of strontium as our diabases but do not show such low $\delta^{18}O$ (Alt, *et al.*, 1996). Gabbros from ODP Hole 735B show much less alteration in strontium isotopes. The range in oxygen isotopes is however equivalent (Hart, *et al.*, 1999). Serpentinites of the southern wall of the Atlantis Massif at the Lost City hydrothermal field site show elevated strontium isotope ratios close to seawater composition (Delacour, *et. al.*, 2008) similar to the two most altered serpentinite samples. However, unlike serpentinites of the IODP Hole U1309B and D, all serpentinites of the southern wall show elevated strontium isotope ratios (Boschi, *et al.*, 2008). The range in oxygen isotope composition is also much wider in the southern wall than in the IODP cores.

Anhydrite samples from TAG (Teagle, *et al.*, 1998b) show elevated strontium isotope ratios comparable to our serpentinite, amphibole vugs and prehnite. Two amphibole vugs are greater in strontium isotope composition for the same range of oxygen isotope composition. Amphibole vugs and prehnite that show similar $^{87}Sr/^{86}Sr$ are however much lower in $\delta^{18}O$ than anhydrite from TAG.

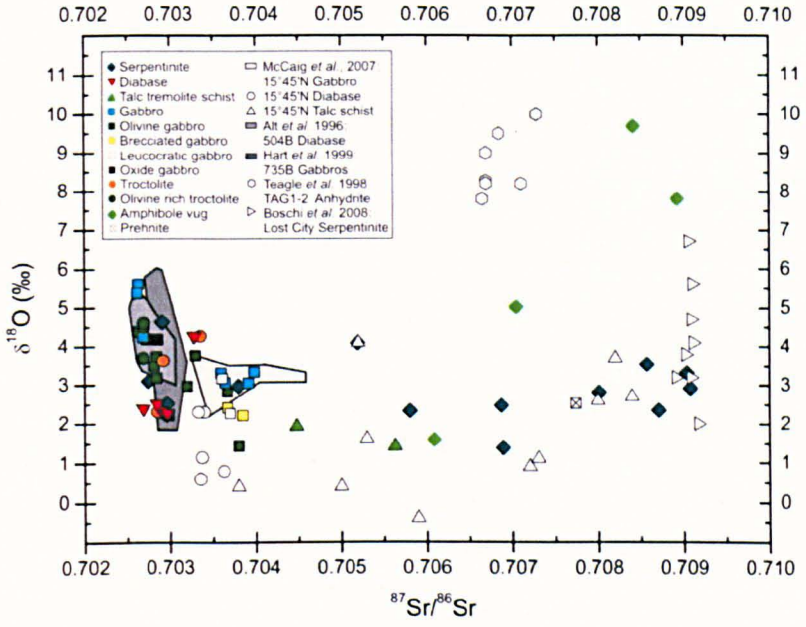


**Figure 5-7: Comparison of $^{87}Sr/^{86}Sr$ versus $\delta^{18}O$ of whole rock from IODP Hole U1309B and D with data from 15°45'N (McCaig, *et al.*, 2007), Hole 504B (Alt, *et al.*, 1996), Hole 735B (Hart, *et al.*, 1999), and serpentinites from the southern wall of the Atlantis Massif (Boschi, *et al.*, 2008). A few micro-samples are also plotted for comparison with anhydrite (Teagle, *et al.*, 1998b).**

# 5.4 Discussion

## 5.4.1 Temperatures of isotopic alteration

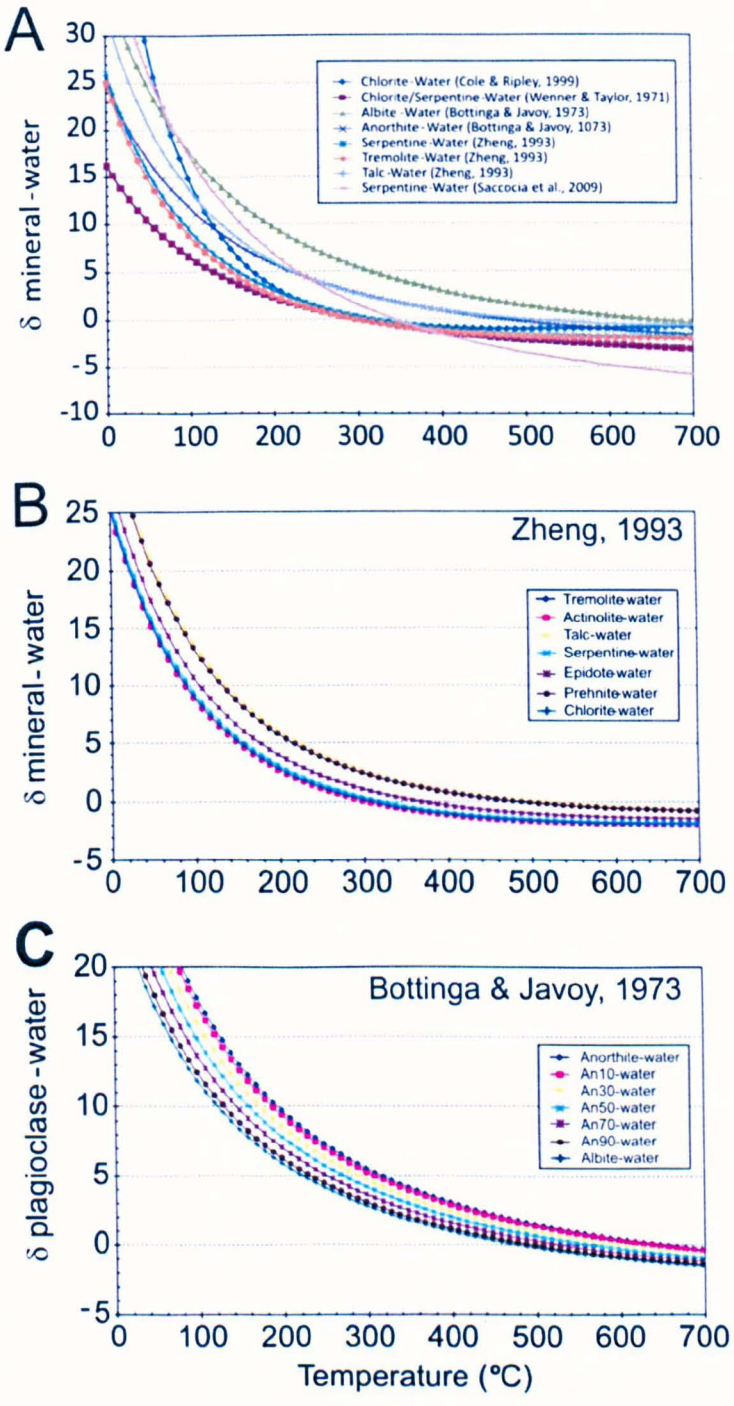


**Figure 5-8: A: Oxygen isotope fractionation curves for different thermometers from the literature. B: Oxygen fractionation curves for different minerals in Zheng (1993); C: Oxygen fractionation curves for plagioclase (Bottinga & Javoy, 1973)**

Oxygen isotopes have a large temperature dependent fractionation. Several experimental studies were carried out to calibrate interaction of minerals with water at different temperatures (*Figure 5-8*). In *Figure 5-8A*, the fractionation curves show disagreement in the delta of mineral-water value for a range in temperature between calibration of the same thermometer. Serpentine – water interaction for instance has been intensly studied (Saccocia, *et al.*, 1998; Saccocia, *et al.*, 2009; Wenner & Taylor, 1971; Zheng, 1993). Estimation of the alteration temperature can be significantly different (shift of 50°C can be observed – see *Figure 5-9*) depending on the equation used. Calculations in this study were done for micro-samples assuming a fluid circulating that is seawater, characterised by $\delta^{18}O$ = 0‰ and are summarised in *Table 5-6*. The influence of the altering fluid oxygen composition is discussed below where a comparison of temperature of alteration of serpentinites obtained with seawater (0‰) and a seawater-derived fluid (1‰ and 2‰) is shown in *Figure 5-9*. Seawater-derived fluid of $\delta^{18}O$ = 1 and 2 ‰ are used to be in agreement with hydrothermal fluids composition (1.7‰) (Shanks III, *et al.*, 1995).

#### 5.4.1.1 Alteration temperatures from whole rocks

Whole rock $\delta^{18}O$ values never exceed that of the unaltered oceanic crust, indicating of alteration occurring at temperatures greater than 200-250°C (Shanks, 2003; Alt, *et al.*, 2007). $\delta^{18}O$ values of serpentinite indicate a minimum alteration temperature of 250°C using the serpentinite-water fractionation curve of Zheng (*1993*) and 360°C using the fractionation curve of Saccocia *et al.* (*2009*). Alteration generating talc-tremolite schist occurred at 230°C (Zheng, 1993) if the schist is 100% tremolite and at 360°C (Saccocia, *et al.*, 2009; Zheng, 1993) if the schist is composed of talc only. Intermediate composition of schist will shift the alteration temperature between those two end members.

### 5.4.1.2 Alteration temperatures from small samples

*Figure 5-3* shows variation of $\delta^{18}O$ for micro-sample with depth. All but four samples show oxygen isotope compositions that scatter between seawater (0‰) and fresh oceanic crust (6‰). Note that hydrothermal fluids have $\delta^{18}O$ = 1.7‰ (Shanks III, *et al.*, 1995).

#### *5.4.1.2.1 Amphibole + clay vugs and amphibole veins*

Results of calculations of alteration temperature show that amphibole + clay vugs (composition determined on shipboard and at Leeds by XRD – see *Figure 2-7*) precipitated at low temperature (between 100 and 160°C and between 115 and 180°C with an evolved fluid $\delta^{18}O$ water of +1‰) (*Figure 5-8B*). One vug sample (U1309B 14R-1 59-66 cm) shows much lower $\delta^{18}O$ (1.29‰) that indicates a higher alteration temperature (245°C). Clays shift the $\delta^{18}O$ towards heavy values. They are assumed to be a late alteration of the amphiboles at low temperature (~100°C). In sample U1309B 14R-1 59-66 cm, clays may not have been included in the powder analysed for oxygen (XRD measurement on shipboard on this sample states clays as possible traces; in other amphibole + clay vugs, clays are stated as minor phases), giving different results to the other amphibole + clay vugs, and a better approximation of amphibole alteration temperature prior to clay alteration. Mass balance calculations are presented in *Table 5-4* and *Table 5-5*. Calculations were made assuming formation of amphibole at 400°C or 300°C using calibration of Zheng (1993) giving $\delta^{18}O$ of -1‰ and 0‰ respectively and formation of chlorite at ~100°C for different calibration curves. Results imply that the percentage of chlorite must be low for sample U1309B 14R-1 59-66, but unreasonably high for other amphibole + clay vugs, indicating that clays could have formed at even lower temperature than 100°C.

Bleached walls related to the amphibole + clay vugs are altered at higher temperature (290 to 400°C) (*Figure 5-8C*).

Amphiboles in vein (U1309B 12R-1 43-46, U1309B 19R-1 121-123, U1309D 5R-3 22-28) precipitate at higher temperature than amphiboles in vugs (200-230°C) (*Figure 5-8B*).

**Table 5-4: Mass balance calculation for the lightest amphibole vug $\delta^{18}O$ = 1.3‰.**

| Lightest amphibole vug $\delta^{18}O$=1.3‰ | Chlorite at ~100°C (Wenner and Taylor, 1971) $\delta^{18}O$=6.5‰ | Chlorite at ~100°C (Zheng,1993) $\delta^{18}O$=9‰ | Chlorite at ~100°C (Cole & Ripley, 1999) $\delta^{18}O$=14‰ |
|---|---|---|---|
| Amphibole (400°C) $\delta^{18}O$=-1‰ | 35% | 25% | 16% |
| Amphibole (300°C) $\delta^{18}O$=0‰ | 20% | 14% | 9% |

**Table 5-5: Mass balance calculation for the heaviest amphibole vug $\delta^{18}O$ = 8.5‰**

| Lightest amphibole vug $\delta^{18}O$=8.5‰ | Chlorite at ~100°C (Wenner and Taylor, 1971) $\delta^{18}O$=6.5‰ | Chlorite at ~100°C (Zheng,1993) $\delta^{18}O$=9‰ | Chlorite at ~100°C (Cole & Ripley, 1999) $\delta^{18}O$=14‰ |
|---|---|---|---|
| Amphibole (400°C) $\delta^{18}O$=-1‰ | - | - | 68% |
| Amphibole (300°C) $\delta^{18}O$=0‰ | - | 95% | 61% |

#### *5.4.1.2.2 Corona textures*

In corona texture, chlorite grows as an alteration product at varying temperature ranging from 245°C to 260°C for sample U1309B 12R-2 17-35 and from 270°C to 280°C for sample U1309D 14R-1 64-67 (Cole & Ripley, 1998; Wenner & Taylor, 1971; Zheng, 1993) (*Table 5-6*, *Figure 5-8A and B*). Tremolite grows as an alteration product at a temperature of 200°C (U1309B 12R-2 17-35) to 265°C (U1309D 14R-1 64-67) (Zheng, 1993) (*Figure 5-8B*). Coronas were inferred to form at temperatures >400°C (Nozaka & Fryer, 2011) indicating that the fluid that circulated at the time of corona formation was unlikely to be a fluid of seawater isotopic composition. Strontium isotope ratios of corona minerals attest for this (*Table 5-2*). According to Zheng (1993), Cole and Ripley (1999) and Wenner and Taylor (1971), the fluid

generating the corona formation at > 400°C must have had $\delta^{18}O$ between 1 and 2‰ for the replacement of plagioclase by chlorite and at least 3‰ for the replacement of olivine by tremolite. However, fluids with different oxygen isotopic composition would mean that corona texture forms in two steps with two different circulating events. This being unlikely, it is probable that the calibration curves are wrong.

#### *5.4.1.2.3 Quartz vein*

One quartz sample (U1309D 27R-1 36-43) shows elevated $\delta^{18}O$ indicating of alteration/precipitation temperature of 210°C (Zheng, 1993) or 250°C (Bottinga & Javoy, 1973). These temperatures agree with temperatures of homogenisation measured on fluid inclusions of quartz vein presented in *Chapter 3.*

#### *5.4.1.2.4 Serpentinites and micro-rodingites*

Prehnite (U1309D 60R-3 35-45) replaced plagioclase in micro-rodingite at temperatures >300°C (*Figure 5-8B; Table 5-6*). This agrees with estimation of temperature of formation for micro-rodingite at temperatures <350°C (Frost, *et al.*, 2008).

*Figure 5-9* shows that the estimated temperature of alteration increases if the fluid is assumed to have already interacted with the rock. During alteration, rocks are losing $^{18}O$ and the fluid is gaining the loss of the rock in exchange. This consequence is more significant with the Zheng equation than for the Saccocia *et al.* equation for serpentinite. A serpentine with the lowest $\delta^{18}O$ of our samples (1.38‰ - U1309B 11R-2 35-51 cm) would have been altered at ~250°C with seawater, but at ~300°C with a fluid for which $\delta^{18}O$ = 1‰, and 370°C with a fluid for which $\delta^{18}O$ = 2‰ using the Zheng (1993) fractionation curves. The same serpentine would have been altered at 295°C with seawater, but at ~320°C and 355°C with a fluid for which $\delta^{18}O$ = 1 and 2‰ using the Saccocia *et al.* (2009) fractionation curves respectively. *Table 5-7* shows a comparative analysis of the alteration temperature of prehnite and serpentine using different properties of the circulating fluid and the two different calibration curves of Zheng (1993) and Saccocia *et al.* (2009) in order to check on the prehnite and serpentine timing

relationship. Results show that unless we consider only the lowest $\delta^{18}O$ value of serpentinites with the Saccocia *et al.* (2009) calibration and seawater circulating in the rock, it is difficult for prehnite and serpentine to be coeval. This is very unlikely, and the conclusion to that matter is that the calibration curves are probably wrong.

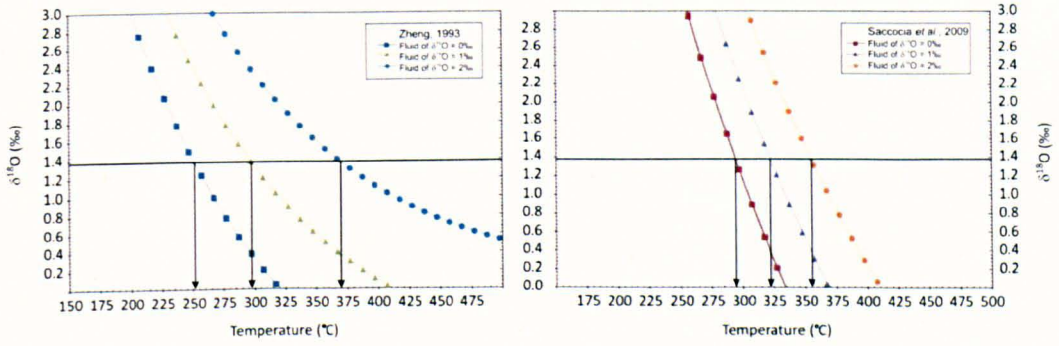


**Figure 5-9: Serpentine – water fractionation curves from Zheng (*1993*) and from Saccocia *et al.* (*2009*). Fractionation is here calculated with seawater, a fluid for which $\delta^{18}O$ = 1‰, and a fluid for which $\delta^{18}O$ = 2‰. $\delta^{18}O$ used here for the serpentine is the minimum value found in our samples (1.38 ‰ – U1309B 11R-2 35-51 cm).**

### 5.4.1.3 Conclusions

- It is unlikely that fluid of seawater oxygen isotopic composition is the altering fluid of gabbros of IODP Hole U1309B and D.
- It is unlikely that the fluid that circulated at the time of corona formation and replacement of clinopyroxene by amphibole in the greenschist and amphibolite facies is a fluid of seawater oxygen isotopic composition. These fluids are representative of hydrothermal fluid oxygen isotopic composition with $\delta^{18}O$ of 1.7‰ - (Shanks III, *et al.*, 1995), and might be comprised between 1 and 2‰.
- It is likely that the fluid circulating in amphibole + clay vugs and in serpentinites and in micro-rodingites is a fluid of seawater isotopic composition (strontium and oxygen).
- Results for corona textures and serpentinites + associated micro-rodingites show that calibration curves are probably wrong.

**Table 5-6: O isotope data for micro-samples and nominal alteration temperature in °C assuming equilibrium with seawater. Calculations are made using published equations (Bottinga & Javoy, 1973; Cole & Ripley, 1998; Saccocia, *et al.*, 2009; Wenner & Taylor, 1971; Zheng, 1993)**

| Sample Nb | Mineral | $\delta^{18}O$ (‰) | Bottinga & Javoy | Saccocia | Zheng | Cole & Ripley | Wenner & Taylor | Comment |
|---|---|---|---|---|---|---|---|---|
| B8R-2 57-67 | Am vug | 5.16 | | | 150 | | | Actinolite+clay |
| | Plg wall | 2.79 | 350-410 | | | | | An50-Ab |
| | Amphibole | 3.17 | | | 185 | | | Actinolite |
| B9R-1 103-108 | Plg | 5.34 | 210-300 | | | | | An-Ab |
| B10R-2 17-35 | Chlorite (corona) | 1.08 | | | 255 | 260 | 245 | Corona |
| | Tremolite (corona) | 2.44 | | | 200 | | | Corona |
| B11R-2 35-51 | Talc (VEIN) | 1.45 | | 360 | 365 | | | |
| | Tremolite (VEIN) | 1.26 | | | 240 | | | |
| | Serpentine | 1.43 | | 290 | 250 | 245 | 230 | |
| B11R-2 62-66 | Talc-Trm Schist | 1.41 | | -/360 | 230/365 | | | Trm/Talc |
| B12R-1 43-46 | Am(VEIN) | 2.06 | | | 210 | | | Actinolite |
| B14R-1 59-66 | Plg wall | 5.95 | 250/285 | | | | | An40/Ab |
| | Am vug | 1.29 | | | 245 | | | Actinolite+clay? |
| B16R-1 33-44 | Yellowish vein | 5.69 | | 260/- | 210/150 | -/165 | -/110 | Talc/Chl |
| B19R-1 121-123 | Am (VEIN) | 1.59 | | | 230 | | | Actinolite |
| D5R-3 22-28 | Am (Dk green) | 2.71 | 120 | | 200 | | | Actinolite |
| | Plg | 4.90 | 260-310 | | | | | An60-Ab |
| D8R-2 56-59 | Am vug | 6.79 | | | 120 | | | Actinolite+clay |
| | Plg wall | 5.84 | 290/250 | | | | | An40/Ab |
| D10R-1 127-129 | Plg (VEIN) | 5.89 | 285 | | | | | Ablbite |
| | Amphibole patch | 0.39 | | | 280 | | | Actinolite |
| D12R-3 46-51 | Am vug | 4.33 | | | 160 | | | Actinolite+clay |
| | Plg wall | 4.38 | 300/340 | | | | | An40/Ab |
| D14R-1 64-67 | Tremolite (corona) | 0.62 | | | 265 | | | Corona |
| | Chlorite (corona) | 0.59 | | | 275 | 280 | 270 | Corona |
| D23R-2 98-101 | Serpentine | 1.38 | | 270 | 250 | 250 | 235 | |
| D27R-1 36-43 | Quartz (VEIN) | 10.38 | 250 | | 210 | | | |
| D31R-1 128-132 | Tremolite (VEIN) | 2.29 | | | 205 | | | |
| | Talc (VEIN) | 1.99 | | | 330 | | | |
| | Serpentine | 2.81 | | 260 | 205 | 210 | 180 | |
| D41R-1 89-92 | Plg (VEIN) | 6.76 | 260 | | | | | Albite |

**Table 5-4 continued**

| Sample Nb | Mineral | $\delta^{18}O$ (‰) | Bottinga & Javoy | Saccocia | Zheng | Cole & Ripley | Wenner & Taylor | Comment |
|---|---|---|---|---|---|---|---|---|
| D60R-3 35-45 | Prehnite | 2.13 | | | 310 | | | |
| | Serpentine | 2.97 | | 255 | 205 | 210 | 180 | |
| D61R-1 15-18 | Prehnite + Garnet +Serp | 4.45 | | | 230 | | | |
| D75R-2 77-80 | Epidote | 0.39 | | | 335 | | | |
| D84R-2 8-17 | Epidote | -0.03 | | | 367 | | | |
| D111R-4 25-26 | Serpentine | 4.09 | | 235 | 175 | 190 | 150 | |
| D136R-2 21-29 | Serpentine | 2.33 | | 270 | 220 | 220 | 200 | |
| D140R-2 57-60 | Hyd alt diabase | 3.08 | | | 195 | 205 | 175 | Chlorite |
| D144R-1 105-116 | Am vug | 8.45 | | | 100 | | | Actinolite+clay |
| | Amphibole | 3.52 | 100 | | 180 | | | Actinolite |
| D228R-2 18-22 | Serpentine | 2.53 | | 265 | 215 | 220 | 190 | |
| | Prehnite + Plg + Serp | 4.38 | | | 235 | | | |
| D235R-2 100-114 | Serpentine | 4.64 | | 220 | 165 | 180 | 135 | |
| D247R-1 128-133 | Serpentine | 2.73 | | 260 | 210 | 210 | 185 | |
| D256R-3 88-93 | Serpentine | 3.10 | | 250 | 200 | 205 | 175 | |
| | Prehnite + Plg + Serp | 5.96 | | | 195 | | | |

**Table 5-7: Alteration temperature of prehnite and serpentine in °C for different properties of circulating fluid and calibration curves**

| Sample | Mineral | $\delta^{18}O$ (‰) | Zheng (1993) $\delta^{18}O$=0‰ | Zheng (1993) $\delta^{18}O$=1‰ | Zheng (1993) $\delta^{18}O$=2‰ | Saccocia *et al.* (2009) $\delta^{18}O$=0‰ | Saccocia *et al.* (2009) $\delta^{18}O$=1‰ | Saccocia *et al.* (2009) $\delta^{18}O$=2‰ |
|---|---|---|---|---|---|---|---|---|
| D23R-2 98-101 | Serpentine | 1.38 | 250 | 300 | 370 | 295 | 320 | 355 |
| D235R-2 100-114 | Serpentine | 4.64 | 165 | 185 | 215 | 225 | 246 | 264 |
| Mean | Serpentine | 3.04 | 200 | 228 | 265 | 255 | 278 | 303 |
| D60R-3 35-45 | Serpentine | 2.97 | 201 | 230 | 268 | 256 | 279 | 305 |
| | Prehnite | 2.13 | 312.5 | 370 | 466 | - | - | - |

### 5.4.2 Model for hydrothermal circulation in the Atlantis Massif

In this section, hydrothermal circulation in the Atlantis Massif is modelled using the TAG hydrothermal cross section (*Figure 5-10*) interpreted from seismicity by deMartin *et al.* (2007). It is assumed that lithologies beneath the TAG field are similar to the ones in the central dome of the Atlantis Massif and that circulation of fluid is focused onto the fault zone as suggested by the strontium and oxygen isotope profiles (*Figure 5-1* and *Figure 5-3*).

Circulation in the fault zone converts peridotites into talc tremolite schist as described for the OCC from 15°45' N (McCaig, *et al.*, 2007) at a depth of ~7-8 km and equilibrium between fluid and rock is reached. However, this reaction involves an increase in the silica activity (Yardley, B., pers. comm.) implying that the fluids have already reacted with silicate rocks (gabbros) at higher temperatures.

Limited amount of fluid escapes into the first 300 mbsf of the footwall and preferential alteration of clinopyroxene of gabbros by amphiboles at temperature <400°C occurs.

Corona textures form at a similar depth (~6-7 km) but at temperature of 400-500°C. However, according to the interpretation of the TAG model (McCaig, *et al.*, 2010), fluids in the footwall are buffered at 400°C along the detachment fault. None of our samples show such high temperature of alteration, with inferred temperatures ranging between 250°C and 300°C (*Table 5-6*). Those temperatures are however estimated assuming a seawater-like fluid with $\delta^{18}O$ of 0‰. In order to get the fluid along the detachment fault buffered at 400°C, fluid circulating in the fault zone must be seawater derived fluid that has evolved to a more negative composition (equivalent to black smoker vent fluids - 1.7‰; see *5.4.1*).

Later on, seawater of the recharge zone circulates through veins and amphibole vugs (sample U1309B 14R-1 59-66, U1309D 8R-2 57-67; *Figure 2-6*) at a temperature of 300-350°C and reaches ultramafic layers to alter

them into serpentinites (see *5.4.4.3*) when the hole is in the low angle part of the fault and further from the vent site (*Figure 5-10B*). Beyond this point, both fault zone and footwall cool rapidly below 300°C.

Circulation of seawater-like fluid alters plagioclase into prehnite in micro-rodingite at depth ≥ 300 mbsf and olivine into serpentine at temperatures of ~300-350°C.

The upper part of the hole is currently below the zeolite facies in terms of temperatures with zeolite veins only developing at depth greater than 700 mbsf.

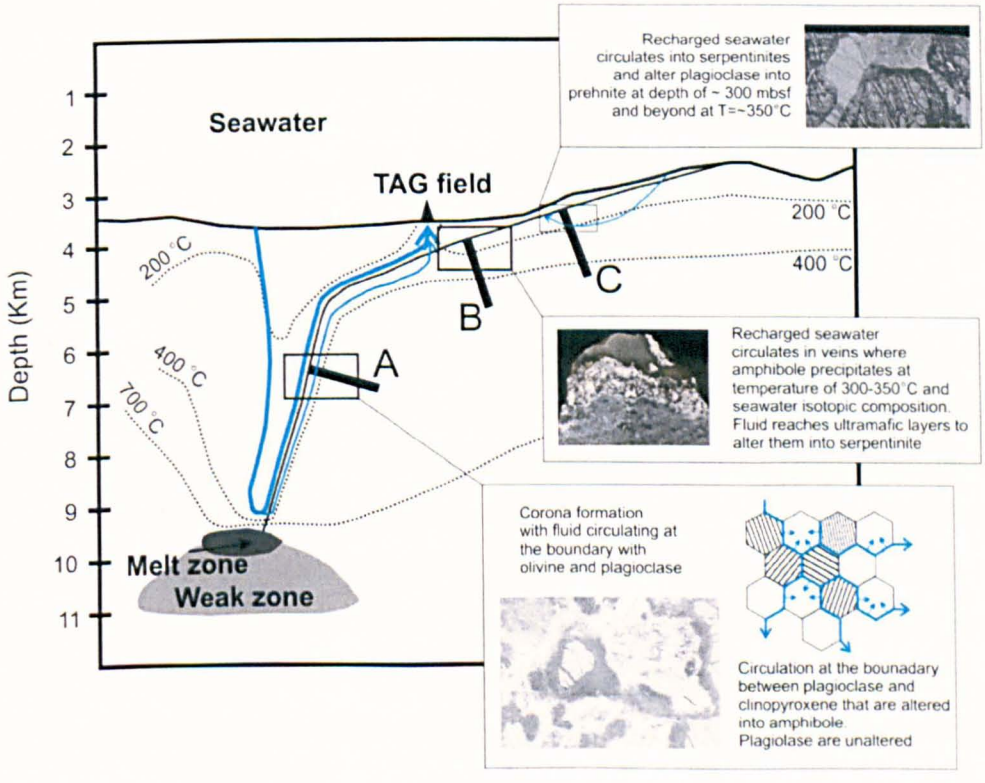


**Figure 5-10: Interpreted cross section at TAG showing fluid flow through IODP Hole U1309D. Blue arrows show fluid flow along the detachment fault. Thickness of the arrows represents the importance of the flux. The fluid flux is greater in the hanging wall than in the footwall. Ultramafic rocks are altered into talc schist in the hanging wall and the fault zone. Circulation in the footwall is limited in the first 300-500 m. A: Gabbros are altered with circulation at the boundary between plagioclase and clinopyroxene that are altered into amphibole and troctolites are altered with circulation at the boundary between plagioclase and olivine to form corona texture. B: Ultramafic layers are altered into serpentinites by fluids that circulate into veins where amphibole precipitates at low temperature. C: Plagioclase are altered into prehnite by recharged seawater.**

## 5.4.3 Transport of Strontium and Oxygen in the oceanic crust

### 5.4.3.1 Water/rock ratio

Water/rock ratios based on mass balance calculations assuming isotopic equilibrium were first applied to stable isotope (Taylor, 1977) and to strontium isotope budgets (Spooner, *et al.*, 1977) as follow:

$$W/R = \frac{X_{rock}\,(r^{i}_{rock} - r^{f}_{rock})}{X_{fluid}(r^{f}_{rock} - r^{i}_{fluid})}, \qquad \text{Equation 5-1}$$

where W/R is the water/rock ratio in a closed system, W the mass of hydrothermal fluid, R the mass of rock being altered, $X_{rock}$ and $X_{fluid}$ the concentration of the rock and the fluid of the element in question respectively, and r the isotope ratio of the element with i being the initial ratio and f the final ratio. In an open system, water/rock ratio is modelled by the integration of the closed system equation (Albarède, 1995).

Water/rock ratios are based on the assumption that fluid and rock have the same isotope composition at equilibrium for strontium (Albarède, *et al.*, 1981). Calculations have been done using seawater end member (7.6 ppm Sr and $^{87}Sr/^{86}Sr$ = 0.70916, (Palmer & Edmond, 1989)), MORB end member for mafic rocks ($^{87}Sr/^{86}Sr$ = 0.70247) and the average of the olivine-rich troctolites as end member for ultramafic rocks ($^{87}Sr/^{86}Sr$ = 0.70269). Results of water/rock calculations for bulk rock are summarised in *Table 5-8*. Results show that conditions are generally rock dominated for mafic rocks except for the ones that show high strontium content, and more likely to be fluid dominated for ultramafic rocks showing elevated strontium isotope ratio.

**Table 5-8: Water/rock ratio for bulk rock samples of IODP Hole U1309B and D.**

| Sample number | Rock type | Sr (ppm) | $^{87}Sr/^{86}Sr$ | W/R |
|---|---|---|---|---|
| B11R-2 23-31 | Serpentinite | 1.0 | 0.708862 | 2.7 |
| B11R-2 62-66 | Talc schist | 1.8 | 0.705631 | 0.2 |
| D1R-1 41-44 | Diabase | 69.0 | 0.702897 | 0.6 |
| D1R-1 72-80* | Diabase | 91.5 | 0.702962 | 1.0 |
| D1R-3 4-8* | Talc-schist | 2.0 | 0.704477 | 0.1 |
| D4R-1 80-89 | Brecciated gabbro | 96.3 | 0.703667 | 2.8 |
| D4R-1 135-137 | Brecciated gabbro | 121.8 | 0.703848 | 4.2 |
| D4R-3 11-14 | Gabbro | 186.7 | 0.703914 | 6.8 |
| D5R-3 22-28 | Gabbro | 162.7 | 0.703983 | 6.3 |
| D6R-1 132-140 | Olivine gabbro | 110.7 | 0.703666 | 3.2 |
| D7R-3 101-102 | Gabbro | 121.2 | 0.703641 | 3.4 |
| D8R-2 56-59 | Olivine gabbro | 151.6 | 0.704287 | 7.4 |
| D10R-1 127-129 | Gabbro | 88.2 | 0.703592 | 2.3 |
| D12R-3 46-51 | Troctolite | 84.5 | 0.702810 | 0.6 |
| D13R-2 8-22 | Troctolitic gabbro | 105.3 | 0.702915 | 1.0 |
| D17R-2 9-17* | Olivine gabbro | 50.0 | 0.702841 | 0.4 |
| D23R-2 29-36 | Olivine rich troctolite | 31.5 | 0.703544 | 0.8 |
| D23R-2 98-101 | Serpentinite | 0.3 | 0.706890 | 0.1 |
| D27R-1 36-42.5 | Olivine gabbro | 50.6 | 0.702822 | 0.4 |
| D31R-1 128-132 | Serpentinite | 1.2 | 0.708012 | 0.7 |
| D31R-2 19-30* | Serpentinite | 32.0 | 0.709036 | 215.9 |
| D40R-1 6-12 | Troctolite | 80.8 | 0.702854 | 0.6 |
| D42R-1 0-8* | Serpentinite | 4.0 | 0.708571 | 5.3 |
| D51R-4 30-38* | Gabbro | 86.0 | 0.702686 | 0.4 |
| D56R-1 35-45 | Serpentinite | 0.4 | 0.708071 | 0.2 |
| D58R-1 22-25 | Serpentinite | 9.6 | 0.708707 | 16.8 |
| D60R-3 35-45 | Serpentinite | 1.8 | 0.703797 | 0.0 |
| D60R-3 35-45* | Troctolite | nd | 0.703354 | - |
| D65R-2 22-30* | Serpentinite | nd | 0.706870 | - |
| D75R-2 77-80 | Olivine gabbro | 334.1 | 0.703802 | 10.9 |
| D77R-4 0-10 | Olivine gabbro | 50.6 | 0.703296 | 0.9 |
| D83R-1 16-26* | Olivine gabbro | 54.0 | 0.702721 | 0.3 |
| D83R-1 53-64* | Olivine gabbro | nd | 0.703202 | - |
| D84R-2 8-17* | Oxide gabbro | nd | 0.703698 | - |
| D87R2 63-71* | Oxide gabbro | 95.0 | 0.702857 | 0.8 |
| D94R-3 46-48 | Diabase | 73.0 | 0.702849 | 0.6 |
| D100R-1 42-46* | Olivine rich troctolite | 44.0 | 0.702688 | 0.2 |
| D111R-4 25-26 | Serpentinite | 8.6 | 0.705194 | 0.7 |
| D116R-1 58-68* | Oxide gabbro | nd | 0.703604 | - |
| D117R-2 24-32 | Olivine gabbro | 47.8 | 0.702980 | 0.5 |
| D127R-1 145-148 | Diabase | 78.3 | 0.702969 | 0.8 |
| D136R-2 21-29 | Serpentinite | 0.2 | 0.705802 | 0.0 |
| D136R-2 21-29* | Olivine gabbro | 29.0 | 0.702814 | 0.2 |
| D137R-2 85-91* | Oxide gabbro | nd | 0.702709 | - |
| D144R-1 105-116 | Olivine gabbro | 102.9 | 0.703381 | 2.1 |
| D155R-2 68-72 | Diabase | 70.9 | 0.702684 | 0.3 |
| D169R-1 90-100* | Gabbro | 101.7 | 0.702627 | 0.3 |
| D180R-1 13-17 | Diabase | 89.6 | 0.703281 | 1.6 |
| D210R-1 43-46 | Olivine gabbro | 49.7 | 0.702622 | 0.2 |
| D227R-3 6-12* | Olivine rich troctolite | 29.8 | 0.702686 | 0.1 |
| D228R-2 18-22 | Serpentinite | 0.8 | 0.702973 | 0.0 |
| D235R-2 100-114 | Serpentinite | 7.6 | 0.702909 | 0.0 |
| D237R-2 6-18* | Olivine rich troctolite | 21.0 | 0.702693 | 0.1 |
| D256R-3 88-93 | Serpentinite | 0.6 | 0.702745 | 0.0 |
| D292R-2 78-88* | Gabbro | nd | 0.702614 | - |

Water/rock calculations were undertaken for micro-samples as well when possible and are summarised in *Table 5-9*. Minerals that crystallise in veins cannot be easily used to calculate water/rock ratios (they are equal to infinity as it does not imply replacement of a mineral by another one). W/R has been done for plagioclase walls of amphibole vugs and for prehnite replacing igneous plagioclase. Initial igneous plagioclase of strontium concentration of 50 ppm is assumed and initial strontium isotope ratio is assumed to be equivalent to MORB ratio. Calculation for actinolite replacing clinopyroxene is modelled with initial clinopyroxene of 2 ppm Sr and $^{87}Sr/^{86}Sr$ of MORB composition. Tremolite replacing olivine in corona texture is submitted to a model assuming olivine with 1 ppm Sr. W/R modelling chlorite from corona texture has been calculated in the same way than plagioclase walls and prehnite. Results show that apart from the tremolite and actinolite replacing clinopyroxene, all W/R are high and conditions are fluid dominated. Calculations in open system have not been conducted. However, following the result tabulated in Delacour *et al.* (*2008*) that shows that in an open system, W/R ratio are much less than in a closed system, we assume that W/R ratio in an open system model will lead to rock dominated conditions except for the prehnite sample (U1309D 60R-3 35-45) that shows very fluid dominated conditions (W/R = 24.3).

**Table 5-9: Water/rock ratio for chosen micro-samples.**

| Sample number | Mineral | Sr (ppm) | $^{87}Sr/^{86}Sr$ | W/R |
|---|---|---|---|---|
| B10R-2 17-35 | Tremolite (corona) | 2.5 | 0.706521 | 0.2 |
| | Chlorite (corona) | 12.2 | 0.704322 | 2.5 |
| B14R-1 59-66 | Plg wall | 238.7 | 0.703957 | 1.9 |
| D5R-3 22-28 | Plg wall | 125 | 0.703980 | 1.9 |
| D8R-2 56-59 | Plg wall | 122 | 0.704152 | 2.2 |
| | Actinolite 1 | 4.3 | 0.704015 | 0.1 |
| | Actinolite 2 | 10.9 | 0.703925 | 0.1 |
| D12R-3 46-51 | Plg wall | 558 | 0.704220 | 2.3 |
| D14R-1 64-67 | Chlorite (corona) | 1 | 0.704830 | 3.6 |
| D60R-3 35-45 | Prehnite | 800 | 0.707736 | 24.3 |
| D75R-2 77-80 | Actinolite | 3.1 | 0.703966 | 0.1 |
| D117R-2 24-32 | Actinolite | 2.8 | 0.704102 | 0.1 |
| D144R-1 105-116 | Actinolite 1 | 1.4 | 0.703662 | 0.1 |
| | Actinolite 2 | 2.3 | 0.703946 | 0.1 |
| D256R-3 88-93 | Prehnite + Plg | 70.6 | 0.702582 | 0.1 |

## 5.4.3.2 Fluid fluxes

### *5.4.3.2.1 Principles*

The total volume of fluid infiltrated or time integrated fluid flux is reflected in the shape and relative displacements of isotopic profiles that record the fluid flow. Time integrated fluid flux depends therefore on the assumption that geochemical fronts for different tracers move along the flow path at rates that depend on the portioning of the tracer between rock and fluid. In purely advective transport with perfect fluid-rock equilibrium, geochemical fronts are sharp steps in composition. Fronts are broadened by diffusion, hydrodynamic dispersion, and kinetic dispersion (Bickle & Baker, 1990a; Bickle, 1992; Bickle & Baker, 1990b; Lassey & Blattner, 1988). Time integrated fluid flux $J_{int}$ is given by:

$$J_{int} = \frac{Z_{GF}}{K_v} \qquad \textbf{Equation 5-2}$$

where $Z_{GF}$ is the advective displacement of the geochemical front, and $K_v$ is the fluid-rock partition coefficient by volume unit given by $X_{fluid}\rho_{fluid}/X_{rock}\rho_{rock}$ where X is the concentration in ppm and $\rho$ is the density.

Motion of an isotopic signature into the rock occurs by advection of fluid along a flow path. The isotopic signature moves through the rock as a sharp front if advection is the only process involved (*Figure 5-11A*). In that case, to a single time integrated fluid flux corresponds an infinite calculated

W/R ratio upstream of the front (100% of alteration) and a W/R ratio calculated as 0 downstream of the front (no alteration) and fluid and rock have a defined isotopic composition at every point along the flow path, at any time.

In reality, advective fronts are broadened by diffusion or dispersive processes (Bickle & Baker, 1990a; Bickle, 1992; Bickle & Teagle, 1992; McCaig, *et al.*, 2010). In this model, fluid and rock have the same strontium isotopic composition at any point along the flow path. A range of isotopic compositions and water/rock ratios for the same time-integrated fluid flux is observed (*Figure 5-11B*).

The most common situation is when the shape of the front is governed by kinetically limited exchange between fluid and rock by a kinetic rate law (Bickle, 1992) (*Figure 5-11C*). In this model, fluid and rock have systematically a different strontium isotopic composition and isotopic equilibrium is never reached.

The shape of the fronts profile depends on the dimensionless Damköhler number, $N_D$, (Bickle, 1992; Bickle & Teagle, 1992; Blattner & Lassey, 1989; Lassey & Blattner, 1988) which is given by

$$N_D = kh/\omega_0 \qquad \textbf{Equation 5-3}$$

where k is the exchange rate for linear kinetic exchange, h is the length scale and $\omega_0$ is the fluid velocity in pore space or crack. At low $N_D$, equilibrium between fluid and rock is never reached and fluid and rock compositions are therefore systematically different.

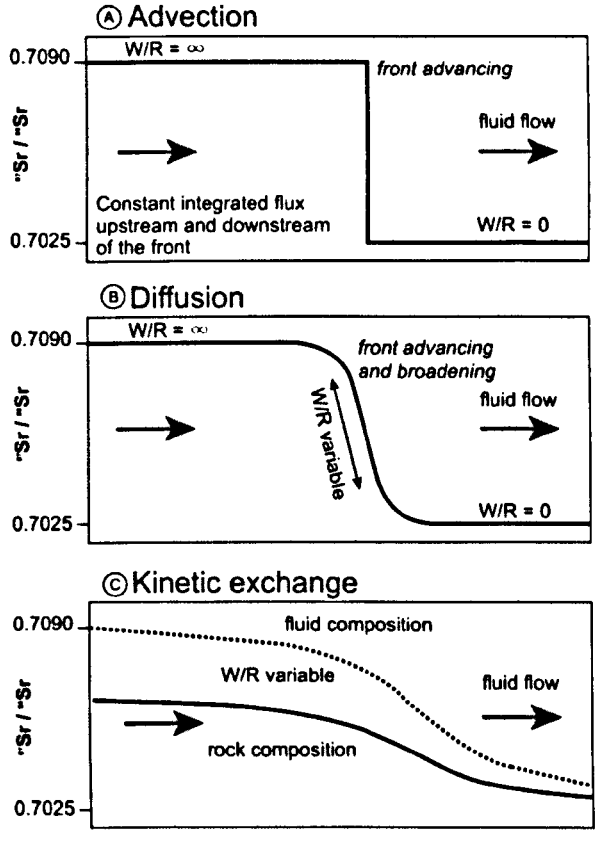


**Figure 5-11: Schematic geochemical fronts from McCaig *et al.* (2010). A: Geochemical front governed by advection only. B: Geochemical front broadened by diffusion or hydrodynamic dispersion. C: Geochemical front broadened by kinetically limited fluid-rock exchange at low $N_D$. At high $N_D$, the shape of the front will tend to be similar to the front broadened by diffusion.**

#### *5.4.3.2.2 Review of previous work on fluid fluxes in oceanic settings*

Bickle and Teagle (1992) described a $^{87}Sr/^{86}Sr$ profile indicating alteration in the recharge zone of the Troodos ophiolite. Calculations show that a minimum time-integrated fluid flux of 2.9 x $10^7$ $kg.m^{-2}$ is required to transport the strontium isotope composition of ~ 0.7054, set in the kinetically controlled exchange zone of extrusive lavas, through the ~ 1 km of sheeted dykes and uppermost gabbros in which fluid flow is inferred to be pervasive with near fluid-rock equilibrium, and into the zones of concentrated upwellings that are the epidosites.

Gillis *et al.* (2005) used the same approach to quantify the volume of fluid that circulates downhole in a section of upper oceanic crust at Hess Deep. Calculations show a time-integrated fluid flux of $3.2 \times 10^6$ kg.m$^{-2}$.

Delacour *et al.* (2008) similarly estimated the volume of fluid that circulates at the Atlantis Massif. Calculations were done assuming kinetically controlled fluid-rock exchange. The calculations are modelling the down flow component. Results show two distinctive time-integrated fluid fluxes depending on the data that are included in the model. The first model gives lower time-integrated fluid fluxes than those calculated for Troodos (Bickle & Teagle, 1992) or Hess Deep (Gillis, *et al.*, 2005) with $2.88 \times 10^5$ kg.m$^{-2}$ assuming a Damköhler number ($N_D$) of 39.1 and an advective displacement of the geochemical front ($Z_{GF}$) of 317.9 m. The second model for which gabbroic samples of the interval 415-500 mbsf are not included in order to give more impact to serpentinite and leucocratic gabbro located at 335.7 mbsf and 574 mbsf respectively, gives a time-integrated fluid flux of $3.7 \times 10^5$ kg.m$^{-2}$ assuming a $N_D$ of 17.2 and a $Z_{GF}$ of 410.6 m.

Teagle *et al.* (2003) used a slightly different approach in that they used the strontium isotopic composition of rocks from DSDP/ODP Hole 504B, and of anhydrite, as a proxy for fluid composition to calculate the recharge flux to the axial high temperature hydrothermal circulation. The strontium isotopic profiles are well fit by a tracer transport mass-balance model that approximates fluid-rock exchange by linear kinetics. The time-integrated fluid flux gives $1.7 \times 10^6$ kg.m$^{-2}$.

McCaig *et al.* (2007) show that the strontium isotopic profile of oceanic crust at 15°45'N indicates that most of the alteration occurs close to the detachment fault. It suggested that flow was concentrated within the detachment fault rocks (talc schists) and a time-integrated fluid flux of ~ $2 \times 10^6$ kg.m$^{-2}$ could be inferred for each kilometer that the fluids advects along the fault-controlled flow path. Recovery of talc shists in the area suggests a flow path to the alteration site of at least 2 km within the fault zone and at least 1 km through the hanging wall, and fluid flux parallel to the fault is

inferred to be at least 5 x $10^6$ kg.m$^{-2}$. This estimation was done using the approach developed by Bickle (1992).

#### *5.4.3.2.3 Quantification of fluid fluxes in the Atlantis Massif*

*Figure 5-12* shows a plot of bulk rock strontium isotope data on a diagram where depth is converted to dimensionless distance and where strontium isotope ratio is converted to dimensionless concentration (Bickle, 1992). Following Delacour (2008), the component of fluid flow downwards in the borehole is constrained using the downhole data as if it was an in situ section. In order to convert depth into dimensionless distance, depth is divided by an assumed $Z_{GF}$ of 400m (supported by the fact that alteration occurs mainly close to the detachment fault – see strontium isotope profile *Figure 5-1* and *Figure 5-3*) and multiplied by 0.001 which is the dimensionless distance scaled to fluid penetration distance. This centres the geochemical front at 0.001 on *Figure 5-12* (Bickle, 1992). In order to convert a strontium isotope ratio into a dimensionless concentration ranging from 0 (not altered) to 1 (100% altered or seawater composition), a lever rule calculation is applied to individual strontium isotope ratios with MORB unaltered value (0.70245) and seawater value (0.7091) as end-members. Solid lines represent rock composition and dashed lines represent fluid compositions (Bickle, 1992). In reality, at the time of alteration the fault is likely to have been covered by a significant overburden in the hanging wall, which the fluid must have passed through in order to reach the analysed samples (McCaig *et al.*, 2010). $Z_{GF}$ should therefore be higher, although there is little constraint on the actual penetration distance. Assuming a higher value of $Z_{GF}$ would compress all the data horizontally towards the 0.001 value on *Figure 5-12*. Consequences for the fit of $N_D$ curves would not be important at low values of $N_D$ but would be quite important for high values of $N_D$.

With a calculated Kv = 0.03 (estimated with an assumed seawater circulating fluid of density = 1000 kg.m$^{-3}$ and Sr content of 7.6 ppm and a rock of gabbroic composition of density = 2900 kg.m$^{-3}$ and a calculated average Sr concentration from samples of IODP Hole U1309B and D of 90 ppm), a $Z_{GF}$ = 400m, the downward component of volume fluid flux would be

at 13333 $m^3.m^{-2}$ and the mass fluid flux would be at ~ 1.33 x $10^7$ $kg.m^{-2}$. If an arbitrary 2km of overburden is added, the integrated flux would increase to 6.67 x $10^7$ $kg.m^{-2}$.

The plot shows that if serpentinites are treated as the fluid composition, fluid and rock fit for a low $N_D$ of ~ 0.1 to 0.3. The justification for treating the serpentinites as fluid compositions is that the low Sr content of peridotite means that they are likely to closely reflect the composition of fluid reaching the site of serpentinisation. However, serpentinites of the top of the hole are probably contaminated by late, low temperature carbonate precipitation (section *5.3.3*). The main support for the serpentinites being representative of high temperature fluid compositions is the high $^{87}Sr/^{86}Sr$ ratios of a prehnite sample from the micro-rodingites. Since this has a Sr content much higher than adjacent plagioclase, it must reflect in large part the composition of local fluid and by implication, coexisting serpentine.

*Figure 5-13* shows a Damköhler plot for micro-samples. Dimensionless distances and dimensionless concentrations were obtained using the same method described for bulk rock and assuming a $Z_{GF}$ of 400 m. Amphibole vugs and associated plagioclase walls fit with a low $N_D$ of ~0.1 to 0.3. These vugs must certainly have precipitated under fluid dominated conditions and reflects high flux pathways. Fluid that circulated in these cracks did not have time to equilibrate with the surrounding rock. Alteration of the walls must have been controlled by diffusion and/or dispersion.

The only prehnite sample yields a slightly higher $N_D$ of ~0.3 to 1. The fluid flux that reaches olivine–rich troctolites must be high but an order of magnitude lower than the high flux pathways that create the amphibole vugs.

Amphibole veins fit with low $N_D$ curves of rock composition indicating that they precipitate under rock dominated conditions at much lower fluid flux with a fluid that tends towards equilibrium with the surrounding rock.

Tremolite from a corona texture indicates a higher $N_D$ of 1 or 3. From its relatively high strontium isotope ratio, the corona is believed to have formed at fluid flux lower than fluid flux that generated the amphibole vugs and the micro-rodingite but higher than the fluid flux that generated amphibole veins. Chlorite is not included in this interpretation as analyses

show strontium content is very low, making the strontium isotope ratio doubtful due to the high blank correction.

Talc-tremolite veins that cut serpentinites form in sequence in which fluid rich in strontium circulates at high flux [low $N_D$] (probably as high as the fluids that circulate in amphibole vugs) to replace serpentine by tremolite. A second circulation event with fluid circulating at lower fluid flux (intermediate strontium isotope ratio and higher $N_D$) generates the replacement of serpentine by talc at the boundaries between tremolite and serpentine.

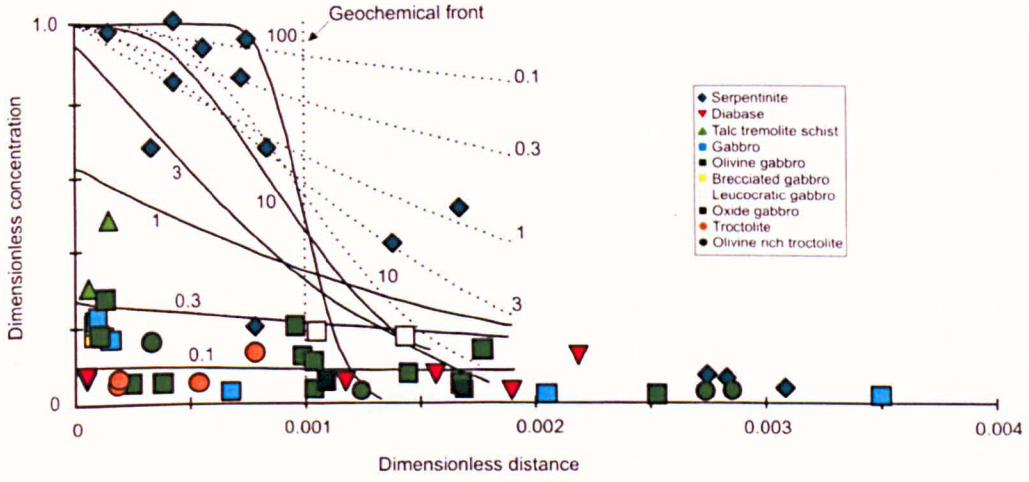


**Figure 5-12: Advective transport with kinetic control on fluid-solid exchange for Damköhler numbers between 0.1 and 100 for bulk rock samples. Solid lines show rock composition and dotted lines show fluid composition. Dimensionless concentration is a conversion of the strontium isotopic ratio and dimensionless distance is a conversion of the depth (see text).**

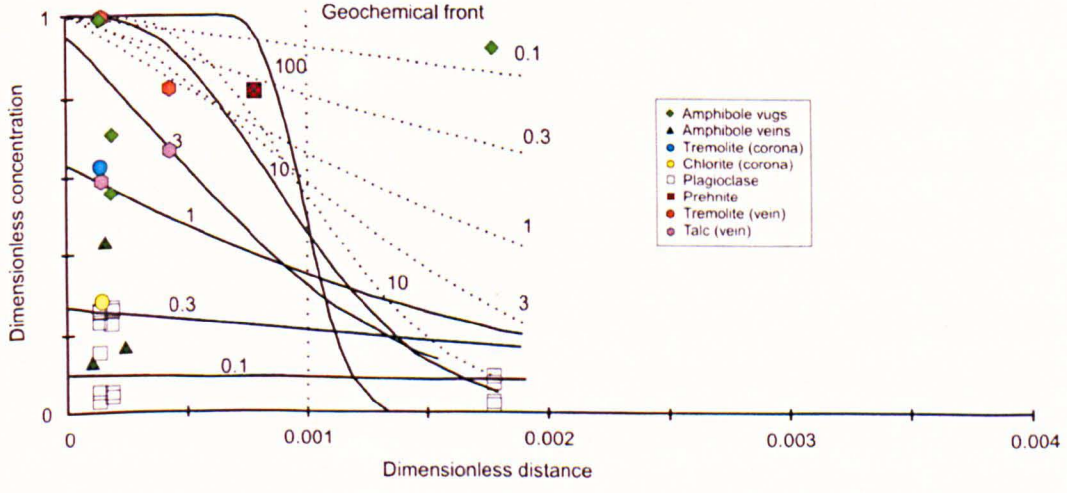


**Figure 5-13: Advective transport with kinetic control on fluid-solid exchange for Damköhler numbers between 0.1 and 100 for micro-samples.**

### 5.4.4 How does seawater reach serpentinite without $^{87}Sr/^{86}Sr$ decreasing?

Serpentinites from the upper part of the core show elevated $^{87}Sr/^{86}Sr$. The $^{87}Sr/^{86}Sr$ ratio of peridotite can readily be altered during serpentinisation because of the high Kv. The strontium isotopic ratio of seawater will not be changed, unlike the rock. However, the system in the Atlantis Massif is dominated by gabbroic rocks (*Chapter 2*). Gabbroic rocks contains minerals such as plagioclase that are rich in strontium (order of 50 to 500 ppm - see content of different plagioclases analysed in *Table 5-2*). In a diffusive/dispersive model (such as described in *5.4.3.2.1*), a fluid that passes through gabbros with strontium isotopic composition of 0.7035, would be in equilibrium with the rock and have the same isotopic composition. Serpentinites in the Atlantis Massif show elevated strontium isotope ratio despite the fact that the massif is dominated by gabbros. This raises a question: How did fluid with a seawater isotopic signature pass through partially altered gabbros to reach thin ultramafic horizons without $^{87}Sr/^{86}Sr$ decreasing? Different models are a possible answer to that question:

- Model 1: Direct link between serpentinite layers and seawater
- Model 2: Fluid path is gabbroic.
- Model 3: Fluid circulates through fractures and veins
- Model 4: Late carbonate precipitation

#### 5.4.4.1 Model 1 – Direct link between serpentinite and seawater

In this model, ultramafic layers are directly connected to seawater. The southern wall of the Atlantis massif is predominantly composed of serpentinised peridotites at ~70% with interlayered gabbro bodies (~30%) (Blackman, *et al.*, 2002; Boschi, *et al.*, 2006; Karson, *et al.*, 2006). The degree of serpentinisation ranges from 70 to 100%. It is suggested that seawater penetrates the oceanic crust at the detachment shear zone (DSZ) consisting of deformed serpentinites and metagabbros marked by focused fluid flow during exhumation (Schroeder & John, 2004). However, Delacour *et al.* (*2008*) suggested that alteration of serpentinites from the southern wall

was associated with the hydrothermal circulation related to the Lost City low-temperature vent field that post-dates the circulation along the detachment fault. Model 1 is unlikely.

#### 5.4.4.2 Model 2 – Gabbroic fluid path

In this model it is suggested that $^{87}Sr$ rich fluid (seawater) reached serpentinite layers via a gabbroic pathway. In order for seawater to reach ultramafic layers and interacts with them without $^{87}Sr/^{86}Sr$ decreasing in a gabbro dominated system, seawater must avoid interaction with plagioclase to minimize isotopic exchange that would lower the seawater strontium signature.

From the observations made on gabbros and alteration features, it is suggested that seawater circulates preferentially at the boundaries between clinopyroxene and plagioclase and along clinopyroxene cleavages. Seawater alters the clinopyroxene into amphiboles that show strontium isotope ratios greater than the bulk rock signature. Seawater can preserve its elevated strontium isotope value until it reaches ultramafic layers to alter them into serpentinites with elevated seawater-like ratios.

However, small samples of amphiboles replacing clinopyroxenes show strontium isotope ratios that are not as high as the serpentinites, and fluid would be expected to have equilibrated with the local minerals before reaching the ultramafic layers. This model is therefore unlikely.

#### 5.4.4.3 Model 3 – Circulation through fractures and veins

Bickle (1992) describes a model where fluid circulates in cracks and interacts with the wall rock by diffusion and/or limited advection. Several samples in our core show veins that are filled with actinolite + clays of elevated strontium isotope ratio (*Table 5-2*; *Figure 5-5*). It is suggested that those veins act as high fluid flux pathways and $^{87}Sr$ rich fluid can pass through gabbros to reach serpentinites. However, the respective $\delta^{18}O$ indicates alteration temperatures for veins and for serpentinites that quite different (*Table 5-2*). The clay content of these vugs can distort the isotopic composition of serpentinite (see *5.3.3*). Fluid that reaches the ultramafic

layers must therefore be from a flow event that precedes the low temperature carbonate alteration of these vugs.

#### 5.4.4.4 Model 4 – Late carbonate precipitation

A leaching experiment (*5.3.3*) shows that serpentinites are likely to be contaminated by late precipitation of carbonate minerals such as magnesite, calcite and/or dolomite that influence the strontium isotope ratio of serpentinite. One prehnite analysis shows however elevated strontium ratio indicating that the serpentinising fluid strontium isotope ratio must have been seawater-like whether or not serpentinites are contaminated by late precipitation of carbonates.

## 5.5 Conclusions

- Isotopic analyses show that fluids circulated mainly close to the detachment fault and that limited amounts of fluid escaped into the footwall. Fluid fluxes can be calculated on the basis of the downhole isotopic profile, it is likely that the main direction of fluid flow was parallel to the fault and hence perpendicular to the Hole.
- Small sample analyses show that oceanic samples are locally more modified than what bulk rock analyses indicate.
- Bulk rock isotopic analyses show that gabbros are little modified while serpentinites show elevated strontium isotope ratios.
- Small sample analyses show that gabbros are heterogeneous, with amphibole vugs and prehnite showing elevated seawater-like values, amphiboles replacing pyroxene intermediate values, and plagioclase commonly retaining igneous values.
- Serpentinites might be contaminated by late carbonate precipitation. However, the elevated strontium isotope ratio of prehnite replacing plagioclase during formation of micro-rodingite argues for the serpentinising fluid being seawater-like.
- Oxygen isotope analyses support the conclusions of metamorphic petrology, that the majority of alteration took place at temperatures > 300 °C.
- The patterns of hydrothermal alteration can be understood in terms of kinetically limited exchange of isotopes between fluid and rock
- High flux pathways such as the amphibole vugs were formed at low effective Damköhler numbers ($N_D$), such that the amphibole reflects the fluid composition while the altered plagioclase in the vug walls have rock-dominated isotopic ratios.
- Tremolite-talc veins also appear to have formed under high flux, low $N_D$ conditions, while tremolite-chlorite coronas and micro-rodingite veins are also quite high flux features.
- The evolution of fluid flow and alteration in the Atlantis OCC can be interpreted in terms of the TAG model in which fluid discharge at black smoker temperatures occurs up the fault zone.

## 5.6 References

Albarède, F., 1995. *Introduction to Geochemical Modeling*, Cambridge University.

Albarède, F., Michard, A., Minster, J. F. & Michard, G., 1981. $^{87}Sr/^{86}Sr$ ratios in hydrothermal waters and deposits from the East Pacific Rise at 21°N. *Earth and Planetary Science Letters*, **55**(2), 229-236.

Alt, J. C., Teagle, D. A. H., Bach, W., Halliday, A. N. & Erzinger, J., 1996. Stable and Strontium Isotopic Profiles Through Hydrothermally Altered Upper Oceanic Crust, Hole 504B. In: *Proceedings of the Ocean Drilling Program, Scientific Results, Vol.148*, JC Alt, H Kinoshita, L B Stokking, and P J Michael.

Alt, J. C., Shanks, W. C., Bach, W., Paulick, H., Garrido, C. J. and Beaudoin, G., 2007. Hydrothermal alteration and microbial sulfate reduction in peridotite and gabbro exposed by detachment faulting at the Mid-Atlantic Ridge, 15°20'N (ODP Leg 209): A sulfur and oxygen isotope study. *Geochemistry, Geophysics, Geosystems*, 8. Q08002, doi/10.1029/2007GC001617

Barrett, T. J. & Friedrichsen, H., 1982. Strontium and oxygen isotopic composition of some basalts form Hole 504B, Costa Rica Rift, DSDP Legs 69 and 70. *Earth and Planetary Science Letters*, **60**, 27-38.

Bickle, M. & Baker, J., 1990a. Migration of reaction and isotopic fronts in infiltration zones: assessments of fluid flux in metamorphic terrains. *Earth and Planetary Science Letters*, **98**(1), 1-13.

Bickle, M. J., 1992. Transport mechanisms by fluid-flow in metamorphic rocks: oxygen and strontium decoupling in the Trois Seigneurs Massif - a consequence of kinetic dispersion? *American Journal of Science*, **292**, 289-316.

Bickle, M. J. & Baker, J., 1990b. Advective-diffusive transport of isotopic fronts: An example from Naxos, Greece. *Earth and Planetary Science Letters*, **97**(1-2), 78-93.

Bickle, M. J. & Teagle, D. A. H., 1992. Strontium alteration in the Troodos ophiolite: implications for fluid fluxes and geochemical transport in mid-ocean ridge hydrothermal systems. *Earth and Planetary Science Letters*, **113**, 219-237.

Blackman, D. K., Ildefonse, B., John, B. E., Ohara, Y., Miller, D. J., McLeod, C. J. & Scientists, E., 2006. Expedition 304/305 summary. *Proceedings of the Integrated Ocean Drilling Program*, **304/305**, 1-60.

Blackman, D. K., Karson, J. A., Smith, D. K., Cann, J. R., Früh-Green, G. L., Gee, J. S., Hurst, S. D., John, B. E., Morgan, J., Nooner, S. L., Ross, D. K., Schroeder, T. J. & Williams, E. A., 2002. Geology of the Atlantis

Massif (Mid-Atlantic Ridge, 30°N): Implications for the evolution of an ultramafic oceanic core complex. *Marine Geophysical Researches*, **23**, 443-469.

Blattner, P. & Lassey, K. R., 1989. Stable-isotope exchange fronts, Damköhler numbers, and fluid to rock ratios. *Chemical Geology*, **78**(3-4), 381-392.

Boschi, C., Dini, A., Fruh-Green, G. L. & Kelley, D. S., 2008. Isotopic and element exchange during serpentinization and metasomatism at the Atlantis Massif (MAR 30N): Insights from B and Sr isotope data. *Geochimica et Cosmochimica Acta*, **72**, 1801-1823.

Boschi, C., Fruh-Green, G. L., Delacour, A., Karson, J. A. & Kelley, D. S., 2006. Mass transfer and fluid flow during detachment faulting and development of an oceanic core complex, Atlantis Massif (MAR 30°N). *Geochemistry Geophysics Geosystems*, **7**(1), 1-39.

Bottinga, Y. & Javoy, M., 1973. Comments on Oxygen isotope geochemistry. *Earth and Planetary Science Letters*, **20**, 250-265.

Cole, D. R. & Ripley, E. M., 1998. Oxygen isotope fractionation between chlorite and water from 170 to 350°C: A preliminary assessment based on partial exchange and flui/rock experiments. *Geochimica et Cosmochimica Acta*, **63**(3/4), 449-457.

Delacour, A., 2007. *Linking serpentinization, fluid fluxes, mass transfer and microbial activity at Lost City: geochemical and isotopic constraints*, Zurich.

Delacour, A., Früh-Green, G. L., Frank, M., Gutjahr, M. & Kelley, D. S., 2008. Sr- and Nd-isotope geochemistry of the Atlantis Massif (30°N, MAR): Implications for fluid fluxes and lithospheric heterogeneity. *Chemical Geology*, **254**(1-2), 19-35.

deMartin, B. J., Sohn, R. A., Canales, J. P. & Humphris, S. E., 2007. Kinematics and geometry of active detachment faulting beneath the TAG hydrothermal field on the Mid-Atlantic Ridge. *Geology*, 711-741.

Frost, B. R., Beard, J. S., McCaig, A. & Condliffe, E., 2008. The formation of micro-rodingite from IODP Hole U1309D: Key to understanding the process of serpentinization. *Journal of Petrology*, **49**(9), 1579-1588.

Gillis, K. M., Coogan, L. A. & Pedersen, R., 2005. Strontium isotope constraints on fluid flow in the upper oceanic crust at the East Pacific Rise. *Earth and Planetary Science Letters*, **232**, 83-94.

Gregory, R. T. & Taylor, H. P., 1981. An oxygen isotope profile in a section of Cretaceous oceanic crust, Samail ophiolite, Oman: evidence for d18O-buffering of the oceans by deep (>5km) seawater-hydrothermal circulation at mid-ocean ridges. *Journal of Geophysical Research*, **86**, 2737-2755.

Hart, S. R., Blusztajn, J., Dick, H. J. B., Meyer, P. S. & Muehlenbachs, K., 1999. The fingerprint of seawater circulation in a 500-meter section of ocean crust gabbros. *Geochimica et Cosmochimica Acta*, **63**(23/24), 4059-4080.

Hart, S. R., Erlank, A. J. & Kable, E. J. D., 1974. Sea floor basalt alteration: some chemical and Sr isotopic effects. *Contrib. Mineral. Petrol.*, **44**, 219-230.

Hodell, D. A., Mueller, P. A. & Garrido, J. R., 1991. Variations in the strontium isotopic composition of seawater during the Neogene. *Geology*, **19**, 24-27.

Karson, J. A., Fruh-Green, G. L., Kelley, D. S., Williams, E. A., Yoerger, D. R. & Jakuba, M., 2006. Detachment shear zone of the Atlantis Massif core complex, Mid-Atlantic Ridge, 30 degrees N. *Geochemistry Geophysics Geosystems*, **7**(6), 1-29.

Klein, F., 2010. $CO_2$-metasomatism and the Formation of Talc in Oceanic Detachment Faults. In: *Chapman Conference on Detachments in Oceanic Lithosphere: Deformation, Magmatism, Fluid Flow, and Ecosystems*, Agros, Cyprus.

Lassey, K. R. & Blattner, P., 1988. Kinetically controlled oxygen isotope exchange between fluid and rock in one-dimensional advective flow. *Geochimica et Cosmochimica Acta*, **52**, 2169-2175.

Macaulay, C. I., Fallick, A. E., Haszeldine, R. S. & Graham, C. M., 2000. Methods of laser-based stable isotope measurement applied to diagenetic cements and hydrocarbon reservoir quality. *Clay Minerals*, **35**, 313-322.

McCaig, A., Delacour, A., Fallick, A. E., Castelain, T. & Früh-Green, G. L., 2010. Detachment Fault Control on Hydrothermal Circulation Systems: Interpreting the Subsurface Beneath the TAG Hydrothermal Field Using the Isotopic and Geological Evolution of Oceanic Core Complexes in the Atlantic, *In* Rona, P. A., Devey, C. W., Dyment, J., Murton, B. J. (ed) Diversity of Hydrothermal Systems on, Slow Spreading Ridges, *AGU Geophysical Monograph*, **108**, AGU, pp; 207-240.

McCaig, A. M., Cliff, R. A., Escartin, J., Fallick, A. E. & MacLeod, C. J., 2007. Oceanic detachment faults focus very large volumes of black smoker fluids. *Geology*, **35**(10), 935-938.

Nozaka, T. & Fryer, P., 2011. Alteration of the Oceanic Lower Crust at a Slow-spreading Axis: Insight from Vein-related Zoned Halos in Olivine Gabbro from Atlantis Massif, Mid-Atlantic Ridge. *Journal of Petrology*, **52** (4), 643-664.

Palmer, M. R. & Edmond, J. M., 1989. The strontium isotope budget of the modern ocean. *Earth and Planetary Science Letters*, **92**(1), 11-26.

Saccocia, P. J., Seewald, J. S. & Shanks III, W. C., 1998. Hydrogen and Oxygen Isotope Fractionation Between Brucite and Aqueous NaCl Solutions from 250 to 450°C. *Geochimica et Cosmochimica Acta*, **62**(3), 485-492.

Saccocia, P. J., Seewald, J. S. & Shanks III, W. C., 2009. Oxygen and hydrogen isotope fractionation in serpentine-water and talc-water systems from 250 to 450 °C, 50 MPa. *Geochimica et Cosmochimica Acta*, **73**(22), 6789-6804.

Schroeder, T. & John, B. E., 2004. Strain localization on an oceanic detachment fault system, Atlantis Massif, 30 degrees N, Mid-Atlantic Ridge. *Geochemistry Geophysics Geosystems*, **5**.

Shanks, W. C., 2003. Stable isotope in seafloor hydrothermal systems, *In Stable Isotope Geochemistry, Reviews in Mineralogy and Geochemistry,* vol. **43**, edited by J. W. Valley and D. R. Cole. pp. 469-525, Mineralogical Society of America

Shanks, W. C., III., Böhlke, J. K., Seal, R. R., II, 1995. Stable isotopes in midocean ridge hydrothermal systems: interactions between fluids, minerals, and organisms. *In* Humphris, S. E., Zierenberg, R. A., Mullineaux, L. S., Thompson, R. E. (Eds.), *Seafloor Hydrothermal Systems: Physical, Chemical, Biological, and Geological Interactions.* Geophysical Monograph, **91**:194-221.

Spooner, E. T. C., Chapman, H. J. & Smewing, J. D., 1977. Strontium isotopic contamination and oxidation during ocean floor hydrothermal metamorphism of the ophiolitic rocks of the Troodos Massif, Cyprus. *Geochimica et Cosmochimica Acta*, **41**(7), 873-877, 879-890.

Taylor, H. P., 1977. Water/rock interactions and the origin of $H_2O$ in granitic batholiths. *Journal of the Geological Society of London*, **133**, 509-558.

Teagle, D. A. H., Alt, J. C. & Halliday, A. N., 1998a. Tracing the evolution of hydrothermal fluids in the upper oceanic crust: Sr-isotopic constraints from DSDP/ODP Holes 504B and 896A. In: *Modern Ocean Floor Processes and the Geological Record* (ed Society, G.), pp. 81-97, Special Publications, London.

Teagle, D. A. H., Alt, J. C., Humphris, S. E. & Halliday, A. N., 1998b. Dissecting an active hydrothermal deposit: the strontium and oxygen isotopic anatomy of the TAG hydrothermal mound_whole rock and silicate minerals. In: *Proceedings of the Ocean Drilling Program, Scientific Results, Vol. 158*, pp. 297-309, P M Herzig, S E Humphris, D J Miller, and R A Zierenberg.

Teagle, D. A. H., Bickle, M. J. & Alt, J. C., 2003. Recharge flux to ocean-ridge black smoker systems: a geochemical estimate from ODP Hole 504B. *Earth and Planetary Science Letters*, **210**, 81-89.

Wenner, D. B. & Taylor, J. H. P., 1971. Temperatures of Serpentinization of Uhramafic Rocks Based on $^{18}O/^{16}O$ Fractionation between Coexisting Serpentine and Magnetite. *Contr. Mineral. and Petrol.*, **32**, 165-185.

Zheng, Y.-F., 1993. Calculation of oxygen isotope fractionation in hydroxyl-bearing silicates. *Earth and Planetary Science Letters*, **120**(3-4), 247-263.

# PAGE MISSING IN ORIGINAL

# Chapter 6. Conclusions and views on potential future work

## 6.1 Conclusions

- Four types of fluid in terms of salinity were identified during microthermometric investigation.
    - Fluid type 1a is a fluid of seawater-like salinity homogenising at temperature of 140-290°C and occurs in quartz veins formed at low pressure and low temperature.
    - Fluid type 1b is also of low salinity (depleted with respect to seawater), but homogenises at higher temperature than 1a and occurs in plagioclase. This fluid was generated by mixing with recharged seawater after supercritical phase separation of a seawater-like fluid at temperatures of 450 to 600°C and pressures of 340 to 550 bars and is estimated to have been trapped at depth of ~5 km, assuming near-hydrostatic fluid pressures
    - Fluid type 3a is a high salinity fluid with respect to seawater, and Fluid type 3b is a halite saturated fluid. Fluid type 3 was found only in evolved trondjhemitic intrusions. These fluids homogenised at temperatures 320->400°C. Brines (type 3b) were generated by condensation of a magmatic fluid at a depth of 7 km and temperature of ~770°C. The associated low salinity vapour-dominated fluid has not been observed.
- No gas phases were identified.
- Fluid chemistry shows variations throughout IODP Hole U1309D samples resulting from the coactions of several processes.
- All samples show enrichment in major cations and heavy metals, except Mg and Sr with respect to seawater. This is consistent with experimental studies.
- Atlantis Massif fluids are not an intermediate composition fluid between seawater and vent fluid. They are inferred to be back-water fluid

that can mix with recharged seawater and interact further with the rock in order to reach vent fluid compositions.

- Fluid rock interactions play a major role in the variation of fluid chemistry at Atlantis Massif. Replacement of clinopyroxene by amphiboles controls the concentration in Mg. Ca and Na are mainly controlled by albitisation. Fe is controlled by steatization and serpentinisation.
- Isotopic analyses show that fluids circulated mainly close to the detachment fault and that limited amounts of fluid escaped into the footwall. Fluid fluxes can be calculated on the basis of the downhole isotopic profile, it is likely that the main direction of fluid flow was parallel to the fault and hence perpendicular to the Hole
- Small sample analyses show that oceanic samples are more altered than what bulk rock analyses indicate. Bulk rock isotopic analyses show that gabbros are little altered while serpentinites show elevated strontium isotope ratios. Small sample analyses show that gabbros are heterogeneous, with amphibole vugs and prehnite showing elevated seawater-like values, amphiboles replacing pyroxene intermediate values, and plagioclase often retaining igneous values
- Serpentinites might be contaminated by late carbonate precipitation. However, the elevated strontium isotope ratio of prehnite replacing plagioclase during formation of micro-rodingite argues for the serpentinising fluid being seawater like
- Oxygen isotope analyses support the conclusions of metamorphic petrology, that the majority of alteration took place at temperatures > 300 °C
- The patterns of hydrothermal alteration can be understood in terms of kinetically limited exchange of isotopes between fluid and rock
- High flux pathways such as the amphibole vugs were formed at low effective Damköhler numbers ($N_D$), such that the amphibole reflects the fluid composition while the altered plagioclase in the vug walls have rock-dominated isotopic ratios

- Tremolite-talc veins also appear to have formed under high flux, low $N_D$ conditions, while tremolite-chlorite coronas and micro-rodingite veins are also quite high flux features
- *Figure 6-1* shows a model for hydrothermal circulation at the Atlantis Massif. In this model, the maximum depth of circulation at Atlantis massif and the main magma supply are unknown unlike the TAG model (deMartin, *et al.*, 2007; McCaig, *et al.*, 2010) used in this study. In the TAG model, isotherms in the hanging wall are inferred from seismicity, whereas in the Atlantis Massif, nothing constrains the thermic regime in the hanging wall. In contrast, in the footwall, isotherms can be constrained by the alteration temperature estimated with the oxygen isotope compositions of minerals. One particular difference from the TAG model in which fluid circulating along the detachment fault is buffered at a temperature of 400 °C, is that fluid can circulate at higher temperature at depth (fluids type 3b were trapped at least at a temperature of 770 °C –see *Chapter 3*), meaning that isotherms were closer to each other and to the detachment fault at depth. At shallower depths, isotherms cannot be as close to the detachment fault as in the TAG model, this being constrained by serpentinisation and by the trapping of seawater-like fluid in late quartz veins under low pressure.

The evolution of fluid flow and alteration in the Atlantis OCC can be interpreted in terms of the TAG model at the limit of what the results of this study constain.

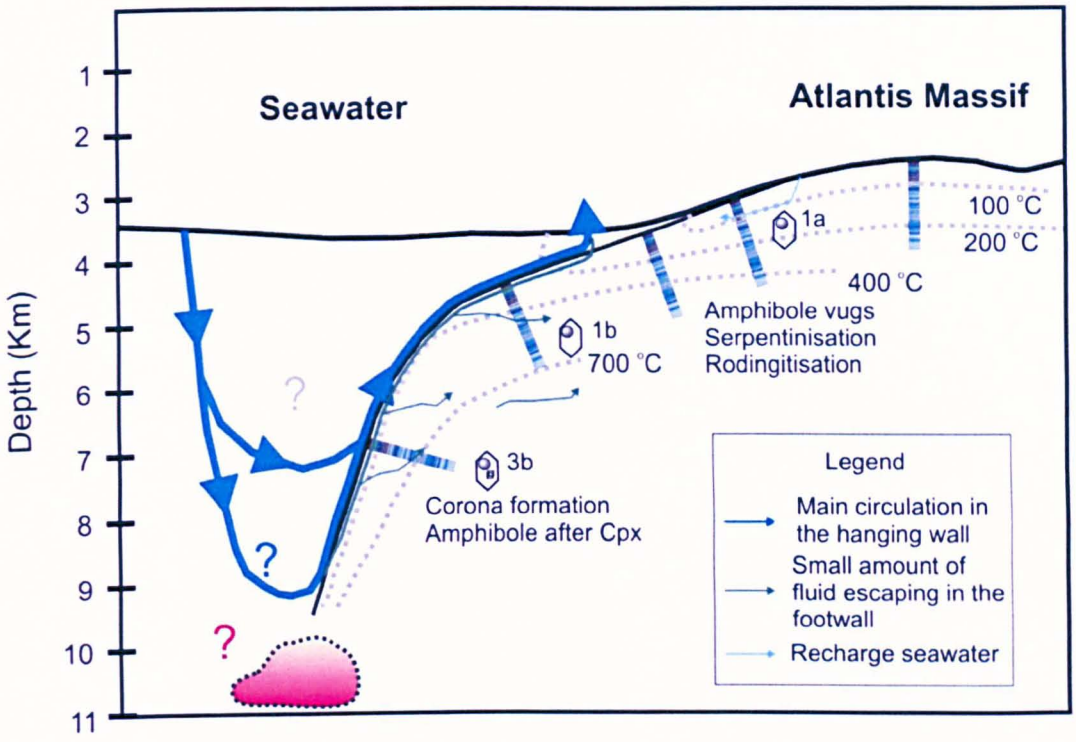


**Figure 6-1: Model for hydrothermal circulation in the Atlantis Massif through time of exhumation.**

## 6.2 Future work

- Measure homogenisation temperature of halite bearing inclusions. Use a microthermometric stage from which the temperature limit is higher than 400°C.
- Microthermometric measurements in plagioclase, olivine and clinopyroxene at various depths to better constrain salinity-temperature variations with depth and with reactions involved in the oceanic crust.
- Try to develop a laser ablation method thto measure the fluid chemistry in other mineral than quartz (such as plagioclase).
- Systematically combine small sample analyses to bulk rock analyses to better constrain the intensity of the alteration.
- Calculate fluid fluxes and water/rock with oxygen isotope data. Compare these results with the ones obtained with strontium.
- Model amphibole vugs on the basis of the crack model of Bickle (1992).

# Appendices

## 1 - Electron microprobe measurements

### Analyses in IODP Hole U1309B

Table 7-1: Microprobe measurement in sample U1309B 7R-1 55-60 cm. Amphibole analyses

| Oxide wt% | Am1 | Am2 | Am3 | Am4 | Am5 | Am6 | Am7 | Am8 | Am9 | Am10 | Am11 | Am12 |
|---|---|---|---|---|---|---|---|---|---|---|---|---|
| $SiO_2$ | 53.441 | 52.729 | 53.339 | 53.208 | 52.089 | 52.192 | 51.212 | 52.888 | 50.989 | 53.555 | 49.183 | 54.254 |
| $TiO_2$ | 0.439 | 0.189 | 0.398 | 0.155 | 0.224 | 0.105 | 0.135 | 0.202 | 0.158 | 0.180 | 1.061 | 0.149 |
| $Al_2O_3$ | 2.473 | 1.060 | 2.603 | 1.088 | 1.712 | 3.517 | 4.721 | 1.703 | 2.248 | 1.435 | 4.065 | 0.712 |
| $Cr_2O_3$ | 0.066 | 0.114 | 0.000 | 0.053 | 0.112 | 0.024 | 0.000 | 0.039 | 0.140 | 0.004 | 0.043 | 0.035 |
| $Fe_2O_3$ | 0.997 | 0.450 | 1.142 | 0.207 | 1.163 | 2.649 | 0.000 | 0.926 | 0.000 | 0.875 | 4.241 | 0.822 |
| FeO | 14.669 | 18.454 | 14.447 | 18.844 | 14.487 | 7.115 | 12.176 | 14.221 | 14.945 | 15.660 | 8.898 | 13.825 |
| MnO | 0.356 | 0.526 | 0.402 | 0.612 | 0.329 | 0.008 | 0.156 | 0.219 | 0.283 | 0.382 | 0.244 | 0.152 |
| MgO | 13.440 | 11.360 | 13.453 | 11.527 | 13.520 | 17.460 | 14.529 | 14.185 | 14.346 | 13.647 | 15.704 | 14.981 |
| CaO | 11.714 | 11.838 | 11.825 | 11.795 | 12.001 | 12.123 | 12.939 | 12.118 | 12.031 | 12.149 | 10.789 | 12.207 |
| $Na_2O$ | 0.452 | 0.178 | 0.423 | 0.134 | 0.319 | 0.415 | 0.466 | 0.243 | 0.244 | 0.225 | 1.051 | 0.181 |
| $K_2O$ | 0.033 | 0.005 | 0.037 | 0.037 | 0.014 | 0.023 | 0.019 | 0.000 | 0.000 | 0.012 | 0.073 | 0.030 |
| $H_2O$ | 2.016 | 2.003 | 2.067 | 2.015 | 1.977 | 2.070 | 2.046 | 2.037 | 1.997 | 2.053 | 1.985 | 2.037 |
| F | 0.112 | 0.000 | 0.000 | 0.000 | 0.084 | 0.000 | 0.000 | 0.000 | 0.000 | 0.000 | 0.028 | 0.028 |
| Cl | 0.000 | 0.013 | 0.008 | 0.026 | 0.000 | 0.019 | 0.018 | 0.018 | 0.022 | 0.022 | 0.123 | 0.049 |
| Total | 100.208 | 98.919 | 100.145 | 99.701 | 98.031 | 97.720 | 98.417 | 98.799 | 97.403 | 100.199 | 97.487 | 99.463 |
| Si | 7.743 | 7.878 | 7.728 | 7.889 | 7.744 | 7.542 | 7.489 | 7.766 | 7.635 | 7.800 | 7.267 | 7.885 |
| $Al_{(IV)}$ | 0.257 | 0.122 | 0.272 | 0.111 | 0.256 | 0.458 | 0.511 | 0.234 | 0.365 | 0.200 | 0.708 | 0.115 |
| $Al_{(VI)}$ | 0.166 | 0.065 | 0.172 | 0.079 | 0.044 | 0.141 | 0.303 | 0.061 | 0.031 | 0.046 | 0.000 | 0.007 |
| Ti | 0.048 | 0.021 | 0.043 | 0.017 | 0.025 | 0.011 | 0.015 | 0.022 | 0.018 | 0.020 | 0.118 | 0.016 |
| Cr | 0.008 | 0.013 | 0.000 | 0.006 | 0.013 | 0.003 | 0.000 | 0.005 | 0.017 | 0.000 | 0.005 | 0.004 |
| $Fe^{3+}$ | 0.109 | 0.051 | 0.125 | 0.023 | 0.130 | 0.288 | 0.000 | 0.102 | 0.000 | 0.096 | 0.471 | 0.090 |
| $Fe^{2+}$ | 1.778 | 2.306 | 1.750 | 2.337 | 1.801 | 0.860 | 1.489 | 1.746 | 1.871 | 1.907 | 1.099 | 1.680 |
| Mn | 0.044 | 0.067 | 0.049 | 0.077 | 0.041 | 0.001 | 0.019 | 0.027 | 0.036 | 0.047 | 0.031 | 0.019 |
| Mg | 2.903 | 2.531 | 2.906 | 2.548 | 2.997 | 3.761 | 3.168 | 3.106 | 3.203 | 2.963 | 3.459 | 3.246 |
| Ca | 1.819 | 1.895 | 1.836 | 1.874 | 1.911 | 1.877 | 2.027 | 1.907 | 1.930 | 1.896 | 1.708 | 1.901 |
| Na | 0.127 | 0.052 | 0.119 | 0.039 | 0.092 | 0.116 | 0.132 | 0.069 | 0.071 | 0.064 | 0.301 | 0.051 |
| K | 0.006 | 0.001 | 0.007 | 0.007 | 0.003 | 0.004 | 0.004 | 0.000 | 0.000 | 0.002 | 0.014 | 0.006 |
| OH | 1.949 | 1.997 | 1.998 | 1.993 | 1.961 | 1.995 | 1.996 | 1.996 | 1.994 | 1.995 | 1.956 | 1.975 |
| F | 0.051 | 0.000 | 0.000 | 0.000 | 0.040 | 0.000 | 0.000 | 0.000 | 0.000 | 0.000 | 0.013 | 0.013 |
| Cl | 0.000 | 0.003 | 0.002 | 0.007 | 0.000 | 0.005 | 0.004 | 0.004 | 0.006 | 0.005 | 0.031 | 0.012 |
| total | 17.006 | 17.001 | 17.007 | 17.007 | 17.057 | 17.062 | 17.157 | 17.045 | 17.176 | 17.042 | 17.181 | 17.019 |
| Nature | Act | Act | Act | Act | Act | Act | MgHb | Act | Act | Act | MgHb | Act |

Table 7-1 (continued)

| Oxide wt% | Am13 | Am14 | Am15 | Am16 | Am17 | Am18 | Am19 | Am20 | Am21 | Am22 | Am23 | Am24 |
|---|---|---|---|---|---|---|---|---|---|---|---|---|
| $SiO_2$ | 47.267 | 55.495 | 53.340 | 48.877 | 53.951 | 49.595 | 55.150 | 50.320 | 55.018 | 51.725 | 53.420 | 54.209 |
| $TiO_2$ | 1.771 | 0.570 | 0.874 | 1.630 | 0.525 | 1.270 | 1.037 | 0.691 | 0.139 | 0.644 | 0.186 | 0.147 |
| $Al_2O_3$ | 7.514 | 1.752 | 3.605 | 6.798 | 2.394 | 5.206 | 3.391 | 4.438 | 1.192 | 3.465 | 1.721 | 1.638 |
| $Cr_2O_3$ | 0.270 | 0.083 | 0.086 | 0.125 | 0.071 | 0.097 | 0.059 | 0.132 | 0.000 | 0.104 | 0.000 | 0.000 |
| $Fe_2O_3$ | 5.063 | 1.770 | 2.433 | 1.687 | 1.560 | 2.843 | 2.044 | 3.960 | 0.000 | 2.541 | 0.662 | 0.139 |
| FeO | 8.567 | 5.436 | 7.819 | 8.798 | 5.250 | 8.668 | 4.121 | 7.769 | 13.449 | 11.446 | 14.277 | 15.898 |
| MnO | 0.151 | 0.000 | 0.040 | 0.251 | 0.043 | 0.142 | 0.150 | 0.240 | 0.325 | 0.328 | 0.275 | 0.232 |
| MgO | 14.430 | 19.698 | 17.171 | 15.808 | 19.748 | 16.153 | 19.807 | 16.617 | 15.156 | 14.585 | 14.062 | 13.582 |
| CaO | 11.368 | 12.659 | 12.518 | 12.012 | 12.810 | 11.873 | 12.577 | 11.911 | 12.982 | 11.747 | 11.803 | 11.972 |
| $Na_2O$ | 1.661 | 0.338 | 0.534 | 0.967 | 0.458 | 1.057 | 0.536 | 0.944 | 0.198 | 0.693 | 0.251 | 0.228 |
| $K_2O$ | 0.116 | 0.017 | 0.028 | 0.037 | 0.029 | 0.225 | 0.000 | 0.040 | 0.000 | 0.050 | 0.015 | 0.024 |
| $H_2O$ | 2.068 | 2.080 | 2.121 | 2.047 | 2.118 | 1.938 | 2.143 | 2.008 | 2.085 | 2.037 | 2.014 | 2.006 |
| F | 0.000 | 0.145 | 0.000 | 0.028 | 0.000 | 0.169 | 0.058 | 0.085 | 0.000 | 0.000 | 0.055 | 0.109 |
| Cl | 0.029 | 0.000 | 0.032 | 0.062 | 0.018 | 0.213 | 0.043 | 0.114 | 0.033 | 0.112 | 0.024 | 0.034 |
| Total | 100.275 | 100.043 | 100.601 | 99.127 | 98.975 | 99.449 | 101.117 | 99.268 | 100.577 | 99.477 | 98.764 | 100.218 |
| Si | 6.829 | 7.742 | 7.511 | 7.059 | 7.621 | 7.176 | 7.580 | 7.264 | 7.881 | 7.510 | 7.829 | 7.866 |
| $Al_{(IV)}$ | 1.171 | 0.258 | 0.489 | 0.941 | 0.379 | 0.824 | 0.420 | 0.736 | 0.119 | 0.490 | 0.171 | 0.134 |
| $Al_{(VI)}$ | 0.109 | 0.030 | 0.109 | 0.216 | 0.019 | 0.063 | 0.130 | 0.019 | 0.082 | 0.102 | 0.126 | 0.147 |
| Ti | 0.192 | 0.060 | 0.093 | 0.177 | 0.056 | 0.138 | 0.107 | 0.075 | 0.015 | 0.070 | 0.021 | 0.016 |
| Cr | 0.031 | 0.009 | 0.010 | 0.014 | 0.008 | 0.011 | 0.006 | 0.015 | 0.000 | 0.012 | 0.000 | 0.000 |
| $Fe^{3+}$ | 0.550 | 0.186 | 0.258 | 0.183 | 0.166 | 0.310 | 0.211 | 0.430 | 0.000 | 0.278 | 0.073 | 0.015 |
| $Fe^{2+}$ | 1.035 | 0.634 | 0.921 | 1.063 | 0.620 | 1.049 | 0.474 | 0.938 | 1.611 | 1.390 | 1.750 | 1.929 |
| Mn | 0.018 | 0.000 | 0.005 | 0.031 | 0.005 | 0.017 | 0.017 | 0.029 | 0.039 | 0.040 | 0.034 | 0.029 |
| Mg | 3.108 | 4.097 | 3.605 | 3.404 | 4.159 | 3.484 | 4.059 | 3.576 | 3.237 | 3.157 | 3.072 | 2.939 |
| Ca | 1.760 | 1.892 | 1.889 | 1.859 | 1.939 | 1.840 | 1.852 | 1.842 | 1.992 | 1.827 | 1.853 | 1.861 |
| Na | 0.465 | 0.091 | 0.146 | 0.271 | 0.125 | 0.297 | 0.143 | 0.264 | 0.055 | 0.195 | 0.071 | 0.064 |
| K | 0.021 | 0.003 | 0.005 | 0.007 | 0.005 | 0.042 | 0.000 | 0.007 | 0.000 | 0.009 | 0.003 | 0.004 |
| OH | 1.993 | 1.936 | 1.992 | 1.972 | 1.996 | 1.870 | 1.965 | 1.933 | 1.992 | 1.972 | 1.969 | 1.942 |
| F | 0.000 | 0.064 | 0.000 | 0.013 | 0.000 | 0.077 | 0.025 | 0.039 | 0.000 | 0.000 | 0.025 | 0.050 |
| Cl | 0.007 | 0.000 | 0.008 | 0.015 | 0.004 | 0.052 | 0.010 | 0.028 | 0.008 | 0.028 | 0.006 | 0.008 |
| total | 17.291 | 17.004 | 17.039 | 17.225 | 17.103 | 17.251 | 17.000 | 17.197 | 17.031 | 17.081 | 17.003 | 17.004 |
| Nature | MgHb | Act | Act | MgHb | Act | MgHb | Act | MgHb | Act | Act | Act | Act |

Table 7-2: Microprobe measurement in sample U1309B 7R-1 55-60 cm. Plagioclase analyses

| Oxide wt% | Plg1 | Plg2 | Plg3 | Plg4 | Plg5 | Plg6 | Plg7 | Plg8 | Plg9 | Plg10 | Plg11 | Plg12 |
|---|---|---|---|---|---|---|---|---|---|---|---|---|
| $SiO_2$ | 56.523 | 67.579 | 54.737 | 69.290 | 53.372 | 64.619 | 53.259 | 58.351 | 66.216 | 66.267 | 57.565 | 66.687 |
| $TiO_2$ | 0.000 | 0.078 | 0.000 | 0.004 | 0.000 | 0.000 | 0.101 | 0.055 | 0.000 | 0.051 | 0.125 | 0.078 |
| $Al_2O_3$ | 27.835 | 20.535 | 28.265 | 19.679 | 29.679 | 21.849 | 28.776 | 26.728 | 21.650 | 21.955 | 26.341 | 21.188 |
| $Fe_2O_3$ | 0.245 | 0.161 | 0.000 | 0.000 | 0.374 | 0.071 | 0.164 | 0.224 | 0.084 | 0.106 | 0.057 | 0.002 |
| MnO | 0.000 | 0.000 | 0.119 | 0.000 | 0.004 | 0.042 | 0.053 | 0.000 | 0.081 | 0.000 | 0.091 | 0.121 |
| MgO | 0.000 | 0.035 | 0.000 | 0.029 | 0.009 | 0.000 | 0.000 | 0.001 | 0.000 | 0.028 | 0.000 | 0.000 |
| CaO | 9.996 | 1.203 | 11.631 | 0.343 | 12.890 | 3.610 | 12.349 | 8.747 | 2.881 | 3.104 | 9.238 | 2.421 |
| $Na_2O$ | 6.161 | 11.464 | 5.503 | 11.772 | 4.733 | 9.536 | 4.977 | 6.658 | 10.285 | 10.285 | 6.640 | 10.813 |
| $K_2O$ | 0.000 | 0.041 | 0.032 | 0.041 | 0.019 | 0.019 | 0.026 | 0.000 | 0.041 | 0.010 | 0.000 | 0.037 |
| Total | 100.760 | 101.096 | 100.287 | 101.158 | 101.080 | 99.746 | 99.705 | 100.764 | 101.238 | 101.806 | 100.057 | 101.347 |
| Si | 2.523 | 2.934 | 2.469 | 2.993 | 2.398 | 2.854 | 2.423 | 2.592 | 2.880 | 2.867 | 2.582 | 2.897 |
| Ti | 0.000 | 0.003 | 0.000 | 0.000 | 0.000 | 0.000 | 0.003 | 0.002 | 0.000 | 0.002 | 0.004 | 0.003 |
| Al | 1.464 | 1.051 | 1.503 | 1.002 | 1.572 | 1.137 | 1.543 | 1.399 | 1.110 | 1.120 | 1.392 | 1.085 |
| Fe3 | 0.008 | 0.005 | 0.000 | 0.000 | 0.013 | 0.002 | 0.006 | 0.007 | 0.003 | 0.003 | 0.002 | 0.000 |
| Mn | 0.000 | 0.000 | 0.005 | 0.000 | 0.000 | 0.002 | 0.002 | 0.000 | 0.003 | 0.000 | 0.003 | 0.004 |
| Mg | 0.000 | 0.002 | 0.000 | 0.002 | 0.001 | 0.000 | 0.000 | 0.000 | 0.000 | 0.002 | 0.000 | 0.000 |
| Ca | 0.478 | 0.056 | 0.562 | 0.016 | 0.620 | 0.171 | 0.602 | 0.416 | 0.134 | 0.144 | 0.444 | 0.113 |
| Na | 0.533 | 0.965 | 0.481 | 0.986 | 0.412 | 0.817 | 0.439 | 0.573 | 0.867 | 0.863 | 0.577 | 0.911 |
| K | 0.000 | 0.002 | 0.002 | 0.002 | 0.001 | 0.001 | 0.002 | 0.000 | 0.002 | 0.001 | 0.000 | 0.002 |
| total | 5.007 | 5.019 | 5.021 | 5.000 | 5.017 | 4.985 | 5.020 | 4.990 | 4.999 | 5.001 | 5.005 | 5.014 |
| An% | 47.8 | 5.8 | 56.7 | 1.8 | 62.1 | 17.2 | 60.4 | 41.6 | 13.7 | 14.6 | 44.7 | 11.7 |

Table 7-3: Microprobe measurement in sample U1309B 8R-2 55-57 cm. Amphibole analyses

| Oxide wt% | Am1 | Am2 | Am3 | Am4 | Am5 | Am6 | Am7 | Am8 | Am9 | Am10 | Am11 | Am12 |
|---|---|---|---|---|---|---|---|---|---|---|---|---|
| $SiO_2$ | 48.767 | 44.974 | 54.714 | 53.835 | 50.370 | 50.056 | 53.225 | 52.734 | 54.898 | 55.988 | 55.514 | 53.194 |
| $TiO_2$ | 0.530 | 1.397 | 0.248 | 0.640 | 0.408 | 0.694 | 0.092 | 0.081 | 0.246 | 0.064 | 0.194 | 0.031 |
| $Al_2O_3$ | 7.951 | 9.872 | 2.752 | 2.553 | 7.404 | 4.327 | 2.343 | 1.859 | 1.861 | 1.234 | 2.354 | 2.739 |
| $Cr_2O_3$ | 0.036 | 0.071 | 0.052 | 0.255 | 0.067 | 0.000 | 0.000 | 0.069 | 0.016 | 0.020 | 0.012 | 0.027 |
| $Fe_2O_3$ | 4.364 | 4.478 | 1.195 | 1.484 | 1.206 | 5.426 | 1.730 | 0.000 | 0.000 | 0.000 | 0.299 | 1.115 |
| FeO | 6.971 | 9.029 | 7.803 | 8.158 | 8.839 | 10.669 | 13.201 | 19.399 | 9.961 | 9.438 | 7.390 | 12.883 |
| MnO | 0.085 | 0.137 | 0.070 | 0.071 | 0.096 | 0.392 | 0.423 | 0.338 | 0.082 | 0.065 | 0.050 | 0.126 |
| MgO | 15.526 | 13.922 | 17.819 | 17.305 | 15.566 | 14.261 | 14.673 | 11.192 | 17.236 | 17.576 | 18.519 | 14.403 |
| CaO | 11.490 | 11.383 | 12.732 | 12.503 | 12.367 | 10.167 | 10.682 | 10.311 | 12.125 | 12.792 | 12.724 | 12.236 |
| $Na_2O$ | 1.342 | 2.231 | 0.312 | 0.324 | 1.123 | 1.096 | 0.441 | 0.312 | 0.240 | 0.148 | 0.340 | 0.235 |
| $K_2O$ | 0.017 | 0.138 | 0.020 | 0.032 | 0.032 | 0.067 | 0.000 | 0.010 | 0.000 | 0.005 | 0.051 | 0.032 |
| $H_2O$ | 2.046 | 2.039 | 2.068 | 2.058 | 2.043 | 2.051 | 2.013 | 1.985 | 2.096 | 2.112 | 2.106 | 2.034 |
| F | 0.057 | 0.028 | 0.117 | 0.088 | 0.115 | 0.000 | 0.084 | 0.000 | 0.000 | 0.000 | 0.058 | 0.056 |
| Cl | 0.051 | 0.003 | 0.016 | 0.025 | 0.000 | 0.006 | 0.016 | 0.065 | 0.000 | 0.013 | 0.000 | 0.009 |
| Total | 99.233 | 99.703 | 99.917 | 99.330 | 99.636 | 99.212 | 98.924 | 98.355 | 98.761 | 99.455 | 99.611 | 99.120 |
| Si | 7.009 | 6.567 | 7.712 | 7.665 | 7.199 | 7.312 | 7.756 | 7.901 | 7.853 | 7.935 | 7.802 | 7.730 |
| $Al_{(IV)}$ | 0.991 | 1.433 | 0.288 | 0.335 | 0.801 | 0.688 | 0.244 | 0.099 | 0.147 | 0.065 | 0.198 | 0.270 |
| $Al_{(VI)}$ | 0.356 | 0.266 | 0.169 | 0.094 | 0.446 | 0.057 | 0.159 | 0.229 | 0.166 | 0.141 | 0.192 | 0.199 |
| Ti | 0.057 | 0.153 | 0.026 | 0.069 | 0.044 | 0.076 | 0.010 | 0.009 | 0.026 | 0.007 | 0.021 | 0.003 |
| Cr | 0.004 | 0.008 | 0.006 | 0.029 | 0.008 | 0.000 | 0.000 | 0.008 | 0.002 | 0.002 | 0.001 | 0.003 |
| $Fe^{3+}$ | 0.472 | 0.492 | 0.127 | 0.159 | 0.130 | 0.597 | 0.190 | 0.000 | 0.000 | 0.000 | 0.032 | 0.122 |
| $Fe^{2+}$ | 0.838 | 1.103 | 0.920 | 0.971 | 1.056 | 1.303 | 1.609 | 2.431 | 1.192 | 1.119 | 0.868 | 1.566 |
| Mn | 0.010 | 0.017 | 0.008 | 0.009 | 0.012 | 0.049 | 0.052 | 0.043 | 0.010 | 0.008 | 0.006 | 0.016 |
| Mg | 3.327 | 3.031 | 3.744 | 3.674 | 3.317 | 3.106 | 3.188 | 2.500 | 3.676 | 3.714 | 3.880 | 3.120 |
| Ca | 1.769 | 1.781 | 1.923 | 1.907 | 1.894 | 1.591 | 1.668 | 1.655 | 1.858 | 1.942 | 1.916 | 1.905 |
| Na | 0.374 | 0.632 | 0.085 | 0.089 | 0.311 | 0.310 | 0.125 | 0.091 | 0.067 | 0.041 | 0.093 | 0.066 |
| K | 0.003 | 0.026 | 0.004 | 0.006 | 0.006 | 0.012 | 0.000 | 0.002 | 0.000 | 0.001 | 0.009 | 0.006 |
| OH | 1.962 | 1.986 | 1.944 | 1.954 | 1.948 | 1.999 | 1.957 | 1.984 | 2.000 | 1.997 | 1.974 | 1.972 |
| F | 0.026 | 0.013 | 0.052 | 0.040 | 0.052 | 0.000 | 0.039 | 0.000 | 0.000 | 0.000 | 0.026 | 0.026 |
| Cl | 0.012 | 0.001 | 0.004 | 0.006 | 0.000 | 0.001 | 0.004 | 0.017 | 0.000 | 0.003 | 0.000 | 0.002 |
| total | 17.211 | 17.508 | 17.012 | 17.006 | 17.223 | 17.102 | 17.000 | 16.968 | 16.997 | 16.975 | 17.017 | 17.006 |
| Nature | MgHb | Ed | Act | Act | MgHb | MgHb | Act | Act | Act | Act | Act | Act |

Table 7-3 (continued)

| Oxide wt% | Am13 | Am14 | Am15 | Am16 | Am17 | Am18 | Am19 | Am20 | Am21 | Am22 | Am23 |
|---|---|---|---|---|---|---|---|---|---|---|---|
| $SiO_2$ | 52.471 | 54.091 | 51.924 | 54.387 | 52.236 | 50.950 | 52.840 | 52.522 | 52.073 | 52.484 | 52.540 |
| $TiO_2$ | 0.129 | 0.113 | 0.210 | 0.040 | 0.161 | 0.259 | 0.110 | 0.160 | 0.109 | 0.062 | 0.048 |
| $Al_2O_3$ | 2.295 | 2.557 | 2.333 | 1.732 | 1.859 | 5.869 | 2.165 | 2.601 | 2.925 | 2.426 | 2.043 |
| $Cr_2O_3$ | 0.053 | 0.043 | 0.023 | 0.000 | 0.027 | 0.020 | 0.092 | 0.050 | 0.000 | 0.000 | 0.023 |
| $Fe_2O_3$ | 1.057 | 0.900 | 0.075 | 0.000 | 0.000 | 1.766 | 0.600 | 1.578 | 2.033 | 1.408 | 1.382 |
| FeO | 18.151 | 9.066 | 17.262 | 9.314 | 17.522 | 6.160 | 17.897 | 15.691 | 15.199 | 18.095 | 18.351 |
| MnO | 0.314 | 0.204 | 0.340 | 0.005 | 0.343 | 0.000 | 0.300 | 0.286 | 0.298 | 0.458 | 0.412 |
| MgO | 11.342 | 17.053 | 11.603 | 16.542 | 11.687 | 17.221 | 11.844 | 12.534 | 12.423 | 11.097 | 11.429 |
| CaO | 11.468 | 12.157 | 11.363 | 12.184 | 11.346 | 11.956 | 11.025 | 11.032 | 11.403 | 11.188 | 11.176 |
| $Na_2O$ | 0.301 | 0.277 | 0.327 | 0.222 | 0.242 | 0.912 | 0.384 | 0.514 | 0.434 | 0.450 | 0.450 |
| $K_2O$ | 0.000 | 0.062 | 0.019 | 0.000 | 0.000 | 0.026 | 0.010 | 0.005 | 0.011 | 0.016 | 0.014 |
| $H_2O$ | 1.990 | 2.087 | 1.914 | 2.041 | 1.989 | 2.069 | 2.021 | 2.033 | 2.029 | 2.020 | 1.951 |
| F | 0.054 | 0.000 | 0.138 | 0.029 | 0.000 | 0.000 | 0.000 | 0.000 | 0.000 | 0.000 | 0.161 |
| Cl | 0.040 | 0.016 | 0.056 | 0.000 | 0.012 | 0.025 | 0.025 | 0.009 | 0.012 | 0.025 | 0.000 |
| Total | 99.665 | 98.627 | 97.587 | 96.496 | 97.424 | 97.233 | 99.313 | 99.015 | 98.949 | 99.729 | 99.980 |
| Si | 7.767 | 7.754 | 7.809 | 7.936 | 7.863 | 7.360 | 7.814 | 7.739 | 7.682 | 7.766 | 7.771 |
| $Al_{(IV)}$ | 0.233 | 0.246 | 0.191 | 0.064 | 0.137 | 0.640 | 0.186 | 0.261 | 0.318 | 0.234 | 0.229 |
| $Al_{(VI)}$ | 0.167 | 0.186 | 0.223 | 0.234 | 0.193 | 0.359 | 0.191 | 0.191 | 0.191 | 0.189 | 0.127 |
| Ti | 0.014 | 0.012 | 0.024 | 0.004 | 0.018 | 0.028 | 0.012 | 0.018 | 0.012 | 0.007 | 0.005 |
| Cr | 0.006 | 0.005 | 0.003 | 0.000 | 0.003 | 0.002 | 0.011 | 0.006 | 0.000 | 0.000 | 0.003 |
| $Fe^{3+}$ | 0.118 | 0.097 | 0.009 | 0.000 | 0.000 | 0.192 | 0.067 | 0.175 | 0.226 | 0.157 | 0.154 |
| $Fe^{2+}$ | 2.247 | 1.087 | 2.171 | 1.137 | 2.206 | 0.744 | 2.213 | 1.933 | 1.875 | 2.239 | 2.270 |
| Mn | 0.039 | 0.025 | 0.043 | 0.001 | 0.044 | 0.000 | 0.038 | 0.036 | 0.037 | 0.057 | 0.052 |
| Mg | 2.503 | 3.645 | 2.602 | 3.599 | 2.623 | 3.709 | 2.611 | 2.753 | 2.732 | 2.448 | 2.520 |
| Ca | 1.819 | 1.867 | 1.831 | 1.905 | 1.830 | 1.850 | 1.747 | 1.742 | 1.802 | 1.774 | 1.771 |
| Na | 0.086 | 0.077 | 0.095 | 0.063 | 0.071 | 0.255 | 0.110 | 0.147 | 0.124 | 0.129 | 0.129 |
| K | 0.000 | 0.011 | 0.004 | 0.000 | 0.000 | 0.005 | 0.002 | 0.001 | 0.002 | 0.003 | 0.003 |
| OH | 1.965 | 1.996 | 1.920 | 1.987 | 1.997 | 1.994 | 1.994 | 1.998 | 1.997 | 1.994 | 1.925 |
| F | 0.025 | 0.000 | 0.066 | 0.013 | 0.000 | 0.000 | 0.000 | 0.000 | 0.000 | 0.000 | 0.075 |
| Cl | 0.010 | 0.004 | 0.014 | 0.000 | 0.003 | 0.006 | 0.006 | 0.002 | 0.003 | 0.006 | 0.000 |
| total | 17.000 | 17.011 | 17.004 | 16.942 | 16.987 | 17.145 | 17.002 | 17.001 | 17.002 | 17.003 | 17.033 |
| Nature | Act | Act | Act | Act | Act | MgHb | Act | Act | Act | Act | Act |

Table 7-4: Microprobe measurements in sample U1309B 8R-2 55-57 cm. Plagioclase analyses

| Oxide wt% | Plg1 | Plg2 | Plg3 | Plg4 | Plg5 | Plg6 | Plg7 |
|---|---|---|---|---|---|---|---|
| $SiO_2$ | 51.823 | 67.541 | 53.379 | 58.551 | 68.235 | 66.981 | 68.460 |
| $TiO_2$ | 0.081 | 0.000 | 0.029 | 0.023 | 0.006 | 0.000 | 0.000 |
| $Al_2O_3$ | 30.255 | 20.059 | 29.643 | 26.704 | 20.486 | 20.556 | 20.068 |
| $Fe_2O_3$ | 0.475 | 0.000 | 0.312 | 0.339 | 0.000 | 0.165 | 0.000 |
| MnO | 0.000 | 0.000 | 0.000 | 0.000 | 0.064 | 0.000 | 0.000 |
| MgO | 0.050 | 0.036 | 0.010 | 0.003 | 0.010 | 0.114 | 0.088 |
| CaO | 13.239 | 0.865 | 12.052 | 8.896 | 1.052 | 1.413 | 0.595 |
| $Na_2O$ | 4.044 | 11.570 | 4.629 | 6.683 | 11.156 | 11.218 | 11.731 |
| $K_2O$ | 0.059 | 0.044 | 0.006 | 0.087 | 0.051 | 0.020 | 0.027 |
| Total | 100.026 | 100.115 | 100.060 | 101.286 | 101.060 | 100.467 | 100.969 |
| Si | 2.356 | 2.956 | 2.413 | 2.591 | 2.955 | 2.927 | 2.968 |
| Ti | 0.003 | 0.000 | 0.001 | 0.001 | 0.000 | 0.000 | 0.000 |
| Al | 1.621 | 1.035 | 1.579 | 1.393 | 1.046 | 1.059 | 1.025 |
| Fe3 | 0.016 | 0.000 | 0.011 | 0.011 | 0.000 | 0.005 | 0.000 |
| Mn | 0.000 | 0.000 | 0.000 | 0.000 | 0.002 | 0.000 | 0.000 |
| Mg | 0.003 | 0.002 | 0.001 | 0.000 | 0.001 | 0.007 | 0.006 |
| Ca | 0.645 | 0.041 | 0.584 | 0.422 | 0.049 | 0.066 | 0.028 |
| Na | 0.356 | 0.982 | 0.406 | 0.573 | 0.937 | 0.950 | 0.986 |
| K | 0.003 | 0.002 | 0.000 | 0.005 | 0.003 | 0.001 | 0.001 |
| total | 5.003 | 5.018 | 4.994 | 4.996 | 4.992 | 5.017 | 5.014 |
| An% | 64.8 | 4.3 | 58.4 | 42.2 | 5.2 | 7.4 | 3.3 |

Table 7-4 (continued)

| Oxide wt% | Plg8 | Plg9 | Plg10 | Plg11 | Plg12 | Plg13 | Plg14 |
|---|---|---|---|---|---|---|---|
| $SiO_2$ | 56.014 | 52.095 | 52.310 | 61.212 | 66.761 | 67.924 | 56.979 |
| $TiO_2$ | 0.000 | 0.000 | 0.091 | 0.000 | 0.000 | 0.000 | 0.010 |
| $Al_2O_3$ | 27.865 | 30.367 | 29.996 | 24.192 | 21.081 | 21.024 | 28.033 |
| $Fe_2O_3$ | 0.000 | 0.251 | 0.232 | 0.364 | 0.000 | 0.161 | 0.203 |
| MnO | 0.000 | 0.000 | 0.045 | 0.000 | 0.142 | 0.022 | 0.063 |
| MgO | 0.000 | 0.038 | 0.023 | 0.019 | 0.000 | 0.032 | 0.000 |
| CaO | 10.145 | 12.935 | 12.973 | 6.045 | 1.284 | 1.529 | 9.563 |
| $Na_2O$ | 5.667 | 4.218 | 4.260 | 8.616 | 11.051 | 11.093 | 6.203 |
| $K_2O$ | 0.011 | 0.036 | 0.042 | 0.110 | 0.045 | 0.045 | 0.033 |
| Total | 99.702 | 99.940 | 99.972 | 100.558 | 100.364 | 101.830 | 101.087 |
| Si | 2.522 | 2.365 | 2.375 | 2.713 | 2.918 | 2.926 | 2.531 |
| Ti | 0.000 | 0.000 | 0.003 | 0.000 | 0.000 | 0.000 | 0.000 |
| Al | 1.479 | 1.625 | 1.605 | 1.263 | 1.086 | 1.068 | 1.468 |
| Fe3 | 0.000 | 0.009 | 0.008 | 0.012 | 0.000 | 0.005 | 0.007 |
| Mn | 0.000 | 0.000 | 0.002 | 0.000 | 0.005 | 0.001 | 0.002 |
| Mg | 0.000 | 0.003 | 0.002 | 0.001 | 0.000 | 0.002 | 0.000 |
| Ca | 0.489 | 0.629 | 0.631 | 0.287 | 0.060 | 0.071 | 0.455 |
| Na | 0.495 | 0.371 | 0.375 | 0.740 | 0.937 | 0.927 | 0.534 |
| K | 0.001 | 0.002 | 0.002 | 0.006 | 0.003 | 0.002 | 0.002 |
| total | 4.986 | 5.004 | 5.004 | 5.023 | 5.008 | 5.002 | 4.999 |
| An% | 48.9 | 63.2 | 63.4 | 28.8 | 6.5 | 7.3 | 45.8 |

Table 7-4 (continued)

| Oxide wt% | Plg15 | Plg16 |
|---|---|---|
| $SiO_2$ | 64.892 | 52.231 |
| $TiO_2$ | 0.000 | 0.036 |
| $Al_2O_3$ | 22.775 | 30.297 |
| $Fe_2O_3$ | 0.049 | 0.404 |
| MnO | 0.000 | 0.000 |
| MgO | 0.000 | 0.024 |
| CaO | 3.004 | 12.697 |
| $Na_2O$ | 9.965 | 4.403 |
| $K_2O$ | 0.010 | 0.046 |
| Total | 100.695 | 100.138 |
| Si | 2.837 | 2.368 |
| Ti | 0.000 | 0.001 |
| Al | 1.173 | 1.619 |
| Fe3 | 0.002 | 0.014 |
| Mn | 0.000 | 0.000 |
| Mg | 0.000 | 0.002 |
| Ca | 0.141 | 0.617 |
| Na | 0.845 | 0.387 |
| K | 0.001 | 0.003 |
| total | 4.998 | 5.010 |
| An% | 14.1 | 61.8 |

Table 7-5: Microprobe measurement in sample U1309B 8R-2 57-60 cm. Amphibole analyses

| Oxide wt% | Am1 | Am2 | Am3 |
|---|---|---|---|
| $SiO_2$ | 55.903 | 57.956 | 53.976 |
| $TiO_2$ | 0.191 | 0.000 | 0.164 |
| $Al_2O_3$ | 0.771 | 0.549 | 2.779 |
| $Cr_2O_3$ | 0.007 | 0.000 | 0.000 |
| $Fe_2O_3$ | 3.476 | 1.696 | 0.000 |
| FeO | 7.879 | 3.754 | 11.491 |
| MnO | 0.259 | 0.093 | 0.062 |
| MgO | 17.735 | 20.651 | 16.739 |
| CaO | 11.237 | 12.810 | 11.886 |
| $Na_2O$ | 0.253 | 0.089 | 0.397 |
| $K_2O$ | 0.000 | 0.007 | 0.030 |
| $H_2O$ | 2.088 | 2.166 | 2.089 |
| F | 0.049 | 0.000 | 0.012 |
| Cl | 0.050 | 0.025 | 0.010 |
| Total | 99.898 | 99.796 | 99.634 |
| Si | 7.892 | 8.000 | 7.717 |
| $Al_{(IV)}$ | 0.108 | 0.000 | 0.283 |
| $Al_{(VI)}$ | 0.020 | 0.089 | 0.185 |
| Ti | 0.020 | 0.000 | 0.018 |
| Cr | 0.001 | 0.000 | 0.000 |
| $Fe^{3+}$ | 0.369 | 0.176 | 0.000 |
| $Fe^{2+}$ | 0.930 | 0.433 | 1.374 |
| Mn | 0.031 | 0.011 | 0.008 |
| Mg | 3.733 | 4.250 | 3.568 |
| Ca | 1.700 | 1.894 | 1.821 |
| Na | 0.069 | 0.024 | 0.110 |
| K | 0.000 | 0.001 | 0.005 |
| OH | 1.966 | 1.994 | 1.992 |
| F | 0.022 | 0.000 | 0.005 |
| Cl | 0.012 | 0.006 | 0.002 |
| total | 16.873 | 16.880 | 17.089 |
| Nature | Act | Trm | Act |

Table 7-6: Microprobe measurement in sample U1309B 14R-1 59-66 cm. Amphibole and wall plagioclase analyses

| Oxide wt% | Am1 | Am2 | Am3 | Am4 | Plg1 | Plg2 |
|---|---|---|---|---|---|---|
| $SiO_2$ | 50.948 | 52.842 | 52.242 | 53.112 | 62.255 | 66.719 |
| $TiO_2$ | 0.972 | 0.268 | 0.217 | 0.412 | 0.000 | 0.000 |
| $Al_2O_3$ | 3.223 | 2.894 | 2.538 | 2.495 | 23.075 | 20.402 |
| $Cr_2O_3$ | 0.023 | 0.000 | 0.000 | 0.011 | | |
| $Fe_2O_3$ | 0.000 | 0.000 | 0.000 | 0.000 | 0.036 | 0.077 |
| FeO | 10.061 | 10.026 | 9.865 | 11.032 | | |
| MnO | 0.000 | 0.111 | 0.159 | 0.135 | 0.000 | 0.042 |
| MgO | 16.392 | 16.960 | 17.171 | 17.155 | 0.000 | 0.000 |
| CaO | 10.875 | 10.483 | 11.293 | 9.912 | 5.212 | 1.930 |
| $Na_2O$ | 0.791 | 0.561 | 0.442 | 0.539 | 8.958 | 11.151 |
| $K_2O$ | 0.036 | 0.005 | 0.005 | 0.051 | 0.023 | 0.002 |
| $H_2O$ | 1.981 | 2.005 | 1.977 | 2.043 | | |
| F | 0.000 | 0.050 | 0.101 | 0.000 | | |
| Cl | 0.122 | 0.058 | 0.026 | 0.031 | | |
| Total | 95.424 | 96.263 | 96.035 | 96.928 | 99.559 | 100.323 |
| Si | 7.590 | 7.754 | 7.712 | 7.763 | 2.773 | 2.925 |
| $Al_{(IV)}$ | 0.410 | 0.246 | 0.288 | 0.237 | 1.211 | 1.054 |
| $Al_{(VI)}$ | 0.157 | 0.254 | 0.153 | 0.193 | | |
| Ti | 0.109 | 0.030 | 0.024 | 0.045 | 0.000 | 0.000 |
| Cr | 0.003 | 0.000 | 0.000 | 0.001 | | |
| $Fe^{3+}$ | 0.000 | 0.000 | 0.000 | 0.000 | 0.001 | 0.003 |
| $Fe^{2+}$ | 1.254 | 1.230 | 1.218 | 1.348 | | |
| Mn | 0.000 | 0.014 | 0.020 | 0.017 | 0.000 | 0.002 |
| Mg | 3.641 | 3.710 | 3.779 | 3.738 | 0.000 | 0.000 |
| Ca | 1.736 | 1.648 | 1.786 | 1.552 | 0.249 | 0.091 |
| Na | 0.228 | 0.160 | 0.126 | 0.153 | 0.774 | 0.948 |
| K | 0.007 | 0.001 | 0.001 | 0.010 | 0.001 | 0.000 |
| OH | 1.969 | 1.962 | 1.946 | 1.992 | | |
| F | 0.000 | 0.023 | 0.047 | 0.000 | | |
| Cl | 0.031 | 0.014 | 0.007 | 0.008 | | |
| total | 17.134 | 17.047 | 17.107 | 17.057 | 5.009 | 5.021 |
| Nature | Act | Act | Act | Act | | |
| An% | | | | | 24.9 | 9.2 |

Table 7-7: Microprobe measurements in sample U1309B 16R-1 45-46 cm. Amphibole analyses

| Oxide wt% | Am1 | Am2 | Am3 | Am4 | Am5 | Am6 | Am7 |
|---|---|---|---|---|---|---|---|
| $SiO_2$ | 54.979 | 46.080 | 51.572 | 45.629 | 54.827 | 52.363 | 53.943 |
| $TiO_2$ | 0.209 | 1.424 | 0.386 | 2.089 | 0.113 | 0.280 | 0.221 |
| $Al_2O_3$ | 1.978 | 8.242 | 3.881 | 8.115 | 2.013 | 5.785 | 3.628 |
| $Cr_2O_3$ | 0.024 | 0.008 | 0.161 | 0.056 | 0.000 | 0.000 | 0.008 |
| $Fe_2O_3$ | 0.135 | 5.265 | 1.131 | 1.526 | 0.000 | 0.518 | 0.533 |
| FeO | 10.235 | 9.447 | 13.064 | 12.831 | 10.437 | 6.549 | 6.161 |
| MnO | 0.042 | 0.324 | 0.281 | 0.438 | 0.114 | 0.052 | 0.086 |
| MgO | 17.269 | 13.277 | 14.144 | 12.969 | 16.961 | 18.366 | 19.167 |
| CaO | 13.075 | 11.537 | 12.841 | 11.732 | 13.049 | 13.182 | 13.275 |
| $Na_2O$ | 0.248 | 1.694 | 0.535 | 2.020 | 0.227 | 0.993 | 0.517 |
| $K_2O$ | 0.043 | 0.488 | 0.055 | 0.491 | 0.041 | 0.053 | 0.046 |
| $H_2O$ | 2.113 | 1.938 | 2.004 | 1.922 | 2.108 | 2.133 | 2.077 |
| F | 0.000 | 0.154 | 0.089 | 0.111 | 0.000 | 0.000 | 0.117 |
| Cl | 0.024 | 0.143 | 0.083 | 0.224 | 0.000 | 0.018 | 0.011 |
| Total | 100.373 | 100.020 | 100.226 | 100.152 | 99.891 | 100.292 | 99.790 |
| Si | 7.778 | 6.746 | 7.478 | 6.735 | 7.797 | 7.344 | 7.574 |
| $Al_{(IV)}$ | 0.222 | 1.254 | 0.522 | 1.265 | 0.203 | 0.656 | 0.426 |
| $Al_{(VI)}$ | 0.108 | 0.168 | 0.141 | 0.147 | 0.135 | 0.301 | 0.175 |
| Ti | 0.022 | 0.157 | 0.042 | 0.232 | 0.012 | 0.030 | 0.023 |
| Cr | 0.003 | 0.001 | 0.018 | 0.007 | 0.000 | 0.000 | 0.001 |
| $Fe^{3+}$ | 0.014 | 0.580 | 0.123 | 0.170 | 0.000 | 0.055 | 0.056 |
| $Fe^{2+}$ | 1.211 | 1.157 | 1.584 | 1.584 | 1.241 | 0.768 | 0.723 |
| Mn | 0.005 | 0.040 | 0.035 | 0.055 | 0.014 | 0.006 | 0.010 |
| Mg | 3.643 | 2.898 | 3.058 | 2.854 | 3.596 | 3.841 | 4.013 |
| Ca | 1.982 | 1.810 | 1.995 | 1.855 | 1.988 | 1.981 | 1.997 |
| Na | 0.068 | 0.481 | 0.150 | 0.578 | 0.063 | 0.270 | 0.141 |
| K | 0.008 | 0.091 | 0.010 | 0.092 | 0.007 | 0.009 | 0.008 |
| OH | 1.994 | 1.893 | 1.939 | 1.892 | 2.000 | 1.996 | 1.945 |
| F | 0.000 | 0.071 | 0.041 | 0.052 | 0.000 | 0.000 | 0.052 |
| Cl | 0.006 | 0.035 | 0.020 | 0.056 | 0.000 | 0.004 | 0.003 |
| total | 17.064 | 17.382 | 17.157 | 17.574 | 17.057 | 17.260 | 17.148 |
| Nature | Act | MgHb | MgHb | Ed | Act | MgHb | Act |

Table 7-7 (continued)

| Oxide wt% | Am1 | Am2 | Am3 | Am4 | Am5 | Am6 | Am7 |
|---|---|---|---|---|---|---|---|
| $SiO_2$ | 53.623 | 46.333 | 44.933 | 45.312 | 43.206 | 47.984 | 47.783 |
| $TiO_2$ | 0.229 | 1.646 | 2.157 | 1.993 | 2.033 | 0.628 | 0.569 |
| $Al_2O_3$ | 4.135 | 8.057 | 9.087 | 8.328 | 9.682 | 7.223 | 7.242 |
| $Cr_2O_3$ | 0.000 | 0.000 | 0.000 | 0.073 | 0.081 | 0.000 | 0.008 |
| $Fe_2O_3$ | 0.000 | 4.087 | 2.157 | 1.641 | 1.844 | 2.369 | 2.264 |
| FeO | 6.452 | 10.587 | 12.891 | 12.926 | 13.379 | 13.882 | 13.689 |
| MnO | 0.100 | 0.308 | 0.094 | 0.222 | 0.362 | 0.417 | 0.299 |
| MgO | 18.839 | 13.155 | 12.613 | 12.678 | 11.981 | 12.045 | 12.090 |
| CaO | 13.333 | 11.811 | 11.576 | 11.821 | 11.751 | 11.873 | 11.663 |
| $Na_2O$ | 0.613 | 1.788 | 2.000 | 1.711 | 2.253 | 1.172 | 1.272 |
| $K_2O$ | 0.061 | 0.185 | 0.384 | 0.382 | 0.541 | 0.077 | 0.088 |
| $H_2O$ | 2.054 | 2.028 | 1.980 | 1.909 | 1.928 | 2.027 | 1.893 |
| F | 0.117 | 0.000 | 0.044 | 0.156 | 0.000 | 0.000 | 0.264 |
| Cl | 0.080 | 0.086 | 0.121 | 0.136 | 0.275 | 0.037 | 0.026 |
| Total | 99.637 | 100.071 | 100.037 | 99.288 | 99.317 | 99.734 | 99.150 |
| Si | 7.548 | 6.778 | 6.631 | 6.735 | 6.485 | 7.066 | 7.077 |
| $Al_{(IV)}$ | 0.452 | 1.222 | 1.369 | 1.265 | 1.515 | 0.934 | 0.923 |
| $Al_{(VI)}$ | 0.235 | 0.167 | 0.211 | 0.193 | 0.197 | 0.320 | 0.341 |
| Ti | 0.024 | 0.181 | 0.239 | 0.223 | 0.230 | 0.070 | 0.063 |
| Cr | 0.000 | 0.000 | 0.000 | 0.009 | 0.010 | 0.000 | 0.001 |
| $Fe^{3+}$ | 0.000 | 0.450 | 0.240 | 0.184 | 0.208 | 0.263 | 0.252 |
| $Fe^{2+}$ | 0.760 | 1.295 | 1.591 | 1.607 | 1.679 | 1.710 | 1.695 |
| Mn | 0.012 | 0.038 | 0.012 | 0.028 | 0.046 | 0.052 | 0.038 |
| Mg | 3.954 | 2.869 | 2.775 | 2.809 | 2.681 | 2.645 | 2.670 |
| Ca | 2.011 | 1.851 | 1.830 | 1.882 | 1.890 | 1.873 | 1.851 |
| Na | 0.167 | 0.507 | 0.572 | 0.493 | 0.656 | 0.335 | 0.365 |
| K | 0.011 | 0.035 | 0.072 | 0.072 | 0.104 | 0.014 | 0.017 |
| OH | 1.929 | 1.979 | 1.949 | 1.892 | 1.930 | 1.991 | 1.870 |
| F | 0.052 | 0.000 | 0.021 | 0.073 | 0.000 | 0.000 | 0.124 |
| Cl | 0.019 | 0.021 | 0.030 | 0.034 | 0.070 | 0.009 | 0.007 |
| total | 17.173 | 17.393 | 17.542 | 17.500 | 17.700 | 17.281 | 17.292 |
| Nature | Act | MgHb | Ed | MgHb | MgHast | MgHb | MgHb |

Table 7-8: Microprobe measurements in sample U1309B 16R-1 45-46 cm. Plagioclase analyses

| Oxide wt% | Plg1 | Plg2 | Plg3 | Plg4 | Plg5 | Plg6 | Plg7 |
|---|---|---|---|---|---|---|---|
| $SiO_2$ | 54.668 | 67.599 | 52.292 | 65.382 | 67.714 | 66.804 | 51.541 |
| $TiO_2$ | 0.000 | 0.007 | 0.000 | 0.000 | 0.000 | 0.000 | 0.000 |
| $Al_2O_3$ | 28.805 | 20.995 | 30.160 | 22.241 | 19.011 | 20.979 | 30.920 |
| $Fe_2O_3$ | 0.215 | 0.114 | 0.338 | 0.231 | 1.002 | 0.000 | 0.200 |
| MnO | 0.143 | 0.000 | 0.000 | 0.000 | 0.042 | 0.125 | 0.020 |
| MgO | 0.000 | 0.004 | 0.039 | 0.000 | 0.911 | 0.000 | 0.000 |
| CaO | 11.811 | 1.400 | 12.789 | 3.186 | 1.186 | 1.648 | 13.638 |
| $Na_2O$ | 5.139 | 11.281 | 4.384 | 9.974 | 10.910 | 10.882 | 3.987 |
| $K_2O$ | 0.036 | 0.033 | 0.030 | 0.042 | 0.041 | 0.021 | 0.006 |
| Total | 100.817 | 101.433 | 100.032 | 101.056 | 100.817 | 100.459 | 100.312 |
| Si | 2.453 | 2.925 | 2.373 | 2.851 | 2.953 | 2.918 | 2.337 |
| Ti | 0.000 | 0.000 | 0.000 | 0.000 | 0.000 | 0.000 | 0.000 |
| Al | 1.523 | 1.070 | 1.613 | 1.143 | 0.977 | 1.080 | 1.652 |
| Fe3 | 0.007 | 0.004 | 0.012 | 0.008 | 0.033 | 0.000 | 0.007 |
| Mn | 0.005 | 0.000 | 0.000 | 0.000 | 0.002 | 0.005 | 0.001 |
| Mg | 0.000 | 0.000 | 0.003 | 0.000 | 0.059 | 0.000 | 0.000 |
| Ca | 0.568 | 0.065 | 0.622 | 0.149 | 0.055 | 0.077 | 0.662 |
| Na | 0.447 | 0.946 | 0.386 | 0.843 | 0.923 | 0.922 | 0.350 |
| K | 0.002 | 0.002 | 0.002 | 0.002 | 0.002 | 0.001 | 0.000 |
| total | 5.006 | 5.012 | 5.009 | 4.996 | 5.004 | 5.003 | 5.009 |
| An% | 57.3 | 6.5 | 62.4 | 14.9 | 11.6 | 8.2 | 66.3 |

Table 7-8 (continued)

| Oxide wt% | Plg8 | Plg9 | Plg10 | Plg11 | Plg12 | Plg13 | Plg14 |
|---|---|---|---|---|---|---|---|
| $SiO_2$ | 66.454 | 53.393 | 65.181 | 52.494 | 65.101 | 69.019 | 65.040 |
| $TiO_2$ | 0.000 | 0.000 | 0.000 | 0.064 | 0.000 | 0.000 | 0.000 |
| $Al_2O_3$ | 21.085 | 29.903 | 21.642 | 30.225 | 21.619 | 20.037 | 22.265 |
| $Fe_2O_3$ | 0.113 | 0.417 | 0.000 | 0.128 | 0.090 | 0.032 | 0.000 |
| MnO | 0.053 | 0.000 | 0.000 | 0.000 | 0.074 | 0.046 | 0.000 |
| MgO | 0.037 | 0.039 | 0.000 | 0.000 | 0.000 | 0.007 | 0.010 |
| CaO | 0.123 | 12.157 | 2.613 | 1.099 | 2.449 | 0.625 | 2.968 |
| $Na_2O$ | 10.323 | 4.800 | 10.224 | 3.943 | 10.233 | 11.549 | 9.745 |
| $K_2O$ | 0.048 | 0.055 | 0.023 | 0.000 | 0.033 | 0.041 | 0.035 |
| Total | 98.236 | 100.764 | 99.683 | 87.953 | 99.599 | 101.356 | 100.063 |
| Si | 2.944 | 2.401 | 2.875 | 2.566 | 2.875 | 2.978 | 2.857 |
| Ti | 0.000 | 0.000 | 0.000 | 0.002 | 0.000 | 0.000 | 0.000 |
| Al | 1.101 | 1.585 | 1.125 | 1.741 | 1.125 | 1.019 | 1.153 |
| Fe3 | 0.004 | 0.014 | 0.000 | 0.005 | 0.003 | 0.001 | 0.000 |
| Mn | 0.002 | 0.000 | 0.000 | 0.000 | 0.003 | 0.002 | 0.000 |
| Mg | 0.002 | 0.003 | 0.000 | 0.000 | 0.000 | 0.000 | 0.001 |
| Ca | 0.006 | 0.586 | 0.124 | 0.058 | 0.116 | 0.029 | 0.140 |
| Na | 0.887 | 0.419 | 0.874 | 0.374 | 0.876 | 0.966 | 0.830 |
| K | 0.003 | 0.003 | 0.001 | 0.000 | 0.002 | 0.002 | 0.002 |
| total | 4.948 | 5.010 | 5.000 | 4.746 | 5.000 | 4.997 | 4.982 |
| An% | 1.0 | 58.8 | 12.4 | 5.8 | 11.9 | 3.1 | 14.0 |

## Analyses in IODP Hole U1309D

Table 7-9: Microprobe measurements in sample U1309D 1R-1 41-44 cm. Amphibole analyses

| Oxide wt% | Am1 | Am2 | Am3 | Am4 | Am5 |
|---|---|---|---|---|---|
| $SiO_2$ | 46.34 | 49.25 | 48.39 | 50.77 | 49.12 |
| $TiO_2$ | 0.33 | 0.40 | 0.39 | 0.31 | 0.14 |
| $Al_2O_3$ | 7.98 | 5.93 | 7.10 | 4.40 | 4.77 |
| $Cr_2O_3$ | 0.00 | 0.30 | 0.32 | 0.00 | 0.00 |
| $Fe_2O_3$ | 3.70 | 1.18 | 2.17 | 2.52 | 3.61 |
| FeO | 14.89 | 14.85 | 12.60 | 12.63 | 15.01 |
| MnO | 0.12 | 0.08 | 0.25 | 0.24 | 0.25 |
| MgO | 10.56 | 12.12 | 12.94 | 13.94 | 11.77 |
| CaO | 12.31 | 12.64 | 12.03 | 11.96 | 11.60 |
| $Na_2O$ | 0.92 | 0.67 | 1.19 | 0.75 | 0.70 |
| $K_2O$ | 0.09 | 0.06 | 0.06 | 0.06 | 0.05 |
| $H_2O$ | 1.97 | 1.99 | 2.01 | 2.04 | 1.92 |
| F | 0.07 | 0.09 | 0.07 | 0.04 | 0.20 |
| Cl | 0.00 | 0.00 | 0.01 | 0.00 | 0.00 |
| Total | 99.27 | 99.55 | 99.53 | 99.66 | 99.15 |
| Si | 6.926 | 7.259 | 7.094 | 7.401 | 7.317 |
| $Al_{(IV)}$ | 1.074 | 0.741 | 0.906 | 0.599 | 0.683 |
| $Al_{(VI)}$ | 0.332 | 0.289 | 0.322 | 0.158 | 0.154 |
| Ti | 0.037 | 0.044 | 0.043 | 0.033 | 0.015 |
| Cr | 0.000 | 0.035 | 0.038 | 0.000 | 0.000 |
| $Fe^{3+}$ | 0.416 | 0.131 | 0.239 | 0.277 | 0.404 |
| $Fe^{2+}$ | 1.861 | 1.830 | 1.545 | 1.540 | 1.870 |
| Mn | 0.015 | 0.010 | 0.032 | 0.030 | 0.032 |
| Mg | 2.352 | 2.664 | 2.828 | 3.031 | 2.614 |
| Ca | 1.972 | 1.996 | 1.889 | 1.868 | 1.850 |
| Na | 0.267 | 0.191 | 0.339 | 0.212 | 0.202 |
| K | 0.016 | 0.012 | 0.011 | 0.010 | 0.010 |
| OH | 1.968 | 1.959 | 1.967 | 1.980 | 1.908 |
| F | 0.031 | 0.041 | 0.031 | 0.020 | 0.092 |
| Cl | 0.001 | 0.000 | 0.002 | 0.000 | 0.000 |
| total | 17.268 | 17.201 | 17.286 | 17.160 | 17.153 |
| Nature | MgHb | MgHb | MgHb | MgHb | MgHb |

Table 7-9 (continued)

| Oxide wt% | Am6 | Am7 | Am8 | Am9 | Am10 |
|---|---|---|---|---|---|
| $SiO_2$ | 49.16 | 49.43 | 47.55 | 50.35 | 48.55 |
| $TiO_2$ | 0.39 | 0.30 | 0.34 | 0.42 | 0.49 |
| $Al_2O_3$ | 5.70 | 4.89 | 6.30 | 6.00 | 5.77 |
| $Cr_2O_3$ | 0.04 | 0.40 | 0.41 | 0.16 | 0.11 |
| $Fe_2O_3$ | 3.09 | 2.82 | 5.05 | 3.55 | 2.95 |
| FeO | 12.49 | 12.53 | 12.01 | 7.97 | 12.35 |
| MnO | 0.27 | 0.26 | 0.37 | 0.26 | 0.27 |
| MgO | 13.30 | 13.40 | 12.73 | 16.35 | 13.21 |
| CaO | 11.42 | 11.77 | 10.95 | 10.80 | 12.00 |
| $Na_2O$ | 0.98 | 0.92 | 1.34 | 1.16 | 1.05 |
| $K_2O$ | 0.06 | 0.06 | 0.05 | 0.04 | 0.07 |
| $H_2O$ | 2.00 | 1.96 | 1.98 | 2.00 | 1.94 |
| F | 0.07 | 0.16 | 0.09 | 0.18 | 0.18 |
| Cl | 0.03 | 0.00 | 0.00 | 0.01 | 0.00 |
| Total | 98.99 | 98.90 | 99.18 | 99.26 | 98.93 |
| Si | 7.237 | 7.295 | 7.040 | 7.232 | 7.174 |
| $Al_{(IV)}$ | 0.763 | 0.705 | 0.960 | 0.768 | 0.826 |
| $Al_{(VI)}$ | 0.226 | 0.147 | 0.140 | 0.248 | 0.178 |
| Ti | 0.044 | 0.033 | 0.038 | 0.045 | 0.054 |
| Cr | 0.005 | 0.046 | 0.048 | 0.018 | 0.012 |
| $Fe^{3+}$ | 0.342 | 0.314 | 0.563 | 0.384 | 0.328 |
| $Fe^{2+}$ | 1.537 | 1.546 | 1.487 | 0.957 | 1.526 |
| Mn | 0.033 | 0.033 | 0.047 | 0.032 | 0.034 |
| Mg | 2.919 | 2.949 | 2.809 | 3.501 | 2.910 |
| Ca | 1.802 | 1.861 | 1.737 | 1.663 | 1.900 |
| Na | 0.280 | 0.262 | 0.384 | 0.322 | 0.301 |
| K | 0.011 | 0.012 | 0.010 | 0.008 | 0.014 |
| OH | 1.962 | 1.927 | 1.959 | 1.915 | 1.917 |
| F | 0.031 | 0.073 | 0.041 | 0.082 | 0.083 |
| Cl | 0.008 | 0.000 | 0.000 | 0.003 | 0.000 |
| total | 17.197 | 17.203 | 17.263 | 17.178 | 17.257 |
| Nature | MgHb | MgHb | MgHb | MgHb | MgHb |

Table 7-10: Microprobe measurements in sample U1309D 1R-1 41-44 cm. Plagioclase analyses

| Oxide wt% | Core of lath 1 | Edge of lath 1 | Core of lath 2 | Edge of lath 2 | Core of lath 3 | Edge of lath 3 | Core of lath 4 | Edge of lath 4 | Core of lath 5 | Edge of lath 5 |
|---|---|---|---|---|---|---|---|---|---|---|
| $SiO_2$ | 67.26 | 54.79 | 68.17 | 53.70 | 51.81 | 68.88 | 51.79 | 60.96 | 52.39 | 61.50 |
| $TiO_2$ | 0.00 | 0.06 | 0.00 | 0.04 | 0.09 | 0.00 | 0.08 | 0.00 | 0.07 | 0.00 |
| $Al_2O_3$ | 21.29 | 27.98 | 20.33 | 28.49 | 30.69 | 20.60 | 30.56 | 24.20 | 29.37 | 24.38 |
| $Fe_2O_3$ | 0.03 | 1.03 | 0.11 | 1.08 | 0.61 | 0.20 | 0.59 | 0.76 | 1.02 | 0.54 |
| MnO | 0.00 | 0.00 | 0.07 | 0.01 | 0.04 | 0.00 | 0.04 | 0.04 | 0.01 | 0.08 |
| MgO | 0.00 | 0.13 | 0.00 | 0.16 | 0.23 | 0.00 | 0.15 | 0.04 | 0.15 | 0.02 |
| CaO | 1.78 | 11.46 | 0.69 | 11.75 | 13.98 | 1.02 | 13.90 | 6.21 | 12.61 | 6.39 |
| $Na_2O$ | 10.46 | 5.25 | 10.95 | 4.93 | 3.64 | 11.02 | 3.63 | 8.16 | 4.52 | 7.98 |
| $K_2O$ | 0.01 | 0.06 | 0.04 | 0.04 | 0.04 | 0.05 | 0.01 | 0.13 | 0.05 | 0.12 |
| Total | 100.82 | 100.74 | 100.36 | 100.19 | 101.13 | 101.76 | 100.75 | 100.48 | 100.17 | 101.01 |
| Si | 2.921 | 2.464 | 2.966 | 2.432 | 2.334 | 2.959 | 2.340 | 2.705 | 2.380 | 2.711 |
| Ti | 0.000 | 0.002 | 0.000 | 0.001 | 0.003 | 0.000 | 0.003 | 0.000 | 0.002 | 0.000 |
| Al | 1.090 | 1.483 | 1.042 | 1.520 | 1.629 | 1.043 | 1.627 | 1.266 | 1.572 | 1.267 |
| Fe3 | 0.001 | 0.035 | 0.004 | 0.037 | 0.021 | 0.006 | 0.020 | 0.025 | 0.035 | 0.018 |
| Mn | 0.000 | 0.000 | 0.003 | 0.000 | 0.002 | 0.000 | 0.002 | 0.002 | 0.000 | 0.003 |
| Mg | 0.000 | 0.008 | 0.000 | 0.011 | 0.015 | 0.000 | 0.010 | 0.002 | 0.010 | 0.001 |
| Ca | 0.083 | 0.552 | 0.032 | 0.570 | 0.675 | 0.047 | 0.673 | 0.295 | 0.614 | 0.302 |
| Na | 0.880 | 0.458 | 0.924 | 0.433 | 0.318 | 0.918 | 0.318 | 0.702 | 0.398 | 0.682 |
| K | 0.000 | 0.003 | 0.002 | 0.002 | 0.002 | 0.003 | 0.001 | 0.007 | 0.003 | 0.007 |
| total | 4.975 | 5.006 | 4.973 | 5.006 | 4.998 | 4.976 | 4.993 | 5.004 | 5.014 | 4.991 |
| An% | 8 | 56 | 3 | 58 | 69 | 5 | 68 | 30 | 62 | 30 |

Table 7-11: Microprobe measurements in sample U1309D 1R-3 9-11 cm. Amphibole analyses

| Oxide wt% | Am1 | Am2 | Am3 | Am4 | Am5 | Am6 | Am7 | Am8 | Am9 | Am10 | Am11 |
|---|---|---|---|---|---|---|---|---|---|---|---|
| $SiO_2$ | 45.584 | 53.161 | 53.597 | 53.258 | 45.979 | 46.775 | 53.663 | 45.267 | 51.515 | 54.400 | 52.115 |
| $TiO_2$ | 1.949 | 0.244 | 0.057 | 0.092 | 1.483 | 1.048 | 0.308 | 2.008 | 0.012 | 0.124 | 0.228 |
| $Al_2O_3$ | 8.942 | 5.317 | 4.859 | 4.187 | 9.744 | 9.325 | 4.658 | 10.015 | 5.750 | 2.054 | 6.746 |
| $Cr_2O_3$ | 0.168 | 0.040 | 0.000 | 0.000 | 0.013 | 0.042 | 0.016 | 0.013 | 0.029 | 0.000 | 0.000 |
| $Fe_2O_3$ | 5.342 | 1.144 | 1.488 | 2.636 | 3.370 | 4.400 | 2.792 | 2.866 | 3.105 | 1.272 | 2.778 |
| FeO | 6.108 | 4.518 | 4.604 | 3.582 | 6.794 | 4.691 | 2.049 | 7.301 | 4.196 | 8.904 | 4.382 |
| MnO | 0.163 | 0.022 | 0.073 | 0.079 | 0.081 | 0.174 | 0.000 | 0.119 | 0.158 | 0.144 | 0.110 |
| MgO | 15.168 | 21.207 | 19.647 | 19.541 | 15.686 | 16.928 | 20.737 | 15.327 | 18.885 | 17.791 | 20.117 |
| CaO | 11.565 | 11.106 | 12.846 | 12.315 | 11.733 | 11.726 | 12.504 | 11.864 | 12.746 | 12.373 | 10.515 |
| $Na_2O$ | 2.018 | 0.890 | 0.748 | 0.806 | 1.887 | 1.824 | 0.766 | 1.815 | 1.022 | 0.334 | 1.288 |
| $K_2O$ | 0.235 | 0.029 | 0.051 | 0.066 | 0.237 | 0.253 | 0.053 | 0.307 | 0.071 | 0.025 | 0.042 |
| $H_2O$ | 2.058 | 2.144 | 2.145 | 2.097 | 2.068 | 2.082 | 2.158 | 2.059 | 2.115 | 2.105 | 2.151 |
| F | 0.031 | 0.057 | 0.035 | 0.123 | 0.015 | 0.035 | 0.023 | 0.015 | 0.049 | 0.013 | 0.047 |
| Cl | 99.331 | 99.879 | 100.151 | 98.782 | 99.089 | 99.303 | 99.727 | 98.976 | 99.654 | 99.540 | 100.519 |
| Total | 45.584 | 53.161 | 53.597 | 53.258 | 45.979 | 46.775 | 53.663 | 45.267 | 51.515 | 54.400 | 52.115 |
| Si | 6.615 | 7.382 | 7.459 | 7.504 | 6.654 | 6.706 | 7.435 | 6.580 | 7.258 | 7.736 | 7.224 |
| $Al_{(IV)}$ | 1.385 | 0.618 | 0.541 | 0.496 | 1.346 | 1.294 | 0.565 | 1.420 | 0.742 | 0.264 | 0.776 |
| $Al_{(VI)}$ | 0.144 | 0.253 | 0.256 | 0.199 | 0.316 | 0.281 | 0.196 | 0.295 | 0.213 | 0.080 | 0.326 |
| Ti | 0.213 | 0.025 | 0.006 | 0.010 | 0.161 | 0.113 | 0.032 | 0.220 | 0.001 | 0.013 | 0.024 |
| Cr | 0.019 | 0.004 | 0.000 | 0.000 | 0.001 | 0.005 | 0.002 | 0.001 | 0.003 | 0.000 | 0.000 |
| $Fe^{3+}$ | 0.583 | 0.120 | 0.156 | 0.280 | 0.367 | 0.475 | 0.291 | 0.314 | 0.329 | 0.136 | 0.290 |
| $Fe^{2+}$ | 0.741 | 0.525 | 0.536 | 0.422 | 0.822 | 0.562 | 0.237 | 0.887 | 0.494 | 1.059 | 0.508 |
| Mn | 0.020 | 0.003 | 0.009 | 0.009 | 0.010 | 0.021 | 0.000 | 0.015 | 0.019 | 0.017 | 0.013 |
| Mg | 3.282 | 4.391 | 4.076 | 4.105 | 3.385 | 3.618 | 4.284 | 3.322 | 3.967 | 3.772 | 4.157 |
| Ca | 1.798 | 1.652 | 1.915 | 1.859 | 1.819 | 1.801 | 1.856 | 1.848 | 1.924 | 1.885 | 1.562 |
| Na | 0.568 | 0.240 | 0.202 | 0.220 | 0.529 | 0.507 | 0.206 | 0.511 | 0.279 | 0.092 | 0.346 |
| K | 0.044 | 0.005 | 0.009 | 0.012 | 0.044 | 0.046 | 0.009 | 0.057 | 0.013 | 0.005 | 0.007 |
| OH | 1.992 | 1.987 | 1.992 | 1.971 | 1.996 | 1.991 | 1.995 | 1.996 | 1.988 | 1.997 | 1.989 |
| Cl | 0.008 | 0.013 | 0.008 | 0.029 | 0.004 | 0.009 | 0.005 | 0.004 | 0.012 | 0.003 | 0.011 |
| total | 17.412 | 17.217 | 17.164 | 17.115 | 17.456 | 17.430 | 17.113 | 17.470 | 17.243 | 17.059 | 17.233 |
| Nature | MgHb | MgHb | MgHb | MgHb | MgHb | MgHb | MgHb | MgHb | MgHb | Act | MgHb |

Table 7-12: Microprobe measurements in sample U1309D 1R-3 9-11 cm. Plagioclase analyses

| Oxide wt% | Plg1 | Plg2 | Plg3 | Plg4 | Plg5 | Plg6 | Plg7 |
|---|---|---|---|---|---|---|---|
| $SiO_2$ | 45.962 | 52.862 | 47.042 | 49.015 | 44.376 | 45.365 | 42.458 |
| $TiO_2$ | 0.000 | 0.000 | 0.000 | 0.000 | 0.000 | 0.043 | 0.048 |
| $Al_2O_3$ | 34.093 | 22.720 | 33.616 | 32.281 | 35.076 | 35.365 | 34.885 |
| $Fe_2O_3$ | 0.347 | 2.314 | 0.619 | 0.553 | 0.559 | 0.388 | 1.640 |
| MnO | 0.076 | 0.000 | 0.000 | 0.019 | 0.059 | 0.000 | 0.000 |
| MgO | 0.036 | 5.155 | 0.082 | 0.280 | 1.000 | 0.052 | 0.910 |
| CaO | 17.147 | 4.525 | 16.557 | 15.398 | 18.303 | 18.527 | 17.758 |
| $Na_2O$ | 1.495 | 5.881 | 2.091 | 2.840 | 0.691 | 0.988 | 0.776 |
| $K_2O$ | 0.005 | 0.060 | 0.023 | 0.014 | 0.077 | 0.009 | 0.051 |
| Total | 99.161 | 93.517 | 100.030 | 100.400 | 100.141 | 100.737 | 98.526 |
| Si | 2.131 | 2.536 | 2.161 | 2.235 | 2.049 | 2.078 | 2.002 |
| Ti | 0.000 | 0.000 | 0.000 | 0.000 | 0.000 | 0.001 | 0.002 |
| Al | 1.863 | 1.284 | 1.820 | 1.735 | 1.909 | 1.909 | 1.938 |
| Fe3 | 0.012 | 0.084 | 0.021 | 0.019 | 0.019 | 0.013 | 0.058 |
| Mn | 0.003 | 0.000 | 0.000 | 0.001 | 0.002 | 0.000 | 0.000 |
| Mg | 0.002 | 0.369 | 0.006 | 0.019 | 0.069 | 0.004 | 0.064 |
| Ca | 0.852 | 0.233 | 0.815 | 0.752 | 0.905 | 0.909 | 0.897 |
| Na | 0.134 | 0.547 | 0.186 | 0.251 | 0.062 | 0.088 | 0.071 |
| K | 0.000 | 0.004 | 0.001 | 0.001 | 0.005 | 0.001 | 0.003 |
| total | 4.999 | 5.056 | 5.011 | 5.014 | 5.020 | 5.003 | 5.035 |
| An% | 85.7 | 60.1 | 82.1 | 77.2 | 97.7 | 91.3 | 96.1 |

Table 7-13: Microprobe measurements in sample U1309D 4R-1 135-137 cm. Amphibole analyses

| Oxide wt% | Am1 | Am2 | Am3 | Am4 | Am5 | Am6 | Am7 | Am8 | Am9 | Am10 | Am11 |
|---|---|---|---|---|---|---|---|---|---|---|---|
| $SiO_2$ | 51.157 | 50.225 | 50.883 | 50.251 | 50.289 | 55.167 | 51.316 | 54.702 | 52.552 | 50.223 | 51.871 |
| $TiO_2$ | 0.462 | 0.890 | 0.294 | 0.208 | 0.126 | 0.041 | 0.232 | 0.264 | 0.136 | 0.154 | 0.146 |
| $Al_2O_3$ | 5.234 | 4.624 | 5.333 | 5.285 | 4.858 | 0.505 | 5.623 | 2.211 | 4.956 | 4.962 | 3.480 |
| $Cr_2O_3$ | 0.130 | 0.260 | 0.128 | 0.028 | 0.000 | 0.030 | 0.000 | 0.000 | 0.033 | 0.020 | 0.018 |
| $Fe_2O_3$ | 3.142 | 3.743 | 4.259 | 3.979 | 3.202 | 0.000 | 4.315 | 1.321 | 2.895 | 3.090 | 1.642 |
| FeO | 4.459 | 8.580 | 4.166 | 6.068 | 12.811 | 11.334 | 5.879 | 7.445 | 6.150 | 12.749 | 13.863 |
| MnO | 0.063 | 0.217 | 0.145 | 0.078 | 0.137 | 0.079 | 0.124 | 0.138 | 0.068 | 0.192 | 0.072 |
| MgO | 18.766 | 16.223 | 18.740 | 17.416 | 13.603 | 16.452 | 17.879 | 19.437 | 18.320 | 13.592 | 14.044 |
| CaO | 11.790 | 11.473 | 11.951 | 11.882 | 11.934 | 13.022 | 11.324 | 12.149 | 12.183 | 11.968 | 11.766 |
| $Na_2O$ | 1.279 | 1.162 | 1.293 | 1.231 | 0.940 | 0.132 | 1.282 | 0.531 | 0.930 | 0.921 | 0.641 |
| $K_2O$ | 0.097 | 0.054 | 0.091 | 0.023 | 0.027 | 0.000 | 0.021 | 0.019 | 0.041 | 0.082 | 0.038 |
| $H_2O$ | 2.069 | 2.073 | 2.082 | 2.059 | 2.042 | 2.073 | 2.111 | 2.120 | 2.123 | 2.051 | 2.041 |
| F | 0.150 | 0.022 | 0.129 | 0.090 | 0.059 | 0.021 | 0.048 | 0.072 | 0.050 | 0.024 | 0.064 |
| Cl | 98.799 | 99.546 | 99.494 | 98.599 | 100.028 | 98.856 | 100.154 | 100.410 | 100.437 | 100.028 | 99.687 |
| Total | 51.157 | 50.225 | 50.883 | 50.251 | 50.289 | 55.167 | 51.316 | 54.702 | 52.552 | 50.223 | 51.871 |
| Si | 7.278 | 7.243 | 7.213 | 7.236 | 7.330 | 7.956 | 7.247 | 7.668 | 7.376 | 7.319 | 7.559 |
| $Al_{(IV)}$ | 0.722 | 0.757 | 0.787 | 0.764 | 0.670 | 0.044 | 0.753 | 0.332 | 0.624 | 0.681 | 0.441 |
| $Al_{(VI)}$ | 0.156 | 0.029 | 0.104 | 0.133 | 0.165 | 0.042 | 0.183 | 0.034 | 0.196 | 0.172 | 0.156 |
| Ti | 0.049 | 0.097 | 0.031 | 0.023 | 0.014 | 0.004 | 0.025 | 0.028 | 0.014 | 0.017 | 0.016 |
| Cr | 0.015 | 0.030 | 0.014 | 0.003 | 0.000 | 0.003 | 0.000 | 0.000 | 0.004 | 0.002 | 0.002 |
| $Fe^{3+}$ | 0.336 | 0.406 | 0.454 | 0.431 | 0.351 | 0.000 | 0.459 | 0.139 | 0.306 | 0.339 | 0.180 |
| $Fe^{2+}$ | 0.531 | 1.035 | 0.494 | 0.731 | 1.562 | 1.367 | 0.694 | 0.873 | 0.722 | 1.554 | 1.689 |
| Mn | 0.008 | 0.027 | 0.017 | 0.010 | 0.017 | 0.010 | 0.015 | 0.016 | 0.008 | 0.024 | 0.009 |
| Mg | 3.981 | 3.488 | 3.960 | 3.739 | 2.956 | 3.538 | 3.765 | 4.062 | 3.834 | 2.953 | 3.051 |
| Ca | 1.797 | 1.773 | 1.815 | 1.833 | 1.864 | 2.012 | 1.713 | 1.825 | 1.832 | 1.869 | 1.837 |
| Na | 0.353 | 0.325 | 0.355 | 0.344 | 0.266 | 0.037 | 0.351 | 0.144 | 0.253 | 0.260 | 0.181 |
| K | 0.018 | 0.010 | 0.016 | 0.004 | 0.005 | 0.000 | 0.004 | 0.003 | 0.007 | 0.015 | 0.007 |
| OH | 1.964 | 1.995 | 1.969 | 1.978 | 1.985 | 1.995 | 1.988 | 1.983 | 1.988 | 1.994 | 1.984 |
| Cl | 0.036 | 0.005 | 0.031 | 0.022 | 0.015 | 0.005 | 0.011 | 0.017 | 0.012 | 0.006 | 0.016 |
| total | 17.243 | 17.217 | 17.262 | 17.250 | 17.199 | 17.013 | 17.208 | 17.125 | 17.175 | 17.205 | 17.129 |
| Nature | MgHb | MgHb | MgHb | MgHb | MgHb | Act | MgHb | Act | MgHb | MgHb | Act |

Table 7-13 (continued)

| Oxide wt% | Am12 | Am13 | Am14 | Am15 | Am16 |
|---|---|---|---|---|---|
| $SiO_2$ | 53.400 | 53.660 | 56.688 | 50.384 | 51.214 |
| $TiO_2$ | 0.355 | 0.628 | 0.060 | 0.384 | 0.144 |
| $Al_2O_3$ | 2.893 | 2.846 | 0.967 | 5.826 | 4.102 |
| $Cr_2O_3$ | 0.127 | 0.170 | 0.007 | 0.094 | 0.043 |
| $Fe_2O_3$ | 2.678 | 2.582 | 0.778 | 4.680 | 2.836 |
| FeO | 6.890 | 6.015 | 5.081 | 6.073 | 13.034 |
| MnO | 0.164 | 0.114 | 0.178 | 0.088 | 0.162 |
| MgO | 18.505 | 19.123 | 21.792 | 17.468 | 13.858 |
| CaO | 11.833 | 12.275 | 12.035 | 11.493 | 11.536 |
| $Na_2O$ | 0.697 | 0.651 | 0.220 | 1.333 | 0.781 |
| $K_2O$ | 0.033 | 0.011 | 0.013 | 0.018 | 0.051 |
| $H_2O$ | 2.098 | 2.128 | 2.154 | 2.084 | 2.051 |
| F | 0.080 | 0.030 | 0.041 | 0.103 | 0.032 |
| Cl | 99.753 | 100.234 | 100.014 | 100.027 | 99.844 |
| Total | 53.400 | 53.660 | 56.688 | 50.384 | 51.214 |
| Si | 7.559 | 7.533 | 7.851 | 7.160 | 7.455 |
| $Al_{(IV)}$ | 0.441 | 0.467 | 0.149 | 0.840 | 0.545 |
| $Al_{(VI)}$ | 0.041 | 0.004 | 0.009 | 0.135 | 0.159 |
| Ti | 0.038 | 0.066 | 0.006 | 0.041 | 0.016 |
| Cr | 0.014 | 0.019 | 0.001 | 0.011 | 0.005 |
| $Fe^{3+}$ | 0.285 | 0.273 | 0.081 | 0.500 | 0.311 |
| $Fe^{2+}$ | 0.816 | 0.706 | 0.588 | 0.722 | 1.587 |
| Mn | 0.020 | 0.014 | 0.021 | 0.011 | 0.020 |
| Mg | 3.905 | 4.002 | 4.500 | 3.701 | 3.008 |
| Ca | 1.795 | 1.846 | 1.786 | 1.750 | 1.799 |
| Na | 0.191 | 0.177 | 0.059 | 0.367 | 0.220 |
| K | 0.006 | 0.002 | 0.002 | 0.003 | 0.009 |
| OH | 1.981 | 1.993 | 1.990 | 1.975 | 1.992 |
| F | 0.019 | 0.007 | 0.010 | 0.025 | 0.008 |
| Cl | 17.111 | 17.109 | 17.053 | 17.241 | 17.134 |
| total | 0.014 | 0.019 | 0.001 | 0.011 | 0.005 |
| Nature | Act | Act | Act | MgHb | MgHb |

Table 7-14: Microprobe measurements in sample U1309D 4R-1 135-137 cm. Plagioclase analyses

| Oxide wt% | Plg 1 | Plg 2 | Plg 3 | Plg 4 | Plg 5 | Plg 6 | Plg 7 | Plg 8 | Plg 9 | Plg 10 | Plg 11 | Plg 12 |
|---|---|---|---|---|---|---|---|---|---|---|---|---|
| $SiO_2$ | 68.251 | 52.284 | 65.291 | 59.935 | 51.292 | 67.850 | 58.900 | 51.669 | 67.229 | 52.079 | 68.555 | 51.226 |
| $TiO_2$ | 0.000 | 0.000 | 0.000 | 0.000 | 0.000 | 0.000 | 0.000 | 0.000 | 0.000 | 0.018 | 0.000 | 0.000 |
| $Al_2O_3$ | 20.211 | 30.379 | 22.156 | 25.981 | 30.920 | 20.522 | 26.067 | 30.630 | 20.818 | 30.531 | 20.089 | 30.686 |
| $Fe_2O_3$ | 0.038 | 0.142 | 0.087 | 0.020 | 0.210 | 0.000 | 0.044 | 0.479 | 0.106 | 0.424 | 0.180 | 0.136 |
| MnO | 0.000 | 0.000 | 0.000 | 0.020 | 0.000 | 0.000 | 0.000 | 0.040 | 0.000 | 0.000 | 0.000 | 0.000 |
| MgO | 0.012 | 0.000 | 0.015 | 0.009 | 0.049 | 0.007 | 0.000 | 0.043 | 0.000 | 0.026 | 0.021 | 0.048 |
| CaO | 0.992 | 13.577 | 3.007 | 7.645 | 13.946 | 0.991 | 7.751 | 13.215 | 1.305 | 13.572 | 0.577 | 13.733 |
| $Na_2O$ | 11.397 | 4.249 | 10.051 | 7.619 | 3.545 | 11.455 | 7.316 | 3.750 | 11.051 | 3.817 | 11.687 | 3.988 |
| $K_2O$ | 0.032 | 0.016 | 0.009 | 0.011 | 0.025 | 0.045 | 0.015 | 0.000 | 0.015 | 0.000 | 0.036 | 0.027 |
| Total | 100.933 | 100.647 | 100.616 | 101.240 | 99.987 | 100.870 | 100.093 | 99.826 | 100.524 | 100.467 | 101.145 | 99.844 |
| Si | 2.961 | 2.362 | 2.857 | 2.643 | 2.332 | 2.947 | 2.627 | 2.350 | 2.931 | 2.355 | 2.967 | 2.335 |
| Ti | 0.000 | 0.000 | 0.000 | 0.000 | 0.000 | 0.000 | 0.000 | 0.000 | 0.000 | 0.001 | 0.000 | 0.000 |
| Al | 1.033 | 1.617 | 1.142 | 1.350 | 1.657 | 1.051 | 1.370 | 1.642 | 1.070 | 1.627 | 1.025 | 1.648 |
| Fe3 | 0.001 | 0.005 | 0.003 | 0.001 | 0.007 | 0.000 | 0.001 | 0.016 | 0.003 | 0.014 | 0.006 | 0.005 |
| Mn | 0.000 | 0.000 | 0.000 | 0.001 | 0.000 | 0.000 | 0.000 | 0.002 | 0.000 | 0.000 | 0.000 | 0.000 |
| Mg | 0.001 | 0.000 | 0.001 | 0.001 | 0.003 | 0.000 | 0.000 | 0.003 | 0.000 | 0.002 | 0.001 | 0.003 |
| Ca | 0.046 | 0.657 | 0.141 | 0.361 | 0.679 | 0.046 | 0.370 | 0.644 | 0.061 | 0.658 | 0.027 | 0.671 |
| Na | 0.959 | 0.372 | 0.853 | 0.651 | 0.313 | 0.965 | 0.633 | 0.331 | 0.934 | 0.335 | 0.981 | 0.352 |
| K | 0.002 | 0.001 | 0.001 | 0.001 | 0.001 | 0.002 | 0.001 | 0.000 | 0.001 | 0.000 | 0.002 | 0.002 |
| total | 5.002 | 5.014 | 4.997 | 5.008 | 4.993 | 5.011 | 5.003 | 4.987 | 5.000 | 4.991 | 5.009 | 5.016 |
| An% | 4.7 | 65.7 | 14.2 | 36.3 | 68.3 | 4.7 | 37.1 | 64.8 | 6.1 | 65.9 | 2.8 | 67.4 |

Table 7-15: Microprobe measurements in sample U1309D 4R-3 11-14 cm. Amphibole analyses

| Oxide wt% | Am1 | Am2 | Am3 | Am4 | Am5 | Am6 | Am7 | Am8 | Am9 | Am10 | Am11 | Am12 | Am13 |
|---|---|---|---|---|---|---|---|---|---|---|---|---|---|
| $SiO_2$ | 51.676 | 48.817 | 49.544 | 55.177 | 53.343 | 51.701 | 51.561 | 52.701 | 54.405 | 53.064 | 53.399 | 53.643 | 55.071 |
| $TiO_2$ | 0.175 | 1.298 | 1.186 | 0.373 | 0.028 | 0.034 | 0.099 | 0.414 | 0.170 | 0.001 | 0.000 | 0.357 | 0.287 |
| $Al_2O_3$ | 6.342 | 5.650 | 4.717 | 2.201 | 2.646 | 2.703 | 4.336 | 4.526 | 1.921 | 4.224 | 0.898 | 2.119 | 1.845 |
| $Cr_2O_3$ | 0.762 | 0.257 | 0.242 | 0.000 | 0.000 | 0.000 | 0.000 | 0.660 | 0.570 | 0.000 | 0.000 | 0.039 | 0.011 |
| $Fe_2O_3$ | 3.217 | 6.076 | 5.465 | 2.781 | 1.554 | 1.356 | 3.068 | 2.620 | 0.545 | 1.747 | 0.894 | 0.985 | 2.660 |
| FeO | 3.606 | 8.205 | 8.386 | 5.407 | 13.216 | 18.001 | 5.363 | 5.532 | 8.174 | 5.724 | 15.354 | 11.714 | 5.314 |
| MnO | 0.189 | 0.294 | 0.212 | 0.109 | 0.169 | 0.291 | 0.114 | 0.060 | 0.163 | 0.150 | 0.355 | 0.249 | 0.188 |
| MgO | 18.660 | 14.922 | 15.246 | 20.215 | 14.305 | 11.778 | 19.578 | 18.356 | 17.940 | 18.761 | 13.950 | 15.444 | 20.348 |
| CaO | 12.245 | 10.443 | 10.031 | 11.081 | 11.710 | 11.250 | 11.178 | 12.260 | 12.923 | 12.571 | 11.751 | 11.744 | 11.071 |
| $Na_2O$ | 1.128 | 1.277 | 1.286 | 0.666 | 0.365 | 0.372 | 0.977 | 0.810 | 0.192 | 0.819 | 0.182 | 0.363 | 0.564 |
| $K_2O$ | 0.048 | 0.094 | 0.274 | 0.038 | 0.015 | 0.037 | 0.025 | 0.038 | 0.010 | 0.021 | 0.026 | 0.011 | 0.023 |
| $H_2O$ | 2.127 | 2.065 | 2.022 | 2.130 | 2.067 | 2.018 | 2.074 | 2.113 | 2.102 | 2.118 | 2.017 | 2.065 | 2.127 |
| Cl | 0.073 | 0.009 | 0.134 | 0.094 | 0.000 | 0.013 | 0.102 | 0.085 | 0.013 | 0.011 | 0.070 | 0.015 | 0.052 |
| Total | 100.248 | 99.406 | 98.746 | 100.272 | 99.419 | 99.554 | 98.476 | 100.176 | 99.129 | 99.211 | 98.897 | 98.747 | 99.561 |
| Si | 7.221 | 7.080 | 7.223 | 7.680 | 7.736 | 7.669 | 7.361 | 7.402 | 7.747 | 7.500 | 7.867 | 7.774 | 7.713 |
| $Al_{(IV)}$ | 0.779 | 0.920 | 0.777 | 0.320 | 0.264 | 0.331 | 0.639 | 0.598 | 0.253 | 0.500 | 0.133 | 0.226 | 0.287 |
| $Al_{(VI)}$ | 0.265 | 0.046 | 0.034 | 0.041 | 0.188 | 0.141 | 0.090 | 0.151 | 0.070 | 0.204 | 0.023 | 0.136 | 0.018 |
| Ti | 0.018 | 0.142 | 0.130 | 0.039 | 0.003 | 0.004 | 0.011 | 0.044 | 0.018 | 0.000 | 0.000 | 0.039 | 0.030 |
| Cr | 0.084 | 0.029 | 0.028 | 0.000 | 0.000 | 0.000 | 0.000 | 0.073 | 0.064 | 0.000 | 0.000 | 0.004 | 0.001 |
| $Fe^{3+}$ | 0.338 | 0.663 | 0.600 | 0.291 | 0.170 | 0.151 | 0.330 | 0.277 | 0.058 | 0.186 | 0.099 | 0.107 | 0.280 |
| $Fe^{2+}$ | 0.421 | 0.995 | 1.022 | 0.629 | 1.603 | 2.233 | 0.640 | 0.650 | 0.973 | 0.677 | 1.892 | 1.420 | 0.622 |
| Mn | 0.022 | 0.036 | 0.026 | 0.013 | 0.021 | 0.037 | 0.014 | 0.007 | 0.020 | 0.018 | 0.044 | 0.031 | 0.022 |
| Mg | 3.887 | 3.227 | 3.314 | 4.195 | 3.093 | 2.605 | 4.167 | 3.844 | 3.809 | 3.953 | 3.064 | 3.337 | 4.249 |
| Ca | 1.833 | 1.623 | 1.567 | 1.653 | 1.820 | 1.788 | 1.710 | 1.845 | 1.972 | 1.904 | 1.855 | 1.824 | 1.661 |
| Na | 0.306 | 0.359 | 0.364 | 0.180 | 0.103 | 0.107 | 0.270 | 0.221 | 0.053 | 0.224 | 0.052 | 0.102 | 0.153 |
| K | 0.009 | 0.017 | 0.051 | 0.007 | 0.003 | 0.007 | 0.005 | 0.007 | 0.002 | 0.004 | 0.005 | 0.002 | 0.004 |
| OH | 1.983 | 1.998 | 1.967 | 1.978 | 2.000 | 1.997 | 1.975 | 1.980 | 1.997 | 1.997 | 1.983 | 1.996 | 1.988 |
| Cl | 0.017 | 0.002 | 0.033 | 0.022 | 0.000 | 0.003 | 0.025 | 0.020 | 0.003 | 0.003 | 0.017 | 0.004 | 0.012 |
| total | 17.185 | 17.137 | 17.135 | 17.048 | 17.003 | 17.072 | 17.237 | 17.118 | 17.039 | 17.169 | 17.034 | 17.002 | 17.042 |
| Nature | MgHb | MgHb | MgHb | Act | Act | Act | MgHb | MgHb | Act | MgHb | Act | Act | Act |

Table 7-15 (continued)

| Oxide wt% | Am14 | Am15 | Am16 | Am17 | Am18 | Am19 | Am20 | Am21 | Am22 | Am23 | Am24 | Am25 | Am26 |
|---|---|---|---|---|---|---|---|---|---|---|---|---|---|
| $SiO_2$ | 52.221 | 53.658 | 54.980 | 53.078 | 53.280 | 53.614 | 56.094 | 56.195 | 53.781 | 54.273 | 53.856 | 56.235 | 57.230 |
| $TiO_2$ | 0.725 | 0.036 | 0.492 | 0.048 | 0.040 | 0.071 | 0.094 | 0.132 | 0.000 | 0.052 | 0.034 | 0.265 | 0.000 |
| $Al_2O_3$ | 3.611 | 2.607 | 1.986 | 3.034 | 2.929 | 2.881 | 1.803 | 1.849 | 2.598 | 4.949 | 2.825 | 1.465 | 1.029 |
| $Cr_2O_3$ | 0.000 | 0.000 | 0.008 | 0.021 | 0.003 | 0.000 | 0.000 | 0.037 | 0.000 | 0.045 | 0.029 | 0.107 | 0.000 |
| $Fe_2O_3$ | 4.134 | 0.930 | 1.303 | 1.784 | 3.369 | 1.280 | 0.878 | 0.568 | 1.666 | 1.702 | 1.224 | 0.891 | 0.094 |
| FeO | 5.349 | 12.985 | 6.332 | 12.090 | 11.893 | 13.970 | 6.989 | 7.182 | 11.736 | 5.287 | 10.406 | 5.323 | 5.345 |
| MnO | 0.097 | 0.220 | 0.181 | 0.226 | 4.455 | 0.156 | 0.109 | 0.023 | 0.368 | 0.000 | 0.386 | 0.047 | 0.004 |
| MgO | 18.402 | 14.735 | 19.625 | 14.544 | 14.264 | 14.265 | 19.034 | 18.996 | 15.329 | 19.144 | 15.793 | 21.314 | 20.714 |
| CaO | 10.998 | 12.113 | 11.372 | 11.829 | 11.258 | 11.409 | 12.982 | 12.978 | 11.769 | 12.706 | 12.566 | 11.610 | 13.027 |
| $Na_2O$ | 0.909 | 0.383 | 0.539 | 0.401 | 0.420 | 0.376 | 0.275 | 0.223 | 0.321 | 0.724 | 0.319 | 0.281 | 0.182 |
| $K_2O$ | 0.130 | 0.049 | 0.011 | 0.000 | 0.014 | 0.030 | 0.014 | 0.006 | 0.000 | 0.031 | 0.000 | 0.005 | 0.005 |
| $H_2O$ | 2.066 | 2.076 | 2.108 | 2.065 | 2.121 | 2.076 | 2.149 | 2.146 | 2.084 | 2.166 | 2.090 | 2.148 | 2.162 |
| Cl | 0.144 | 0.007 | 0.071 | 0.015 | 0.019 | 0.014 | 0.009 | 0.018 | 0.005 | 0.023 | 0.011 | 0.040 | 0.000 |
| Total | 98.786 | 99.799 | 99.008 | 99.134 | 104.064 | 100.143 | 100.430 | 100.353 | 99.656 | 101.102 | 99.538 | 99.731 | 99.793 |
| Si | 7.445 | 7.741 | 7.753 | 7.694 | 7.515 | 7.728 | 7.819 | 7.833 | 7.734 | 7.491 | 7.717 | 7.812 | 7.935 |
| $Al_{(IV)}$ | 0.555 | 0.259 | 0.247 | 0.306 | 0.485 | 0.272 | 0.181 | 0.167 | 0.266 | 0.509 | 0.283 | 0.188 | 0.065 |
| $Al_{(VI)}$ | 0.052 | 0.184 | 0.083 | 0.212 | 0.002 | 0.218 | 0.115 | 0.136 | 0.174 | 0.296 | 0.194 | 0.051 | 0.103 |
| Ti | 0.078 | 0.004 | 0.052 | 0.005 | 0.004 | 0.008 | 0.010 | 0.014 | 0.000 | 0.005 | 0.004 | 0.028 | 0.000 |
| Cr | 0.000 | 0.000 | 0.001 | 0.002 | 0.000 | 0.000 | 0.000 | 0.004 | 0.000 | 0.005 | 0.003 | 0.012 | 0.000 |
| $Fe^{3+}$ | 0.444 | 0.101 | 0.138 | 0.195 | 0.358 | 0.139 | 0.092 | 0.060 | 0.180 | 0.177 | 0.132 | 0.093 | 0.010 |
| $Fe^{2+}$ | 0.638 | 1.567 | 0.747 | 1.466 | 1.403 | 1.684 | 0.815 | 0.837 | 1.411 | 0.610 | 1.247 | 0.618 | 0.620 |
| Mn | 0.012 | 0.027 | 0.022 | 0.028 | 0.532 | 0.019 | 0.013 | 0.003 | 0.045 | 0.000 | 0.047 | 0.006 | 0.000 |
| Mg | 3.912 | 3.169 | 4.126 | 3.143 | 3.000 | 3.066 | 3.956 | 3.948 | 3.287 | 3.939 | 3.374 | 4.414 | 4.282 |
| Ca | 1.680 | 1.872 | 1.718 | 1.837 | 1.701 | 1.762 | 1.939 | 1.938 | 1.813 | 1.879 | 1.929 | 1.728 | 1.935 |
| Na | 0.251 | 0.107 | 0.147 | 0.113 | 0.115 | 0.105 | 0.074 | 0.060 | 0.089 | 0.194 | 0.089 | 0.076 | 0.049 |
| K | 0.024 | 0.009 | 0.002 | 0.000 | 0.003 | 0.006 | 0.002 | 0.001 | 0.000 | 0.005 | 0.000 | 0.001 | 0.001 |
| OH | 1.965 | 1.998 | 1.983 | 1.996 | 1.995 | 1.997 | 1.998 | 1.996 | 1.999 | 1.995 | 1.997 | 1.991 | 2.000 |
| Cl | 0.035 | 0.002 | 0.017 | 0.004 | 0.005 | 0.003 | 0.002 | 0.004 | 0.001 | 0.005 | 0.003 | 0.009 | 0.000 |
| total | 17.089 | 17.041 | 17.035 | 17.000 | 17.117 | 17.005 | 17.016 | 17.001 | 17.000 | 17.110 | 17.018 | 17.027 | 17.001 |
| Nature | MgHb | Act | Act | Act | Mn Act | Act | Act | Act | Act | MgHb | Act | Act | Act |

Table 7-16: Microprobe measurements in sample U1309D 4R-1 135-137 cm. Plagioclase analyses

| Oxide wt% | Plg1 | Plg2 | Plg3 | Plg4 | Plg5 | Plg6 | Plg7 | Plg8 | Plg9 | Plg10 | Plg11 | Plg12 | Plg13 | Plg14 |
|---|---|---|---|---|---|---|---|---|---|---|---|---|---|---|
| $SiO_2$ | 47.897 | 64.972 | 64.591 | 47.426 | 47.725 | 54.060 | 65.577 | 51.716 | 68.795 | 47.262 | 67.796 | 47.482 | 56.315 | 66.096 |
| $TiO_2$ | 0.000 | 0.000 | 0.000 | 0.015 | 0.001 | 0.000 | 0.000 | 0.027 | 0.000 | 0.005 | 0.000 | 0.000 | 0.000 | 0.019 |
| $Al_2O_3$ | 33.626 | 22.430 | 22.412 | 34.095 | 33.447 | 29.750 | 21.853 | 31.415 | 20.559 | 33.651 | 20.195 | 33.379 | 27.708 | 21.364 |
| $Fe_2O_3$ | 0.090 | 0.000 | 0.155 | 0.052 | 0.227 | 0.045 | 0.000 | 0.000 | 0.000 | 0.139 | 0.075 | 0.243 | 0.033 | 0.000 |
| MnO | 0.000 | 0.000 | 0.000 | 0.093 | 0.000 | 0.060 | 0.012 | 0.025 | 0.002 | 0.000 | 0.000 | 0.058 | 0.113 | 0.068 |
| MgO | 0.014 | 0.000 | 0.032 | 0.000 | 0.027 | 0.000 | 0.000 | 0.000 | 0.000 | 0.000 | 0.000 | 0.005 | 0.000 | 0.009 |
| CaO | 17.033 | 3.355 | 3.506 | 17.191 | 16.950 | 11.904 | 2.571 | 14.062 | 0.653 | 17.083 | 0.791 | 16.799 | 9.546 | 2.313 |
| $Na_2O$ | 2.067 | 9.729 | 9.486 | 1.803 | 2.191 | 4.758 | 9.988 | 3.694 | 11.258 | 2.027 | 11.217 | 2.017 | 6.319 | 10.562 |
| $K_2O$ | 0.025 | 0.065 | 0.059 | 0.000 | 0.035 | 0.017 | 0.049 | 0.000 | 0.058 | 0.019 | 0.066 | 0.017 | 0.049 | 0.051 |
| Total | 100.752 | 100.551 | 100.241 | 100.675 | 100.603 | 100.594 | 100.050 | 100.939 | 101.325 | 100.186 | 100.140 | 100.000 | 100.083 | 100.482 |
| Si | 2.182 | 2.846 | 2.839 | 2.162 | 2.179 | 2.427 | 2.878 | 2.329 | 2.966 | 2.167 | 2.961 | 2.180 | 2.529 | 2.892 |
| Ti | 0.000 | 0.000 | 0.000 | 0.001 | 0.000 | 0.000 | 0.000 | 0.001 | 0.000 | 0.000 | 0.000 | 0.000 | 0.000 | 0.001 |
| Al | 1.805 | 1.158 | 1.161 | 1.832 | 1.800 | 1.574 | 1.130 | 1.667 | 1.044 | 1.819 | 1.040 | 1.806 | 1.467 | 1.102 |
| Fe3 | 0.003 | 0.000 | 0.005 | 0.002 | 0.008 | 0.002 | 0.000 | 0.000 | 0.000 | 0.005 | 0.002 | 0.008 | 0.001 | 0.000 |
| Mn | 0.000 | 0.000 | 0.000 | 0.004 | 0.000 | 0.002 | 0.000 | 0.001 | 0.000 | 0.000 | 0.000 | 0.002 | 0.004 | 0.003 |
| Mg | 0.001 | 0.000 | 0.002 | 0.000 | 0.002 | 0.000 | 0.000 | 0.000 | 0.000 | 0.000 | 0.000 | 0.000 | 0.000 | 0.001 |
| Ca | 0.831 | 0.157 | 0.165 | 0.840 | 0.829 | 0.573 | 0.121 | 0.678 | 0.030 | 0.839 | 0.037 | 0.826 | 0.459 | 0.108 |
| Na | 0.183 | 0.826 | 0.808 | 0.159 | 0.194 | 0.414 | 0.850 | 0.322 | 0.941 | 0.180 | 0.950 | 0.180 | 0.550 | 0.896 |
| K | 0.001 | 0.004 | 0.003 | 0.000 | 0.002 | 0.001 | 0.003 | 0.000 | 0.003 | 0.001 | 0.004 | 0.001 | 0.003 | 0.003 |
| total | 5.006 | 4.990 | 4.984 | 5.000 | 5.015 | 4.993 | 4.983 | 4.998 | 4.984 | 5.012 | 4.994 | 5.003 | 5.014 | 5.005 |
| An% | 83.2 | 15.7 | 16.7 | 84.3 | 83.1 | 57.5 | 12.1 | 67.9 | 3.0 | 83.9 | 3.7 | 82.9 | 46.4 | 11.2 |

Table 7-17: Microprobe measurements in sample U1309D 5R-3 22-28 cm. Amphibole analyses

| Oxide wt% | Am1 | Am2 | Am3 | Am4 | Am5 | Am6 | Am7 | Am8 |
|---|---|---|---|---|---|---|---|---|
| $SiO_2$ | 46.741 | 47.454 | 52.743 | 49.001 | 53.433 | 50.032 | 50.945 | 45.334 |
| $TiO_2$ | 0.996 | 0.505 | 0.095 | 0.908 | 0.310 | 0.718 | 0.291 | 0.000 |
| $Al_2O_3$ | 7.476 | 5.839 | 1.727 | 4.872 | 1.591 | 3.191 | 2.325 | 2.978 |
| $Cr_2O_3$ | 0.172 | 0.178 | 0.000 | 0.348 | 0.227 | 0.011 | 0.000 | 0.000 |
| $Fe_2O_3$ | 1.568 | 1.985 | 0.000 | 1.090 | 0.548 | 1.368 | 1.119 | 0.078 |
| FeO | 4.927 | 3.966 | 9.437 | 7.122 | 4.992 | 7.772 | 5.440 | 10.169 |
| MnO | 0.077 | 0.085 | 0.221 | 0.081 | 0.132 | 0.072 | 0.128 | 0.138 |
| MgO | 17.885 | 18.314 | 16.104 | 16.399 | 19.798 | 17.002 | 19.075 | 12.831 |
| CaO | 10.468 | 10.991 | 11.916 | 11.515 | 11.564 | 10.316 | 10.202 | 9.834 |
| $Na_2O$ | 1.520 | 1.316 | 0.080 | 0.907 | 0.275 | 0.690 | 0.458 | 0.325 |
| $K_2O$ | 0.100 | 0.076 | 0.016 | 0.154 | 0.025 | 0.102 | 0.020 | 0.011 |
| $H_2O$ | 1.998 | 1.945 | 2.001 | 1.968 | 2.036 | 1.934 | 1.936 | 1.751 |
| Cl | 0.000 | 0.080 | 0.000 | 0.000 | 0.000 | 0.061 | 0.062 | 0.000 |
| Total | 0.027 | 0.007 | 0.006 | 0.124 | 0.068 | 0.074 | 0.071 | 0.015 |
| Si | 6.991 | 7.169 | 7.896 | 7.346 | 7.802 | 7.569 | 7.699 | 7.745 |
| $Al_{(IV)}$ | 1.009 | 0.831 | 0.104 | 0.654 | 0.198 | 0.431 | 0.301 | 0.255 |
| $Al_{(VI)}$ | 0.309 | 0.209 | 0.201 | 0.207 | 0.076 | 0.138 | 0.113 | 0.344 |
| Ti | 0.112 | 0.057 | 0.011 | 0.102 | 0.034 | 0.082 | 0.033 | 0.000 |
| Cr | 0.020 | 0.021 | 0.000 | 0.041 | 0.026 | 0.001 | 0.000 | 0.000 |
| $Fe^{3+}$ | 0.177 | 0.226 | 0.000 | 0.123 | 0.060 | 0.156 | 0.127 | 0.010 |
| $Fe^{2+}$ | 0.616 | 0.501 | 1.182 | 0.893 | 0.610 | 0.983 | 0.688 | 1.453 |
| Mn | 0.010 | 0.011 | 0.028 | 0.010 | 0.016 | 0.009 | 0.016 | 0.020 |
| Mg | 3.988 | 4.125 | 3.595 | 3.666 | 4.310 | 3.835 | 4.298 | 3.268 |
| Ca | 1.677 | 1.779 | 1.911 | 1.850 | 1.809 | 1.672 | 1.652 | 1.800 |
| Na | 0.441 | 0.385 | 0.023 | 0.264 | 0.078 | 0.202 | 0.134 | 0.108 |
| K | 0.019 | 0.015 | 0.003 | 0.029 | 0.005 | 0.020 | 0.004 | 0.002 |
| OH | 1.993 | 1.960 | 1.998 | 1.968 | 1.983 | 1.952 | 1.952 | 1.996 |
| F | 0.000 | 0.038 | 0.000 | 0.000 | 0.000 | 0.029 | 0.030 | 0.000 |
| Cl | 0.007 | 0.002 | 0.002 | 0.032 | 0.017 | 0.019 | 0.018 | 0.004 |
| total | 17.369 | 17.330 | 16.954 | 17.185 | 17.025 | 17.098 | 17.066 | 17.005 |
| Nature | MgHb | MgHb | Act | MgHb | Act | Act | Act | Act |

Table 7-17 (continued)

| Oxide wt% | Am9 | Am10 | Am11 | Am12 | Am13 | Am14 | Am15 | Am16 |
|---|---|---|---|---|---|---|---|---|
| $SiO_2$ | 48.778 | 50.088 | 51.697 | 52.763 | 52.420 | 54.067 | 52.174 | 49.418 |
| $TiO_2$ | 0.136 | 0.470 | 0.024 | 0.029 | 0.144 | 0.183 | 0.277 | 0.016 |
| $Al_2O_3$ | 1.933 | 2.767 | 1.155 | 2.159 | 3.859 | 2.123 | 2.305 | 0.799 |
| $Cr_2O_3$ | 0.000 | 0.032 | 0.005 | 0.000 | 0.016 | 0.016 | 0.032 | 0.032 |
| $Fe_2O_3$ | 0.464 | 2.029 | 0.000 | 0.000 | 2.475 | 1.252 | 1.197 | 0.015 |
| FeO | 5.113 | 6.885 | 14.469 | 11.345 | 3.672 | 5.794 | 5.539 | 14.065 |
| MnO | 0.078 | 0.157 | 0.539 | 0.198 | 0.085 | 0.114 | 0.158 | 0.418 |
| MgO | 18.339 | 17.372 | 12.159 | 14.876 | 19.653 | 19.835 | 19.252 | 12.634 |
| CaO | 9.136 | 10.347 | 11.655 | 11.940 | 10.764 | 10.798 | 10.344 | 11.343 |
| $Na_2O$ | 0.474 | 0.737 | 0.029 | 0.164 | 1.000 | 0.601 | 0.599 | 0.033 |
| $K_2O$ | 0.003 | 0.068 | 0.016 | 0.025 | 0.023 | 0.023 | 0.013 | 0.019 |
| $H_2O$ | 1.764 | 1.914 | 1.913 | 2.010 | 2.066 | 2.028 | 2.010 | 1.868 |
| Cl | 0.210 | 0.079 | 0.043 | 0.000 | 0.000 | 0.096 | 0.000 | 0.000 |
| Total | 0.034 | 0.106 | 0.019 | 0.000 | 0.060 | 0.062 | 0.061 | 0.010 |
| Si | 7.811 | 7.592 | 7.997 | 7.871 | 7.552 | 7.759 | 7.724 | 7.922 |
| $Al_{(IV)}$ | 0.189 | 0.408 | 0.003 | 0.129 | 0.448 | 0.241 | 0.276 | 0.078 |
| $Al_{(VI)}$ | 0.175 | 0.086 | 0.207 | 0.250 | 0.207 | 0.118 | 0.126 | 0.073 |
| Ti | 0.016 | 0.054 | 0.003 | 0.003 | 0.016 | 0.020 | 0.031 | 0.002 |
| Cr | 0.000 | 0.004 | 0.001 | 0.000 | 0.002 | 0.002 | 0.004 | 0.004 |
| $Fe^{3+}$ | 0.056 | 0.231 | 0.000 | 0.000 | 0.268 | 0.135 | 0.133 | 0.002 |
| $Fe^{2+}$ | 0.685 | 0.873 | 1.872 | 1.415 | 0.442 | 0.695 | 0.686 | 1.886 |
| Mn | 0.011 | 0.020 | 0.071 | 0.025 | 0.010 | 0.014 | 0.020 | 0.057 |
| Mg | 4.378 | 3.926 | 2.804 | 3.308 | 4.221 | 4.244 | 4.249 | 3.020 |
| Ca | 1.567 | 1.680 | 1.932 | 1.908 | 1.661 | 1.660 | 1.641 | 1.948 |
| Na | 0.147 | 0.217 | 0.009 | 0.047 | 0.279 | 0.167 | 0.172 | 0.010 |
| K | 0.001 | 0.013 | 0.003 | 0.005 | 0.004 | 0.004 | 0.002 | 0.004 |
| OH | 1.884 | 1.935 | 1.974 | 2.000 | 1.985 | 1.941 | 1.985 | 1.997 |
| F | 0.106 | 0.038 | 0.021 | 0.000 | 0.000 | 0.044 | 0.000 | 0.000 |
| Cl | 0.009 | 0.027 | 0.005 | 0.000 | 0.015 | 0.015 | 0.015 | 0.003 |
| total | 17.037 | 17.104 | 16.901 | 16.963 | 17.112 | 17.059 | 17.063 | 17.005 |
| Nature | Act | Act | Act | Act | Trem | Act | Act | Act |

Table 7-18: Microprobe measurements in sample U1309D 5R-3 107-110 cm. Amphibole analyses

| Oxide wt% | Am1 | Am2 | Am3 | Am4 | Am5 | Am6 | Am7 | Am8 | Am9 | Am10 | Am11 |
|---|---|---|---|---|---|---|---|---|---|---|---|
| $SiO_2$ | 56.19 | 47.23 | 43.65 | 58.51 | 46.61 | 41.40 | 57.10 | 57.66 | 57.36 | 48.55 | 52.84 |
| $TiO_2$ | 0.01 | 0.54 | 0.07 | 0.00 | 0.47 | 0.03 | 0.00 | 0.02 | 0.00 | 0.78 | 0.48 |
| $Al_2O_3$ | 0.81 | 10.30 | 12.09 | 0.09 | 10.94 | 15.44 | 0.58 | 0.55 | 0.36 | 9.45 | 3.73 |
| $Cr_2O_3$ | 0.02 | 0.18 | 0.00 | 0.00 | 0.09 | 0.00 | 0.04 | 0.01 | 0.00 | 0.78 | 0.39 |
| $Fe_2O_3$ | 0.70 | 2.94 | 5.20 | 0.00 | 4.14 | 4.70 | 0.00 | 0.50 | 0.13 | 1.42 | 0.72 |
| FeO | 4.19 | 3.54 | 8.56 | 3.28 | 2.99 | 10.60 | 6.74 | 4.77 | 3.63 | 6.23 | 9.35 |
| MnO | 0.19 | 0.09 | 0.22 | 0.14 | 0.09 | 0.21 | 0.25 | 0.28 | 0.24 | 0.13 | 0.18 |
| MgO | 21.27 | 18.24 | 13.24 | 22.61 | 18.03 | 11.04 | 21.31 | 21.52 | 22.08 | 17.80 | 16.87 |
| CaO | 12.58 | 12.22 | 12.45 | 13.24 | 12.08 | 12.16 | 12.58 | 13.04 | 13.29 | 10.64 | 12.82 |
| $Na_2O$ | 0.21 | 2.20 | 2.05 | 0.09 | 2.22 | 2.39 | 0.17 | 0.14 | 0.13 | 1.78 | 0.59 |
| $K_2O$ | 0.01 | 0.13 | 0.09 | 0.01 | 0.11 | 0.14 | 0.01 | 0.00 | 0.01 | 0.13 | 0.02 |
| $H_2O$ | 2.12 | 2.12 | 2.03 | 2.19 | 2.12 | 2.01 | 2.17 | 2.18 | 2.16 | 2.10 | 2.11 |
| Cl | 0.04 | 0.01 | 0.07 | 0.02 | 0.01 | 0.10 | 0.01 | 0.00 | 0.00 | 0.09 | 0.00 |
| Total | 98.34 | 99.75 | 99.71 | 100.17 | 99.90 | 100.23 | 100.97 | 100.67 | 99.39 | 99.86 | 100.08 |
| Si | 7.894 | 6.674 | 6.390 | 8.000 | 6.590 | 6.089 | 7.885 | 7.927 | 7.946 | 6.869 | 7.516 |
| $Al_{(IV)}$ | 0.106 | 1.318 | 1.610 | 0.000 | 1.410 | 1.911 | 0.094 | 0.073 | 0.054 | 1.131 | 0.484 |
| $Al_{(VI)}$ | 0.029 | 0.400 | 0.476 | 0.014 | 0.413 | 0.765 | 0.000 | 0.016 | 0.005 | 0.445 | 0.142 |
| Ti | 0.001 | 0.058 | 0.007 | 0.000 | 0.050 | 0.004 | 0.000 | 0.002 | 0.000 | 0.083 | 0.052 |
| Cr | 0.003 | 0.020 | 0.000 | 0.000 | 0.010 | 0.000 | 0.004 | 0.001 | 0.000 | 0.087 | 0.043 |
| $Fe^{3+}$ | 0.074 | 0.313 | 0.573 | 0.000 | 0.440 | 0.520 | 0.000 | 0.052 | 0.014 | 0.151 | 0.077 |
| $Fe^{2+}$ | 0.493 | 0.419 | 1.048 | 0.375 | 0.353 | 1.304 | 0.778 | 0.549 | 0.420 | 0.737 | 1.112 |
| Mn | 0.023 | 0.011 | 0.028 | 0.016 | 0.011 | 0.026 | 0.029 | 0.032 | 0.028 | 0.015 | 0.021 |
| Mg | 4.455 | 3.847 | 2.890 | 4.615 | 3.801 | 2.421 | 4.388 | 4.411 | 4.560 | 3.754 | 3.576 |
| Ca | 1.893 | 1.853 | 1.952 | 1.941 | 1.830 | 1.916 | 1.862 | 1.920 | 1.972 | 1.613 | 1.954 |
| Na | 0.057 | 0.603 | 0.581 | 0.025 | 0.609 | 0.682 | 0.045 | 0.037 | 0.035 | 0.488 | 0.162 |
| K | 0.002 | 0.024 | 0.016 | 0.002 | 0.020 | 0.026 | 0.002 | 0.000 | 0.001 | 0.023 | 0.003 |
| OH | 1.990 | 1.999 | 1.983 | 1.996 | 1.999 | 1.975 | 1.999 | 2.000 | 1.999 | 1.979 | 2.000 |
| Cl | 0.010 | 0.001 | 0.017 | 0.004 | 0.001 | 0.025 | 0.001 | 0.000 | 0.001 | 0.021 | 0.000 |
| total | 17.029 | 17.548 | 17.572 | 16.997 | 17.538 | 17.664 | 17.088 | 17.019 | 17.036 | 17.397 | 17.142 |
| Nature | Trem | Edenite | MgHast | Trem | Edenite | Pargasite | Act | Act | Trem | MgHb | Act |

Table 7-19: Microprobe measurements in sample U1309D 5R-3 107-110 cm. Plagioclase analyses

| Oxide wt% | Plg1 | Plg2 | Plg3 | Plg4 | Plg5 | Plg6 | Plg7 | Plg8 | Plg9 | Plg10 |
|---|---|---|---|---|---|---|---|---|---|---|
| $SiO_2$ | 48.391 | 48.096 | 49.919 | 48.342 | 47.932 | 47.890 | 48.166 | 48.786 | 48.646 | 48.121 |
| $TiO_2$ | 0.003 | 0.000 | 0.000 | 0.040 | 0.006 | 0.000 | 0.070 | 0.000 | 0.015 | 0.000 |
| $Al_2O_3$ | 33.509 | 32.964 | 32.145 | 33.162 | 33.391 | 33.173 | 33.193 | 33.041 | 32.404 | 33.404 |
| $Fe_2O_3$ | 0.172 | 0.295 | 0.130 | 0.472 | 0.447 | 0.203 | 0.344 | 0.264 | 0.350 | 0.331 |
| MnO | 0.000 | 0.032 | 0.000 | 0.000 | 0.028 | 0.000 | 0.000 | 0.032 | 0.000 | 0.059 |
| MgO | 0.058 | 0.046 | 0.027 | 0.034 | 0.077 | 0.030 | 0.048 | 0.037 | 0.041 | 0.033 |
| CaO | 16.662 | 16.659 | 15.521 | 17.112 | 16.595 | 16.930 | 16.565 | 16.532 | 15.502 | 16.845 |
| $Na_2O$ | 2.274 | 2.291 | 2.900 | 2.015 | 2.123 | 2.118 | 2.110 | 2.152 | 2.536 | 2.003 |
| $K_2O$ | 0.036 | 0.049 | 0.007 | 0.002 | 0.000 | 0.018 | 0.023 | 0.002 | 0.234 | 0.016 |
| Total | 101.105 | 100.432 | 100.649 | 101.179 | 100.599 | 100.362 | 100.519 | 100.846 | 99.728 | 100.812 |
| Si | 2.195 | 2.199 | 2.265 | 2.194 | 2.186 | 2.190 | 2.197 | 2.215 | 2.233 | 2.190 |
| Ti | 0.000 | 0.000 | 0.000 | 0.001 | 0.000 | 0.000 | 0.002 | 0.000 | 0.001 | 0.000 |
| Al | 1.791 | 1.776 | 1.719 | 1.774 | 1.795 | 1.788 | 1.784 | 1.768 | 1.753 | 1.792 |
| Fe3 | 0.006 | 0.010 | 0.004 | 0.016 | 0.015 | 0.007 | 0.012 | 0.009 | 0.012 | 0.011 |
| Mn | 0.000 | 0.001 | 0.000 | 0.000 | 0.001 | 0.000 | 0.000 | 0.001 | 0.000 | 0.002 |
| Mg | 0.004 | 0.003 | 0.002 | 0.002 | 0.005 | 0.002 | 0.003 | 0.003 | 0.003 | 0.002 |
| Ca | 0.810 | 0.816 | 0.755 | 0.832 | 0.811 | 0.830 | 0.810 | 0.804 | 0.762 | 0.821 |
| Na | 0.200 | 0.203 | 0.255 | 0.177 | 0.188 | 0.188 | 0.187 | 0.189 | 0.226 | 0.177 |
| K | 0.002 | 0.003 | 0.000 | 0.000 | 0.000 | 0.001 | 0.001 | 0.000 | 0.014 | 0.001 |
| total | 5.008 | 5.011 | 5.001 | 4.998 | 5.002 | 5.006 | 4.996 | 4.991 | 5.003 | 4.997 |
| An% | 81.4 | 82.0 | 75.6 | 83.5 | 81.7 | 83.2 | 81.3 | 80.8 | 76.5 | 82.6 |

Table 7-20: Microprobe measurements in sample U1309D 6R-1 132-140 cm. Amphibole analyses

| Oxide wt% | Am1 | Am2 | Am3 | Am4 | Am5 | Am6 |
|---|---|---|---|---|---|---|
| $SiO_2$ | 49.123 | 43.017 | 50.217 | 54.119 | 54.717 | 51.804 |
| $TiO_2$ | 0.297 | 3.262 | 0.195 | 0.305 | 0.273 | 0.430 |
| $Al_2O_3$ | 7.545 | 11.902 | 7.535 | 3.304 | 1.926 | 5.698 |
| $Cr_2O_3$ | 0.016 | 0.681 | 0.016 | 0.268 | 0.156 | 0.011 |
| $Fe_2O_3$ | 3.025 | 0.515 | 2.968 | 0.219 | 1.956 | 2.512 |
| FeO | 4.076 | 6.514 | 4.378 | 6.524 | 4.195 | 4.391 |
| MnO | 0.080 | 0.143 | 0.000 | 0.055 | 0.038 | 0.017 |
| MgO | 18.737 | 15.780 | 18.317 | 18.741 | 20.767 | 19.121 |
| CaO | 11.315 | 11.988 | 12.034 | 12.750 | 12.297 | 12.267 |
| $Na_2O$ | 1.842 | 2.852 | 1.446 | 0.624 | 0.397 | 0.805 |
| $K_2O$ | 0.159 | 0.175 | 0.056 | 0.045 | 0.043 | 0.068 |
| $H_2O$ | 2.088 | 2.020 | 2.109 | 2.091 | 2.127 | 2.127 |
| F | 0.000 | 0.078 | 0.009 | 0.061 | 0.000 | 0.000 |
| Cl | 0.036 | 0.020 | 0.029 | 0.012 | 0.029 | 0.009 |
| Total | 98.339 | 98.947 | 99.310 | 99.118 | 98.921 | 99.260 |
| Si | 7.023 | 6.255 | 7.098 | 7.644 | 7.686 | 7.295 |
| $Al_{(IV)}$ | 0.977 | 1.745 | 0.902 | 0.356 | 0.314 | 0.705 |
| $Al_{(VI)}$ | 0.294 | 0.294 | 0.353 | 0.194 | 0.005 | 0.240 |
| Ti | 0.032 | 0.357 | 0.021 | 0.032 | 0.029 | 0.046 |
| Cr | 0.002 | 0.078 | 0.002 | 0.030 | 0.017 | 0.001 |
| $Fe^{3+}$ | 0.325 | 0.056 | 0.316 | 0.023 | 0.207 | 0.266 |
| $Fe^{2+}$ | 0.487 | 0.792 | 0.518 | 0.771 | 0.493 | 0.517 |
| Mn | 0.010 | 0.018 | 0.000 | 0.007 | 0.005 | 0.002 |
| Mg | 3.994 | 3.421 | 3.860 | 3.947 | 4.349 | 4.014 |
| Ca | 1.733 | 1.867 | 1.822 | 1.929 | 1.851 | 1.851 |
| Na | 0.511 | 0.804 | 0.396 | 0.171 | 0.108 | 0.220 |
| K | 0.029 | 0.032 | 0.010 | 0.008 | 0.008 | 0.012 |
| OH | 1.991 | 1.959 | 1.989 | 1.970 | 1.993 | 1.998 |
| F | 0.000 | 0.036 | 0.004 | 0.027 | 0.000 | 0.000 |
| Cl | 0.009 | 0.005 | 0.007 | 0.003 | 0.007 | 0.002 |
| total | 17.416 | 17.720 | 17.298 | 17.112 | 17.071 | 17.169 |
| Nature | MgHb | Ti pargasite | MgHb | Act | Act | MgHb |

Table 7-21: Microprobe measurements in sample U1309D 7R-3 101-102 cm. Amphibole analyses

| Oxide wt% | Am1 | Am2 | Am3 | Am4 | Am5 | Am6 | Am7 | Am8 | Am9 |
|---|---|---|---|---|---|---|---|---|---|
| $SiO_2$ | 49.400 | 49.179 | 55.201 | 52.577 | 50.769 | 51.373 | 53.482 | 50.590 | 43.476 |
| $TiO_2$ | 0.947 | 1.033 | 0.154 | 0.093 | 0.399 | 0.075 | 0.456 | 0.273 | 0.205 |
| $Al_2O_3$ | 4.629 | 4.521 | 1.322 | 0.517 | 4.164 | 4.813 | 3.120 | 5.519 | 11.889 |
| $Cr_2O_3$ | 0.125 | 0.152 | 0.099 | 0.392 | 0.818 | 0.444 | 0.464 | 0.063 | 0.063 |
| $Fe_2O_3$ | 6.069 | 4.074 | 2.430 | 0.000 | 2.320 | 6.917 | 3.833 | 2.247 | 4.825 |
| FeO | 8.449 | 9.045 | 5.868 | 20.379 | 9.384 | 3.612 | 5.380 | 9.876 | 7.482 |
| MnO | 0.285 | 0.279 | 0.194 | 0.707 | 0.100 | 0.189 | 0.175 | 0.159 | 0.220 |
| MgO | 14.809 | 15.570 | 19.931 | 9.875 | 15.879 | 17.844 | 19.028 | 15.438 | 14.359 |
| CaO | 10.853 | 11.351 | 11.285 | 12.372 | 11.783 | 11.082 | 11.116 | 12.193 | 11.325 |
| $Na_2O$ | 1.193 | 1.186 | 0.508 | 0.089 | 0.867 | 1.405 | 0.829 | 0.970 | 2.675 |
| $K_2O$ | 0.288 | 0.223 | 0.055 | 0.018 | 0.009 | 0.069 | 0.025 | 0.054 | 0.272 |
| $H_2O$ | 2.014 | 2.040 | 2.116 | 1.985 | 2.044 | 2.112 | 2.100 | 2.059 | 1.985 |
| Cl | 0.167 | 0.032 | 0.048 | 0.004 | 0.069 | 0.038 | 0.138 | 0.076 | 0.218 |
| Total | 99.227 | 98.686 | 99.212 | 99.008 | 98.606 | 99.973 | 100.146 | 99.517 | 98.995 |
| Si | 7.202 | 7.198 | 7.778 | 7.935 | 7.383 | 7.259 | 7.510 | 7.299 | 6.387 |
| $Al_{(IV)}$ | 0.795 | 0.780 | 0.219 | 0.065 | 0.617 | 0.741 | 0.490 | 0.701 | 1.613 |
| $Al_{(VI)}$ | 0.000 | 0.000 | 0.000 | 0.027 | 0.096 | 0.061 | 0.027 | 0.238 | 0.446 |
| Ti | 0.104 | 0.114 | 0.016 | 0.011 | 0.044 | 0.008 | 0.048 | 0.030 | 0.023 |
| Cr | 0.014 | 0.018 | 0.011 | 0.047 | 0.094 | 0.050 | 0.052 | 0.007 | 0.007 |
| $Fe^{3+}$ | 0.666 | 0.449 | 0.258 | 0.000 | 0.254 | 0.736 | 0.405 | 0.244 | 0.533 |
| $Fe^{2+}$ | 1.030 | 1.107 | 0.691 | 2.572 | 1.141 | 0.427 | 0.632 | 1.192 | 0.919 |
| Mn | 0.035 | 0.035 | 0.023 | 0.090 | 0.012 | 0.023 | 0.021 | 0.019 | 0.027 |
| Mg | 3.219 | 3.397 | 4.187 | 2.222 | 3.443 | 3.759 | 3.984 | 3.321 | 3.145 |
| Ca | 1.695 | 1.780 | 1.704 | 2.001 | 1.836 | 1.678 | 1.672 | 1.885 | 1.783 |
| Na | 0.337 | 0.337 | 0.139 | 0.026 | 0.244 | 0.385 | 0.226 | 0.271 | 0.762 |
| K | 0.054 | 0.042 | 0.010 | 0.003 | 0.002 | 0.012 | 0.004 | 0.010 | 0.051 |
| OH | 1.959 | 1.992 | 1.989 | 1.999 | 1.983 | 1.991 | 1.967 | 1.981 | 1.946 |
| Cl | 0.041 | 0.008 | 0.011 | 0.001 | 0.017 | 0.009 | 0.033 | 0.019 | 0.054 |
| total | 17.152 | 17.255 | 17.036 | 16.999 | 17.166 | 17.138 | 17.070 | 17.217 | 17.697 |
| Nature | MgHb | MgHb | Act | FeAct | MgHb | MgHb | Act | MgHb | MgHast |

Table 7-21 (continued)

| Oxide wt% | Am10 | Am11 | Am12 | Am13 | Am14 | Am15 | Am16 | Am17 |
|---|---|---|---|---|---|---|---|---|
| $SiO_2$ | 44.042 | 41.724 | 49.479 | 49.476 | 50.013 | 47.868 | 55.441 | 51.440 |
| $TiO_2$ | 0.163 | 0.790 | 1.107 | 0.246 | 0.352 | 1.407 | 0.178 | 0.081 |
| $Al_2O_3$ | 10.710 | 13.180 | 3.921 | 5.645 | 4.980 | 4.994 | 1.435 | 2.497 |
| $Cr_2O_3$ | 0.011 | 0.078 | 0.151 | 0.048 | 0.000 | 0.193 | 0.391 | 0.415 |
| $Fe_2O_3$ | 3.669 | 4.981 | 5.895 | 8.427 | 0.000 | 6.322 | 0.800 | 0.709 |
| FeO | 8.519 | 8.162 | 8.378 | 2.661 | 10.206 | 8.985 | 6.957 | 18.587 |
| MnO | 0.107 | 0.196 | 0.212 | 0.188 | 0.217 | 0.141 | 0.119 | 0.139 |
| MgO | 13.983 | 13.458 | 14.995 | 17.771 | 17.839 | 13.936 | 20.349 | 10.837 |
| CaO | 11.206 | 11.476 | 10.830 | 10.724 | 10.764 | 10.522 | 11.725 | 12.202 |
| $Na_2O$ | 2.389 | 2.894 | 1.239 | 2.022 | 2.060 | 1.589 | 0.434 | 0.294 |
| $K_2O$ | 0.141 | 0.184 | 0.337 | 0.158 | 0.121 | 0.399 | 0.006 | 0.000 |
| $H_2O$ | 1.951 | 1.959 | 2.010 | 2.080 | 2.048 | 1.981 | 2.140 | 2.000 |
| Cl | 0.216 | 0.289 | 0.139 | 0.088 | 0.061 | 0.183 | 0.006 | 0.025 |
| Total | 97.108 | 99.372 | 98.693 | 99.535 | 98.661 | 98.520 | 99.982 | 99.226 |
| Si | 6.582 | 6.154 | 7.251 | 7.055 | 7.267 | 7.079 | 7.761 | 7.688 |
| $Al_{(IV)}$ | 1.418 | 1.846 | 0.677 | 0.945 | 0.733 | 0.870 | 0.237 | 0.312 |
| $Al_{(VI)}$ | 0.469 | 0.446 | 0.000 | 0.003 | 0.120 | 0.000 | 0.000 | 0.128 |
| Ti | 0.018 | 0.088 | 0.122 | 0.026 | 0.038 | 0.157 | 0.019 | 0.009 |
| Cr | 0.001 | 0.009 | 0.017 | 0.005 | 0.000 | 0.023 | 0.043 | 0.049 |
| $Fe^{3+}$ | 0.413 | 0.553 | 0.650 | 0.904 | 0.000 | 0.704 | 0.084 | 0.080 |
| $Fe^{2+}$ | 1.065 | 1.007 | 1.027 | 0.317 | 1.240 | 1.111 | 0.815 | 2.323 |
| Mn | 0.014 | 0.024 | 0.026 | 0.023 | 0.027 | 0.018 | 0.014 | 0.018 |
| Mg | 3.116 | 2.960 | 3.276 | 3.778 | 3.865 | 3.073 | 4.247 | 2.415 |
| Ca | 1.794 | 1.814 | 1.700 | 1.638 | 1.676 | 1.667 | 1.759 | 1.954 |
| Na | 0.692 | 0.828 | 0.352 | 0.559 | 0.580 | 0.456 | 0.118 | 0.085 |
| K | 0.027 | 0.035 | 0.063 | 0.029 | 0.022 | 0.075 | 0.001 | 0.000 |
| OH | 1.945 | 1.928 | 1.965 | 1.979 | 1.985 | 1.954 | 1.999 | 1.994 |
| Cl | 0.055 | 0.072 | 0.035 | 0.021 | 0.015 | 0.046 | 0.001 | 0.006 |
| total | 17.609 | 17.762 | 17.162 | 17.284 | 17.569 | 17.232 | 17.097 | 17.061 |
| Nature | Edenite | MgHast | MgHb | MgHb | Edenite | MgHb | Act | Act |

Table 7-22: Microprobe measurements in sample U1309D 7R-3 101-102 cm. Plagioclase analyses

| Oxide wt% | Plg1 | Plg2 | Plg3 | Plg4 | Plg5 | Plg6 | Plg7 | Plg8 | Plg9 | Plg10 |
|---|---|---|---|---|---|---|---|---|---|---|
| $SiO_2$ | 48.428 | 53.852 | 60.236 | 67.389 | 54.248 | 61.148 | 65.820 | 54.547 | 67.927 | 51.979 |
| $TiO_2$ | 0.102 | 0.065 | 0.000 | 0.000 | 0.008 | 0.000 | 0.000 | 0.000 | 0.000 | 0.000 |
| $Al_2O_3$ | 32.812 | 29.720 | 25.750 | 21.161 | 29.118 | 24.598 | 21.883 | 28.726 | 20.505 | 31.144 |
| $Fe_2O_3$ | 0.335 | 0.000 | 0.142 | 0.092 | 0.002 | 0.137 | 0.041 | 0.087 | 0.077 | 0.000 |
| MnO | 0.014 | 0.001 | 0.012 | 0.000 | 0.000 | 0.000 | 0.053 | 0.000 | 0.000 | 0.000 |
| MgO | 0.007 | 0.000 | 0.006 | 0.007 | 0.007 | 0.009 | 0.000 | 0.003 | 0.000 | 0.000 |
| CaO | 16.122 | 11.577 | 7.309 | 1.498 | 11.181 | 6.147 | 2.940 | 11.168 | 0.751 | 13.501 |
| $Na_2O$ | 2.450 | 5.119 | 7.675 | 10.697 | 5.186 | 8.404 | 10.136 | 5.100 | 11.401 | 3.886 |
| $K_2O$ | 0.000 | 0.021 | 0.015 | 0.060 | 0.055 | 0.067 | 0.012 | 0.000 | 0.068 | 0.038 |
| Total | 100.270 | 100.355 | 101.145 | 100.904 | 99.805 | 100.510 | 100.885 | 99.631 | 100.729 | 100.548 |
| Si | 2.213 | 2.424 | 2.656 | 2.925 | 2.451 | 2.707 | 2.871 | 2.467 | 2.952 | 2.346 |
| Ti | 0.004 | 0.002 | 0.000 | 0.000 | 0.000 | 0.000 | 0.000 | 0.000 | 0.000 | 0.000 |
| Al | 1.767 | 1.577 | 1.338 | 1.082 | 1.551 | 1.283 | 1.125 | 1.531 | 1.050 | 1.656 |
| Fe3 | 0.012 | 0.000 | 0.005 | 0.003 | 0.000 | 0.005 | 0.001 | 0.003 | 0.003 | 0.000 |
| Mn | 0.001 | 0.000 | 0.000 | 0.000 | 0.000 | 0.000 | 0.002 | 0.000 | 0.000 | 0.000 |
| Mg | 0.000 | 0.000 | 0.000 | 0.000 | 0.000 | 0.001 | 0.000 | 0.000 | 0.000 | 0.000 |
| Ca | 0.789 | 0.558 | 0.345 | 0.070 | 0.541 | 0.292 | 0.137 | 0.541 | 0.035 | 0.653 |
| Na | 0.217 | 0.447 | 0.656 | 0.900 | 0.454 | 0.721 | 0.857 | 0.447 | 0.961 | 0.340 |
| K | 0.000 | 0.001 | 0.001 | 0.003 | 0.003 | 0.004 | 0.001 | 0.000 | 0.004 | 0.002 |
| total | 5.003 | 5.009 | 5.001 | 4.984 | 5.002 | 5.012 | 4.995 | 4.990 | 5.004 | 4.997 |
| An% | 79.0 | 55.8 | 34.6 | 7.0 | 54.2 | 29.2 | 13.9 | 54.1 | 3.5 | 65.3 |

Table 7-22 (continued)

| Oxide wt% | Plg11 | Plg12 | Plg13 | Plg14 | Plg15 | Plg16 | Plg17 | Plg18 | Plg19 | Plg20 |
|---|---|---|---|---|---|---|---|---|---|---|
| $SiO_2$ | 59.242 | 67.207 | 65.258 | 51.422 | 67.192 | 49.465 | 55.451 | 65.618 | 49.156 | 63.615 |
| $TiO_2$ | 0.004 | 0.046 | 0.000 | 0.015 | 0.000 | 0.062 | 0.027 | 0.000 | 0.005 | 0.000 |
| $Al_2O_3$ | 26.603 | 21.499 | 22.577 | 31.056 | 21.159 | 32.166 | 28.759 | 21.725 | 32.829 | 22.357 |
| $Fe_2O_3$ | 0.168 | 0.053 | 0.000 | 0.477 | 0.188 | 0.328 | 0.123 | 0.122 | 0.184 | 0.038 |
| MnO | 0.000 | 0.000 | 0.000 | 0.035 | 0.135 | 0.030 | 0.000 | 0.000 | 0.000 | 0.042 |
| MgO | 0.019 | 0.021 | 0.010 | 0.069 | 0.000 | 0.000 | 0.000 | 0.000 | 0.004 | 0.000 |
| CaO | 8.001 | 2.052 | 3.439 | 13.978 | 1.455 | 15.258 | 10.392 | 2.852 | 15.771 | 3.018 |
| $Na_2O$ | 7.316 | 10.706 | 9.544 | 3.844 | 10.699 | 2.966 | 5.713 | 9.859 | 2.750 | 10.090 |
| $K_2O$ | 0.000 | 0.056 | 0.013 | 0.021 | 0.164 | 0.028 | 0.072 | 0.037 | 0.032 | 0.019 |
| Total | 101.353 | 101.640 | 100.841 | 100.917 | 100.992 | 100.303 | 100.537 | 100.213 | 100.731 | 99.179 |
| Si | 2.613 | 2.903 | 2.847 | 2.322 | 2.919 | 2.255 | 2.483 | 2.878 | 2.232 | 2.830 |
| Ti | 0.000 | 0.001 | 0.000 | 0.001 | 0.000 | 0.002 | 0.001 | 0.000 | 0.000 | 0.000 |
| Al | 1.383 | 1.095 | 1.161 | 1.653 | 1.083 | 1.728 | 1.518 | 1.123 | 1.757 | 1.172 |
| Fe3 | 0.006 | 0.002 | 0.000 | 0.016 | 0.006 | 0.011 | 0.004 | 0.004 | 0.006 | 0.001 |
| Mn | 0.000 | 0.000 | 0.000 | 0.001 | 0.005 | 0.001 | 0.000 | 0.000 | 0.000 | 0.002 |
| Mg | 0.001 | 0.001 | 0.001 | 0.005 | 0.000 | 0.000 | 0.000 | 0.000 | 0.000 | 0.000 |
| Ca | 0.378 | 0.095 | 0.161 | 0.676 | 0.068 | 0.745 | 0.499 | 0.134 | 0.767 | 0.144 |
| Na | 0.626 | 0.897 | 0.807 | 0.337 | 0.901 | 0.262 | 0.496 | 0.838 | 0.242 | 0.870 |
| K | 0.000 | 0.003 | 0.001 | 0.001 | 0.009 | 0.002 | 0.004 | 0.002 | 0.002 | 0.001 |
| total | 5.006 | 4.997 | 4.977 | 5.012 | 4.991 | 5.006 | 5.005 | 4.979 | 5.008 | 5.019 |
| An% | 37.9 | 9.6 | 16.1 | 68.2 | 7.3 | 74.6 | 49.9 | 13.4 | 76.8 | 14.5 |

Table 7-23: Microprobe measurements in sample U1309D 8R-2 22-26 cm. Amphibole analyses

| Oxide wt% | Am1 | Am2 | Am3 | Am4 | Am5 | Am6 | Am7 | Am8 | Am9 | Am10 |
|---|---|---|---|---|---|---|---|---|---|---|
| $SiO_2$ | 54.038 | 48.394 | 55.933 | 45.305 | 52.615 | 57.707 | 57.317 | 52.319 | 53.074 | 57.382 |
| $TiO_2$ | 0.000 | 0.004 | 0.040 | 0.144 | 0.111 | 0.015 | 0.041 | 0.147 | 0.031 | 0.055 |
| $Al_2O_3$ | 3.986 | 8.593 | 2.516 | 11.526 | 6.381 | 0.847 | 0.609 | 4.851 | 5.212 | 0.803 |
| $Cr_2O_3$ | 0.000 | 0.000 | 0.048 | 0.026 | 0.005 | 0.000 | 0.000 | 0.069 | 0.062 | 0.000 |
| $Fe_2O_3$ | 2.640 | 0.000 | 2.280 | 3.659 | 5.293 | 0.540 | 0.793 | 3.401 | 1.555 | 0.809 |
| FeO | 3.398 | 9.426 | 3.149 | 7.655 | 3.366 | 3.401 | 2.869 | 3.924 | 2.916 | 2.432 |
| MnO | 0.216 | 0.253 | 0.140 | 0.000 | 0.100 | 0.091 | 0.148 | 0.100 | 0.083 | 0.144 |
| MgO | 20.405 | 16.003 | 21.167 | 14.670 | 20.220 | 22.483 | 22.129 | 19.423 | 20.815 | 22.407 |
| CaO | 12.649 | 13.039 | 12.509 | 12.408 | 8.830 | 12.601 | 13.235 | 12.230 | 13.303 | 13.294 |
| $Na_2O$ | 0.829 | 1.510 | 0.489 | 1.934 | 1.293 | 0.185 | 0.208 | 0.749 | 1.119 | 0.230 |
| $K_2O$ | 0.025 | 0.096 | 0.028 | 0.114 | 0.334 | 0.046 | 0.030 | 0.069 | 0.051 | 0.023 |
| $H_2O$ | 2.156 | 2.074 | 2.174 | 2.066 | 2.156 | 2.184 | 2.167 | 2.126 | 2.125 | 2.166 |
| Cl | 0.029 | 0.018 | 0.022 | 0.020 | 0.062 | 0.006 | 0.019 | 0.025 | 0.159 | 0.054 |
| Total | 100.371 | 99.409 | 100.495 | 99.527 | 100.766 | 100.107 | 99.565 | 99.432 | 100.505 | 99.799 |
| Si | 7.491 | 6.981 | 7.694 | 6.559 | 7.262 | 7.915 | 7.914 | 7.357 | 7.347 | 7.892 |
| $Al_{(IV)}$ | 0.509 | 1.019 | 0.306 | 1.441 | 0.738 | 0.085 | 0.086 | 0.643 | 0.653 | 0.108 |
| $Al_{(VI)}$ | 0.142 | 0.442 | 0.102 | 0.525 | 0.301 | 0.052 | 0.013 | 0.161 | 0.197 | 0.022 |
| Ti | 0.000 | 0.000 | 0.004 | 0.016 | 0.012 | 0.002 | 0.004 | 0.016 | 0.003 | 0.006 |
| Cr | 0.000 | 0.000 | 0.005 | 0.003 | 0.001 | 0.000 | 0.000 | 0.008 | 0.007 | 0.000 |
| $Fe^{3+}$ | 0.275 | 0.000 | 0.236 | 0.399 | 0.550 | 0.056 | 0.082 | 0.360 | 0.162 | 0.084 |
| $Fe^{2+}$ | 0.394 | 1.137 | 0.362 | 0.927 | 0.389 | 0.390 | 0.331 | 0.462 | 0.338 | 0.280 |
| Mn | 0.025 | 0.031 | 0.016 | 0.000 | 0.012 | 0.011 | 0.017 | 0.012 | 0.010 | 0.017 |
| Mg | 4.217 | 3.442 | 4.341 | 3.166 | 4.161 | 4.597 | 4.555 | 4.072 | 4.296 | 4.595 |
| Ca | 1.879 | 2.015 | 1.844 | 1.925 | 1.306 | 1.852 | 1.958 | 1.843 | 1.973 | 1.959 |
| Na | 0.223 | 0.422 | 0.130 | 0.543 | 0.346 | 0.049 | 0.056 | 0.204 | 0.300 | 0.061 |
| K | 0.004 | 0.018 | 0.005 | 0.021 | 0.059 | 0.008 | 0.005 | 0.012 | 0.009 | 0.004 |
| OH | 1.993 | 1.996 | 1.995 | 1.995 | 1.986 | 1.999 | 1.996 | 1.994 | 1.963 | 1.987 |
| Cl | 0.007 | 0.004 | 0.005 | 0.005 | 0.015 | 0.001 | 0.004 | 0.006 | 0.037 | 0.013 |
| total | 17.160 | 17.508 | 17.045 | 17.524 | 17.134 | 17.016 | 17.022 | 17.150 | 17.295 | 17.028 |
| Nature | MgHb | MgHb | Trem | Edenite | MgHb | Trem | Trem | MgHb | MgHb | Trem |

Table 7-23 (continued)

| Oxide wt% | Am11 | Am12 | Am13 | Am14 | Am15 | Am16 | Am17 | Am18 | Am19 | Am20 |
|---|---|---|---|---|---|---|---|---|---|---|
| $SiO_2$ | 43.626 | 57.223 | 51.590 | 56.015 | 58.014 | 51.993 | 57.156 | 42.883 | 51.569 | 46.775 |
| $TiO_2$ | 3.139 | 0.000 | 0.129 | 0.000 | 0.000 | 0.174 | 0.099 | 2.774 | 0.278 | 0.340 |
| $Al_2O_3$ | 12.162 | 1.124 | 7.059 | 0.690 | 0.365 | 6.856 | 0.741 | 10.739 | 5.063 | 9.350 |
| $Cr_2O_3$ | 0.029 | 0.022 | 0.019 | 0.000 | 0.000 | 0.011 | 0.030 | 0.150 | 0.000 | 0.048 |
| $Fe_2O_3$ | 1.805 | 0.000 | 1.333 | 0.000 | 0.000 | 3.152 | 0.501 | 2.940 | 4.138 | 2.743 |
| FeO | 4.150 | 2.847 | 6.201 | 2.742 | 2.813 | 3.704 | 4.791 | 8.550 | 5.622 | 7.977 |
| MnO | 0.063 | 0.009 | 0.124 | 0.000 | 0.129 | 0.026 | 0.125 | 0.157 | 0.146 | 0.143 |
| MgO | 16.869 | 22.510 | 19.668 | 25.002 | 22.572 | 19.639 | 21.182 | 13.634 | 17.576 | 15.219 |
| CaO | 11.862 | 13.724 | 10.660 | 11.143 | 13.555 | 11.716 | 12.936 | 11.435 | 11.117 | 12.173 |
| $Na_2O$ | 2.924 | 0.301 | 1.095 | 0.207 | 0.113 | 1.280 | 0.116 | 2.544 | 0.943 | 1.724 |
| $K_2O$ | 0.215 | 0.022 | 0.052 | 0.049 | 0.037 | 0.082 | 0.000 | 0.276 | 0.053 | 0.109 |
| $H_2O$ | 2.080 | 2.157 | 2.135 | 2.133 | 2.182 | 2.159 | 2.160 | 2.013 | 2.090 | 2.041 |
| Cl | 0.016 | 0.098 | 0.036 | 0.069 | 0.002 | 0.029 | 0.015 | 0.024 | 0.036 | 0.073 |
| Total | 98.941 | 100.037 | 100.101 | 98.050 | 99.782 | 100.821 | 99.851 | 98.119 | 98.632 | 98.716 |
| Si | 6.275 | 7.861 | 7.213 | 7.809 | 7.969 | 7.196 | 7.917 | 6.366 | 7.364 | 6.809 |
| $Al_{(IV)}$ | 1.725 | 0.139 | 0.787 | 0.113 | 0.031 | 0.804 | 0.083 | 1.634 | 0.636 | 1.191 |
| $Al_{(VI)}$ | 0.337 | 0.043 | 0.376 | 0.000 | 0.028 | 0.314 | 0.038 | 0.245 | 0.216 | 0.413 |
| Ti | 0.340 | 0.000 | 0.014 | 0.000 | 0.000 | 0.018 | 0.010 | 0.310 | 0.030 | 0.037 |
| Cr | 0.003 | 0.002 | 0.002 | 0.000 | 0.000 | 0.001 | 0.003 | 0.018 | 0.000 | 0.006 |
| $Fe^{3+}$ | 0.195 | 0.000 | 0.140 | 0.000 | 0.000 | 0.328 | 0.052 | 0.328 | 0.445 | 0.301 |
| $Fe^{2+}$ | 0.499 | 0.327 | 0.725 | 0.320 | 0.323 | 0.429 | 0.555 | 1.061 | 0.671 | 0.971 |
| Mn | 0.008 | 0.001 | 0.015 | 0.000 | 0.015 | 0.003 | 0.015 | 0.020 | 0.018 | 0.018 |
| Mg | 3.618 | 4.611 | 4.100 | 5.196 | 4.623 | 4.052 | 4.375 | 3.018 | 3.742 | 3.303 |
| Ca | 1.828 | 2.020 | 1.597 | 1.664 | 1.995 | 1.737 | 1.920 | 1.819 | 1.701 | 1.898 |
| Na | 0.815 | 0.080 | 0.297 | 0.056 | 0.030 | 0.343 | 0.031 | 0.732 | 0.261 | 0.487 |
| K | 0.039 | 0.004 | 0.009 | 0.009 | 0.006 | 0.014 | 0.000 | 0.052 | 0.010 | 0.020 |
| OH | 1.996 | 1.977 | 1.992 | 1.984 | 2.000 | 1.993 | 1.996 | 1.994 | 1.991 | 1.982 |
| Cl | 0.004 | 0.023 | 0.009 | 0.016 | 0.000 | 0.007 | 0.004 | 0.006 | 0.009 | 0.018 |
| total | 17.683 | 17.089 | 17.274 | 17.167 | 17.020 | 17.241 | 17.000 | 17.604 | 17.093 | 17.453 |
| Nature | TiPargasite | Trem | MgHb | Trem | Trem | MgHb | Act | Ti Hast | MgHb | MgHb |

Table 7-24: Microprobe measurements in sample U1309D 8R-2 22-26 cm. Plagioclase analyses

| Oxide wt% | Plg1 | Plg2 | Plg3 | Plg4 | Plg5 | Plg6 | Plg7 | Plg8 | Plg9 | Plg10 | Plg11 | Plg12 | Plg13 | Plg14 |
|---|---|---|---|---|---|---|---|---|---|---|---|---|---|---|
| $SiO_2$ | 48.657 | 48.019 | 47.054 | 46.804 | 48.006 | 47.829 | 43.900 | 63.301 | 55.107 | 62.239 | 47.825 | 48.669 | 47.199 | 48.346 |
| $TiO_2$ | 0.000 | 0.025 | 0.000 | 0.000 | 0.000 | 0.000 | 0.000 | 0.000 | 0.000 | 0.000 | 0.045 | 0.000 | 0.000 | 0.000 |
| $Al_2O_3$ | 32.547 | 32.825 | 34.123 | 34.020 | 33.008 | 33.079 | 34.941 | 22.754 | 27.003 | 23.535 | 32.684 | 32.680 | 32.596 | 33.449 |
| $Fe_2O_3$ | 0.279 | 0.000 | 0.139 | 0.196 | 0.297 | 0.200 | 0.056 | 0.081 | 0.169 | 0.122 | 0.121 | 0.179 | 0.370 | 0.118 |
| MnO | 0.004 | 0.000 | 0.032 | 0.000 | 0.000 | 0.191 | 0.000 | 0.054 | 0.000 | 0.054 | 0.032 | 0.000 | 0.000 | 0.000 |
| MgO | 0.000 | 0.010 | 0.000 | 0.007 | 0.032 | 0.037 | 0.009 | 0.007 | 0.004 | 0.039 | 0.000 | 0.034 | 0.085 | 0.010 |
| CaO | 15.736 | 16.357 | 17.050 | 17.266 | 16.549 | 16.458 | 18.519 | 3.493 | 8.742 | 4.452 | 15.605 | 15.677 | 16.162 | 16.004 |
| $Na_2O$ | 2.531 | 2.606 | 1.807 | 1.844 | 2.380 | 2.268 | 0.725 | 9.356 | 6.358 | 8.965 | 2.409 | 2.682 | 2.329 | 2.391 |
| $K_2O$ | 0.039 | 0.030 | 0.000 | 0.011 | 0.032 | 0.006 | 0.000 | 0.031 | 0.032 | 0.050 | 0.011 | 0.030 | 0.069 | 0.021 |
| Total | 99.793 | 99.872 | 100.205 | 100.148 | 100.304 | 100.068 | 98.150 | 99.077 | 97.415 | 99.456 | 98.732 | 99.951 | 98.810 | 100.339 |
| Si | 2.231 | 2.205 | 2.156 | 2.149 | 2.197 | 2.194 | 2.064 | 2.816 | 2.538 | 2.769 | 2.215 | 2.228 | 2.193 | 2.204 |
| Ti | 0.000 | 0.001 | 0.000 | 0.000 | 0.000 | 0.000 | 0.000 | 0.000 | 0.000 | 0.000 | 0.002 | 0.000 | 0.000 | 0.000 |
| Al | 1.758 | 1.777 | 1.842 | 1.841 | 1.780 | 1.788 | 1.936 | 1.193 | 1.466 | 1.234 | 1.784 | 1.763 | 1.785 | 1.797 |
| Fe3 | 0.010 | 0.000 | 0.005 | 0.007 | 0.010 | 0.007 | 0.002 | 0.003 | 0.006 | 0.004 | 0.004 | 0.006 | 0.013 | 0.004 |
| Mn | 0.000 | 0.000 | 0.001 | 0.000 | 0.000 | 0.007 | 0.000 | 0.002 | 0.000 | 0.002 | 0.001 | 0.000 | 0.000 | 0.000 |
| Mg | 0.000 | 0.001 | 0.000 | 0.000 | 0.002 | 0.003 | 0.001 | 0.000 | 0.000 | 0.003 | 0.000 | 0.002 | 0.006 | 0.001 |
| Ca | 0.773 | 0.805 | 0.837 | 0.849 | 0.811 | 0.809 | 0.933 | 0.167 | 0.431 | 0.212 | 0.774 | 0.769 | 0.805 | 0.782 |
| Na | 0.225 | 0.232 | 0.160 | 0.164 | 0.211 | 0.202 | 0.066 | 0.807 | 0.568 | 0.773 | 0.216 | 0.238 | 0.210 | 0.211 |
| K | 0.002 | 0.002 | 0.000 | 0.001 | 0.002 | 0.000 | 0.000 | 0.002 | 0.002 | 0.003 | 0.001 | 0.002 | 0.004 | 0.001 |
| total | 4.999 | 5.022 | 5.001 | 5.010 | 5.014 | 5.010 | 5.001 | 4.990 | 5.011 | 5.000 | 4.998 | 5.008 | 5.015 | 5.001 |
| An% | 77.3 | 80.6 | 83.8 | 85.0 | 81.4 | 81.9 | 93.3 | 16.9 | 43.2 | 21.7 | 77.6 | 77.1 | 81.0 | 78.3 |

Table 7-25: Microprobe measurement in sample U1309D 10R-1 127-129 cm. Amphibole and plagioclase analyses of leucocratic vein

| Oxide wt% | Am1 | Am2 | Plg1 | Plg2 |
|---|---|---|---|---|
| $SiO_2$ | 48.446 | 53.238 | 58.690 | 67.628 |
| $TiO_2$ | 0.949 | 0.331 | 0.000 | 0.029 |
| $Al_2O_3$ | 5.169 | 2.885 | 26.200 | 20.322 |
| $Cr_2O_3$ | 0.051 | 0.134 | | |
| $Fe_2O_3$ | 0.000 | 0.000 | 0.000 | 0.097 |
| FeO | 16.657 | 12.645 | | |
| MnO | 0.254 | 0.089 | 0.000 | 0.022 |
| MgO | 12.529 | 14.542 | 0.022 | 0.013 |
| CaO | 10.305 | 12.473 | 7.915 | 0.918 |
| $Na_2O$ | 1.047 | 0.373 | 7.276 | 11.450 |
| $K_2O$ | 0.332 | 0.000 | 0.035 | 0.022 |
| $H_2O$ | 1.898 | 2.051 | | |
| F | 0.095 | 0.000 | | |
| Cl | 0.183 | 0.049 | | |
| Total | 97.914 | 98.810 | 100.138 | 100.501 |
| Si | 7.301 | 7.736 | 2.619 | 2.949 |
| $Al_{(IV)}$ | 0.699 | 0.264 | 1.378 | 1.044 |
| $Al_{(VI)}$ | 0.219 | 0.230 | | |
| Ti | 0.108 | 0.036 | 0.000 | 0.001 |
| Cr | 0.006 | 0.015 | | |
| $Fe^{3+}$ | 0.000 | 0.000 | 0.000 | 0.003 |
| $Fe^{2+}$ | 2.099 | 1.537 | | |
| Mn | 0.032 | 0.011 | 0.000 | 0.001 |
| Mg | 2.815 | 3.150 | 0.001 | 0.001 |
| Ca | 1.664 | 1.942 | 0.378 | 0.043 |
| Na | 0.306 | 0.105 | 0.629 | 0.968 |
| K | 0.064 | 0.000 | 0.002 | 0.001 |
| OH | 1.908 | 1.988 | | |
| F | 0.045 | 0.000 | | |
| Cl | 0.047 | 0.012 | | |
| total | 17.314 | 17.026 | 5.008 | 5.011 |
| Nature | MgHb | Act | | |
| An% | | | 38.0 | 4.5 |

Table 7-26: Microprobe measurement in sample U1309D 12R-3 46-51 cm. Amphibole analyses

| Oxide wt% | Am1 | Am2 |
|---|---|---|
| $SiO_2$ | 50.995 | 53.194 |
| $TiO_2$ | 0.256 | 0.134 |
| $Al_2O_3$ | 4.004 | 1.960 |
| $Cr_2O_3$ | 0.026 | 0.083 |
| $Fe_2O_3$ | 2.505 | 1.738 |
| FeO | 12.930 | 13.493 |
| MnO | 0.216 | 0.294 |
| MgO | 14.054 | 15.247 |
| CaO | 11.074 | 10.737 |
| $Na_2O$ | 0.770 | 0.541 |
| $K_2O$ | 0.118 | 0.042 |
| $H_2O$ | 2.032 | 2.000 |
| F | 0.000 | 0.123 |
| Cl | 0.053 | 0.027 |
| Total | 99.033 | 99.613 |
| Si | 7.473 | 7.722 |
| $Al_{(IV)}$ | 0.527 | 0.278 |
| $Al_{(VI)}$ | 0.165 | 0.058 |
| Ti | 0.028 | 0.015 |
| Cr | 0.003 | 0.010 |
| $Fe^{3+}$ | 0.276 | 0.190 |
| $Fe^{2+}$ | 1.585 | 1.638 |
| Mn | 0.027 | 0.036 |
| Mg | 3.071 | 3.300 |
| Ca | 1.739 | 1.670 |
| Na | 0.219 | 0.152 |
| K | 0.022 | 0.008 |
| OH | 1.987 | 1.937 |
| F | 0.000 | 0.056 |
| Cl | 0.013 | 0.007 |
| total | 17.134 | 17.076 |
| Nature | MgHb | Act |

Table 7-27: Microprobe measurement in sample U1309D 17R-2 59-61 cm. Amphibole and plagioclase analyses

| Oxide wt% | Am1 | Am2 | Plg1 | Plg2 |
|---|---|---|---|---|
| $SiO_2$ | 53.980 | 54.138 | 60.784 | 68.977 |
| $TiO_2$ | 0.277 | 0.123 | 0.035 | 0.008 |
| $Al_2O_3$ | 2.755 | 1.490 | 25.917 | 20.975 |
| $Cr_2O_3$ | 0.000 | 0.026 | | |
| $Fe_2O_3$ | 0.000 | 0.000 | 0.000 | 0.002 |
| FeO | 11.361 | 17.242 | | |
| MnO | 0.262 | 0.239 | 0.000 | 0.000 |
| MgO | 16.705 | 12.564 | 0.000 | 0.000 |
| CaO | 11.197 | 12.022 | 7.627 | 1.387 |
| $Na_2O$ | 0.769 | 0.215 | 7.826 | 11.583 |
| $K_2O$ | 0.047 | 0.006 | 0.014 | 0.039 |
| $H_2O$ | 1.991 | 2.016 | | |
| F | 0.196 | 0.071 | | |
| Cl | 0.040 | 0.016 | | |
| Total | 99.580 | 100.168 | 102.203 | 102.971 |
| Si | 7.728 | 7.902 | 2.654 | 2.939 |
| $Al_{(IV)}$ | 0.272 | 0.098 | 1.334 | 1.053 |
| $Al_{(VI)}$ | 0.193 | 0.159 | | |
| Ti | 0.030 | 0.014 | 0.001 | 0.000 |
| Cr | 0.000 | 0.003 | | |
| $Fe^{3+}$ | 0.000 | 0.000 | 0.000 | 0.000 |
| $Fe^{2+}$ | 1.360 | 2.105 | | |
| Mn | 0.032 | 0.030 | 0.000 | 0.000 |
| Mg | 3.566 | 2.734 | 0.000 | 0.000 |
| Ca | 1.718 | 1.880 | 0.357 | 0.063 |
| Na | 0.213 | 0.061 | 0.663 | 0.957 |
| K | 0.009 | 0.001 | 0.001 | 0.002 |
| OH | 1.902 | 1.963 | | |
| F | 0.089 | 0.033 | | |
| Cl | 0.010 | 0.004 | | |
| total | 17.120 | 16.986 | 5.009 | 5.014 |
| Nature | Act | Act | | |
| An% | | | 35.7 | 6.3 |

Table 7-28: Microprobe measurement in sample U1309D 40R-1 21-24. Plagioclase analyses.

| Oxide wt% | Plg 1 | Plg 2 |
|---|---|---|
| $SiO_2$ | 70.21 | 69.89 |
| $TiO_2$ | 0.03 | 0.01 |
| $Al_2O_3$ | 20.36 | 20.52 |
| $Fe_2O_3$ | 0.00 | 0.00 |
| MnO | 0.04 | 0.00 |
| MgO | 0.00 | 0.00 |
| CaO | 0.58 | 0.81 |
| $Na_2O$ | 11.64 | 11.57 |
| $K_2O$ | 0.06 | 0.04 |
| Total | 102.93 | 102.83 |
| Si | 2.981 | 2.971 |
| Ti | 0.001 | 0.000 |
| Al | 1.019 | 1.028 |
| Fe3 | 0.000 | 0.000 |
| Mn | 0.001 | 0.000 |
| Mg | 0.000 | 0.000 |
| Ca | 0.026 | 0.037 |
| Na | 0.958 | 0.953 |
| K | 0.003 | 0.002 |
| total | 4.990 | 4.992 |
| An% | 2.8 | 3.7 |

Table 7-29: Microprobe measurement in sample U1309D 41R-1 89-92 cm. Plagioclase analyses

| Oxide wt% | Plg 1 | Plg 2 | Plg 3 |
|---|---|---|---|
| $SiO_2$ | 68.101 | 70.217 | 51.141 |
| $TiO_2$ | 0.000 | 0.041 | 0.077 |
| $Al_2O_3$ | 20.318 | 19.915 | 32.177 |
| $Fe_2O_3$ | 0.123 | 0.020 | 0.178 |
| MnO | 0.087 | 0.005 | 0.002 |
| MgO | 0.000 | 0.034 | 0.000 |
| CaO | 1.904 | 0.396 | 15.166 |
| $Na_2O$ | 10.598 | 12.299 | 3.039 |
| $K_2O$ | 0.416 | 0.020 | 0.032 |
| Total | 101.547 | 102.947 | 101.812 |
| Si | 2.946 | 2.986 | 2.289 |
| Ti | 0.000 | 0.001 | 0.003 |
| Al | 1.036 | 0.998 | 1.698 |
| Fe3 | 0.004 | 0.001 | 0.006 |
| Mn | 0.003 | 0.000 | 0.000 |
| Mg | 0.000 | 0.002 | 0.000 |
| Ca | 0.088 | 0.018 | 0.727 |
| Na | 0.889 | 1.014 | 0.264 |
| K | 0.023 | 0.001 | 0.002 |
| total | 4.990 | 5.021 | 4.989 |
| An% | 9.1 | 2.0 | 72.8 |

Table 7-30: Microprobe measurement in sample U1309D 60R-3 35-45 cm. Prehnite and hydrogrossular analyses

| Oxide wt% | Prh1 | Prh2 | Prh3 | Prh4 | Prh5 | Prh6 | Prh7 | Hglr1 | Hglr2 | Hglr3 |
|---|---|---|---|---|---|---|---|---|---|---|
| $SiO_2$ | 42.01 | 42.07 | 42.91 | 41.98 | 43.26 | 42.88 | 42.97 | 36.58 | 36.63 | 35.99 |
| $TiO_2$ | 0.000 | 0.021 | 0.049 | 0.053 | 0.000 | 0.068 | 0.000 | 0.030 | 0.053 | 0.108 |
| $Al_2O_3$ | 24.57 | 24.82 | 25.05 | 25.27 | 24.89 | 24.76 | 25.41 | 21.03 | 22.00 | 20.84 |
| $Fe_2O_3$ | 0.280 | 0.279 | 0.207 | 0.211 | 0.113 | 0.129 | 0.214 | 1.858 | 0.899 | 3.141 |
| MnO | 0.168 | 0.072 | 0.073 | 0.003 | 0.12 | 0.000 | 0.074 | 0.171 | 0.172 | 0.288 |
| MgO | 0.006 | 0.008 | 0.009 | 0.046 | 0.039 | 0.017 | 0.000 | 0.635 | 0.068 | 0.152 |
| CaO | 26.97 | 26.72 | 26.76 | 26.55 | 26.72 | 26.79 | 25.46 | 35.80 | 37.32 | 36.43 |
| $Na_2O$ | 0.095 | 0.043 | 0.024 | 0.054 | 0.04 | 0.105 | 0.18 | 0.021 | 0.039 | 0.011 |
| $K_2O$ | 0.000 | 0.004 | 0.000 | 0.004 | 0.007 | 0.004 | 0.000 | 0.001 | 0.025 | 0.016 |
| $H_2O$ | 4.244 | 4.25 | 4.307 | 4.261 | 4.316 | 4.292 | 4.292 | | | |
| Total | 98.35 | 98.29 | 99.39 | 98.43 | 99.51 | 99.04 | 98.59 | 96.13 | 97.21 | 96.97 |
| Si | 5.894 | 5.895 | 5.934 | 5.866 | 5.971 | 5.951 | 5.963 | 0.242 | 0.239 | 0.238 |
| Ti | 0.000 | 0.002 | 0.005 | 0.006 | 0.000 | 0.007 | 0.000 | 0.000 | 0.000 | 0.001 |
| Al | 4.063 | 4.098 | 4.082 | 4.163 | 4.050 | 4.050 | 4.156 | 0.164 | 0.169 | 0.162 |
| Fe3 | 0.030 | 0.029 | 0.022 | 0.022 | 0.012 | 0.013 | 0.022 | 0.010 | 0.005 | 0.017 |
| Mn | 0.020 | 0.009 | 0.009 | 0.000 | 0.014 | 0.000 | 0.009 | 0.001 | 0.001 | 0.002 |
| Mg | 0.001 | 0.002 | 0.002 | 0.010 | 0.008 | 0.004 | 0.000 | 0.006 | 0.001 | 0.002 |
| Ca | 4.054 | 4.012 | 3.965 | 3.975 | 3.951 | 3.984 | 3.786 | 0.253 | 0.261 | 0.258 |
| Na | 0.026 | 0.012 | 0.006 | 0.015 | 0.011 | 0.028 | 0.048 | 0.000 | 0.000 | 0.000 |
| K | 0.000 | 0.001 | 0.000 | 0.001 | 0.001 | 0.001 | 0.000 | 0.000 | 0.000 | 0.000 |
| OH | 3.972 | 3.972 | 3.973 | 3.972 | 3.974 | 3.974 | 3.974 | | | |
| total | 18.05 | 18.03 | 17.99 | 18.03 | 17.99 | 18.01 | 17.96 | 0.68 | 0.68 | 0.68 |

Table 7-31: Microprobe measurement in sample U1309D 75R-2 77-80 cm. Plagioclase analyses

| Oxide wt% | Plg1 | Plg2 | Plg3 | Plg4 | Plg5 | Plg6 | Plg7 | Plg8 | Plg9 | Plg10 | Plg11 | Plg12 | Plg13 | Plg14 |
|---|---|---|---|---|---|---|---|---|---|---|---|---|---|---|
| $SiO_2$ | 67.247 | 65.131 | 66.848 | 65.402 | 59.219 | 60.123 | 59.652 | 59.123 | 58.961 | 59.374 | 65.470 | 64.890 | 65.448 | 66.375 |
| $TiO_2$ | 0.064 | 0.000 | 0.000 | 0.000 | 0.000 | 0.024 | 0.018 | 0.039 | 0.000 | 0.036 | 0.037 | 0.000 | 0.000 | 0.013 |
| $Al_2O_3$ | 21.788 | 22.735 | 21.495 | 22.768 | 25.798 | 25.462 | 26.133 | 25.662 | 25.663 | 26.149 | 21.853 | 22.156 | 21.779 | 21.262 |
| $Fe_2O_3$ | 0.000 | 0.000 | 0.059 | 0.000 | 0.332 | 0.422 | 0.403 | 0.304 | 0.334 | 0.670 | 0.085 | 0.000 | 0.001 | 0.033 |
| MnO | 0.039 | 0.000 | 0.051 | 0.020 | 0.041 | 0.014 | 0.000 | 0.000 | 0.003 | 0.000 | 0.032 | 0.000 | 0.000 | 0.000 |
| MgO | 0.000 | 0.011 | 0.000 | 0.038 | 0.020 | 0.017 | 0.036 | 0.026 | 0.020 | 0.054 | 0.000 | 0.000 | 0.000 | 0.000 |
| CaO | 1.618 | 3.209 | 1.629 | 3.028 | 7.690 | 7.803 | 7.663 | 7.967 | 7.939 | 7.712 | 2.424 | 2.492 | 2.588 | 2.052 |
| $Na_2O$ | 10.389 | 9.785 | 10.239 | 9.220 | 6.972 | 7.546 | 7.010 | 6.677 | 6.924 | 7.095 | 10.191 | 9.916 | 9.943 | 10.356 |
| $K_2O$ | 0.011 | 0.015 | 0.008 | 0.017 | 0.105 | 0.056 | 0.066 | 0.090 | 0.071 | 0.075 | 0.030 | 0.011 | 0.032 | 0.006 |
| Total | 101.156 | 100.886 | 100.329 | 100.493 | 100.177 | 101.467 | 100.981 | 99.888 | 99.915 | 101.165 | 100.122 | 99.465 | 99.791 | 100.097 |
| Si | 2.909 | 2.841 | 2.915 | 2.854 | 2.639 | 2.650 | 2.635 | 2.641 | 2.636 | 2.623 | 2.874 | 2.864 | 2.880 | 2.907 |
| Ti | 0.002 | 0.000 | 0.000 | 0.000 | 0.000 | 0.001 | 0.001 | 0.001 | 0.000 | 0.001 | 0.001 | 0.000 | 0.000 | 0.000 |
| Al | 1.111 | 1.169 | 1.105 | 1.171 | 1.355 | 1.323 | 1.361 | 1.351 | 1.352 | 1.362 | 1.131 | 1.153 | 1.129 | 1.098 |
| Fe3 | 0.000 | 0.000 | 0.002 | 0.000 | 0.011 | 0.014 | 0.013 | 0.010 | 0.011 | 0.022 | 0.003 | 0.000 | 0.000 | 0.001 |
| Mn | 0.001 | 0.000 | 0.002 | 0.001 | 0.002 | 0.001 | 0.000 | 0.000 | 0.000 | 0.000 | 0.001 | 0.000 | 0.000 | 0.000 |
| Mg | 0.000 | 0.001 | 0.000 | 0.002 | 0.001 | 0.001 | 0.002 | 0.002 | 0.001 | 0.004 | 0.000 | 0.000 | 0.000 | 0.000 |
| Ca | 0.075 | 0.150 | 0.076 | 0.142 | 0.367 | 0.368 | 0.363 | 0.381 | 0.380 | 0.365 | 0.114 | 0.118 | 0.122 | 0.096 |
| Na | 0.871 | 0.828 | 0.866 | 0.780 | 0.602 | 0.645 | 0.600 | 0.578 | 0.600 | 0.608 | 0.867 | 0.849 | 0.848 | 0.879 |
| K | 0.001 | 0.001 | 0.000 | 0.001 | 0.006 | 0.003 | 0.004 | 0.005 | 0.004 | 0.004 | 0.002 | 0.001 | 0.002 | 0.000 |
| total | 4.970 | 4.989 | 4.965 | 4.951 | 4.983 | 5.005 | 4.979 | 4.969 | 4.985 | 4.989 | 4.993 | 4.984 | 4.981 | 4.983 |
| An% | 7.6 | 15.1 | 7.8 | 14.5 | 37.0 | 37.0 | 36.5 | 38.3 | 38.2 | 36.9 | 11.5 | 11.8 | 12.2 | 9.6 |

Table 7-31(continued)

| Oxide wt% | Plg15 | Plg16 | Plg17 | Plg18 | Plg19 | Plg20 | Plg21 | Plg22 | Plg23 | Plg24 | Plg25 | Plg26 | Plg27 | Plg28 |
|---|---|---|---|---|---|---|---|---|---|---|---|---|---|---|
| $SiO_2$ | 67.819 | 65.413 | 65.167 | 67.267 | 65.344 | 67.545 | 65.923 | 59.583 | 59.748 | 59.894 | 66.462 | 66.364 | 58.675 | 66.311 |
| $TiO_2$ | 0.018 | 0.000 | 0.000 | 0.004 | 0.048 | 0.000 | 0.000 | 0.000 | 0.029 | 0.000 | 0.000 | 0.000 | 0.067 | 0.000 |
| $Al_2O_3$ | 20.326 | 22.055 | 22.150 | 20.713 | 21.792 | 21.583 | 21.769 | 26.215 | 26.044 | 26.192 | 22.588 | 22.101 | 26.200 | 21.498 |
| $Fe_2O_3$ | 0.113 | 0.000 | 0.000 | 0.051 | 0.000 | 0.059 | 0.000 | 0.591 | 0.430 | 0.123 | 0.201 | 0.000 | 0.308 | 0.000 |
| MnO | 0.000 | 0.015 | 0.000 | 0.000 | 0.000 | 0.060 | 0.011 | 0.030 | 0.002 | 0.000 | 0.000 | 0.062 | 0.000 | 0.042 |
| MgO | 0.022 | 0.020 | 0.000 | 0.014 | 0.006 | 0.000 | 0.000 | 0.032 | 0.033 | 0.000 | 0.000 | 0.000 | 0.027 | 0.000 |
| CaO | 0.675 | 2.805 | 2.867 | 1.187 | 2.391 | 1.795 | 2.134 | 7.738 | 7.748 | 7.391 | 2.997 | 2.515 | 8.130 | 2.385 |
| $Na_2O$ | 10.934 | 10.072 | 10.151 | 10.866 | 9.810 | 9.812 | 10.180 | 7.089 | 7.052 | 7.355 | 9.169 | 9.674 | 6.706 | 10.095 |
| $K_2O$ | 0.013 | 0.013 | 0.027 | 0.038 | 0.006 | 0.038 | 0.021 | 0.056 | 0.094 | 0.019 | 0.004 | 0.004 | 0.041 | 0.029 |
| Total | 99.920 | 100.393 | 100.362 | 100.140 | 99.397 | 100.892 | 100.038 | 101.334 | 101.180 | 100.974 | 101.421 | 100.720 | 100.154 | 100.360 |
| Si | 2.963 | 2.865 | 2.858 | 2.940 | 2.882 | 2.924 | 2.890 | 2.627 | 2.636 | 2.643 | 2.871 | 2.887 | 2.617 | 2.898 |
| Ti | 0.001 | 0.000 | 0.000 | 0.000 | 0.002 | 0.000 | 0.000 | 0.000 | 0.001 | 0.000 | 0.000 | 0.000 | 0.002 | 0.000 |
| Al | 1.047 | 1.139 | 1.145 | 1.067 | 1.133 | 1.101 | 1.125 | 1.362 | 1.354 | 1.362 | 1.150 | 1.133 | 1.377 | 1.107 |
| Fe3 | 0.004 | 0.000 | 0.000 | 0.002 | 0.000 | 0.002 | 0.000 | 0.020 | 0.014 | 0.004 | 0.007 | 0.000 | 0.010 | 0.000 |
| Mn | 0.000 | 0.001 | 0.000 | 0.000 | 0.000 | 0.002 | 0.000 | 0.001 | 0.000 | 0.000 | 0.000 | 0.002 | 0.000 | 0.002 |
| Mg | 0.001 | 0.001 | 0.000 | 0.001 | 0.000 | 0.000 | 0.000 | 0.002 | 0.002 | 0.000 | 0.000 | 0.000 | 0.002 | 0.000 |
| Ca | 0.032 | 0.132 | 0.135 | 0.056 | 0.113 | 0.083 | 0.100 | 0.366 | 0.366 | 0.349 | 0.139 | 0.117 | 0.388 | 0.112 |
| Na | 0.926 | 0.855 | 0.863 | 0.921 | 0.839 | 0.823 | 0.865 | 0.606 | 0.603 | 0.629 | 0.768 | 0.816 | 0.580 | 0.856 |
| K | 0.001 | 0.001 | 0.002 | 0.002 | 0.000 | 0.002 | 0.001 | 0.003 | 0.005 | 0.001 | 0.000 | 0.000 | 0.002 | 0.002 |
| total | 4.974 | 4.993 | 5.002 | 4.987 | 4.969 | 4.938 | 4.981 | 4.987 | 4.983 | 4.989 | 4.935 | 4.955 | 4.979 | 4.976 |
| An% | 3.3 | 13.4 | 13.5 | 5.6 | 11.3 | 8.5 | 10.1 | 36.9 | 36.9 | 34.9 | 13.9 | 11.9 | 39.0 | 11.3 |

Table 7-32: Microprobe measurement in sample U1309D 144R-1 105-116 cm. Amphibole analyses

| Oxide wt% | Am1 | Am2 |
|---|---|---|
| $SiO_2$ | 49.022 | 49.343 |
| $TiO_2$ | 0.175 | 0.217 |
| $Al_2O_3$ | 3.015 | 3.938 |
| $Cr_2O_3$ | 0.069 | 0.020 |
| $Fe_2O_3$ | 1.524 | 2.946 |
| FeO | 26.245 | 20.030 |
| MnO | 0.433 | 0.343 |
| MgO | 5.816 | 9.451 |
| CaO | 10.891 | 10.710 |
| $Na_2O$ | 0.414 | 0.698 |
| $K_2O$ | 0.055 | 0.099 |
| $H_2O$ | 1.897 | 1.927 |
| F | 0.000 | 0.000 |
| Cl | 0.154 | 0.248 |
| Total | 99.710 | 99.970 |
| Si | 7.591 | 7.434 |
| $Al_{(IV)}$ | 0.409 | 0.566 |
| $Al_{(VI)}$ | 0.141 | 0.133 |
| Ti | 0.020 | 0.025 |
| Cr | 0.008 | 0.002 |
| $Fe^{3+}$ | 0.178 | 0.334 |
| $Fe^{2+}$ | 3.399 | 2.524 |
| Mn | 0.057 | 0.044 |
| Mg | 1.343 | 2.123 |
| Ca | 1.807 | 1.729 |
| Na | 0.124 | 0.204 |
| K | 0.011 | 0.019 |
| OH | 1.960 | 1.937 |
| F | 0.000 | 0.000 |
| Cl | 0.040 | 0.063 |
| total | 17.088 | 17.135 |
| Nature | Fe Act | Fe Hb |

# 2 - Microthermometric measurements

Table 7-33: Microthermometric measurements of sample U1309D 1R-1 41-44 cm quartz vein – wafer number 62965. Tm = Temperature of melting of ice. Th = Temperature of homogenisation.

| Study Zone | Inclusion Nb | Origin | Tm | Salinity | Th | Fluid type |
|---|---|---|---|---|---|---|
| 1 | 1 | Primary | -2.2 | 3.71 | 149.1 | 1a |
| | 2 | Primary | -2.1 | 3.55 | 166.2 | 1a |
| | 3 | Primary | -2.1 | 3.55 | 161.7 | 1a |
| | 4 | | -2.2 | 3.71 | 165.1 | 1a |
| | 5 | Primary | -2.3 | 3.87 | - | 1a |
| | 6 | Primary | -2.1 | 3.55 | 160.9 | 1a |
| | 7 | Primary | -2.2 | 3.71 | 161 | 1a |
| | 8 | Primary | -2.2 | 3.71 | 161 | 1a |
| | 9 | Primary | -2.2 | 3.71 | 156.4 | 1a |
| | 10 | Primary | -2.1 | 3.55 | 168.6 | 1a |
| 2 | 1 | Primary | -2 | 3.39 | 229.2 | 1a |
| | 2 | Primary | -2.1 | 3.55 | 197.5 | 1a |
| | 3 | Primary | -2.1 | 3.55 | 183.2 | 1a |
| | 4 | Primary | -2.1 | 3.55 | 194.9 | 1a |
| | 5 | Primary | -2.6 | 4.34 | 229.6 | 1a |
| | 6 | Primary | -2.2 | 3.71 | 219.5 | 1a |
| | 7 | Primary | -2.2 | 3.71 | 238.7 | 1a |
| | 8 | Primary | -2.2 | 3.71 | 174.5 | 1a |
| 3 | 1 | Primary | -1.9 | 3.23 | - | 1a |
| | 2 | Primary | -1.9 | 3.23 | - | 1a |
| | 3 | Primary | -1.9 | 3.23 | 285 | 1a |
| | 4 | Primary | -2 | 3.39 | 196.4 | 1a |
| | 5 | Primary | -2.2 | 3.71 | 169.6 | 1a |
| | 6 | Primary | -2.1 | 3.55 | 160.5 | 1a |
| 5 | 1 | Primary | -2.6 | 4.34 | 190.6 | 1a |
| | 2 | Primary | -2.6 | 4.34 | 186.2 | 1a |
| | 3 | Primary | -2.6 | 4.34 | 185.8 | 1a |
| | 4 | Primary | -2.7 | 4.49 | 182.9 | 1a |
| | 5 | Primary | -2.6 | 4.34 | 184.6 | 1a |
| 6 | 1 | Primary | -1.9 | 3.23 | 193.3 | 1a |
| | 2 | Primary | -1.9 | 3.23 | 189.3 | 1a |
| | 3 | Primary | -2 | 3.39 | 178.7 | 1a |
| | 4 | Primary | -1.9 | 3.23 | 162.9 | 1a |
| | 5 | Primary | -1.9 | 3.23 | 169.9 | 1a |
| | 6 | Primary | -1.9 | 3.23 | 171.4 | 1a |
| 7 | 1 | Primary | -1.8 | 3.06 | 197.6 | 1a |
| | 2 | Primary | -1.9 | 3.23 | 178.3 | 1a |
| 8 | 1 | Primary | 2.3 | -4.33 | 128 | 1a |
| | 2 | Primary | -1.9 | 3.23 | 147.7 | 1a |
| | 3 | Primary | 9 | -20.01 | - | 1a |
| 9 | 1 | Primary | -2.8 | 4.65 | 163 | 1a |

Table 7-33 (continued)

| Study Zone | Inclusion Nb | Origin | Tm | Salinity | Th | Fluid type |
|---|---|---|---|---|---|---|
| 10 | 1 | Primary | -2.2 | 3.71 | 161.7 | 1a |
| | 2 | Primary | -2.2 | 3.71 | 174 | 1a |
| | 3 | Primary | -2.1 | 3.55 | 163.1 | 1a |
| | 4 | Primary | -2.2 | 3.71 | 165.5 | 1a |
| | 5 | Primary | -2.3 | 3.87 | 163.2 | 1a |
| | 6 | Primary | -2.3 | 3.87 | 168.1 | 1a |
| | 7 | Primary | -2.3 | 3.87 | 166.1 | 1a |
| | 8 | Primary | -2.4 | 4.03 | 184.6 | 1a |
| | 9 | Primary | -2.3 | 3.87 | 202.9 | 1a |
| | 10 | Primary | | - | 214.6 | 1a |
| | 11 | Primary | -2.2 | 3.71 | 164.7 | 1a |
| | 12 | Primary | -2.3 | 3.87 | 162.7 | 1a |
| | 13 | Primary | -2.3 | 3.87 | 162.8 | 1a |
| | 14 | Primary | -2.3 | 3.87 | 164.5 | 1a |
| | 15 | Primary | -2.3 | 3.87 | 158.2 | 1a |
| | 16 | Primary | -2.2 | 3.71 | 219.7 | 1a |
| | 17 | Primary | | - | 206.1 | 1a |
| | 18 | Primary | -2.3 | 3.87 | 211.1 | 1a |
| | 19 | Primary | -2.4 | 4.03 | 199.9 | 1a |
| | 20 | Primary | -2.2 | 3.71 | 163.6 | 1a |
| | 21 | Primary | -2.2 | 3.71 | 163.2 | 1a |
| | 22 | Primary | -2.2 | 3.71 | 174.5 | 1a |
| | 23 | Primary | -2.2 | 3.71 | 166.7 | 1a |
| | 25 | Primary | -3 | 4.96 | 163.5 | 1a |
| | 26 | Primary | -3.1 | 5.11 | 170.3 | 1a |

Table 7-34: Microthermometric measurements in sample U1309D 5R-3 107-110 quartz vein – wafer number 62968

| Study Zone | Inclusion Nb | Origin | Tm | Salinity | Th | Fluid type |
|---|---|---|---|---|---|---|
| 1a | 1 | Secondary | -1.9 | 3.23 | 75 | 1b |
| | 3 | Secondary | -0.2 | 0.35 | 292 | 1b |
| | 4 | Secondary | -0.2 | 0.35 | 262 | 1b |
| | 5 | Secondary | -0.3 | 0.53 | 311 | 1b |
| | 7 | Secondary | -0.2 | 0.35 | 262 | 1b |
| | 8 | Secondary | -0.2 | 0.35 | 263 | 1b |
| | 9 | Secondary | -0.3 | 0.53 | 308 | 1b |
| | 10 | Secondary | -0.3 | 0.53 | 298 | 1b |
| | 11 | Secondary | -0.2 | 0.35 | - | 1b |
| | 12 | Secondary | -0.2 | 0.35 | 254 | 1b |
| | 13 | Secondary | -0.3 | 0.53 | 307 | 1b |
| | 14 | Secondary | -0.4 | 0.70 | 278 | 1b |
| | 15 | Secondary | -0.2 | 0.35 | - | 1b |
| | 16 | Secondary | -0.3 | 0.53 | 250 | 1b |
| | 17 | Secondary | -0.2 | 0.35 | 303 | 1b |
| | 18 | Secondary | -0.2 | 0.35 | 256 | 1b |
| 4b | 1 | Secondary | -0.4 | 0.70 | 218 | 1b |
| | 2 | Secondary | -0.4 | 0.70 | - | 1b |
| | 3 | Secondary | -0.4 | 0.70 | - | 1b |
| | 4 | Secondary | -0.6 | 1.05 | 192 | 1b |
| | 5 | Secondary | -0.4 | 0.70 | - | 1b |
| | 6 | Secondary | -0.5 | 0.88 | 185 | 1b |
| | 7 | Secondary | -0.3 | 0.53 | 245 | 1b |
| | 8 | Secondary | -0.4 | 0.70 | 233 | 1b |
| | 9 | Secondary | -0.4 | 0.70 | - | 1b |
| | 10 | Secondary | -0.4 | 0.70 | 250 | 1b |
| | 11 | Secondary | -0.3 | 0.53 | 281 | 1b |
| | 12 | Secondary | -0.3 | 0.53 | 222 | 1b |
| | 13 | Secondary | -0.4 | 0.70 | 216 | 1b |
| | 14 | Secondary | -0.4 | 0.70 | 210 | 1b |
| | 15 | Secondary | -0.4 | 0.70 | 144 | 1b |
| | 16 | Secondary | -0.5 | 0.88 | 189 | 1b |
| | 17 | Secondary | -0.3 | 0.53 | 180 | 1b |
| | 18 | Secondary | -0.4 | 0.70 | - | 1b |
| | 19 | Secondary | -0.9 | 1.57 | - | 1b |
| | 20 | Secondary | - | - | 217 | 1b |
| | 21 | Secondary | - | - | 219 | 1b |
| | 22 | Secondary | -0.3 | 0.53 | - | 1b |
| | 23 | Secondary | -0.8 | 1.40 | - | 1b |
| | 24 | Secondary | -0.5 | 0.88 | 225 | 1b |
| | 25 | Secondary | -1.4 | 2.41 | - | 1b |
| | 26 | Secondary | -1.4 | 2.41 | - | 1b |
| | 27 | Secondary | -0.3 | 0.53 | - | 1b |
| | 28 | Secondary | -1 | 1.74 | - | 1b |
| | 29 | Secondary | -0.4 | 0.70 | 220 | 1b |
| | 30 | Secondary | -0.4 | 0.70 | - | 1b |
| | 31 | Secondary | -1.4 | 2.41 | - | 1b |
| | 32 | Secondary | -0.4 | 0.70 | 266 | 1b |
| | 34 | Secondary | -0.6 | 1.05 | - | 1b |
| | 35 | Secondary | -1.5 | 2.57 | 202 | 1b |

Table 7-34 (continued)

| Study Zone | Inclusion Nb | Origin | Tm | Salinity | Th | Fluid type |
|---|---|---|---|---|---|---|
| 4b (continued) | 36 | Secondary | -0.6 | 1.05 | - | 1b |
| | 37 | Secondary | -0.4 | 0.70 | - | 1b |
| | 38 | Secondary | -0.4 | 0.70 | 340 | 1b |
| | 39 | Secondary | -0.3 | 0.53 | 258 | 1b |
| | 40 | Secondary | -0.3 | 0.53 | - | 1b |
| | 41 | Secondary | -0.6 | 1.05 | - | 1b |
| | 42 | Secondary | -0.4 | 0.70 | 210 | 1b |
| | 43 | Secondary | -1.2 | 2.07 | 315 | 1b |
| | 44 | Secondary | -1.5 | 2.57 | - | 1b |
| | 45 | Secondary | -0.6 | 1.05 | - | 1b |
| | 46 | Secondary | -0.5 | 0.88 | - | 1b |
| | 47 | Secondary | -0.6 | 1.05 | - | 1b |
| | 48 | Secondary | -1 | 1.74 | - | 1b |
| | 49 | Secondary | -0.3 | 0.53 | 256 | 1b |
| | 1 | Secondary | -0.3 | 0.53 | 274 | 1b |
| | 2 | Secondary | -0.2 | 0.35 | 264 | 1b |
| | 3 | Secondary | -0.3 | 0.53 | 253 | 1b |
| | 4 | Secondary | -0.2 | 0.35 | 300 | 1b |
| | 5 | Secondary | -0.2 | 0.35 | 275 | 1b |
| | 6 | Secondary | -0.1 | 0.18 | 281 | 1b |
| | 7 | Secondary | -0.2 | 0.35 | 260 | 1b |
| | 8 | Secondary | -0.2 | 0.35 | 216 | 1b |
| | 9 | Secondary | -0.3 | 0.53 | 305 | 1b |
| | 10 | Secondary | -0.2 | 0.35 | 246 | 1b |
| | 11 | Secondary | -3.6 | 5.86 | - | 1b |
| | 12 | Secondary | -0.2 | 0.35 | 290 | 1b |
| | 13 | Secondary | -0.3 | 0.53 | - | 1b |
| | 14 | Secondary | -0.4 | 0.70 | 230 | 1b |
| | 15 | Secondary | -0.3 | 0.53 | 293 | 1b |
| | 16 | Secondary | -0.3 | 0.53 | 232 | 1b |
| | 17 | Secondary | -0.3 | 0.53 | 218 | 1b |
| | 18 | Secondary | -0.3 | 0.53 | 286 | 1b |
| | 19 | Secondary | -0.4 | 0.70 | 220 | 1b |
| | 20 | Secondary | -0.3 | 0.53 | 227 | 1b |
| | 21 | Secondary | -0.3 | 0.53 | 246 | 1b |
| | 22 | Secondary | -0.3 | 0.53 | 224 | 1b |
| | 23 | Secondary | -0.2 | 0.35 | 223 | 1b |
| | 24 | Secondary | -0.3 | 0.53 | 219 | 1b |
| | 25 | Secondary | -0.3 | 0.53 | - | 1b |
| | 26 | Secondary | -0.3 | 0.53 | 217 | 1b |
| | 27 | Secondary | -0.3 | 0.53 | 206 | 1b |
| | 28 | Secondary | -0.4 | 0.70 | 254 | 1b |
| | 29 | Secondary | -0.2 | 0.35 | 232 | 1b |
| | 30 | Secondary | -0.3 | 0.53 | 230 | 1b |

Table 7-35: Microthermometric measurements in sample U1309D 10R-1 117-129 quartz vein – wafer number 62970.

| Study Zone | Inclusion Nb | Origin | Tm | Salinity | Th | Fluid type |
|---|---|---|---|---|---|---|
| 1a | 1 | Secondary | -2.6 | 4.3 | 239.0 | 1a |
| | 2 | Secondary | -2.2 | 3.7 | 245.7 | 1a |
| | 3 | Secondary | -1 | 1.7 | 252.0 | 1b |
| | 4 | Secondary | -2.3 | 3.9 | 267.3 | 1a |
| | 5 | Secondary | -1.4 | 2.4 | 260.5 | 1b |
| | 6 | Secondary | -2.3 | 3.9 | 261.2 | 1a |
| | 7 | Secondary | -2.4 | 4.0 | 259.0 | 1a |
| | 8 | Secondary | -2.4 | 4.0 | 261.3 | 1a |
| | 9 | Secondary | -2.3 | 3.9 | 220.0 | 1a |
| | 10 | Secondary | -2.3 | 3.9 | 268.0 | 1a |
| | 11 | Secondary | -2.3 | 3.9 | 234.8 | 1a |
| 2a | 1 | Secondary | -1.7 | 2.9 | 278.9 | 1a |
| | 2 | Secondary | - | - | 250.8 | - |
| | 4 | Secondary | -1.8 | 3.1 | 268.5 | 1a |
| | 5 | Secondary | -1.9 | 3.2 | 291.5 | 1a |
| | 6 | Secondary | -2.2 | 3.7 | 268.3 | 1a |
| | 7 | Secondary | -1.8 | 3.1 | 237.8 | 1a |
| | 8 | Secondary | -1.8 | 3.1 | 290.3 | 1a |
| | 9 | Secondary | -2.1 | 3.5 | 282.7 | 1a |
| | 10 | Secondary | -1.8 | 3.1 | - | 1a |
| | 13 | Secondary | -1.7 | 2.9 | 293.0 | 1a |
| | 14 | Secondary | -1.6 | 2.7 | 290.0 | 1a |
| | 15 | Secondary | -1.8 | 3.1 | 255.3 | 1a |
| | 16 | Secondary | -1.8 | 3.1 | 233.5 | 1a |
| 1b1 | 1 | Secondary | -1.4 | 2.4 | 278.1 | 1b |
| | 2 | Secondary | -0.8 | 1.4 | 315.0 | 1b |
| | 3 | Secondary | -0.5 | 0.9 | 294.5 | 1b |
| | 4 | Secondary | -1.4 | 2.4 | 288.8 | 1b |
| | 5 | Secondary | -0.8 | 1.4 | 290.9 | 1b |
| | 6 | Secondary | -1.8 | 3.1 | 290.1 | 1a |
| | 7 | Secondary | -1.8 | 3.1 | 287.5 | 1a |
| | 8 | Secondary | - | - | 282.5 | - |
| | 9 | Secondary | -1.8 | 3.1 | 281.0 | 1a |
| | 10 | Secondary | -0.9 | 1.6 | 287.6 | 1b |
| | 11 | Secondary | - | - | 291.8 | - |
| | 12 | Secondary | -0.8 | 1.4 | 298.8 | 1b |
| | 13 | Secondary | -0.8 | 1.4 | 296.0 | 1b |
| | 14 | Secondary | -3.5 | 5.7 | 272.8 | 1a |
| | 15 | Secondary | - | - | 280.4 | - |
| | 16 | Secondary | - | - | 278.9 | - |
| | 17 | Secondary | - | - | 273.5 | - |
| | 18 | Secondary | -0.8 | 1.4 | 300.8 | 1b |
| | 19 | Secondary | -1 | 1.7 | 288.9 | 1b |
| | 20 | Secondary | -0.4 | 0.7 | 293.2 | 1b |
| | 21 | Secondary | -0.5 | 0.9 | 320.3 | 1b |
| | 23 | Secondary | -0.6 | 1.1 | 295.5 | 1b |
| | 24 | Secondary | -0.8 | 1.4 | 292.6 | 1b |
| | 25 | Secondary | -1.4 | 2.4 | 306.6 | 1b |
| | 26 | Secondary | -0.5 | 0.9 | 288.2 | 1b |
| | 27 | Secondary | -1.8 | 3.1 | 284.0 | 1a |
| | 28 | Secondary | -0.8 | 1.4 | 284.8 | 1b |
| | 29 | Secondary | -0.5 | 0.9 | 291.7 | 1b |
| | 30 | Secondary | -0.5 | 0.9 | 311.5 | 1b |
| | 31 | Secondary | -0.5 | 0.9 | 295.8 | 1b |

Table 7-35 (continued)

| Study zone | Inclusion Nb | Origin | Tm | Salinity | Th | Fluid type |
|---|---|---|---|---|---|---|
| 1b1 (continued) | 32 | Secondary | -0.9 | 1.6 | 294.5 | 1b |
| | 33 | Secondary | -0.5 | 0.9 | 300.9 | 1b |
| | 34 | Secondary | -0.9 | 1.6 | 298.8 | 1b |
| | 35 | Secondary | -0.9 | 1.6 | 297.4 | 1b |
| | 36 | Secondary | -0.8 | 1.4 | 284.6 | 1b |
| 1b3 | 1 | Secondary | -0.7 | 1.2 | 307.8 | 1b |
| | 23 | Secondary | -0.8 | 1.4 | 305.5 | 1b |
| | 4 | Secondary | -0.7 | 1.2 | 295.9 | 1b |
| | 5 | Secondary | -0.6 | 1.1 | - | 1b |
| | 6 | Secondary | -0.7 | 1.2 | 304.9 | 1b |
| | 7 | Secondary | -0.6 | 1.1 | - | 1b |
| | 8 | Secondary | -0.8 | 1.4 | - | 1b |
| | 9 | Secondary | -0.7 | 1.2 | - | 1b |
| | 10 | Secondary | -0.5 | 0.9 | - | 1b |
| | 11 | Secondary | -0.6 | 1.1 | - | 1b |
| | 12 | Secondary | -2 | 3.4 | - | 1a |
| | 13 | Secondary | -2 | 3.4 | 288.8 | 1a |
| | 14 | Secondary | -0.9 | 1.6 | - | 1b |
| | 15 | Secondary | -1 | 1.7 | 297.8 | 1b |
| | 16 | Secondary | -0.8 | 1.4 | 300.6 | 1b |
| | 17 | Secondary | -1.1 | 1.9 | 301.6 | 1b |
| | 18 | Secondary | -1.2 | 2.1 | 305.5 | 1b |
| | 19 | Secondary | -1.3 | 2.2 | 293.5 | 1b |

Table 7-36: Microthermometric measurements in sample U1309D 40R-1 6-12 quartz vein – wafer number 63519.

| Study zone | Inclusion Nb | Origin | Tm | Salinity | Th | Fluid type |
|---|---|---|---|---|---|---|
| 1a2 | 2 | Primary | -2 | 3.4 | 172.4 | 1a |
| | 3 | Primary | -2 | 3.4 | - | 1a |
| | 4 | Primary | - | - | 143.5 | - |
| | 5 | Primary | - | - | 187.0 | - |
| | 8 | Primary | -2.1 | 3.5 | 184.0 | 1a |
| | 9 | Primary | - | - | 169.5 | - |
| | 10 | Primary | -2.2 | 3.7 | 238.8 | 1a |
| | 11 | Primary | -2.3 | 3.9 | 167.0 | 1a |
| | 12 | Primary | -2.2 | 3.7 | 189.5 | 1a |
| | 13 | Primary | - | - | 167 | - |
| | 15 | Primary | -1.9 | 3.2 | - | 1a |

Table 7-37: Microthermometric measurements in sample U1309D 40R-1 17-19 quartz vein– wafer number 63520

| Study zone | Inclusion Nb | Origin | Tm | Salinity | Th | Fluid type |
|---|---|---|---|---|---|---|
| 1a | 1 | Primary | -1.8 | 3.1 | 202.5 | 1a |
| | 2 | Primary | -1.8 | 3.1 | 144.5 | 1a |
| | 4 | Primary | -1.4 | 2.4 | 135.0 | 1a |
| | 5 | Primary | -1.6 | 2.7 | 193.0 | 1a |
| | 6 | Primary | -2.0 | 3.4 | | 1a |
| | 7 | Primary | -1.8 | 3.1 | 201.0 | 1a |
| | 8 | Primary | -1.9 | 3.2 | 210.0 | 1a |

Table 7-37 (continued)

| Study zone | Inclusion Nb | Origin | Tm | Salinity | Th | Fluid type |
|---|---|---|---|---|---|---|
| 1a (continued) | 9 | Primary | - | - | 198.5 | 1a |
| | 10 | Primary | -2.0 | 3.4 | 211.0 | 1a |
| | 11 | Primary | -1.9 | 3.2 | 213.0 | 1a |
| | 12 | Primary | -1.8 | 3.1 | 175.0 | 1a |
| | 13 | Primary | -1.8 | 3.1 | 220.0 | 1a |
| | 14 | Primary | -2.0 | 3.4 | 206.0 | 1a |
| | 15 | Primary | -2.0 | 3.4 | - | 1a |
| | 17 | Primary | -1.8 | 3.1 | 141.0 | 1a |
| | 18 | Primary | -2.0 | 3.4 | 193.5 | 1a |
| | 19 | Primary | -2.0 | 3.4 | 214.0 | 1a |
| | 20 | Primary | -1.9 | 3.2 | - | 1a |
| | 21 | Primary | -2.0 | 3.4 | - | 1a |
| | 22 | Primary | -2.0 | 3.4 | 206.5 | 1a |
| | 23 | Primary | -1.9 | 3.2 | 206.5 | 1a |
| | 24 | Primary | -2.0 | 3.4 | 203.5 | 1a |
| | 25 | Primary | -1.9 | 3.2 | 202.0 | 1a |
| | 26 | Primary | -2.0 | 3.4 | 203.5 | 1a |
| | 27 | Primary | -1.9 | 3.2 | 204.6 | 1a |
| | 28 | Primary | -1.9 | 3.2 | 223.7 | 1a |
| | 29 | Primary | -1.9 | 3.2 | 208.5 | 1a |
| | 30 | Primary | -1.9 | 3.2 | 206.0 | 1a |
| | 31 | Primary | -1.6 | 2.7 | 210.3 | 1a |
| | 32 | Primary | -1.6 | 2.7 | 210.0 | 1a |
| | 33 | Primary | -1.6 | 2.7 | 188.5 | 1a |
| | 34 | Primary | -1.6 | 2.7 | 196.4 | 1a |
| | 35 | Primary | -1.6 | 2.7 | 189.5 | 1a |
| | 36 | Primary | -1.7 | 2.9 | 235.8 | 1a |
| | 37 | Primary | -1.6 | 2.7 | 200.6 | 1a |
| | 38 | Primary | -1.6 | 2.7 | 197.2 | 1a |
| | 39 | Primary | -1.6 | 2.7 | 199.3 | 1a |
| | 40 | Primary | -2.0 | 3.4 | 214.5 | 1a |
| | 41 | Primary | -1.7 | 2.9 | 209.0 | 1a |
| | 42 | Primary | -1.9 | 3.2 | - | 1a |
| | 43 | Primary | -1.9 | 3.2 | 210.0 | 1a |
| 2a | 1 | Primary | -2.0 | 3.4 | 229.0 | 1a |
| | 2 | Primary | -2.0 | 3.4 | 228.8 | 1a |
| | 3 | Primary | -2.0 | 3.4 | 229.5 | 1a |
| | 4 | Primary | -1.9 | 3.2 | 238.1 | 1a |
| | 5 | Primary | -1.9 | 3.2 | 251.0 | 1a |
| | 6 | Primary | -2.1 | 3.5 | 229.5 | 1a |
| | 7 | Primary | -2.0 | 3.4 | 227.4 | 1a |
| | 8 | Primary | -2.0 | 3.4 | 226.4 | 1a |
| | 9 | Primary | -1.8 | 3.1 | 229.4 | 1a |
| | 10 | Primary | -2.0 | 3.4 | 231.5 | 1a |
| | 11 | Primary | -2.0 | 3.4 | 226.0 | 1a |
| | 12 | Primary | -1.9 | 3.2 | 239.0 | 1a |
| | 13 | Primary | -1.9 | 3.2 | 225.1 | 1a |
| | 14 | Primary | -2.0 | 3.4 | 219.9 | 1a |
| | 16 | Primary | -2.0 | 3.4 | 222.0 | 1a |
| | 17 | Primary | - | - | 224.0 | - |
| | 18 | Primary | -2.0 | 3.4 | 227.5 | 1a |
| 3a | 1 | Primary | -2.2 | 3.7 | 289.5 | 1a |
| | 2 | Primary | -2.2 | 3.7 | 258.0 | 1a |
| | 3 | Primary | -2.0 | 3.4 | 202.2 | 1a |
| | 5 | Primary | -2.0 | 3.4 | 169.8 | 1a |
| | 6 | Primary | -2.0 | 3.4 | 201.5 | 1a |
| | 7 | Primary | -2.0 | 3.4 | 199.6 | 1a |

Table 7-37 (continued)

| Study zone | Inclusion Nb | Origin | Tm | Salinity | Th | Fluid type |
|---|---|---|---|---|---|---|
| 3a (continued) | 8 | Primary | -1.9 | 3.2 | 201.0 | 1a |
| | 9 | Primary | -2.0 | 3.4 | 198.0 | 1a |
| | 10 | Primary | -2.0 | 3.4 | 195.4 | 1a |
| | 11 | Primary | -1.9 | 3.2 | 211.5 | 1a |
| | 12 | Primary | -2.0 | 3.4 | 194.0 | 1a |
| | 13 | Primary | -2.0 | 3.4 | 201.6 | 1a |
| | 14 | Primary | -2.0 | 3.4 | 205.0 | 1a |
| | 16 | Primary | -2.0 | 3.4 | 228.0 | 1a |
| | 17 | Primary | -2.0 | 3.4 | 196.8 | 1a |
| | 18 | Primary | -2.1 | 3.5 | 270.0 | 1a |
| | 19 | Primary | -2.0 | 3.4 | 197.0 | 1a |
| | 20 | Primary | -2.0 | 3.4 | 201.4 | 1a |
| | 21 | Primary | -2.0 | 3.4 | 204.7 | 1a |
| | 22 | Primary | -2.1 | 3.5 | 201.4 | 1a |
| | 23 | Primary | -2.2 | 3.7 | 204.6 | 1a |
| | 24 | Primary | -2.0 | 3.4 | 204.5 | 1a |
| | 25 | Primary | -2.1 | 3.5 | 184.3 | 1a |
| | 26 | Primary | -2.0 | 3.4 | 161.3 | 1a |

Table 7-38: Microthermometric measurements in sample U1309D 40R-1 21-24 quartz vein– wafer number 62973

| Study zone | Inclusion Nb | Origin | Tm | Salinity | Th | Fluid type |
|---|---|---|---|---|---|---|
| 5 | 1 | Primary | -2.0 | 3.4 | 156.4 | 1a |
| | 2 | Primary | -2.0 | 3.4 | 163.5 | 1a |
| | 3 | Primary | -1.8 | 3.1 | 156.5 | 1a |
| | 4 | Primary | -2.2 | 3.7 | 204.9 | 1a |
| | 5 | Primary | -2.0 | 3.4 | 166.0 | 1a |
| | 7 | Primary | -2.2 | 3.7 | - | 1a |
| | 8 | Primary | -2.1 | 3.5 | 174.5 | 1a |
| | 9 | Primary | -2.1 | 3.5 | - | 1a |
| | 10 | Primary | -2.1 | 3.5 | 161.0 | 1a |
| | 11 | Primary | -2.1 | 3.5 | 124.5 | 1a |
| | 12 | Primary | -2.1 | 3.5 | 165.0 | 1a |
| | 13 | Primary | -2.0 | 3.4 | 171.0 | 1a |
| | 14 | Primary | -2.1 | 3.5 | - | 1a |
| | 15 | Primary | -2.0 | 3.4 | 180.8 | 1a |
| | 16 | Primary | -2.0 | 3.4 | 181.5 | 1a |
| | 17 | Primary | -2.0 | 3.4 | 170.3 | 1a |
| | 18 | Primary | -2.0 | 3.4 | 160.0 | 1a |
| | 19 | Primary | -1.9 | 3.2 | 150.5 | 1a |
| | 20 | Primary | -2.0 | 3.4 | 162.5 | 1a |
| | 21 | Primary | -2.0 | 3.4 | 159.5 | 1a |
| | 24 | Primary | -2.0 | 3.4 | 160.9 | 1a |
| | 25 | Primary | -2.0 | 3.4 | 168.4 | 1a |
| | 26 | Primary | -2.0 | 3.4 | 155.0 | 1a |
| | 27 | Primary | -1.9 | 3.2 | - | 1a |
| | 29 | Primary | -1.9 | 3.2 | 144.0 | 1a |
| 6 | 4 | Primary | -2.0 | 3.4 | - | 1a |
| | 5 | Primary | - | - | 144.6 | |
| | 7 | Primary | -2.0 | 3.4 | 167.7 | 1a |
| | 8 | Primary | -2.0 | 3.4 | 168.0 | 1a |
| | 9 | Primary | -2.0 | 3.4 | 179.4 | 1a |
| | 11 | Primary | -2.0 | 3.4 | 143.5 | 1a |
| | 13 | Primary | -2.0 | 3.4 | 149.0 | 1a |

Table 7-38 (continued)

| Study zone | Inclusion Nb | Origin | Tm | Salinity | Th | Fluid type |
|---|---|---|---|---|---|---|
| 6 (continued) | 14 | Primary | -2.0 | 3.4 | 144.2 | 1a |
| | 17 | Primary | -1.9 | 3.2 | 149.5 | 1a |
| | 18 | Primary | -2.2 | 3.7 | 164.5 | 1a |
| | 19 | Primary | -2.0 | 3.4 | 160.6 | 1a |
| | 23 | Primary | -2.0 | 3.4 | 146.5 | 1a |
| | 27 | Primary | -2.0 | 3.4 | 158.0 | 1a |
| | 28 | Primary | -1.9 | 3.2 | 162.0 | 1a |
| | 32 | Primary | -1.8 | 3.1 | 153.8 | 1a |
| | 33 | Primary | -2.0 | 3.4 | 167.3 | 1a |
| | 34 | Primary | -1.8 | 3.1 | 151.5 | 1a |
| | 35 | Primary | -2.0 | 3.4 | 179.9 | 1a |
| | 36 | Primary | -2.0 | 3.4 | 159.0 | 1a |
| | 37 | Primary | -1.9 | 3.2 | 147.4 | 1a |
| | 38 | Primary | -2.4 | 4.0 | - | 1a |
| | 39 | Primary | -2.0 | 3.4 | 149.5 | 1a |
| | 40 | Primary | - | - | 153.0 | - |
| | 41 | Primary | -2.0 | 3.4 | 151.0 | 1a |
| | 43 | Primary | -2.2 | 3.7 | 168.0 | 1a |
| | 44 | Primary | -2.0 | 3.4 | 157.4 | 1a |
| | 46 | Primary | -2.0 | 3.4 | 188.9 | 1a |
| | 47 | Primary | -1.9 | 3.2 | 177.6 | 1a |
| | 48 | Primary | -2.0 | 3.4 | 166.0 | 1a |
| | 49 | Primary | -2.0 | 3.4 | 173.0 | 1a |
| 13 | 1 | Primary | -1.7 | 2.9 | - | 1a |
| | 2 | Primary | -2.3 | 3.9 | 156.0 | 1a |
| | 3 | Primary | -2.4 | 4.0 | 166.2 | 1a |
| | 4 | Primary | -2.2 | 3.7 | 155.8 | 1a |
| | 5 | Primary | -2.4 | 4.0 | 139.0 | 1a |
| | 7 | Primary | -2.3 | 3.9 | 146.5 | 1a |
| | 8 | Primary | -2.2 | 3.7 | 173.5 | 1a |
| | 9 | Primary | -2.0 | 3.4 | 173.0 | 1a |
| | 10 | Primary | -2.0 | 3.4 | 162.5 | 1a |
| | 11 | Primary | -2.0 | 3.4 | 173.5 | 1a |
| | 12 | Primary | -1.9 | 3.2 | 177.7 | 1a |
| | 13 | Primary | -2.1 | 3.5 | 150.3 | 1a |

Table 7-39: Microthermometric measurements in sample U1309D 40R-1 21-24 quartz grain of trondjhemite – wafer number 62973. Thd = Halite dissolution temperature

| Study zone | Inclusion Nb | Origin | Tm | Salinity | $T_{Hd}$ | Th | Fluid type |
|---|---|---|---|---|---|---|---|
| 1 | 1 | Primary? | -6.8 | 10.2 | - | >400.0 | 3a |
| | 4 | Primary? | -8.6 | 12.4 | - | >400.0 | 3a |
| | 5 | Primary? | -13.6 | 17.4 | - | 314.5 | 3a |
| | 6 | Primary? | -8.6 | 12.4 | - | - | 3a |
| | 7 | Primary? | -2.4 | 4.0 | - | - | 1a? |
| | 9 | Primary? | -13.6 | 17.4 | - | >400.0 | 3a |
| | 10 | Primary? | -13.6 | 17.4 | - | >400.0 | 3a |
| | 11 | Primary? | -13.6 | 17.4 | - | >400.0 | 3a |
| | 12 | Primary? | -8.4 | 12.2 | - | >400.0 | 3a |
| | 13 | Primary? | -13.6 | 17.4 | - | >400.0 | 3a |
| | 14 | Primary? | -8.6 | 12.4 | - | >400.0 | 3a |
| | 15 | Primary? | -3.0 | 5.0 | - | - | 1a? |
| | 18 | Primary? | -2.4 | 4.0 | - | - | 1a? |

Table 7-39 (continued)

| Study zone | Inclusion Nb | Origin | Tm | Salinity | $T_{Hd}$ | Th | Fluid type |
|---|---|---|---|---|---|---|---|
| 1 (continued) | 19 | Primary? | -17.6 | 20.7 | - | 394.8 | 3a |
| | 20 | Primary? | -16.9 | 20.1 | - | - | 3a |
| | 21 | Primary? | -6.2 | 9.5 | - | 377.0 | 3a |
| | 36 | Primary? | -8.6 | 12.4 | - | - | 3a |
| | 23 | Primary? | -38.5 | 31.1 | 184 | 384.8 | 3b |
| | 24 | Primary? | -39.8 | 34.4 | 245 | >400.0 | 3b |
| | 25 | Primary? | -35.5 | - | - | >400.0 | - |
| | 26 | Primary? | -42.4 | 35.0 | 255 | 336.4 | 3b |
| | 27 | Primary? | -37.0 | 35.7 | 266 | 368.1 | 3b |
| | 28 | Primary? | -35.0 | - | - | >400.0 | - |
| | 29 | Primary? | -41.0 | 34.9 | 254 | 391.5 | 3b |
| | 30 | Primary? | -35.7 | 37.7 | 294 | >400.0 | 3b |
| | 32 | Primary? | -35.0 | - | - | 376.4 | - |
| | 33 | Primary? | -35.1 | - | - | 393.6 | - |
| | 34 | Primary? | -25.9 | - | - | >400.0 | - |
| | 35 | Primary? | - | 36.9 | 283 | 349.8 | 3b |

# 3 - LA-ICPMS data

Table 7-40: Measurements in sample U1309D 1R-1 41-44 cm zone 1 quartz vein– wafer number 62965. Numbers preceded by "<" mean that concentrations were under the detection limit. Cl concentrations are obtained by calculation from microthermometry. Averages and median calculations are always made with concentrations above the detection limit

| Analyte | Fi1 | Fi2 | Fi4 (+6) | Fi9 | Fi10 | Average | Median |
|---|---|---|---|---|---|---|---|
| Li | 59.8 | 38.9 | <9.2 | <28.8 | <35.0 | 40.6 | 36.9 |
| Na | 11250.9 | 9864.9 | 7596.5 | 10396.5 | 9847.5 | 9791.2 | 9864.9 |
| Mg | 6.0 | 41.7 | 24.9 | 170.2 | 43.9 | 57.3 | 41.7 |
| Cl | 22493.7 | 21524.4 | 22493.7 | 22493.7 | 21524.4 | 22106.0 | 24493.7 |
| K | 348.0 | 341.1 | 161.5 | 998.6 | 325.1 | 434.9 | 341.1 |
| Ca | <2507.8 | <3146.9 | 5906.9 | <2567.1 | <3160.8 | 5906.9 | 5906.9 |
| Cu | <16.2 | 41.9 | 26.4 | 283.8 | 62.1 | 103.5 | 52.0 |
| Zn | 22.6 | <23.9 | 35.2 | <16.0 | <30.3 | 28.9 | 28.9 |
| As | <24.5 | <35.8 | <9.2 | <26.9 | <38.1 | <26.9 | <26.9 |
| Rb | <2.2 | <2.8 | <0.6 | <1.9 | <3.2 | <2.1 | <2.2 |
| Sb | <4.5 | <6.1 | <1.7 | 13.0 | 7.9 | 10.4 | 10.4 |
| Cs | <1.3 | <1.3 | <0.3 | <2.2 | <1.6 | <1.3 | <1.3 |

Table 7-41: Measurements in sample U1309D 1R-1 41-44 cm zone 2 quartz vein– wafer number 62965

| Analyte | Fi1 | Fi2 | Fi3 | Fi5 | Average | Median |
|---|---|---|---|---|---|---|
| Li | 39,2 | 50,9 | 47,3 | 47,2 | 46,2 | 47,2 |
| Na | 9568,5 | 10519,0 | 11164,0 | 13263,1 | 11128,7 | 10841,5 |
| Mg | <5,9 | 375,4 | 20,5 | 40,2 | 145,4 | 40,2 |
| Cl | 20550,7 | 21524,4 | 21524,4 | 26321,6 | 22480,2 | 21524,4 |
| K | <195,8 | 265,9 | 361,9 | <244,4 | 313,9 | 313,9 |
| Ca | <2962,6 | <2053,6 | <2041,6 | <2822,6 | <2470,1 | <2438,1 |
| Cu | 68,6 | <19,2 | <16,8 | 187,9 | 128,2 | 128,2 |
| Zn | <30,0 | <18,4 | <25,1 | 36,9 | 36,9 | 36,9 |
| As | <33,7 | <26,9 | <22,2 | <41,9 | <31,2 | <30,3 |
| Rb | <4,2 | 1,6 | <1,8 | <3,2 | 1,6 | 1,6 |
| Sb | 37,4 | <7,5 | <3,4 | 8,2 | 22,8 | 22,8 |
| Cs | <2,4 | <0,7 | <1,4 | <2,5 | <1,7 | <1,9 |

Table 7-42: Measurements in sample U1309D 1R-1 41-44 cm zone 3 quartz vein– wafer number 62965

| Analyte | Fi4 | Fi4bis | Fi4av | Fi5 | Fi3 | Fi1 | Average | Median |
|---|---|---|---|---|---|---|---|---|
| Li | <29,8 | 69,8 | 49,8 | <16,6 | 51,7 | 104,0 | 68,8 | 60,7 |
| Na | 9698,1 | 10282,5 | 9990,3 | 9731,6 | 9664,2 | 9768,9 | 9855,9 | 9750,3 |
| Mg | 70,1 | 5,2 | 37,6 | 176,7 | 6,1 | 42,9 | 56,4 | 40,3 |
| Cl | 20550,7 | 20550,7 | 20550,7 | 22493,7 | 19571,6 | 19571,6 | 19571,6 | 19571,6 |
| K | <178,5 | 178,6 | <178,5 | 296,8 | 285,3 | 609,1 | 342,5 | 291,1 |
| Ca | <2815,8 | <2305,1 | <2560,5 | 3604,7 | <2285,4 | 1691,7 | 2648,2 | 2648,2 |
| Cu | <28,4 | <21,4 | <24,9 | 170,0 | <19,5 | 203,1 | 186,5 | 186,5 |
| Zn | <26,1 | 31,2 | <28,6 | 62,4 | 39,3 | 112,6 | 61,4 | 50,8 |
| As | <31,2 | <26,5 | <28,8 | <9,9 | <26,5 | <11,3 | <22,3 | <26,5 |
| Rb | <4,6 | <3,6 | <4,1 | <1,5 | <2,7 | 1,0 | 1,0 | 1,0 |
| Sb | <5,8 | <4,4 | <5,1 | <2,8 | <5,5 | <1,7 | <4,2 | <4,8 |
| Cs | <2,1 | <1,6 | <1,8 | <0,6 | <2,0 | <0,6 | <1,5 | <1,7 |

Table 7-43: Measurements in sample U1309D 40R-1 17-19 cm zone 1 quartz vein– wafer number 63520

| Analyte | Fi1 | Fi1bis | Fi1av | Fi2 | Fi11 | Fi13 | Fi17 | Fi20 |
|---|---|---|---|---|---|---|---|---|
| Na | 6799,6 | 6835,3 | 6817,5 | 6150,3 | 6468,0 | 6526,4 | 6044,5 | 7075,4 |
| Mg | 158,0 | 162,7 | 160,4 | 90,6 | 109,8 | 143,8 | 62,0 | 200,2 |
| Cl | 18587,1 | 18587,1 | 18587,1 | 18587,1 | 19571,6 | 18587,1 | 18587,1 | 19571,6 |
| K | 4455,5 | 4603,5 | 4529,5 | 1425,5 | 1784,1 | 2811,7 | 1162,6 | 4549,5 |
| Ca | <1669,4 | <1559,5 | <1614,4 | <3540,5 | 3884,9 | <2256,9 | <3862,0 | 2056,9 |
| Mn | <2,0 | <1,8 | <1,9 | 27,9 | <3,8 | <3,2 | <4,1 | 7,3 |
| Fe | <504,6 | <497,9 | <501,2 | <979,6 | <555,6 | 1084,0 | <936,0 | 236,1 |
| Cu | | | | | <24,1 | 112,8 | | |
| Zn | | | | | 84,8 | 95,1 | | |
| Sr | 4,4 | 4,5 | 4,4 | 2,4 | 1,6 | 1,9 | 5,4 | 3,5 |
| Pb | | | | | 7,63 | 7,5 | | |

Table 7-43 (continued)

| Analyte | Fi22 | Fi24 | Fi27 | Fi31 | Fi32 | Fi34 | Fi37 | Fi39 |
|---|---|---|---|---|---|---|---|---|
| Na | 6777,3 | 7733,0 | 6722,1 | 6139,1 | 5584,0 | 5318,4 | 5523,2 | 5758,6 |
| Mg | 108,3 | 145,9 | 125,7 | 150,5 | 127,9 | 131,6 | 159,3 | 299,6 |
| Cl | 20550,7 | 20550,7 | 19571,6 | 16604,0 | 16604,0 | 16604,0 | 16604,0 | 16604,0 |
| K | 1726,9 | 5719,9 | 3087,0 | 4316,5 | 1738,4 | 905,6 | 1796,6 | 2291,8 |
| Ca | <3963,8 | <1437,6 | 3179,7 | 1353,5 | <2703,7 | 3553,6 | 2952,1 | 1731,3 |
| Mn | <8,9 | <2,3 | <0,8 | 3,3 | <7,0 | <2,7 | <2,4 | 3,2 |
| Fe | <935,1 | <290,1 | 322,9 | 299,0 | <983,4 | <709,3 | <601,0 | 1247,2 |
| Cu | | 49,8 | | | | | | 49,1 |
| Zn | | 75,1 | | | | | | 114,2 |
| Sr | 7,5 | 2,1 | 3,4 | 6,3 | 2,9 | 7,7 | 4,5 | 2,5 |
| Pb | | 3,4 | | | | | | 10,1 |

Table 7-43 (continued)

| Analyte | Fi40 | Fi41 | Fi41bis | Fi 41av | Fi43 | Average | Median |
|---|---|---|---|---|---|---|---|
| Na | 6882,1 | 6118,2 | 6026,9 | 6072,6 | 6063,4 | 6354,1 | 6150,3 |
| Mg | 229,3 | 306,8 | 127,7 | 217,3 | 703,6 | 186,7 | 150,5 |
| Cl | 20550,7 | 17598,3 | 17598,3 | 17598,3 | 19571,6 | 18441,7 | 18587,1 |
| K | 2432,1 | 2699,0 | 2739,4 | 2719,2 | 1365,5 | 2802,8 | 2699,0 |
| Ca | 3622,0 | 2104,2 | 2937,4 | 2520,8 | 3800,8 | 2808,1 | 2944,7 |
| Mn | 1,8 | 1,5 | 0,3 | 0,9 | <0,3 | 5,8 | 2,5 |
| Fe | 407,1 | 641,3 | 153,5 | 397,4 | 89,5 | 487,8 | 360,2 |
| Cu | 68,9 | 153,7 | 34,3 | 94,0 | 63,8 | 78,3 | 66,4 |
| Zn | 102,1 | 197,2 | 28,2 | 112,7 | 35,2 | 93,8 | 95,1 |
| Sr | 2,4 | 2,7 | 1,5 | 2,1 | 1,4 | 3,6 | 2,9 |
| Pb | 10,9 | 7,4 | 3,8 | 5,6 | 2,4 | 6,5 | 7,4 |

Table 7-44: Measurements in sample U1309D 40R-1 17-19 cm zone 2 quartz vein– wafer number 63520

| Analyte | Fi4 | Fi5 | Fi6 | Fi13 | Average | Median |
|---|---|---|---|---|---|---|
| Na | 6844,2 | 5181,3 | 7500,0 | 6547,2 | 6518,2 | 6695,7 |
| Mg | 575,9 | 2826,7 | 139,5 | 185,6 | 931,9 | 380,7 |
| Cl | 19571,6 | 19571,6 | 21524,4 | 19571,6 | 20059,8 | 19571,6 |
| K | 3920,5 | 869,8 | 3357,0 | 2008,4 | 2538,9 | 2682,7 |
| Ca | <1736,1 | 1349,8 | <2991,0 | 3605,6 | 2477,7 | 2477,7 |
| Mn | <3,4 | <0,8 | <4,7 | <1,5 | <2,6 | <2,4 |
| Fe | <472,1 | 99,9 | 895,2 | 428,2 | 474,5 | 428,2 |
| Cu | 66,6 | 23,1 | 34,8 | 32,8 | 39,3 | 33,8 |
| Zn | 53,1 | 6,4 | 57,4 | 275,1 | 98,0 | 55,3 |
| Sr | 3,8 | 1,1 | 3,2 | 2,0 | 2,5 | 2,6 |
| Pb | <2,5 | 1,3 | <3,1 | 3,7 | 2,5 | 2,5 |

Table 7-45: Measurements in sample U1309D 40R-1 17-19 cm zone 3 quartz vein– wafer number 63520

| Analyte | Fi3 | Fi5 | Fi8 | Fi13 | Fi16 | Fi17 | Average | Median |
|---|---|---|---|---|---|---|---|---|
| Na | 6338,7 | 6865,5 | 6231,2 | 6434,2 | 6318,5 | 6426,1 | 6435,7 | 6382,4 |
| Mg | 367,9 | 515,9 | 178,9 | 327,9 | 282,3 | 771,5 | 407,4 | 347,9 |
| Cl | 20550,7 | 20550,7 | 19571,6 | 20550,7 | 20550,7 | 20550,7 | 20387,5 | 20550,7 |
| K | 349,4 | 1624,1 | 835,4 | 529,3 | 384,2 | 1469,2 | 865,2 | 682,3 |
| Ca | <4616,3 | 2871,0 | 4294,2 | 4416,5 | 5051,7 | 3620,7 | 4050,8 | 4294,2 |
| Mn | <5,0 | 2,8 | <5,0 | <6,4 | <2,9 | 1,2 | 2,0 | 2,0 |
| Fe | <903,7 | 570,4 | 782,0 | <1005,4 | 464,4 | 415,1 | 558,0 | 517,4 |
| Cu | 41,1 | 891,0 | 37,1 | <41,2 | 69,0 | 79,4 | 223,5 | 69,0 |
| Zn | <25,0 | 275,8 | 73,2 | 76,5 | 43,3 | 54,0 | 104,6 | 73,2 |
| Sr | 6,2 | 25,8 | 5,1 | 5,9 | 2,5 | 5,8 | 8,5 | 5,8 |
| Pb | 25,0 | 80,5 | <5,4 | <5,8 | 9,6 | 5,8 | 30,2 | 17,3 |

Table 7-46: Measurements in sample U1309D 40R-1 21-24 cm zone 5 quartz vein– wafer number 62973

| Analyte | Fi1 | Fi3 | Fi5 | Fi6 | Fi7 | Fi8 | Fi12 | Fi13 |
|---|---|---|---|---|---|---|---|---|
| Li | <44,9 | <37,7 | <61,4 | <37,5 | <24,4 | <16,5 | <19,8 | <55,3 |
| Na | 7442,6 | 6404,3 | 6591,2 | 7943,7 | 7903,3 | 7859,7 | 7437,1 | 7010,8 |
| Mg | 7,2 | 233,8 | 109,1 | 371,6 | 467,7 | 432,2 | 456,4 | 387,9 |
| Cl | 20550,7 | 18587,1 | 20550,7 | 20965,0 | 22493,7 | 21524,4 | 21524,4 | 20550,7 |
| K | <273,3 | 1573,5 | 689,0 | 2825,4 | 2157,9 | 2207,1 | 1463,0 | 1472,5 |
| Ca | <4737,0 | <3434,5 | <5047,5 | <2606,9 | 3693,7 | 3226,6 | 3945,9 | <3651,4 |
| Mn | | | | | | | | |
| Ni | | | | | | | | |
| Co | | | | | | | | |
| Cu | <75,2 | 213,7 | <54,5 | 157,9 | 234,4 | 262,7 | 230,8 | 353,1 |
| As | <75,6 | <52,8 | <92,1 | <48,3 | <27,2 | <24,4 | <25,6 | <79,7 |
| Rb | <2,1 | <2,2 | 2,8 | 3,3 | 2,8 | 2,2 | 2,1 | <2,7 |
| Sr | <1,6 | 16,5 | 7,0 | 16,9 | 16,9 | 12,5 | 13,0 | 13,2 |
| Ag | | | | | | | | |
| Pb | <6,1 | 31,3 | 9,9 | 31,8 | 60,7 | 57,2 | 58,6 | 63,2 |

Table 7-46 (continued)

| Analyte | Fi14 | Fi15 | Fi17 | Fi18 | Fi21 | Fi24 | Fi25 | Average | Median |
|---|---|---|---|---|---|---|---|---|---|
| Li | <31,5 | | | | | | | 22,1 | 22,1 |
| Na | 7489,0 | 9925,4 | 10370,7 | 10036,0 | 9876,2 | 5561,5 | 6479,8 | 7920,6 | 7674,4 |
| Mg | 490,7 | 246,5 | 209,9 | 272,6 | 648,1 | 2710,6 | 1006,4 | 574,5 | 410,0 |
| Cl | 21524,4 | 20550,7 | 20550,7 | 20550,7 | 20550,7 | 20550,7 | 20550,7 | 20787,5 | 20550,7 |
| K | 2338,5 | 1436,0 | 1581,9 | 710,0 | 1177,6 | 740,1 | 1133,4 | 1536,1 | 1467,7 |
| Ca | 3321,2 | 1529,4 | 1145,1 | <1458,5 | <1103,1 | 1760,6 | 3432,0 | 2832,1 | 3321,2 |
| Mn | | <130,8 | <81,8 | <174,4 | <97,7 | 45,9 | 93,3 | 69,6 | 69,6 |
| Ni | | | | | | <14,7 | 75,8 | 75,8 | 75,8 |
| Co | | | | | | <0,6 | 1,4 | 1,4 | 1,4 |
| Cu | 293,3 | 194,5 | 270,4 | 573,3 | 219,5 | 168,6 | 232,2 | 249,6 | 231,5 |
| As | <25,2 | <81,8 | <46,3 | <122,5 | | | | 26,0 | 25,6 |
| Rb | 3,5 | <4,3 | 2,4 | <9,5 | | | | 2,7 | 2,6 |
| Sr | 14,6 | 10,5 | 6,9 | 6,8 | 6,0 | 4,1 | 11,6 | 11,2 | 12,1 |
| Ag | | | | | | <2,4 | 10,7 | 10,7 | 10,7 |
| Pb | 60,8 | 31,8 | 33,7 | 37,2 | 200,1 | 114,0 | 483,1 | 91,0 | 57,9 |

Table 7-47: Measurements in sample U1309D 40R-1 21-24 cm zone 6 and 13 quartz vein– wafer number 62973

| Analyte | Fi17a | Average | Median | Fi8 | Fi9 | Fi11 | Fi12 | Average | Median |
|---|---|---|---|---|---|---|---|---|---|
| Na | 6265,8 | 6265,8 | 6265,8 | 6322,1 | 6009,8 | 5083,8 | 6101,9 | 5879,4 | 6055,8 |
| Mg | 939,9 | 939,9 | 939,9 | 1819,0 | 2112,4 | 3714,6 | 182,9 | 1957,2 | 1965,7 |
| Cl | 19571,6 | 19571,6 | 19571,6 | 22493,7 | 20550,7 | 20550,7 | 19571,6 | 20791,7 | 20550,7 |
| K | 1356,4 | 1356,4 | 1356,4 | 519,7 | <1064,1 | 414,7 | 820,2 | 584,9 | 519,7 |
| Ca | 3039,7 | 3039,7 | 3039,7 | 3901,5 | <1310,9 | 593,3 | 4918,7 | 3137,8 | 3901,5 |
| Mn | <35,6 | <35,6 | <35,6 | <10,2 | <25,0 | <2,5 | <10,6 | <12,1 | <10,4 |
| Fe | | | | 38,3 | <1417,9 | 350,0 | 124,4 | 170,9 | 124,4 |
| Ni | 73,8 | 73,8 | 73,8 | | | | | | |
| Co | 2,3 | 2,3 | 2,3 | | | | | | |
| Cu | 333,1 | 333,1 | 333,1 | | | | | | |
| Sr | 14,3 | 14,3 | 14,3 | 2,8 | <4,6 | 1,0 | 13,3 | 5,7 | 2,8 |
| Ag | 14,0 | 14,0 | 14,0 | | | | | | |
| Pb | 456,8 | 456,8 | 456,8 | | | | | | |

Table 7-48: Measurements in sample U1309D 40R-1 21-24 cm quartz grain of trondjehmite– wafer number 62973

| Analyte | Fi23 | Fi26 | Fi27 | Fi29 | Fi35 | Average | Median |
|---|---|---|---|---|---|---|---|
| Na | 72266,7 | 97644,0 | 126499,7 | 73825,1 | 76732,0 | 89393,5 | 76732,0 |
| Mg | 184,0 | 1148,6 | 2153,2 | 2969,6 | 789,3 | 1449,0 | 1148,6 |
| Cl | 188661,1 | 212258,9 | 216566,0 | 211712,9 | 223784,8 | 210596,7 | 212258,9 |
| K | 53728,1 | 41019,4 | 7556,5 | 21039,0 | 24011,5 | 29470,9 | 24011,5 |
| Ca | 10015,9 | 6146,6 | 2265,3 | 20844,9 | 37053,8 | 15265,3 | 10015,9 |
| Mn | 7562,8 | 6851,3 | 1452,6 | 930,6 | 806,7 | 3520,8 | 1452,6 |
| Fe | | | | 25219,9 | 11629,2 | 18424,5 | 18424,5 |
| Ni | 421,7 | 622,2 | 1492,4 | | | 845,4 | 622,2 |
| Co | 13,2 | 13,2 | 10,1 | | | 12,2 | 13,2 |
| Cu | 125,8 | 697,6 | 890,9 | | | 571,4 | 697,6 |
| Sr | 22,0 | 25,0 | 16,3 | 29,3 | 21,2 | 22,8 | 22,0 |
| Ag | 117,6 | 624,8 | 1584,6 | | | 775,7 | 624,8 |
| Pb | 75,5 | 124,8 | 180,2 | | | 126,8 | 124,8 |

# 4 - Chemical processing for strontium analyses

## General procedures

Isotopic analysis by TIMS requires the strontium to be analyzed in the form of a pure salt. For silicate rocks this means the silicate minerals have to be decomposed and brought into solution in an appropriate acid.

The strontium can then be separated by cation exchange. In order to minimize contamination of the samples, all the labware used is either Teflon® or quartz glass and special quality reagents are used. The amount of sample used (and how much spike is added to determine concentration) depends on the concentrations of strontium and rubidium in the sample. Order of magnitude estimates of concentration are therefore required in advance, and can be estimated.

## Detailed procedure for rock samples analysis

A clean 15mL Savillex® screw-cap vial for each sample or blank determination is dried and cooled in preparation for weighing.

Immediately before weighing the vials are "zapped" with an anti-static pistol to reduce electrostatic charge build-up. The balance is then zeroed and each beaker is weighed empty in turn, the required amount of sample added and the weighing repeated. The mixed Rb-Sr spike is added at this stage. The amount of spike is read from the chart using a 'ball-park' estimate of the concentrations. Then the spike bottle is weighed and the required amount of spike is transferred into the sample vial, without loss. The spike bottle is then re-weighed and the amount of spike added to the sample is calculated from the loss in weight of the spike bottle. This procedure minimizes errors caused by evaporation losses from the spike drop during transfer. The gain in weight of the sample vial should always be recorded as well, as a cross-check. It will usually be 1- 2mg less than the bottle loss estimate.

The samples are then wetted with ca. 10µL concentrated sub-boiling distilled nitric acid/mg of sample and then, as soon as any initial vigorous reaction has subsided, 50µLs of 48% HF/mg sample are added from the dispenser bottle. The beakers are sealed and the samples left to digest on the hotplate overnight. The beakers are tapped to dislodge any drops of acid from the caps and then the screw caps are carefully removed and the excess acid plus $SiF_4$ are evaporated off under infra-red lamp and the sample taken to dryness. 1 mL concentrated sub-boiling distilled nitric acid is added to each sample, and then evaporated under the lamps again to breakdown fluorides. The dried samples are then taken into solution in 6mls of 6M hydrochloric acid. It is important that a clear solution is obtained at this stage. For that the samples screw caped are placed under infra -red-lamp. The samples are then dried again. 1.5 mLs of 2.5M hydrochloric acid are then added to each sample.

At this stage the cation exchange columns are conditioned with 2.5M hydrochloric acid.

The sample solution, together with any solids, is transferred to a cleaned 1.8ml disposable centrifuge tube and the sample centrifuged for 15 minutes. After centrifugation the tubes are carefully removed, avoiding any mechanical shock that would disturb any precipitate.

1 mL of clear supernatant sample solution is then picked up with a cleaned disposable Pasteur pipette and transferred to the cation exchange column drop by drop taking care not to stir up the top of the resin bed. After the sample solution has soaked into the resin bed, two 1mL volumes of clean 2.5M hydrochloric acid are used to rinse down the top of the narrow part of the column, each time allowing the acid to soak into the resin bed. From this point, further volumes of 2.5M hydrochloric acid are added to the column according to the calibration on the column chart. Apart from the rubidium and strontium collection volumes the acid is allowed to run to waste in the Pyrex beakers.

After the strontium has been collected the columns are immediately cleaned following the recipe on the column chart.

The strontium fraction is dried down under the lamps, re-dissolved in 1 mL 2.5M hydrochloric acid and passed through the column a second time. After the second column pass the strontium fraction is dried down and is then ready for mass spectrometry.

## Sample preparation for small sample analysis

### Sample preparation before loading onto the cation exchange columns

A clean 7ml Savillex screw-cap vial for each sample or blank determination is dried and cooled. The sample is transferred to an empty vial. Dilute Blue Rb-Sr spike is added at this stage based on expected Sr concentrations. The amount of spike added to the sample has to be the less possible knowing that the sample has not been weight due to its small size. The spike bottle is weighed before and after added it to the sample and the amount of spike added to the sample is calculated from the loss in weight of the spike bottle.

The samples are then wetted with ca. 10µL of concentrated UpA nitric acid and then, as soon as any initial vigorous reaction has subsided, 50µLs of 48% UpA HF are added. The beakers are sealed and the samples left to digest on the hotplate for at least 24 hours. At this stage, the following detailed of the procedure for the preparation of the samples can be undertaken in the same time than the preparation of the columns. The beakers are tapped to dislodge any drops of acid from the caps and then the screw caps are carefully removed and the excess acid plus $SiF_4$ are evaporated off under the infra-red lamp and the sample taken to dryness. 100µl UpA nitric acid is added to each sample, and then evaporated under the lamps again to breakdown fluorides. The dried samples are then taken into solution in 100µl of 6M UpA HCl. After complete solution is achieved the samples are dried and converted back to nitrate by evaporation with 50µl UpA of concentrated $HNO_3$. 180µl of 3M UpA $HNO_3$ is added to each sample. If the samples do not go into complete solution at this stage they are centrifuged immediately before loading onto the Sr-spec columns.

**Separation of Strontium using Sr-Spec**

Fresh resin and frits are used for each elution due to memory effects of the resin. The following cleaning procedures should be carried out in order to minimise blanks. Immediately prior to sample elution the following preparation is carried out on each column.

- Place frit in column and push half way into column with clean stainless rod.
- Fill column reservoir with $H_2O$ and push frit home.
- Rinse with several reservoir volumes (the reservoir has a capacity of approximately 800µl) of $H_2O$.
- Fill column with water and add resin to column, allowing it to settle through water.
- Wash resin with full reservoir of $H_2O$.
- Wash resin with half a reservoir of 5% $H_2SO_4$.
- Wash resin with 1 full reservoir of $H_2O$.
- Wash column with 1 full column 0.05M UpA $HNO_3$.

Resin has to be conditioned with 100µl 3M UpA nitric acid. Samples are loaded in 300µl 3M UpA $HNO_3$. The sides of the columns are rinsed with 50µl 3M UpA $HNO_3$. Columns are successively eluted with 600µL of 3M UpA $HNO_3$, and with 50µL of 0.05M UpA $HNO_3$. The original vial, which has been previously cleaned, is then placed under the columns to collect 350mL of 0.05 UpA $HNO_3$, which is the Sr fraction. The strontium fraction is dried down under the lamps with 1µL of $H_3PO_4$, re-dissolved in 50µL of 3M UpA $HNO_3$ and a second column pass is processed, starting again from the conditioning of the resin and finishing with Sr fraction collection. Add 1-2µL of $HClO_4$ and 1µL of $H_3PO_4$ before the final evaporation to dryness. The $HClO_4$ is necessary to remove organics which get stripped from the Sr spec resin during elution. Once the fraction dried down, the samples are then ready for mass spectrometry.

## Filament loading

After column separation, samples have to be loaded on a tungsten filament that will be heated in the mass spectrometer. Tungsten filament are first of all welded on holders and put in an outgasser machine in order to remove any impurities and to avoid any contamination from laboratory and from the user.

To load the sample on the filament, we use polyethylene dam, which are previously cleaned and dried up with acetone, and a TaCl loading solution. A small amount of loading solution is transferred in the sample vial, and sample plus loading solution are picked up with a micro pipette and transferred onto the filament. The filament is then progressively heated till the sample dries up. Every batch of five samples plus blank, is accompanied with one or two standards NIST SRM987 ($^{87}Sr/^{86}Sr = 0.71024$).

# 5 – Sample preparation for leaching experiment

The sample was reduced to powder using a dentis drill. A clean 7ml Savillex screw-cap vial for each sample (residue and leachate) is dried and cooled. The powder is wetted in 1 mL of 2.5 M HCl for 5 minutes in an ultrasonic bath. The sample + acid are transferred into a tube to be centrifuge for ~15 minutes. The supernatant is immediately collected after centrifugation, transferred into an empty clean vial, spiked and dried down. The residue is also transferred into an empty clean vial and dried down. The appropriate amount of spike is added. At this point, the sample is treated as a sample for strontium isotopic ratio determination (see *Appendix 4*). The dried down leachate is converted to nitrate prior to being prepared for strontium isotope determination.